JYU DISSERTATIONS 623

Olli Koskivaara

Non-Equilibrium Quantum Phenomena in the Early Universe

UNIVERSITY OF JYVÄSKYLÄ
FACULTY OF MATHEMATICS
AND SCIENCE

JYU DISSERTATIONS 623

Olli Koskivaara

Non-Equilibrium Quantum Phenomena in the Early Universe

Esitetään Jyväskylän yliopiston matemaattis-luonnontieteellisen tiedekunnan suostumuksella
julkisesti tarkastettavaksi yliopiston Ylistönrinteen salissa FYS1
huhtikuun 28. päivänä 2023 kello 12.

Academic dissertation to be publicly discussed, by permission of
the Faculty of Mathematics and Science of the University of Jyväskylä,
in Ylistönrinne, auditorium FYS1, on April 28, 2023 at 12 o'clock noon.

JYVÄSKYLÄN YLIOPISTO
UNIVERSITY OF JYVÄSKYLÄ

JYVÄSKYLÄ 2023

Editors
Ilari Maasilta
Department of Physics, University of Jyväskylä
Ville Korkiakangas
Open Science Centre, University of Jyväskylä

ISBN 978-951-39-9520-1 (PDF)
URN:ISBN:978-951-39-9520-1
ISSN 2489-9003

Permanent link to this publication: http://urn.fi/URN:ISBN:978-951-39-9520-1

Luonnontutkija heräsi plastic-teltassaan aamun sarastaessa. Hän oli täällä suuren järven ympäristössä tutkimassa erilaisia luonnonilmiöitä. Hän omisti paljon, suunnattoman paljon tietoa ja tästä johtuen hän ei enää ajatellutkaan samalla lailla kuin muut, tyhmemmät ihmiset.

— Veikko Huovinen, Kukin tavallaan
(Hirri, 1950)

ABSTRACT

Koskivaara, Olli
Non-equilibrium quantum phenomena in the early universe

We develop and apply to physical problems non-equilibrium quantum field theory techniques. With the mathematical framework provided by the 2PI effective action formalism we write down quantum transport equations for spatially homogeneous and isotropic systems, including coherence effects. The equations are based on the coherent quasiparticle approximation (cQPA), which predicts that quantum coherence effects are condensed on a singular shell at $k_0 = 0$ in the phase space of the system. We verify the existence of this shell by constructing the two-point function of the fermionic system exactly for a specific time-dependent mass profile, and give a comprehensive analysis of the phase space structures. We also use the exact solution to study the range of validity of the semiclassical approximation, finding out that its range of applicability may be much larger than what is suggested by naïve estimates.

We derive simple moment equations for scalar systems in which the loop interactions in the 2PI expansion are local. The equations are then used to study the coupled evolution of one- and two-point functions in two different setups. First, we study the Mexican hat -potential as a representative of a phase transition. Using the Hartree approximation in the 2PI loop expansion, we identify the processes of spinodal decomposition and parametric resonance in the time evolution of the coupled system. We discuss the processes in detail, finding out for example that the spinodal effects can allow the one-point function to cross a classically forbidden potential barrier. The second setup considers a non-minimally coupled spectator field during reheating after inflation. Similarly to the other system we establish the existence of spinodal and parametric effects, this time induced by the oscillating Ricci scalar. We compare the results to those obtained earlier with adiabatic methods, finding out that the non-equilibrium quantum effects can dramatically change the particle production efficiency.

Our results emphasize the important and intricate role quantum effects play in non-equilibrium systems. The accurate description of phenomena such as baryogenesis, early universe phase transitions in general and (p)reheating demands for field theoretic techniques capable of treating these non-equilibrium effects properly. Out methods provide new techniques to tackle this challenging task.

TIIVISTELMÄ (ABSTRACT IN FINNISH)

Koskivaara, Olli
Epätasapainokvantti-ilmiöitä varhaisessa maailmankaikkeudessa

Tässä väitöskirjassa kehitetään ja sovelletaan fysiikan ongelmiin kvanttikenttäteoreettisia tekniikoita epätasapainotilanteissa. Spatiaalisesti homogeenisille ja isotrooppisille systeemeille johdetaan koherenssiefektit sisältävä kvanttikuljetusteoria, lähtien 2PI-formalismista efektiiviselle aktiolle. Teorian (koherentti kvasihiukkasapproksimaatio eli cQPA) mukaan kvanttikoherenssiefektit ilmenevät systeemin faasiavaruudessa singulaarisella $k_0 = 0$ -kuorella. Kuoren olemassaolo todennetaan ja faasiavaruusrakennetta tarkastellaan yleisemmin konstruoimalla fermionisen systeemin kaksipistefunktio eksaktisti tietyn ajasta riippuvan massaprofiilin tapauksessa. Eksakteja ratkaisuja käytetään myös semiklassisen approksimaation toiminta-alueen tutkimiseen. Approksimaation havaitaan toimivan odotettua laajemmalla alueella.

Systeemeille, joissa silmukat 2PI-kehitelmässä ovat lokaaleja, johdetaan skalaarikenttien tapauksessa yksinkertaiset momenttiyhtälöt. Näitä yhtälöitä käytetään yksi- ja kaksipistefunktioiden kytketyn kehityksen tutkimiseen kahdessa eri asetelmassa. Ensimmäisessä tapauksessa tarkastellaan ”meksikolaishattupotentiaalia” esimerkkinä faasitransitiosta. Silmukkakehitelmän Hartree-approksimaatiossa systeemin aikakehityksessä identifioidaan kaksi ilmiötä: spinodaalinen dekompositio ja parametrinen resonanssi. Ilmiöitä tarkastellaan yksityiskohtaisesti. Spinodaalisten efektien havaitaan muun muassa mahdollistavan tunneloitumisen klassisesti kielletyn potentiaalivallin läpi. Toisessa asetelmassa tutkitaan gravitaatioon epäminimaalisesti kytkettyä spektaattorikenttää inflaation jälkeisen uudelleenlämmityksen aikana. Spinodaalisten ja parametristen efektien olemassaolo todennetaan jälkeen, tällä kertaa oskilloivan Riccin skalaarin aiheuttamina. Vertailemalla tuloksia aiemmin adiabaattisilla menetelmillä saatuihin havaitaan, että epätasapainokvanttiefektit voivat dramaattisesti muuttaa hiukkastuoton tehokkuutta.

Työn tulokset alleviivaavat kvanttiefektien tärkeää ja monimutkaista roolia epätasapainosysteemeissä. Ilmiöiden kuten baryogeneesi, yleiset varhaisen maailmankaikkeuden faasitransitiot sekä inflaation jälkeinen uudelleenlämmitys tarkka kuvailu vaatii epätasapainoefektien käsittelyä kenttäteoreettisin menetelmin. Tässä työssä kehitetyt tekniikat tarjoavat uusia työkaluja tähän haastavaan tehtävään.

Author

Olli Koskivaara
Department of Physics
University of Jyväskylä
Finland

Supervisor

Professor Kimmo Kainulainen
Department of Physics
University of Jyväskylä
Finland

Reviewers

Professor Arttu Rajantie
Department of Physics
Imperial College London
The United Kingdom

Professor Kimmo Tuominen
Department of Physics
University of Helsinki
Finland

Opponent

Professor Anders Tranberg
Department of Mathematics and Natural Sciences
University of Stavanger
Norway

PREFACE

The research leading to this thesis was conducted at the Physics Department of the University of Jyväskylä during the years 2016–2022.

First of all, I wish to thank my supervisor Prof. Kimmo Kainulainen. The journey has been long with many twists and turns, but with your guidance and enthusiasm it has been *fun*. On the way your approach to theoretical physics has truly taught me how making science is a balance between art and engineering.

I am also thankful to Senior Lecturer Sami Nurmi for additional guidance and for collaboration on one of the articles. Your voice of reason was indispensable. Quantum transport is a tricky business, and I am grateful to the rest of the cQPA-gang, Dr. Henri Jukkala, Mr. Harri Parkkinen and Mr. Pyry Rahkila, for many valuable discussions on these intriguing subjects. Another source of support has been the Würzburg collective working on similar problems. I wish to thank Prof. Werner Porod, Prof. Haye Hinrichsen, Mr. Thomas Garratt, Mr. Alexandre Alvarez, Mr. Amitayus Banik and Mr. Adam Büchner for collaboration and research visits, with special thanks to Thomas for hospitality, discussions and walks on the vineyard. An important part of my studies in physics were fellow students, of whom I especially wish to thank Lic. Juuso Leskinen, Mr. Tapani Stylman and Ms. Laura Laulumaa for countless conversations on physics and beyond.

I am thankful to Prof. Arttu Rajantie and Prof. Kimmo Tuominen for carefully pre-examining the original manuscript and for useful comments, and to Prof. Anders Tranberg for agreeing to be my opponent. I thank the teachers and administrators of the Physics Department for making this a pleasant environment to study and work. Financial support from the Magnus Ehrnrooth foundation is gratefully acknowledged.

Finally, I express my deepest gratitude to my family, and especially Iitu, for their love and support.

In Jyväskylä, March 2023
Olli Koskivaara

LIST OF INCLUDED ARTICLES

PI Henri Jukkala, Kimmo Kainulainen and Olli Koskivaara. **Quantum transport and the phase space structure of the Wightman functions**. *Journal of High Energy Physics*, **01** 012, (2020).

PII Kimmo Kainulainen and Olli Koskivaara. **Non-equilibrium dynamics of a scalar field with quantum backreaction**. *Journal of High Energy Physics*, **12** 190, (2021).

PIII Kimmo Kainulainen, Olli Koskivaara and Sami Nurmi. **Tachyonic production of dark relics: a non-perturbative quantum study**. *Journal of High Energy Physics*, **04** 043, (2023).

This PhD thesis consists of the ensuing introductory part and the articles listed above. The author had a significant role in developing the theoretical framework and performing the analytical calculations in all three articles. The numerical analysis of article [PIII] was carried out entirely by the author, and the author also had a leading role in most of the programming in articles [PI] and [PII]. The author wrote the first drafts of articles [PI] and [PII] and participated equally in writing article [PIII].

CONTENTS

1 INTRODUCTION

The Standard Model (SM) of particle physics is arguably one of the most successful scientific theories developed until the present day. It describes the interactions of the known elementary particles via the strong, weak and electromagnetic forces, thus encompassing three of the four fundamental forces. The fourth one, gravity, is described by the equally triumphant theory of general relativity, operating on the other end of the spectrum from micro- to macroscopic. The predictions of the Standard Model have been experimentally verified to extreme accuracy. The final missing piece included in the particle content of the Standard Model, the Higgs boson, was discovered in 2012 by the ATLAS [1] and CMS [2] experiments.

Despite its tremendous success, the Standard Model has also deficiencies. Notable examples are its inability to explain the observed non-zero neutrino masses, the existence of dark matter and dark energy and the abundance of matter over antimatter. As mentioned above, it also does not explain gravity, and combining the Standard Model and general relativity remains indeed the Holy Grail of theoretical physics. These and other shortcomings of the model have led to a rich field of so-called Beyond Standard Model theories, which try to fill in the gaps either by extending the original model in various ways or by taking some completely novel viewpoints.

The language of the Standard Model and of modern particle physics in general is quantum field theory (QFT). In spite of its name, quantum field theory is not actually a specific well-defined theory, but rather a vast toolbox of mathematical machinery and different physical principles. An important aspect of research in theoretical physics is refining this toolbox and developing new theoretical methods and approaches required by different problems. This calls for both conceptual and mathematical endeavours.

A specific theoretical branch that is under constant development and underlies a great deal of this thesis's subject matter is *non-equilibrium quantum field theory*. The usual quantum field theory covered in standard textbooks and capable of modelling most particle physics scenarios at a satisfactory level assumes that the quantum fields under examination are in their ground states, which

means that they do not exhibit non-trivial time evolution. There are however many phenomena in which the assumption of quantum states being in equilibrium does not hold. Various examples can be found in cosmology (phase transitions in the early universe, inflationary dynamics), in accelerator-based particle physics (relativistic heavy ion collisions) as well as in condensed matter physics (Bose–Einstein condensation). This thesis concerns aspects of certain non-equilibrium quantum field theory formalisms.

The structure of this thesis is as follows. In chapter 2 some early universe scenarios are reviewed to motivate the study of non-equilibrium quantum dynamics. In chapter 3 the two-particle irreducible formalism of non-equilibrium quantum field theory is summarized. This will lay out the basic mathematical framework for the ensuing parts. In chapter 4 quantum transport equations at different levels of approximation are introduced. Chapter 5 is devoted to applications of the presented formalism in specific scenarios. This chapter also encapsulates the core results of the publications included in this thesis. Chapter 6 collects the conclusions and the outlook of the thesis.

Throughout the thesis we use the "mostly-minus" convention for the signature of the Minkowski (and the FLRW) metric: $\eta_{\mu\nu} = \eta^{\mu\nu} = \mathrm{diag}(1, -1, -1, -1)$. A space-time four-vector is in general denoted as $x = (t, \boldsymbol{x}) = (x_0, \boldsymbol{x})$. Unless otherwise specified, we work in natural units: $c = \hbar = k_\mathrm{B} = 1$.

2 PHYSICAL MOTIVATION

Basic cosmology and the arguments behind inflation are reviewed. Baryogenesis is introduced.

2.1 Expanding universe

Cosmology is a branch of physics that studies the structure and evolution of the universe as a whole. The modern widely accepted cosmology framework successfully explains a wide variety of phenomena, starting from a hot and high density state to the present universe. One of the basic properties of the observed universe is its apparent homogeneity and isotropy: at large scales in every direction and at every point the universe is essentially the same. Obviously this is not the case at small scales – the universe is filled with complex structures from organisms to galaxies – but at the scales exceeding a hundred million light-years or so, the assumption of isotropy and homogeneity, called the *cosmological principle*, holds already well [3–5]. In the early universe the principle was even more accurate, as large structures had not formed yet, as can be directly seen in the uniformity of the cosmic microwave background (CMB) radiation.

Mathematically a homogeneous and isotropic universe is most generally described by the Friedmann–Lemaître–Robertson–Walker (FLRW) metric, which with our signature convention is [6]

$$\mathrm{d}s^2 = \mathrm{d}t^2 - a^2(t)\left[\frac{\mathrm{d}r^2}{1-Kr^2} + r^2\mathrm{d}\theta^2 + r^2\sin^2(\theta)\mathrm{d}\phi^2\right]. \tag{2.1}$$

Here t is the cosmic (or proper) time, $a(t)$ is the scale factor determining the time evolution of spatial distances and (r, θ, ϕ) are comoving spherical coordinates. K is a parameter describing the curvature of space: $K = 0$ corresponds to flat space while $K > 0$ and $K < 0$ correspond to spaces with positive (closed) and negative curvature (open), respectively. Observations have shown that our universe is extremely close to flatness [7]. In this limit the above space-time line-element in

Cartesian (x, y, x)-coordinates is simply

$$\mathrm{d}s^2 = g_{\mu\nu}\mathrm{d}x^\mu \mathrm{d}x^\nu = \mathrm{d}t^2 - a^2(t)\left(\mathrm{d}x^2 + \mathrm{d}y^2 + \mathrm{d}z^2\right), \tag{2.2}$$

which defines the Cartesian flat-space metric tensor $g_{\mu\nu}$. Finally, by defining the conformal time η via $a\mathrm{d}\eta \doteq \mathrm{d}t$, the line-element can be written simply $\mathrm{d}s^2 = a^2(\eta)\left(\mathrm{d}\eta^2 - \mathrm{d}\boldsymbol{x}^2\right)$. In this case the flat FLRW metric $g_{\mu\nu}$ is related to the Minkowski metric $\eta_{\mu\nu}$ by $g_{\mu\nu} = a^2\eta_{\mu\nu}$.

The evolution of the metric, and hence of the scale factor a, is dictated by the Einstein equations [6]

$$G_{\mu\nu} \doteq R_{\mu\nu} - \frac{1}{2}g_{\mu\nu}R = \frac{8\pi}{M_{\mathrm{Pl}}^2}T_{\mu\nu}, \tag{2.3}$$

where $G_{\mu\nu}$ is the Einstein tensor, $R_{\mu\nu}$ is the Ricci curvature tensor, $R \doteq g^{\mu\nu}R_{\mu\nu}$ is the Ricci scalar, $T_{\mu\nu}$ is the energy-momentum tensor and M_{Pl} is the Planck mass. These equations connect the geometry of the space-time (left-hand side) and the energy content of the universe (right-hand side).[1] In accordance with the cosmological principle the energy-momentum tensor is assumed to be described by an ideal fluid, in which case the Einstein equations (2.3) together with the flat FLRW metric (2.2) imply the *Friedmann equations* [6]

$$\left(\frac{\partial_t a}{a}\right)^2 = \frac{8\pi}{3M_{\mathrm{Pl}}^2}\rho, \tag{2.4a}$$

$$\frac{\partial_t^2 a}{a} = -\frac{4\pi}{3M_{\mathrm{Pl}}^2}(\rho + 3p), \tag{2.4b}$$

where ρ and p describe the energy density and pressure of the universe, respectively. Equation (2.4a) has on the left hand side the *Hubble parameter* $H \doteq \frac{\partial_t a}{a}$ characterizing the rate of expansion of the universe.

The Friedmann equations (2.4) describe the evolution of the scale factor a for a given energy-pressure-content, which has varied during the history of our universe. From equation (2.4b) we see that a content with $\rho + 3p < 0$ leads to an interesting situation: accelerated expansion, $\partial_t^2 a > 0$. This is not just a curiosity of the equation – it is what the present state of the universe appears to be. Several observations indicate that out universe is at the moment expanding at an accelerating pace [7]. The cause of this acceleration, dubbed *dark energy*, is an unknown component of the energy content of the universe. Explaining the physical mechanisms giving rise to dark energy is one of the great challenges in modern cosmology.

The present dark energy dominated era is not the only time we believe accelerated expansion took place in the evolution of the universe. There are reasons to believe that in its early stages the universe expanded acceleratingly

[1] As J. A. Wheeler put it in his autobiography [8]: *"Spacetime tells matter how to move; matter tells spacetime how to curve."*

during an epoch called *inflation*.

2.2 Dynamics of inflation

The motivation[2] to conjure up a phase of accelerated expansion in the early universe originally stemmed from some oddities in the standard cosmology picture: the horizon problem (why do seemingly causally disconnected regions share the same temperature spectrum), the flatness problem (in a matter/radiation-dominated universe the observed flatness requires an extreme fine-tuning of initial conditions) and the lack of certain (topological) relics [13–18]. In addition to reconciling these issues a major asset of the inflationary scenario has since become its prediction of density perturbations, which can work as a seed for all the structure created later in the universe [6, 19, 20].

The obvious question is: assuming an inflationary stage took place, what caused it? The question remains open, but the simplest known solution would be a single scalar field ϕ, generally called the *inflaton* field, with a suitable potential $V(\phi)$ [21]. The action of such a generic scalar field is written as

$$\mathcal{S}_\phi = \int \mathrm{d}^4x\sqrt{-g}\Big[-\frac{1}{2}g^{\mu\nu}(\nabla_\mu\phi)(\nabla_\nu\phi) - V(\phi)\Big], \tag{2.5}$$

where $g \doteq \det(g^{\mu\nu})$ and ∇_μ is the covariant derivative [6]. For a homogeneous field $\phi(t)$ in a flat FLRW-space-time this action implies the following energy density and pressure [22]:

$$\rho_\phi = \frac{1}{2}(\partial_t\phi)^2 + V(\phi), \tag{2.6a}$$

$$p_\phi = \frac{1}{2}(\partial_t\phi)^2 - V(\phi). \tag{2.6b}$$

Therefore the condition for accelerated expansion, $\rho + 3p < 0$, is according to equations (2.6) satisfied if the energy density and the pressure of the inflaton are dominated by its potential energy: $V(\phi) > (\partial_t\phi)^2$. Qualitatively this condition essentially means, that the slope of the potential should (at some region) be flat enough for the inflaton to slowly roll towards its minimum without acquiring enough kinetic energy to turn $\partial_t^2 a$ negative. This is the idea behind the so-called *slow-roll inflation* [14, 23], which, with various applications and extensions, has to date probably remained the most popular model of inflation. Typically in this scenario the inflaton field first slowly rolls down its potential in a region with $V(\phi) \gg (\partial_t\phi)^2$ – this is where the fluctuations observable in the CMB are generated [22]. Gradually the field acquires more kinetic energy until the equality $V(\phi) = (\partial_t\phi)^2$ is reached and inflation ends. The field continues to

[2] It should be mentioned, that the predictive power of inflation has over the ages also been subject to criticism by several scientists, see e.g. references [9–12].

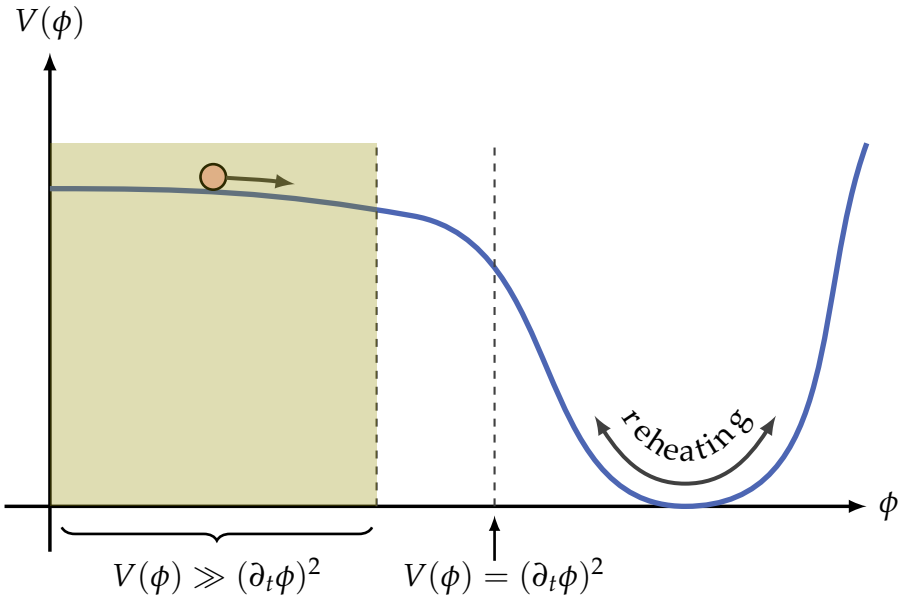

FIGURE 1 A schematic picture of a generic potential for slow-roll inflation. Initially the field rolls slowly in a region where its energy is dominated by the potential. Gradually it acquires more kinetic energy, and inflation ends when the kinetic energy starts to dominate. The field winds up oscillating around the minimum of the potential and reheats the universe.

roll down the potential and finally ends up oscillating around a minimum in a *reheating* phase. These generic features of slow-roll inflation are depicted in figure 1.

While the accelerated expansion accounts for the large scale problems such as horizon and flatness, the reheating phase following it becomes equally important. After inflation the universe is in a cold state[3], and the oscillatory phase provides a way to heat up the universe as the inflaton decays into other degrees of freedom. This is needed for the later standard evolution of the universe (Big Bang Nucleosynthesis) to proceed [27]. The detailed dynamics of reheating are generally highly complicated and depend strongly on the specific model and its particle content. Especially interesting are processes, in which the coupling of the oscillating inflaton field to other particles creates effectively time-dependent masses, which can lead to efficient particle production via parametric resonance [28–31] and spinodal instabilities [32–38]. These processes entail complicated quantum dynamics, and their accurate description requires the use of non-equilibrium quantum field theory techniques [39]. In section 5.2 we will use our quantum transport methods to study a toy model exhibiting the main qualitative features that appear in generic reheating scenarios.

Dynamics of fields other than the inflaton can also lead to interesting phenomena during reheating. As an example in section 5.3 we study a scenario, in which the oscillations of the inflaton during reheating result in spinodal and parametric particle production of a subdominant scalar field coupled to the in-

[3] There is an exception called *warm inflation*, in which particles are produced already during inflation [24–26].

flaton via the curvature scalar R. This spectator field serves as a candidate for the observed dark matter abundance [35,36,40].

2.3 Baryogenesis

Another interesting early universe concept is related to the matter content of the universe. In addition to usual matter consisting of (baryonic) particles the Standard Model also predicts the existence of antimatter, or antiparticles. These antiparticles are indeed seen in particle experiments and are present in cosmic rays, but only in tiny amounts. This disproportionality between baryons and antibaryons in the observable universe is usually quantified by the non-vanishing of the *baryon-to-photon ratio* η, which has e.g. from CMB-measurements found out to be [41]

$$\eta \doteq \frac{n_B}{n_\gamma} = (6.129 \pm 0.039) \times 10^{-10}, \tag{2.7}$$

where $n_B \doteq n_b - n_{\bar{b}}$ is the difference between baryon and antibaryon number densities and n_γ is the photon number density. The Standard Model does not fundamentally bring forth any asymmetry between particles and antiparticles, which poses the obvious question: why is there something instead of nothing? This issue concerning the observed *baryon asymmetry* is one of the big unanswered questions in physics.

One could say the asymmetry is just an initial condition for our universe, but this would not fit with the inflationary paradigm presented in the previous section: any initial abundance of baryons (or antibaryons, for that matter) would have been diluted away during the epoch of exponential expansion that stretched space by a factor of e^{60} at least [42]. Hence, assuming an inflationary epoch indeed took place, there is a need for a post-inflationary mechanism that produced the observed baryon asymmetry. Such a hypothetical mechanism is generally called *baryogenesis*.

In 1967 the Russian physicist Andrei Sakharov published a paper [43], in which he outlined three necessary ingredients that every successful baryogenesis model has to include:

(i) ***Baryon number violation.***

(ii) ***C- and CP-violation.***

(iii) ***Interactions out of thermal equilibrium.***

In the second condition C and P refer to charge and parity transformations, respectively. These requirements, nowadays known as the *Sakharov conditions*, are qualitatively fulfilled already within the Standard Model, but unfortunately they fall quantitatively short of being able to produce the observed baryon abundance. The electroweak phase transition, while providing non-equilibrium conditions, is known to be a crossover instead of a (strongly) first order one for

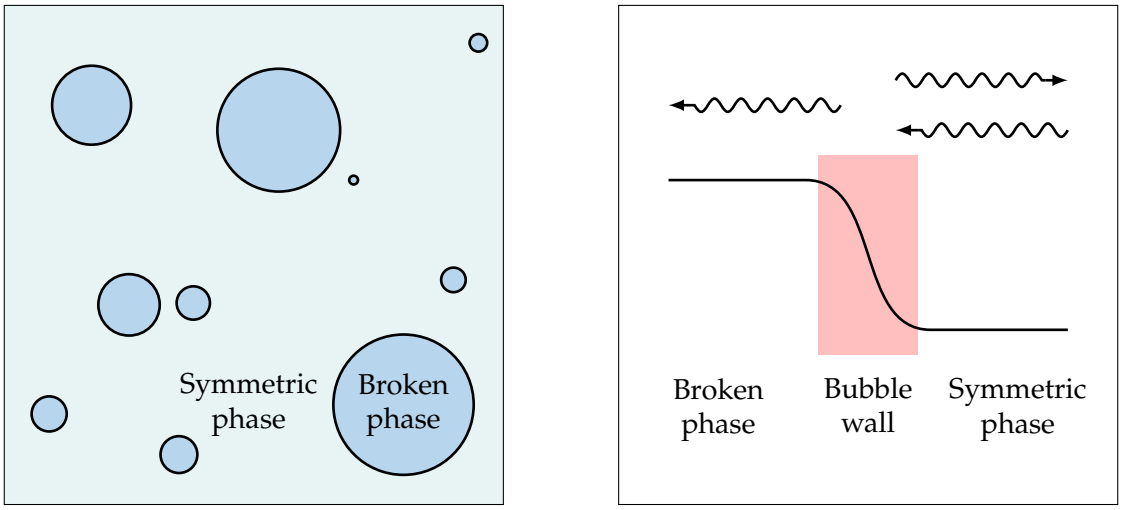

FIGURE 2 Features of a first order phase transition. The transition proceeds through nucleation and expansion of broken phase bubbles in the symmetric phase, as shown in the left panel. Microscopic effects become important at the bubble wall, where particles experience quantum reflection as illustrated in the right panel.

the observed mass of the Higgs boson at 125 GeV [44, 45]. The non-equilibrium conditions offered by such a transition are not sufficient for the needed baryon asymmetry [46]. Secondly, even if the transition was of first order, the amount of *CP*-violation induced by the CKM matrix is too small [47–49]. Baryon number is violated by anomalous non-perturbative (sphaleron) processes in the electroweak sector [50, 51], but without the other two conditions this is not enough. All in all, beyond Standard Model physics is needed for a working baryogenesis model [52]. Many baryogenesis mechanisms have been developed over time, but none of them has of yet been experimentally verified. Some of the most notable ones include electroweak baryogenesis [53], leptogenesis [54], the Affleck–Dine mechanism [55], and different GUT- and Planck-scale baryogenesis scenarios [42,56]. Our focus will be on the electroweak baryogenesis (EWBG), whose accurate description requires quantum transport techniques such as the ones developed in this thesis. Our techniques have also been applied to leptogenesis [57,58].

The electroweak baryogenesis relies on a strongly first order phase transition, which proceeds via nucleation of bubbles of the new (broken) phase in the original (symmetric) phase, as illustrated in the left panel of figure 2. Conditions near the bubble walls enable a way to generate a baryon asymmetry. The rapid expansion of the phase transition front provides conditions for the departure from equilibrium. Combined with the *CP*-violating interactions this leads to a chiral asymmetry in front of the transition wall, which drives the creation of the baryon asymmetry via the anomalous sphaleron processes which are unsuppressed in the symmetric phase (see e.g. reference [59]). The popularity of the electroweak baryogenesis stems from its minimal extensions to the Standard Model (most of the ingredients are already there) and from its testability (electroweak scale physics is well reachable by modern particle accelerators), and a

variety of models have indeed been introduced [60–64].

Of crucial importance in actual calculations within electroweak baryogenesis are the particle interactions at the wall – this is where the source asymmetry is generated. The situation, illustrated in the right panel of figure 2, is essentially a quantum reflection problem, whose description requires advanced quantum transport techniques in the presence of decohering collisions. There exist semiclassical approaches [65–70], designed to work for thick bubble walls, but in the thin wall limit the quantum effects become more dominant and more advanced techniques are needed. In this work we have developed non-equilibrium quantum field theory techniques suitable for these purposes. Specifically in article [PI] we studied a CP-violating wall as a toy model for the electroweak phase transition, revealing novel quantum effects as well as studying the range of applicability of the semiclassical approach. Also the quantum transport equations developed and used in articles [PII] and [PIII] are methodologically similar to the techniques in article [PI] and therefore relevant for the electroweak baryogenesis scenario.

3 NON-EQUILIBRIUM QUANTUM FIELD THEORY AND THE 2PI FORMALISM

The Schwinger–Keldysh formalism for out-of-equilibrium quantum systems is outlined. The 2PI effective action is introduced and equations of motion for the one- and two-point functions are derived.

3.1 The Schwinger–Keldysh formalism

In the usual vacuum (zero temperature) quantum field theory, used to study for example scattering processes, the asymptotic initial and final states of the particles are assumed to exist and be free. This allows for the typical "in-out" computations of transition amplitudes between the states, and such a machinery indeed works extremely well in the usual experimental setups such as particle accelerators, where the energy of the particles is large compared to the surrounding temperature and particle densities are typically modest: temperature excitations do not affect the processes and asymptotic states can be reasonably defined since there are not many particles interfering with each other. When it comes to computing (time-dependent) expectation values, the old "in-out" framework is obviously inadequate and one needs instead an "in-in" formalism.

If the temperature of the surroundings is comparable to the energy of the particles, the usual zero temperature -formalism must be improved to be able to treat thermal corrections. Some of the commonly used techniques are the imaginary time formalism [71], the real time formalism [72] and thermo field dynamics [73]. These *finite temperature* or *thermal field theories* assume that the system is in thermal equilibrium, and allow for perturbative calculations much in the same way as with the zero temperature quantum field theory.

If one wishes to go yet further and study non-equilibrium quantum systems, a different standpoint is needed. When we are interested in actual time evolution of quantum fields out of equilibrium, the density operator describing the state of the system is not known – we either wish to solve it or the n-point

functions defined by it. The Schwinger–Keldysh formalism, accompanied with the 2PI effective action -methods introduced shortly, provides an "in-in" formalism capable of handling with the corresponding time-dependent expectation values.

3.1.1 Closed time-path

The *Schwinger–Keldysh* or the *closed time-path (CTP) formalism* is a technique for calculating non-equilibrium expectation values of quantum objects, first developed by J. Schwinger for quantum mechanics [74], then refined to quantum field theory by his students P. M. Bakshi and K. T. Mahanthappa [75–77] and independently applied to statistical field theory by L. Keldysh [78]. Let us suppose we are studying a non-equilibrium system and we are interested in the time evolution of the expectation value of an observable $\mathcal{O}$. Mathematically this is given by

$$\langle \mathcal{O} \rangle = \mathrm{Tr}\big[\rho \mathcal{O}\big], \tag{3.1}$$

where ρ is the density matrix of the system, for which the normalization $\mathrm{Tr}[\rho] \doteq 1$ was assumed.[4] In thermal equilibrium the analytic form of ρ is known, e.g. $\rho \propto \mathrm{e}^{-H/T}$. For out-of-equilibrium systems the particular form of ρ is unknown – we can merely assume that we can specify it at some initial time t_{in}. The objective in non-equilibrium quantum field theory is then to find the time evolution of the density matrix, or equivalently of all the n-point functions defined by its initial value:

$$G^{(n)}(x_1, x_2, \ldots, x_n) \doteq \mathrm{Tr}\big[\hat{\rho}\hat{\phi}(x_1)\hat{\phi}(x_2)\cdots\hat{\phi}(x_n)\big], \tag{3.2}$$

where $\hat{\rho}$ and $\hat{\phi}$ are Heisenberg field operators and ϕ is an exemplary real scalar field.

Let us now focus on the two-point function $G^{(2)}$ and demonstrate the need for a closed time-path. We start by writing the propagator in terms of Schrödinger field operators $\hat{\phi}_{\mathrm{S}}$:

$$\langle \hat{\phi}(x_1)\hat{\phi}(x_2)\rangle = \mathrm{Tr}\big[\hat{\rho}\hat{U}(t_{\mathrm{in}}, t_1)\hat{\phi}_{\mathrm{S}}(\boldsymbol{x}_1)\hat{U}(t_1, t_{\mathrm{in}})\hat{U}(t_{\mathrm{in}}, t_2)\hat{\phi}_{\mathrm{S}}(\boldsymbol{x}_2)\hat{U}(t_2, t_{\mathrm{in}})\big], \tag{3.3}$$

where $\hat{U}(t_1, t_2)$ is the time evolution operator and $\hat{\rho} = \hat{\rho}(t_{\mathrm{in}})$. We will utilize a basis of field eigenstates $|\varphi_a\rangle$ of the Schrödinger field operator, $\hat{\phi}_{\mathrm{S}}(\boldsymbol{x})|\varphi_a\rangle = \varphi_a(\boldsymbol{x})|\varphi_a\rangle$, which is complete and orthonormal:

$$\int [\mathscr{D}\varphi_a]|\varphi_a\rangle\langle\varphi_a| = \mathbb{1}, \qquad \langle\varphi_a|\varphi_b\rangle = \delta[\varphi_a - \varphi_b] = \prod_{\boldsymbol{x}} \delta(\varphi_a(\boldsymbol{x}) - \varphi_b(\boldsymbol{x})), \tag{3.4}$$

where the functional integral measure is $[\mathscr{D}\varphi] \doteq \prod_{\boldsymbol{x}} \mathrm{d}\varphi(\boldsymbol{x})$ [71,79]. We shall also

[4] The role of the trace operation is to reduce the number of degrees of freedom: from a microscopic variable $\mathcal{O}$ with a large number of degrees of freedom we obtain a macroscopic quantity $\langle\mathcal{O}\rangle$ with just a few. The density matrix ρ operates between these two.

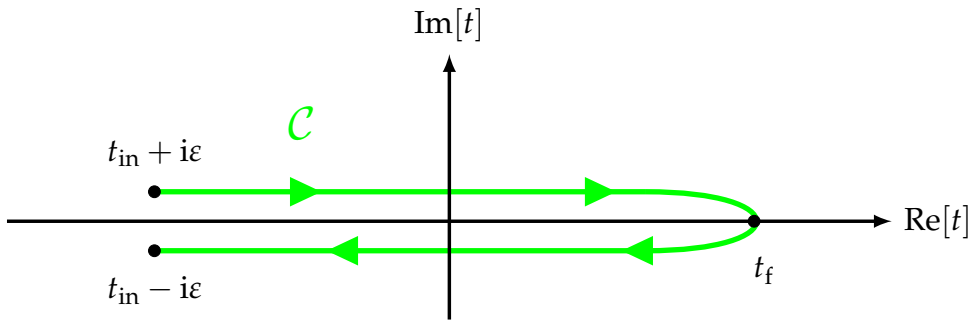

FIGURE 3 The Schwinger–Keldysh contour $\mathcal{C}$, running from an initial time $t_{\text{in}} + \mathrm{i}\varepsilon$ to a final time t_{f} and back to $t_{\text{in}} - \mathrm{i}\varepsilon$. The small imaginary parts $\pm\mathrm{i}\varepsilon$ are essential for the convergence of the (path) integrals. For visualization purposes the contour has been shifted clearly above and below the Re$[t]$-axis.

need the path integral representation of the transition amplitude:

$$\langle\varphi_b|\hat{U}(t_2,t_1)|\varphi_a\rangle = \int[\mathscr{D}\phi]\,\mathrm{e}^{\mathrm{i}\int_{t_1}^{t_2}\mathrm{d}t\int\mathrm{d}^3x\,\mathcal{L}[\phi(x)]} \doteq \int_{\varphi_a}^{\varphi_b}[\mathscr{D}\phi]\,\mathrm{e}^{\mathrm{i}\mathcal{S}[\phi]_{t_1}^{t_2}}, \tag{3.5}$$
$$\phi(t_1,\boldsymbol{x})=\varphi_a(\boldsymbol{x})$$
$$\phi(t_2,\boldsymbol{x})=\varphi_b(\boldsymbol{x})$$

where the integration in $[\mathscr{D}\phi] \doteq \prod_x \mathrm{d}\phi(x)$ is restricted by the conditions $\phi(t_1,\boldsymbol{x}) = \varphi_a(\boldsymbol{x})$ and $\phi(t_2,\boldsymbol{x}) = \varphi_b(\boldsymbol{x})$ [80].

Armed with these functional tools, together with the standard properties $\hat{U}(t_1,t_3)\hat{U}(t_3,t_2) = \hat{U}(t_1,t_2)$ and $\hat{U}(t_1,t_2) = \hat{U}^\dagger(t_2,t_1)$ of the time evolution operator, we can write the two-point function (3.3) as

$$\begin{aligned}
\langle\hat{\phi}(x_1)\hat{\phi}(x_2)\rangle &= \int\prod_{i=1}^{5}[\mathscr{D}\varphi_{a_i}]\langle\varphi_{a_1}|\hat{\rho}|\varphi_{a_2}\rangle\langle\varphi_{a_2}|\hat{U}(t_{\text{in}},t_1)\hat{\phi}_{\text{S}}(\boldsymbol{x}_1)|\varphi_{a_3}\rangle\langle\varphi_{a_3}|\hat{U}(t_1,t_{\text{f}})|\varphi_{a_4}\rangle \\
&\qquad\times\langle\varphi_{a_4}|\hat{U}(t_{\text{f}},t_2)\hat{\phi}_{\text{S}}(\boldsymbol{x}_2)|\varphi_{a_5}\rangle\langle\varphi_{a_5}|\hat{U}(t_2,t_{\text{in}})|\varphi_{a_1}\rangle \\
&= \int\prod_{i=1}^{5}[\mathscr{D}\varphi_{a_i}]\langle\varphi_{a_1}|\hat{\rho}|\varphi_{a_2}\rangle\int_{\varphi_{a_3}}^{\varphi_{a_2}}[\mathscr{D}\phi_1]\,\mathrm{e}^{\mathrm{i}\mathcal{S}[\phi_1]_{t_1}^{t_{\text{in}}}}\varphi_{a_3}(\boldsymbol{x}_1)\int_{\varphi_{a_4}}^{\varphi_{a_3}}[\mathscr{D}\phi_2]\,\mathrm{e}^{\mathrm{i}\mathcal{S}[\phi_2]_{t_{\text{f}}}^{t_1}} \\
&\qquad\times\int_{\varphi_{a_5}}^{\varphi_{a_4}}[\mathscr{D}\phi_3]\,\mathrm{e}^{\mathrm{i}\mathcal{S}[\phi_3]_{t_2}^{t_{\text{f}}}}\varphi_{a_5}(\boldsymbol{x}_2)\int_{\varphi_{a_1}}^{\varphi_{a_5}}[\mathscr{D}\phi_4]\,\mathrm{e}^{\mathrm{i}\mathcal{S}[\phi_4]_{t_{\text{in}}}^{t_2}} \\
&= \int_{i\in\{1,2,4\}}\prod[\mathscr{D}\varphi_{a_i}]\langle\varphi_{a_1}|\hat{\rho}|\varphi_{a_2}\rangle\int_{\varphi_{a_4}}^{\varphi_{a_2}}[\mathscr{D}\phi^-]\,\phi^-(x_1)\mathrm{e}^{\mathrm{i}\mathcal{S}[\phi^-]_{t_{\text{f}}}^{t_{\text{in}}}}\int_{\varphi_{a_1}}^{\varphi_{a_4}}[\mathscr{D}\phi^+]\,\phi^+(x_2)\mathrm{e}^{\mathrm{i}\mathcal{S}[\phi^+]_{t_{\text{in}}}^{t_{\text{f}}}} \\
&= \int[\mathscr{D}\phi^+][\mathscr{D}\phi^-]\langle\phi^+|\hat{\rho}|\phi^-\rangle\phi^-(x_1)\phi^+(x_2)\mathrm{e}^{\mathrm{i}\mathcal{S}[\phi^+]_{t_{\text{in}}}^{t_{\text{f}}}-\mathrm{i}\left(\mathcal{S}[\phi^-]_{t_{\text{in}}}^{t_{\text{f}}}\right)^*}\Big|_{\phi^-(t_{\text{f}},\boldsymbol{x})=\phi^+(t_{\text{f}},\boldsymbol{x})},
\end{aligned} \tag{3.6}$$

where the states $|\phi^\pm\rangle$ correspond to $\phi^\pm(t_{\text{in}},\boldsymbol{x})$. What we have obtained is a familiar-looking path integral representation, but with two distinct time branches: a forward branch for ϕ^+ from t_{in} to some final time t_{f}, and a backward branch for ϕ^- from t_{f} to t_{in}. This corresponds to the Schwinger–Keldysh contour $\mathcal{C}$,

which is depicted in figure 3.

The point we wanted to make with the above calculation is that if we wish to use the familiar path integral techniques in a non-equilibrium setting, the time-integration has to be performed on a closed path. Although we here considered the two-point function, the argument generalizes readily to other objects. In what follows, all time-dependent objects are expected to live on the complex time contour, unless otherwise specified. E.g. in integrations this is denoted by a subscript $\mathcal{C}$. We will also in general suppress operator hats from now on and use the shorthand notation $\mathcal{S}_\mathcal{C} \doteq \mathcal{S}[\phi^+] - \mathcal{S}[\phi^-]^*$ for the CTP-action.

3.1.2 Propagators

For many applications the quantities of interest are related to the two-point function of the system. In the Schwinger–Keldysh formalism we can write a generic propagator of a real scalar field as

$$\mathrm{i}\Delta(u,v) = \langle \mathcal{T}_\mathcal{C}\{\phi(u)\phi(v)\}\rangle, \tag{3.7}$$

where $\mathcal{T}_\mathcal{C}$ denotes time-ordering along the contour $\mathcal{C}$. When moving to real time prescription the propagator then splits naturally into four pieces, depending on which branches of the contour the time arguments lie on. To this end we define

$$\mathrm{i}\Delta^{\mathrm{F}}(u,v) \doteq \mathrm{i}\Delta^{++}(u,v) \doteq \langle \mathcal{T}\{\phi(u)\phi(v)\}\rangle, \tag{3.8a}$$
$$\mathrm{i}\Delta^{\overline{\mathrm{F}}}(u,v) \doteq \mathrm{i}\Delta^{--}(u,v) \doteq \langle \overline{\mathcal{T}}\{\phi(u)\phi(v)\}\rangle, \tag{3.8b}$$
$$\mathrm{i}\Delta^{<}(u,v) \doteq \mathrm{i}\Delta^{+-}(u,v) \doteq \langle \phi(v)\phi(u)\rangle, \tag{3.8c}$$
$$\mathrm{i}\Delta^{>}(u,v) \doteq \mathrm{i}\Delta^{-+}(u,v) \doteq \langle \phi(u)\phi(v)\rangle, \tag{3.8d}$$

where $\mathcal{T}$ and $\overline{\mathcal{T}}$ are the usual time- and anti-time-ordering operators. The superscripts $a, b \in \{+,-\}$ in Δ^{ab} denote the location of the time arguments on the contour: for example for $\Delta^{++}(u,v)$ both u_0 and v_0 lie on the upper branch of $\mathcal{C}$, whereas for $\Delta^{+-}(u,v)$ the second time argument v_0 is situated on the lower branch. The mixed cases $\Delta^< = \Delta^{+-}$ and $\Delta^> = \Delta^{-+}$ are called the *Wightman functions*.

Only two of the four propagators above are actually independent. Indeed, by explicitly opening up the time-ordering one can write the Feynman and anti-Feynman propagators in terms of the Wightman functions:

$$\Delta^{\mathrm{F}}(u,v) = \theta(u_0 - v_0)\Delta^>(u,v) + \theta(v_0 - u_0)\Delta^<(u,v), \tag{3.9a}$$
$$\Delta^{\overline{\mathrm{F}}}(u,v) = \theta(v_0 - u_0)\Delta^>(u,v) + \theta(u_0 - v_0)\Delta^<(u,v). \tag{3.9b}$$

The above relations also establish the equality $\Delta^{\mathrm{F}} + \Delta^{\overline{\mathrm{F}}} = \Delta^> + \Delta^<$. Even though two propagators suffice, there is a great number of auxiliary propagators with different interpretations and advantages in specific formulations. Two commonly used are the *spectral* and *statistical propagator* [81–83], which we define as

$\mathcal{A}(u,v) \doteq \frac{1}{2}\langle[\phi(u),\phi(v)]\rangle$ and $F(u,v) \doteq -\frac{\mathrm{i}}{2}\langle\{\phi(u),\phi(v)\}\rangle$, respectively. Spectral properties of the system are encoded in $\mathcal{A}$, while F contains statistical information such as occupation numbers [81]. These are again related to the Wightman functions by $\mathcal{A} = \frac{\mathrm{i}}{2}(\Delta^{>} - \Delta^{<})$ and $F = \frac{1}{2}(\Delta^{>} + \Delta^{<})$.

Another commonly used pair of two-point functions consists of the *retarded* and *advanced propagators* Δ^{r} and Δ^{a}:

$$\begin{aligned}\mathrm{i}\Delta^{\mathrm{r}}(u,v) &\doteq 2\theta(u_0 - v_0)\mathcal{A}(u,v)\\ &= \theta(u_0 - v_0)\left[\mathrm{i}\Delta^{>}(u,v) - \mathrm{i}\Delta^{<}(u,v)\right]\\ &= \mathrm{i}\Delta^{\mathrm{F}}(u,v) - \mathrm{i}\Delta^{<}(u,v),\end{aligned} \tag{3.10a}$$

$$\begin{aligned}\mathrm{i}\Delta^{\mathrm{a}}(u,v) &\doteq -2\theta(v_0 - u_0)\mathcal{A}(u,v)\\ &= \theta(v_0 - u_0)\left[\mathrm{i}\Delta^{<}(u,v) - \mathrm{i}\Delta^{>}(u,v)\right]\\ &= \mathrm{i}\Delta^{\mathrm{F}}(u,v) - \mathrm{i}\Delta^{>}(u,v).\end{aligned} \tag{3.10b}$$

These are used e.g. in the cQPA-formalism, which will be discussed in section 4.2. In the same context we also define the Hermitian propagator $\Delta^{\mathrm{H}} \doteq \frac{1}{2}(\Delta^{\mathrm{r}} + \Delta^{\mathrm{a}})$, which then allows for the decomposition $\Delta^{\mathrm{r/a}} = \Delta^{\mathrm{H}} \mp \mathrm{i}\mathcal{A}$.

All the definitions and decompositions above can be similarly done for fermionic two-point functions, the only difference being a minus sign here and there due to the anticommutativity of fermionic fields, c.f. references [69, 81]. Furthermore, the definitions will generalize to any other two-point objects introduced later on, such as the self-energies Π and Σ.

3.2 The 2PI effective action

In the previous section we saw how the so-called Schwinger–Keldysh formalism can be used to write non-equilibrium objects using path integrals. Next we shall review the 2PI effective action methods, which provide a way to derive consistent equations of motion for the one- and two-point functions of the system. The need for such techniques stems from the fact that using ordinary perturbation theory in non-equilibrium quantum field theory leads to certain problems such as secularity (solutions contain spurious terms growing with powers of time) and pinch singularities [81, 84].

We will work with a real scalar field ϕ (see e.g. reference [79] for the generalization to fermions). The starting point is the non-equilibrium generating functional, defined as [81, 85]

$$Z[J_1, J_2] \doteq \mathrm{Tr}\left[\hat{\rho}\,\mathcal{T}_{\mathcal{C}}\left\{\mathrm{e}^{\mathrm{i}\int_{\mathcal{C}}\mathrm{d}^4x\,\phi(x)J_1(x) + \frac{\mathrm{i}}{2}\int_{\mathcal{C}}\mathrm{d}^4x\,\mathrm{d}^4y\,\phi(x)J_2(x,y)\phi(y)}\right\}\right], \tag{3.11}$$

where $\hat{\rho}$ is an initial (non-equilibrium) density matrix and $J_{1,2}$ are local and non-local sources. Time-integration is performed along the Schwinger–Keldysh contour $\mathcal{C}$ presented in the previous section, and $\mathcal{T}_{\mathcal{C}}$ is the accordant time-ordering

operator along the contour. Equivalently to classical statistical systems, Z contains all the essential information of the non-equilibrium quantum field theory. Especially the non-equilibrium *n-point (Green's) functions* of equation (3.2) are obtained as functional derivatives with respect to the local source J_1:

$$G^{(n)}(x_1, x_2, \ldots, x_n) = \left. \frac{\delta^n Z[J_1, J_2]}{\mathrm{i}\delta J_1(x_1)\, \mathrm{i}\delta J_1(x_2) \ldots \mathrm{i}\delta J_1(x_n)} \right|_{J_1 = J_2 = 0}, \tag{3.12}$$

where the sources are set to zero in the end.

The derivation of the *2PI effective action* from the generating functional (3.11) proceeds by writing the functional in a path integral representation, assuming a Gaussian form for the initial density matrix and double Legendre transforming the generator of connected correlation functions $W[J_1, J_2] \doteq -\mathrm{i} \ln(Z[J_1, J_2])$ with respect to the two sources. The derivation is lengthy, and its details can be found e.g. in references [81,85]. For our purposes it suffices to know the final result for the 2PI effective action [86]:

$$\Gamma_{2\mathrm{PI}}[\varphi, G] = \mathcal{S}_{\mathcal{C}}[\varphi] + \frac{\mathrm{i}}{2}\mathrm{Tr}_{\mathcal{C}}\left[\ln\left(G^{-1}\right)\right] + \frac{\mathrm{i}}{2}\mathrm{Tr}_{\mathcal{C}}\left[G_0^{-1}G\right] + \Gamma_2[\varphi, G], \tag{3.13}$$

where $\mathcal{S}_{\mathcal{C}}$ is the classical (CTP) action, $\varphi(x) \doteq \langle \phi(x) \rangle$ is the macroscopic field[5] and $G(x, y)$ is the connected two-point function, describing fluctuations around φ. The trace involves integration over the Schwinger–Keldysh contour $\mathcal{C}$ of figure 3, and the classical inverse propagator is defined as

$$\mathrm{i}G_0^{-1}(x, y; \varphi) \doteq \frac{\delta^2 \mathcal{S}_{\mathcal{C}}[\varphi]}{\delta\varphi(x)\delta\varphi(y)}. \tag{3.14}$$

Finally, Γ_2 consists of all 2PI (two-particle irreducible) vacuum graphs with lines corresponding to the full propagator G and interaction rules read from the shifted Lagrangian density $\mathcal{L}[\phi \to \varphi + \phi_q]$, with ϕ_q being the quantum fluctuation.

In the 2PI effective action $\Gamma_{2\mathrm{PI}}$ both the one-point function φ and the two-point correlation function G are dynamical variables. It therefore provides a way to consistently study their coupled dynamics without resorting to standard perturbation theory techniques, which may be problematic in the non-equilibrium setting. The method also generalizes to higher order *n-particle irreducible (nPI)* effective actions, which can be formulated by adding more non-local sources to the partition function (3.11). A higher order (in n) action does however not a priori provide a more accurate picture, as for example for a given m-loop expansion all nPI effective actions with $n \geq m$ can be shown to be equivalent [87]. Typically one of the lowest order actions already provides a complete and self-consistent treatment for practical purposes [81].

For a chosen Γ_2 the equations of motion for the one- and two-point func-

[5] With many other names used in literature, such as the classical, mean, average and background field. We will mostly be referring to φ as the one-point function.

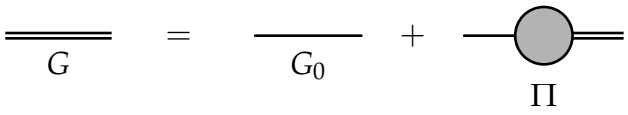

FIGURE 4 A generic structure of a Schwinger–Dyson equation, corresponding to equation (3.18). G is the full two-point function, G_0^{-1} is the classical inverse propagator and Π is the self-energy.

tions are obtained as the stationary conditions of the effective action:

$$\frac{\delta\Gamma_{2\mathrm{PI}}[\varphi, G]}{\delta\varphi} = 0, \tag{3.15a}$$

$$\frac{\delta\Gamma_{2\mathrm{PI}}[\varphi, G]}{\delta G} = 0. \tag{3.15b}$$

In particular, equation (3.15b) gives rise to the Schwinger–Dyson equation

$$G_0^{-1}(x,y) = G^{-1}(x,y) + \Pi(x,y), \tag{3.16}$$

where we defined the self-energy

$$\Pi(x,y) \doteq 2\mathrm{i}\,\frac{\delta\Gamma_2[\varphi, G]}{\delta G(y,x)} \tag{3.17}$$

via the interaction term Γ_2. Multiplying the Schwinger–Dyson equation (3.16) with $G(y,z)$, integrating over y, and further multiplying the resulting equation with $G_0(w,x)$ and integrating over x results in the often-used alternative form

$$G(w,z) = G_0(w,z) + \int_{\mathcal{C}} \mathrm{d}^4x\,\mathrm{d}^4y\, G_0(w,x)\Pi(x,y)G(y,z)\,, \tag{3.18}$$

which has the familiar graphical interpretation depicted in figure 4.

It is useful to divide the self-energy into a singular (local) and a non-singular (non-local) part:

$$\Pi(x,y) = \delta_{\mathcal{C}}^{(4)}(x-y)\Pi_{\mathrm{sg}}(x) + \Pi_{\mathrm{nsg}}(x,y). \tag{3.19}$$

If one now further assumes a standard form for the kinetic term of the action $\mathcal{S}$ and writes

$$\mathrm{i}G_0^{-1}(x,y) = -\left[\Box + M^2(x)\right]\delta_{\mathcal{C}}^{(4)}(x-y), \tag{3.20}$$

and then defines an effective mass squared function as the entire singular portion,

$$M_{\mathrm{eff}}^2(x) \doteq M^2(x) + \mathrm{i}\Pi_{\mathrm{sg}}(x), \tag{3.21}$$

the Schwinger–Dyson equation can be written in the transparent form

$$\mathrm{i}\left[\Box_x + M^2_{\mathrm{eff}}(x)\right] G(x,y) = \delta^{(4)}_{\mathcal{C}}(x-y) + \int_{\mathcal{C}} \mathrm{d}^4 z\, \Pi_{\mathrm{nsg}}(x,z) G(z,y), \tag{3.22}$$

where the last term on the right is called the *memory integral* or the *collision term*. Since in the 2PI setting both φ and G are dynamical variables, the above equation is coupled to that of the one-point function, given by the stationarity condition (3.15a),

$$\frac{\delta \mathcal{S}_{\mathcal{C}}[\varphi]}{\delta\varphi(x)} + \frac{\mathrm{i}}{2}\frac{\delta}{\delta\varphi(x)} \mathrm{Tr}_{\mathcal{C}}\left[G_0^{-1} G\right] + \frac{\delta\Gamma_2[\varphi, G]}{\delta\varphi(x)} = 0, \tag{3.23}$$

via the self-energy terms. For example in the case of a Lagrangian density $\mathcal{L} = \frac{1}{2}(\partial_\mu\phi)^2 - V(\phi)$ with a real polynomial potential $V(\phi) = \sum_{n=1}^{\infty} \xi_n \phi^n$ we have

$$\begin{aligned}\Bigg[\Box + \frac{1}{2} G(x,x) \sum_{n=3}^{\infty} n(n-1)(n-2)\xi_n \varphi^{n-4}(x) \\ + \sum_{n=1}^{\infty} n\xi_n \varphi^{n-2}(x)\Bigg]\varphi(x) = \frac{\delta\Gamma_2[\varphi,G]}{\delta\varphi(x)}.\end{aligned} \tag{3.24}$$

for the equation of motion for the one-point function.

So far we have written all the equations in contour notation, where it is understood that all objects live on the complex time contour $\mathcal{C}$. For further calculations it is useful to also write down the evolution equations in real time, i.e., explicitly for the components G^{ab} defined in equations (3.8). In this branch notation the Schwinger–Dyson equation (3.22) becomes [69]

$$\mathrm{i}\Big[\Box_x + M^2_{\mathrm{eff}}(x)\Big] G^{ac}(x,y) = a\delta^{ac}\delta^{(4)}(x-y) + b\int \mathrm{d}^4 z\, \Pi^{ab}_{\mathrm{nsg}}(x,z) G^{bc}(z,y), \tag{3.25}$$

where summation over b is implied, time-integration is still understood to be limited to $[t_{\mathrm{in}}, t_{\mathrm{f}}]$ and the self-energy function is given by

$$\Pi^{ab}(x,y) = 2\mathrm{i}ab\,\frac{\delta\Gamma_2[\varphi,G]}{\delta G^{ba}(y,x)} = a\delta^{ab}\delta^{(4)}(x-y)\Pi_{\mathrm{sg}}(x) + \Pi^{ab}_{\mathrm{nsg}}(x,y). \tag{3.26}$$

In the following chapter we will use the Schwinger–Dyson equations and 2PI methods introduced above to derive more applicable quantum transport equations.

4 QUANTUM TRANSPORT EQUATIONS

The Schwinger–Dyson equations implied by the 2PI effective action are written in the Wigner representation. The coherent quasiparticle approximation (cQPA) is introduced in the spatially homogeneous and isotropic case. General moment equations for local interactions are discussed.

4.1 Kadanoff–Baym, Wigner, and all that

The Schwinger–Dyson equations (3.22) derived from the 2PI effective action are in principle still as general as the full quantum field theory itself. As such they are therefore ineffective for solving any practical problems, and developing tractable approximation schemes is the first step towards realistic modelling of actual physical phenomena. We will now study the equations a bit more, most importantly writing them in a so-called Wigner representation. We will first work with the fermionic case, as it is of interest for the application of our approximation scheme introduced later in section 4.2. Section 4.3 deals with the bosonic case, including a derivation of generic transport equations in terms of moment functions.

As a starting point we take the fermionic version of the Schwinger–Dyson equation (3.25), which can be written as

$$\int \mathrm{d}^4z\, S_0^{-1}(x,z)S^{ac}(z,y) = a\delta^{ac}\delta^{(4)}(x-y) + b\int \mathrm{d}^4z\, \Sigma^{ab}(x,z)S^{bc}(z,y), \qquad (4.1)$$

where $S^{ab}(x,y)$ and $\Sigma^{ab}(x,y) \doteq -\mathrm{i}\delta\Gamma_2/\delta S^{ba}(y,x)$ are the fermionic two-point function and self-energy, respectively [79]. The self-energy is defined with a different prefactor compared to the case of a real scalar (3.17) due to the Grassmann nature of fermionic path integrals. Studying equation (4.1) for different branch indices explicitly and using the propagator definitions and relations of

section 3.1.2 allows us to split it into two pieces:

$$\int \mathrm{d}^4z \Big[S_0^{-1}(x,z) - \Sigma^{\mathrm{a,r}}(x,z)\Big] S^{\mathrm{a,r}}(z,y) = \delta^{(4)}(x-y), \tag{4.2a}$$

$$\int \mathrm{d}^4z \Big[S_0^{-1}(x,z) - \Sigma^{\mathrm{r}}(x,z)\Big] S^{<,>}(z,y) = \int \mathrm{d}^4z\, \Sigma^{<,>}(x,z) S^{\mathrm{a}}(z,y), \tag{4.2b}$$

Equations (4.2a) are called the pole equations, containing information on spectral properties of the system, while (4.2b) are called the kinetic or Kadanoff–Baym equations, describing dynamics and statistical properties.

Equations (4.2) are still coupled integro-differential equations for the two-point functions and self-energies, and as such often too complicated for practical purposes. For deriving kinetic equations apt for tractable approximations it is useful to introduce the *Wigner transformation*. For a generic function of two arguments $\mathcal{O}(u,v)$ this is defined as[6]

$$\mathcal{O}(k,x) \doteq \int \mathrm{d}^4r\, \mathrm{e}^{\mathrm{i}k\cdot r}\, \mathcal{O}\Big(x+\frac{r}{2}, x-\frac{r}{2}\Big), \tag{4.3}$$

where $r \doteq u-v$ and $x \doteq \frac{1}{2}(u+v)$ are the relative and average coordinates, respectively, characterizing the internal (microscopic) and external (macroscopic) behaviour of the system. In order to write equations (4.2) in a Wigner representation, we will need the following identity: the Wigner transformation of a generic convolution integral $C(u,v) = \int \mathrm{d}^4w\, A(u,w)B(w,v)$ is given by [69]

$$C(k,x) = \mathrm{e}^{-\mathrm{i}\diamondsuit}\big\{A(k,x)\big\}\big\{B(k,x)\big\}. \tag{4.4}$$

The diamond (Moyal) operator $\diamondsuit$ is for a pair of functions $f(k,x)$ and $g(k,x)$ defined as the operation

$$\diamondsuit\{f\}\{g\} \doteq \frac{1}{2}\big[(\partial_x f)\cdot(\partial_k g) - (\partial_k f)\cdot(\partial_x g)\big]. \tag{4.5}$$

The above definition can be used to construct $\diamondsuit^n$ for any $n \in \mathbb{N}$, and $\mathrm{e}^{-\mathrm{i}\diamondsuit}$ is then defined through a Taylor series.

Using the identity (4.4) we can write the evolution equations (4.2) in the Wigner representation as[7]

$$\Big(\not{k} + \frac{\mathrm{i}}{2}\not{\partial}_x\Big) S^{\mathrm{a,r}} - \mathrm{e}^{-\mathrm{i}\diamondsuit}\big\{\Sigma_m^{\mathrm{a,r}}\big\}\big\{S^{\mathrm{a,r}}\big\} = \mathbb{1}, \tag{4.6a}$$

$$\Big(\not{k} + \frac{\mathrm{i}}{2}\not{\partial}_x\Big) S^{<,>} - \mathrm{e}^{-\mathrm{i}\diamondsuit}\big\{\Sigma_m^{\mathrm{r}}\big\}\big\{S^{<,>}\big\} = \mathrm{e}^{-\mathrm{i}\diamondsuit}\big\{\Sigma^{<,>}\big\}\big\{S^{\mathrm{a}}\big\}, \tag{4.6b}$$

[6] Note the usual misnomer: we denote the Wigner (Fourier) transform with the same letter as the original function.

[7] Strictly speaking this requires sending $t_{\mathrm{in}} \to -\infty$ and $t_{\mathrm{out}} \to \infty$ in the Schwinger–Keldysh contour $\mathcal{C}$ due to the Wigner transformation. This does not affect the relevant properties of our systems of interest [69].

where we have assumed that all mass contributions from S_0^{-1} have been absorbed into the local parts of the self-energies $\Sigma^{\mathrm{r,a}}$ – this is denoted by $\Sigma_m^{\mathrm{r,a}}$. We also omitted the arguments (k, x) for a more compact notation. Equations (4.6) are still as general as the original Schwinger–Dyson equation (4.1)[8], but they provide a good starting point for the derivation of kinetic transport equations with different approximations. The cQPA, outlined in the next section, is an example of such an approximation scheme.

Before going to more specific formulations, it is worthwhile to take a closer look at the Wigner-transformed evolution equations (4.6), and especially of the diamond expansion. As such the gradient exponential mixes derivatives inconveniently, and performing systematic gradient approximations might be tricky. The situation can be elucidated by defining an *out-transformed* quantity as

$$\mathcal{O}_{\mathrm{out}}(k, x) \doteq \int \mathrm{d}^4 z \, \mathrm{e}^{\mathrm{i}k\cdot(x-z)} \mathcal{O}(x, z). \tag{4.7}$$

This function can be shown to be related to the usual Wigner transform through a differential exponential:

$$\mathcal{O}_{\mathrm{out}}(k, x) = \mathrm{e}^{\frac{\mathrm{i}}{2}\partial_x\cdot\partial_k} \, \mathcal{O}(k, x). \tag{4.8}$$

Using the out-transformation a typical collision term can be written as

$$\mathrm{e}^{-\mathrm{i}\diamondsuit}\Big\{\Sigma(k, x)\Big\}\Big\{S(k, x)\Big\} = \mathrm{e}^{-\frac{\mathrm{i}}{2}\partial_x^\Sigma\cdot\partial_k}\left[\Sigma_{\mathrm{out}}\left(k + \frac{\mathrm{i}}{2}\partial_x,\, x\right) S(k, x)\right], \tag{4.9}$$

where the expression ∂_x^Σ means a derivative operating solely on Σ_{out} [PI].

Using equation (4.9) we can write the Wigner-transformed equations as

$$\mathfrak{D} S^{\mathrm{a,r}} - \mathrm{e}^{-\frac{\mathrm{i}}{2}\partial_x^\Sigma\cdot\partial_k}\left[\Sigma^{\mathrm{a,r}}_{m\,\mathrm{out}}(\mathfrak{D}, x) S^{\mathrm{a,r}}\right] = \mathbb{1}, \tag{4.10a}$$

$$\mathfrak{D} S^{<,>} - \mathrm{e}^{-\frac{\mathrm{i}}{2}\partial_x^\Sigma\cdot\partial_k}\left[\Sigma^{\mathrm{r}}_{m\,\mathrm{out}}(\mathfrak{D}, x) S^{<,>}\right] = \mathrm{e}^{-\frac{\mathrm{i}}{2}\partial_x^\Sigma\cdot\partial_k}\left[\Sigma^{<,>}_{m\,\mathrm{out}}(\mathfrak{D}, x) S^{\mathrm{a}}\right], \tag{4.10b}$$

where all the propagators still have arguments (k, x) and we defined the differential operator $\mathfrak{D} \doteq k + \frac{\mathrm{i}}{2}\partial_x$. This form of the Kadanoff–Baym equations, first derived in article [PI], is extremely useful when it comes to gradient expansions or integrating over k since, instead of the mixing diamond operator $\diamondsuit$, one has a *total* derivative in k. Furthermore, the k-derivatives come paired with ∂_x^Σ, so if the self-energy Σ (and consequently Σ_{out}) varies slowly in the external coordinate x, one obtains a controlled gradient expansion.

[8] We assume that the kinetic term of the action if of a canonical form, leading to the generic structure $S_0^{-1}(u, v) = \big[\mathrm{i}\partial\!\!\!/_u - f(u)\big]\delta^{(4)}(u - v)$.

4.2 The cQPA for fermions

The coherent quasiparticle approximation (cQPA) is a comprehensive approximation scheme of the Kadanoff–Baym equations (4.2) (for bosons as well as for fermions) for systems with certain symmetries. It was first introduced in reference [88] and subsequently applied and developed further in references [89–94], with a recent extension to include finite width effects in reference [57]. At the heart of the theory is the existence of a novel shell structure in the phase space of the system: in addition to the usual mass shell solutions, there are singular shells encoding quantum coherence effects in the system. In the spatially homogeneous and isotropic case (we are not considering flavour mixing here) there is one such shell, situated at zero frequency ($k_0 = 0$) between the usual $k_0 = \pm\omega_{\boldsymbol{k}}$ -solutions, while for static cases with planar symmetry (i.e., with translation invariance lost in one spatial direction) it occurs at a momentum with $k_z = 0$, where z is the spatial coordinate orthogonal to the symmetry plane.

In this thesis we will stick to the spatially homogeneous and isotropic cQPA and mostly concentrate on the non-interacting case, as it allows for phase space studies and clear comparison for exact and semiclassical cases. As a background, on top of which interactions can be added, we take a Lagrangian density of a fermion with a time-dependent and complex mass:

$$\mathcal{L} = \mathrm{i}\bar{\psi}\partial\!\!\!/\psi - m^*(t)\bar{\psi}_{\mathrm{R}}\psi_{\mathrm{L}} - m(t)\bar{\psi}_{\mathrm{L}}\psi_{\mathrm{R}}, \tag{4.11}$$

where $\psi_{\mathrm{R,L}} \doteq P_{\mathrm{R,L}}\psi$, $P_{\mathrm{R}} \doteq \frac{1}{2}(1+\gamma^5)$ and $P_{\mathrm{L}} \doteq \frac{1}{2}(1-\gamma^5)$. The time-dependence (and more generally space-time-dependence) of the mass $m(t) \doteq m_{\mathrm{R}}(t) + \mathrm{i}m_{\mathrm{I}}(t)$ can be generated for example by an interaction of the fermion field ψ with a scalar field ϕ, i.e., through a Yukawa-type interaction $\mathcal{L}_{\mathrm{Yukawa}} = -\alpha\bar{\psi}\phi\psi$, where the scalar field obtains a (space-)time-dependent complex vacuum expectation value $\langle\phi(x)\rangle$. The motivation for this kind of an effective Lagrangian density is obtaining a toy model containing the qualitative requirements for baryogenesis. With the model (4.11) in mind, we now proceed to establish the basic structure of the cQPA.

The derivation of the cQPA is essentially a two-step procedure. First the spectral structure of the two-point functions is obtained at the level of free equations of motion – this is where the novel coherence shell is found. After this the shell structure is used as an ansatz for the full equations of motion, resulting in evolution equations containing quantum coherence effects. We begin by considering the Wigner-transformed Kadanoff–Baym equation (4.6b) for the lesser Wightman function $S^<$ (the case for $S^>$ is analogous). It can be shown [PI, 94], that in the absence of gradient corrections and collision terms and with the Lagrangian density of equation (4.11) the Hermitian part of equation (4.6b) can be written as

$$2k_0\bar{S}^<_{\boldsymbol{k}}(k_0,t) = \big\{\mathcal{H}_{\boldsymbol{k}}(t), \bar{S}^<_{\boldsymbol{k}}(k_0,t)\big\}, \tag{4.12}$$

where $\mathcal{H}_{\boldsymbol{k}}(t) \doteq \boldsymbol{\alpha}\cdot\boldsymbol{k} + \gamma^0\big[m_{\mathrm{R}}(t) + \mathrm{i}\gamma^5 m_{\mathrm{I}}(t)\big]$ with $\alpha^i \doteq \gamma^0\gamma^i$ for the space-like

gamma matrices, $\{\circ,\circ\}$ denotes the usual anticommutator and we defined the barred two-point function $\bar{S} \doteq iS\gamma^0$. We also introduced the notation $\mathcal{O}_k(k_0,t)$ for the Wigner transform in the spatially homogeneous and isotropic case, as the spatial part of the transformation reduces to the usual Fourier transformation. Note that equation (4.12) contains no derivatives (they appear in the anti-Hermitian part) – it instead contains information on the phase space structure of the system and is accordingly called the constraint equation. Our goal is then to reveal the possible phase space structures allowed by the equation, and to this end we introduce a convenient parametrization of the Wightman function.

We define the helicity and energy projection operators as

$$\mathcal{P}^{(4)}_{h\boldsymbol{k}} \doteq \frac{1}{2}\Big(\mathbb{1} + h\hat{h}_{\boldsymbol{k}}\Big), \qquad \mathcal{P}^{\varepsilon}_{\boldsymbol{k}} \doteq \frac{1}{2}\left(\mathbb{1} + \varepsilon\,\frac{\mathcal{H}_{\boldsymbol{k}}}{\omega_{\boldsymbol{k}}}\right), \tag{4.13}$$

where $\omega_{\boldsymbol{k}} \doteq \sqrt{|\boldsymbol{k}|^2 + |m(t)|^2}$ and $\hat{h}_{\boldsymbol{k}} \doteq (\boldsymbol{\alpha}\cdot\hat{\boldsymbol{k}})\gamma^5$ is the helicity operator with $\hat{\boldsymbol{k}} \doteq \boldsymbol{k}/|\boldsymbol{k}|$. The helicity h and the on-shell energy sign index ε take values $\{-1,1\}$, and it is straightforward to show that $\hat{h}_{\boldsymbol{k}}\mathcal{P}^{(4)}_{h\boldsymbol{k}} = h\mathcal{P}^{(4)}_{h\boldsymbol{k}}$ and $\mathcal{H}_{\boldsymbol{k}}\mathcal{P}^{\varepsilon}_{\boldsymbol{k}} = \varepsilon\omega_{\boldsymbol{k}}\mathcal{P}^{\varepsilon}_{\boldsymbol{k}}$. Most importantly, it can be shown that the eight matrices

$$\mathcal{B}^{\varepsilon_1\varepsilon_2}_{h\boldsymbol{k}} \doteq \mathcal{P}^{(4)}_{h\boldsymbol{k}}\mathcal{P}^{\varepsilon_1}_{\boldsymbol{k}}\gamma^0\mathcal{P}^{\varepsilon_2}_{\boldsymbol{k}} \tag{4.14}$$

with $h,\varepsilon_1,\varepsilon_2 \in \{-1,1\}$ span the Dirac subalgebra of a spatially homogeneous and isotropic system [57, 94]. Accordingly, we can with no loss of generality parametrize out two-point function as

$$\bar{S}^{<}_{\boldsymbol{k}}(k_0,t) \doteq \sum_{h,\,\varepsilon_1,\,\varepsilon_2} \mathcal{B}^{\varepsilon_1\varepsilon_2}_{h\boldsymbol{k}}(t)\, D^{\varepsilon_1\varepsilon_2}_{h\boldsymbol{k}}(k_0,t), \tag{4.15}$$

where $D^{\varepsilon_1\varepsilon_2}_{h\boldsymbol{k}}(k_0,t)$ are eight unknown coefficient functions.

Inserting the decomposition (4.15) into the constraint equation (4.12) and using the properties of the projection operators one can derive the following equations for the coefficient functions:

$$\big(k_0 - \varepsilon\omega_{\boldsymbol{k}}\big)D^{\varepsilon\varepsilon}_{h\boldsymbol{k}}(k_0,t) = 0, \tag{4.16a}$$

$$k_0\, D^{\varepsilon(-\varepsilon)}_{h\boldsymbol{k}}(k_0,t) = 0. \tag{4.16b}$$

These equations admit the distributional solutions

$$D^{\varepsilon\varepsilon}_{h\boldsymbol{k}}(k_0,t) = 2\pi\,\frac{\varepsilon\omega_{\boldsymbol{k}}}{m_{\mathrm{R}}}\, f^{m\varepsilon}_{h\boldsymbol{k}}\,\delta(k_0 - \varepsilon\omega_{\boldsymbol{k}}), \tag{4.17a}$$

$$D^{\varepsilon(-\varepsilon)}_{h\boldsymbol{k}}(k_0,t) = 2\pi f^{c\varepsilon}_{h\boldsymbol{k}}\,\delta(k_0), \tag{4.17b}$$

where $f^{m\varepsilon}_{h\boldsymbol{k}}(t)$ and $f^{c\varepsilon}_{h\boldsymbol{k}}(t)$ are called the mass-shell and coherence functions, respectively. The odd-looking normalization for $f^{m\varepsilon}_{h\boldsymbol{k}}$ in equation (4.17a) is chosen

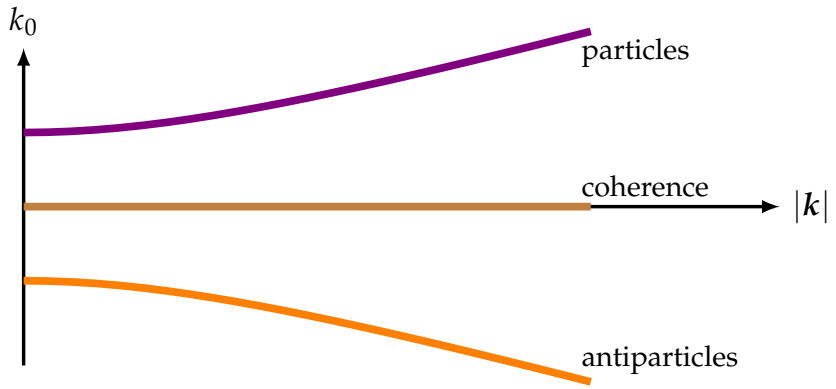

FIGURE 5 The general phase space structure of the spectral cQPA two-point functions in the $(k_0, |\boldsymbol{k}|)$-space. The particle (violet) and antiparticle (orange) solutions follow the familiar mass-shells at $k_0 = \pm\sqrt{\boldsymbol{k}^2 + |m|^2}$, while their mutual coherence (brown) is situated at $k_0 = 0$.

in such a way that when the entire Wightman function

$$\bar{S}^<_{\boldsymbol{k}}(k_0, t) = 2\pi \sum_{h,\varepsilon} \left[\mathcal{B}^{\varepsilon\varepsilon}_{h\boldsymbol{k}} \frac{\varepsilon\omega_{\boldsymbol{k}}}{m_{\mathrm{R}}} f^{m\varepsilon}_{h\boldsymbol{k}} \delta(k_0 - \varepsilon\omega_{\boldsymbol{k}}) + \mathcal{B}^{\varepsilon(-\varepsilon)}_{h\boldsymbol{k}} f^{c\varepsilon}_{h\boldsymbol{k}} \delta(k_0) \right] \tag{4.18}$$

is compared to the standard thermal propagator [72], the mass-shell functions correspond to the familiar Fermi–Dirac distributions: $f^{m\varepsilon}_{h\boldsymbol{k}} \xrightarrow{\text{thermal}} n_{\mathrm{FD}}(\varepsilon\omega_{\boldsymbol{k}})$, where $n_{\mathrm{FD}}(k_0) \doteq \left(\mathrm{e}^{k_0/T} + 1\right)^{-1}$ [94].

Equation (4.18) is for our later purposes the most important result of this section. It shows the cQPA phase space structure we described already earlier: in addition to the familiar mass shells $\sim \delta(k_0 \mp \omega_{\boldsymbol{k}})$ there is a zero frequency shell $\sim \delta(k_0)$. The information carried by this shell is interpreted as the quantum coherence between positive and negative frequency (particle and antiparticle) states [88,91]. Figure 5 illustrates the full phase space structure of the correlator. The existence of the novel singular shell at $k_0 = 0$ is exceptional, which is why in section 5.1 we study the phase space of the Wightman function in an exactly solvable system, not relying on the cQPA-methods. This allows us to ultimately verify the shell structure beyond the cQPA-formalism.

Although the shell structure is the aspect of most interest for the purpose of this thesis, for the cQPA-method it is just the first step. As already mentioned earlier, the second step is to use the cQPA two-point function (4.18) as an ansatz in the anti-Hermitian part of equation (4.6b), this time with all the gradients and interactions included. This eventually results in transport equations for the phase space densities $\partial_t f^{(m,c)\varepsilon}_{h\boldsymbol{k}}$. Here we just quote the final result from article [PI]:

$$\partial_t f^{m\varepsilon}_{h\boldsymbol{k}} = \frac{\varepsilon}{2} \sum_{\tilde{\varepsilon}} \Xi^{\tilde{\varepsilon}}_{h\boldsymbol{k}} f^{c\tilde{\varepsilon}}_{h\boldsymbol{k}} + \frac{\varepsilon\omega_{\boldsymbol{k}}}{m_{\mathrm{R}}} \operatorname{Tr}\left[\mathcal{C}_{\mathrm{coll}} \mathcal{B}^{\varepsilon\varepsilon}_{h\boldsymbol{k}}\right], \tag{4.19a}$$

$$\partial_t f^{c\varepsilon}_{h\boldsymbol{k}} = -2\varepsilon \mathrm{i}\omega_{\boldsymbol{k}} f^{c\varepsilon}_{h\boldsymbol{k}} + \xi_{\boldsymbol{k}} \Xi^{-\varepsilon}_{h\boldsymbol{k}} \left(\frac{m_{\mathrm{R}}}{\omega_{\boldsymbol{k}}} f^{c\varepsilon}_{h\boldsymbol{k}} - \frac{1}{2} \sum_{\tilde{\varepsilon}} \tilde{\varepsilon} f^{m\tilde{\varepsilon}}_{h\boldsymbol{k}} \right) + \xi_{\boldsymbol{k}} \operatorname{Tr}\left[\mathcal{C}_{\mathrm{coll}} \mathcal{B}^{(-\varepsilon)\varepsilon}_{h\boldsymbol{k}}\right], \tag{4.19b}$$

where the collision term is

$$\mathcal{C}_{\text{coll}} = \sum_{h,\varepsilon}\left\{\left[\frac{1}{2}\bar{\Sigma}^{<}_{\boldsymbol{k}}(\varepsilon\omega_{\boldsymbol{k}}) - f^{m\varepsilon}_{h\boldsymbol{k}}\,\bar{\Sigma}^{\mathcal{A}}_{\boldsymbol{k}}(\varepsilon\omega_{\boldsymbol{k}})\right]\mathcal{B}^{\varepsilon\varepsilon}_{h\boldsymbol{k}} - f^{c\varepsilon}_{h\boldsymbol{k}}\,\bar{\Sigma}^{\mathcal{A}}_{\boldsymbol{k}}(\varepsilon\omega_{\boldsymbol{k}})\mathcal{B}^{\varepsilon(-\varepsilon)}_{h\boldsymbol{k}}\right\} + \text{H. c.} \quad (4.20)$$

with H. c. denoting the Hermitian conjugate of the first term and we have defined

$$\Xi^{\varepsilon}_{h\boldsymbol{k}} \doteq \partial_t\left(\frac{m_{\text{R}}}{\omega_{\boldsymbol{k}}}\right) + \mathrm{i}\frac{\varepsilon h|\boldsymbol{k}|}{\omega^2_{\boldsymbol{k}}}\,\partial_t m_{\text{I}}, \qquad \xi_{\boldsymbol{k}} \doteq \frac{\omega^2_{\boldsymbol{k}}}{\omega^2_{\boldsymbol{k}} - m^2_{\text{R}}}. \quad (4.21)$$

The barred self-energies are defined with the γ^0-matrix positioned oppositely to the barred propagators, $\bar{\Sigma}^{<} \doteq \mathrm{i}\gamma^0\Sigma^{<}$ and $\bar{\Sigma}^{\mathcal{A}} \doteq \gamma^0\Sigma^{\mathcal{A}}$, but the splitting to Wightman and spectral components is equivalent.

Even though equations (4.19) might look complicated on the surface, the problem has been reduced to first order differential equations for the phase space densities with the time-dependent mass and self-energies from chosen interactions as input. In the article [PI] we applied these equations to solve the phase space densities for certain exemplary self-energies.

4.3 General moment equations for scalars

The cQPA is an approximative method, whose advantage lies in its high applicability to interacting theories while maintaining information on quantum coherence effects. In certain cases and for certain quantities the Schwinger–Dyson equation (3.22) coupled to the equation of motion of the one-point function (3.23) can however be solved exactly with surprisingly compact methods. The key idea is to turn the Schwinger–Dyson equations into *moment equations*, as will be detailed next. We will work with bosonic equations, as they will be relevant for the applications considered later in sections 5.2 and 5.3.

The first step in using the 2PI action (3.13) to study any realistic model is choosing the diagram or diagrams that are included in the interaction part Γ_2 – this will depend on the type of interactions present in the model and on the accuracy to which one wishes to study it. Suppose that the chosen Γ_2 consists of solely local diagrams, rendering also the self-energy of equations (3.17) and (3.19) local ($\Pi_{\text{nsg}} = 0$). In this case the bosonic Schwinger–Dyson equation is simply

$$\mathrm{i}\left[\Box_x + M^2_{\text{eff}}(x)\right] G(x,y) = \delta^{(4)}_{\mathcal{C}}(x-y), \quad (4.22)$$

where the effective mass function is defined in equation (3.21). By definition M_{eff} in general depends on G itself via the self-energy, but this does not affect the structure of the equations we develop. If we furthermore assume again that the system is spatially homogeneous and isotropic, the corresponding equation

in Wigner space and for the lesser Wightman function can be shown to be

$$\left[\frac{1}{4}\partial_t^2 - k^2 - \mathrm{i}k_0\partial_t + \mathrm{e}^{-\frac{\mathrm{i}}{2}\partial_t^M \partial_{k_0}} M^2_{\mathrm{eff}}(t)\right] G^<_{\boldsymbol{k}}(k_0, t) = 0, \tag{4.23}$$

where the time derivative ∂_t^M in the exponential only acts on the effective mass function M^2_{eff}. On top of this there is in general also an equation for the one-point function from equation (3.23), which couples through the effective mass function which can be a function of both the one- and the (local) two-point function.

Equation (4.23) is still highly complicated due to the infinite tower of t- and k_0-derivatives arising from the exponential. We can however cast its essential features into a much simpler form by considering the *moment functions* defined by $G^<_{\boldsymbol{k}}$:

$$\rho_{n\boldsymbol{k}}(t) \doteq \int \frac{\mathrm{d}k_0}{2\pi}\, k_0^n\, G^<_{\boldsymbol{k}}(k_0, t). \tag{4.24}$$

The trick is that since the t- and k_0-derivatives in equation (4.23) come in pairs, integrations over k_0 will give rise to neglectable surface terms, truncating the gradient exponential. Indeed, first splitting equation (4.23) into real and imaginary parts:

$$\left[k^2 - \tfrac{1}{4}\,\partial_t^2 - \cos\left(\tfrac{1}{2}\partial_t^M \partial_{k_0}\right) M^2_{\mathrm{eff}}(t)\right] G^<_{\boldsymbol{k}}(k_0, t) = 0, \tag{4.25a}$$

$$\left[k\cdot\partial_t + \sin\left(\tfrac{1}{2}\partial_t^M \partial_{k_0}\right) M^2_{\mathrm{eff}}(t)\right] G^<_{\boldsymbol{k}}(k_0, t) = 0, \tag{4.25b}$$

and then integrating both equations over k_0 and furthermore integrating equation (4.25b) weighted by k_0 gives rise to the following equations for the three lowest moments:

$$\left(\frac{1}{4}\partial_t^2 + |\boldsymbol{k}|^2 + M^2_{\mathrm{eff}}\right)\rho_{0\boldsymbol{k}} - \rho_{2\boldsymbol{k}} = 0, \tag{4.26a}$$

$$\partial_t \rho_{1\boldsymbol{k}} = 0, \tag{4.26b}$$

$$\partial_t \rho_{2\boldsymbol{k}} - \frac{1}{2}\left[\partial_t\left(M^2_{\mathrm{eff}}\right)\right]\rho_{0\boldsymbol{k}} = 0. \tag{4.26c}$$

As we can see, the equation for $\rho_{1\boldsymbol{k}}$ decouples at this level, and the remaining equations for $\rho_{0\boldsymbol{k}}$ and $\rho_{2\boldsymbol{k}}$ form a closed set of simple coupled differential equations.

In spite of their simplicity, equations (4.26) are still completely exact per se – the only approximation has been the choice that Γ_2 consists of local diagrams, which dictates the form of the effective mass function M^2_{eff}. This mass function will eventually in general be a function of the one-point function $\varphi(t)$ and the local two-point function $G(t,t)$, which coincides with the three-momentum integral of the zeroth moment function:

$$G(t,t) = \int \frac{\mathrm{d}^3\boldsymbol{k}}{(2\pi)^3}\, \rho_{0\boldsymbol{k}}(t). \tag{4.27}$$

Because the local two-point function is a divergent quantity, the definition of M^2_{eff} requires a careful renormalization procedure, which is carried out in detail in article [PII].

The simple form of equations (4.26) is deceiving. For a given model they are to be solved along with the equation (3.23) for the one-point function φ, and all the equations are further coupled through the effective mass function $M^2_{\text{eff}}(\varphi(t), G(t,t))$, which itself generally depends on the (local) two-point function and accordingly has to be solved from a gap equation. The moment functions obtained as solutions are not as general as the full two-point function $G^<(x,y)$ we began with due to the k_0-integration. Yet they contain all the information relevant for the quantities we are usually mostly interested in, such as the local two-point function $G(t,t)$, particle and energy densities and currents and the evolution of the one-point function.

4.3.1 Friction

Finally, we mention adding friction to the moment equations. Even though equations (4.26) as such only hold in the collisionless case (i.e., for a local self-energy), they can rather easily be generalized to include phenomenological dissipative terms. Similar moment equations with collision terms were studied in reference [90] with a refined cQPA-analysis given in reference [93]. Our purpose with the applications considered later is not to perform first principles calculations of collision integrals from interactions, but we do wish to study the effects of friction qualitatively. To this end it is enough to know the general structure of the moment equations (4.26) with collision terms, which according to reference [90] is

$$\left(\frac{1}{4}\partial_t^2 + |\boldsymbol{k}|^2 + M^2_{\text{eff}}\right)\rho_{0k} - \rho_{2k} = -\#_1\partial_t\rho_{0k}, \tag{4.28a}$$

$$\partial_t\rho_{1k} = -\#_2\left(\rho_{1k} - \rho^{\text{eq}}_{1k}\right), \tag{4.28b}$$

$$\partial_t\rho_{2k} - \frac{1}{2}\left[\partial_t\left(M^2_{\text{eff}}\right)\right]\rho_{0k} = -\#_2\left(\rho_{2k} - \rho^{\text{eq}}_{2k}\right), \tag{4.28c}$$

where ρ^{eq}_{ik} are equilibrium moment functions, the form of which can be chosen separately for each problem at hand, and $\#_{1,2}$ are coefficients that arise from the collision terms. In general these coefficients $\#_{1,2}$ are some functions of three-momentum and time, but for a phenomenological analysis they can be taken to be constants.

The moment equations derived in this section provide a compact way to study the coupled time evolution of the one- and the two-point functions in non-equilibrium settings with the backreaction of the two-point function properly accounted for. In articles [PII] and [PIII] we have used these equations to study a model with spontaneous symmetry breaking potential and the evolution of a spectator field during inflationary reheating. Although we have here restricted ourselves to the spatially homogeneous and isotropic situation, which is the case

in our applications, moment equations similar to the ones considered above can also be derived in the planar symmetric case, where not time but one spatial coordinate is non-trivial [90].

5 APPLICATIONS

The phase space structure of the fermionic Wightman function is established and compared to the cQPA in an analytically solvable case. The range of validity of the semiclassical approximation is studied. The moment equations presented in the previous chapter are applied to study the interplay of the one- and two-point functions in two different setups. Section 5.1 is related to article [PI], while sections 5.2 and 5.3 are related to articles [PII] and [PIII], respectively.

5.1 The kink-profile

In order to study in more detail the properties of the cQPA introduced in section 4.2, we will now specify a certain form for the time-dependent mass profile $m(t)$. Namely, we will use a hyperbolic tangent function, the so-called "kink" profile:

$$m(t) = m_1 + m_2 \tanh\left(-\frac{t}{\tau_w}\right). \tag{5.1}$$

Here both $m_1 = m_{1R} + \mathrm{i}m_{1I}$ and $m_2 = m_{2R} + \mathrm{i}m_{2I}$ are constant and in general complex coefficients while the parameter τ_w determines the "width" of the profile in time. This kind of a mass profile is frequently used in studies of phase transitions and simple baryogenesis scenarios, as it is a smooth and easily scalable function interpolating between two different asymptotic values, such as two distinct vacua [95–99]. For our purposes the main advantage of the profile (5.1) is that the Dirac equation can be analytically solved for such a time-dependent mass.

Indeed, the solutions for a space-dependent profile with real coefficients were studied in reference [95] and extended to the case of perturbative imaginary parts in reference [96]. The exact solutions in the case of a temporal profile with general complex coefficients, such as the one in equation (5.1), were finally derived in reference [97]. These solutions will serve as useful tools for us, as they allow us to construct the Wightman function exactly in the collisionless case and

compare the phase phase structure of the resulting object to that predicted by the cQPA – this will be done in section 5.1.2. We will also use the kink-profile to study the range of validity of the semiclassical approach in section 5.1.3. First we will however review the exact solutions and construct the corresponding Wightman function out of them. For a more detailed presentation, see article [PI] and reference [100].

5.1.1 Exact solutions

The Dirac equation implied by the Lagrangian density (4.11) is

$$\left[\mathrm{i}\partial\!\!\!/ - P_{\mathrm{R}} m(t) - P_{\mathrm{L}} m^*(t)\right]\psi = 0. \tag{5.2}$$

We will now outline how to solve this equation for the mass profile of equation (5.1). In our spatially homogeneous and isotropic case the field can be expanded with the usual (anti)commutation rules in terms of creation and annihilation operators, $\hat{a}_{hk}$ and $\hat{b}_{hk}$, and some time-dependent mode functions, $U_{hk}(t)$ and $V_{hk}(t)$, as

$$\hat{\psi}(t,\boldsymbol{x}) = \sum_h \int \frac{\mathrm{d}^3\boldsymbol{k}}{(2\pi)^3 2\omega_-}\left[\hat{a}_{hk} U_{hk}(t)\mathrm{e}^{\mathrm{i}\boldsymbol{k}\cdot\boldsymbol{x}} + \hat{b}^\dagger_{hk} V_{hk}(t)\mathrm{e}^{-\mathrm{i}\boldsymbol{k}\cdot\boldsymbol{x}}\right], \tag{5.3}$$

where $h \in \{-1,1\}$ labels the helicity and we denote $\omega_\pm \doteq \omega_k(t \to \pm\infty)$. Since helicity is conserved in the system [101], we further decompose the mode functions as

$$U_{hk}(t) = \begin{bmatrix}\eta_{hk}(t)\\ \zeta_{hk}(t)\end{bmatrix} \otimes \xi_{hk}, \tag{5.4a}$$

$$V_{hk}(t) = \begin{bmatrix}\bar{\eta}_{hk}(t)\\ \bar{\zeta}_{hk}(t)\end{bmatrix} \otimes \xi_{hk}, \tag{5.4b}$$

where ξ_{hk} is the helicity two-eigenspinor, obeying $(\boldsymbol{\sigma}\cdot\hat{\boldsymbol{k}})\xi_{hk} = h\xi_{hk}$ with $\boldsymbol{\sigma} \doteq (\sigma_1,\sigma_2,\sigma_2)$ consisting of the three Pauli matrices σ_i.[9] Substituting the expansion (5.3) with the decompositions (5.4) to the Dirac equation (5.2) results after some algebra in the following equations for the one-dimensional mode functions:

$$\mathrm{i}\partial_t \eta_{hk} + h|\boldsymbol{k}|\eta_{hk} = m\zeta_{hk}, \tag{5.5a}$$

$$\mathrm{i}\partial_t \zeta_{hk} - h|\boldsymbol{k}|\zeta_{hk} = m^*\eta_{hk}, \tag{5.5b}$$

from which the equations for the antiparticle functions $\bar{\eta}_{hk}$ and $\bar{\zeta}_{hk}$ are obtained by performing the replacements $h \to -h$ and $m \to -m^*$.

So far we have not utilized the specific time-dependence of the mass func-

[9] We work in the chiral (or Weyl) basis, in which the Dirac gamma matrices are $\gamma^0 = \sigma_1 \otimes \mathbb{1}_2$, $\gamma^i = \mathrm{i}\sigma_2 \otimes \sigma_i$ and $\gamma^5 = -\sigma_3 \otimes \mathbb{1}_2$ [80]. In this case the helicity operator defined below equation (4.13) is $\hat{h}_k = \mathbb{1}_2 \otimes (\boldsymbol{\sigma}\cdot\hat{\boldsymbol{k}})$.

tion. For general mass profiles equations (5.5) have to be solved numerically, but as already mentioned earlier, for the kink-profile (5.1) an analytical solution can be found. The derivation of the solutions can be found in reference [97], and here we will just quote the main result. By introducing a further decomposition of the mode functions as $\phi^{\pm}_{h\boldsymbol{k}}(t) = \frac{1}{\sqrt{2}}\left[\eta_{h\boldsymbol{k}}(t) \pm \zeta_{h\boldsymbol{k}}(t)\right]$ and $\bar{\phi}^{\pm}_{h\boldsymbol{k}}(t) = \frac{1}{\sqrt{2}}\left[\bar{\eta}_{h\boldsymbol{k}}(t) \pm \bar{\zeta}_{h\boldsymbol{k}}(t)\right]$ it turns out that the solutions can be written in terms of Gauss hypergeometric functions:

$$\phi^{\pm(1)}_{h\boldsymbol{k}} = C^{\pm(1)}_{h\boldsymbol{k}}\, z^{\alpha}(1-z)^{\beta}\, {}_2F_1(a_{\pm}, b_{\pm}, c; z), \tag{5.6a}$$
$$\phi^{\pm(2)}_{h\boldsymbol{k}} = C^{\pm(2)}_{h\boldsymbol{k}}\, z^{-\alpha}(1-z)^{\beta}\, {}_2F_1(1+a_{\pm}-c, 1+b_{\pm}-c, 2-c; z), \tag{5.6b}$$

where $C^{\pm(1)}_{h\boldsymbol{k}}$ and $C^{\pm(2)}_{h\boldsymbol{k}}$ are constants, the superscripts (1) and (2) label the two linearly independent solutions and we have defined

$$\begin{aligned} &z \doteq \frac{1}{2}\left[1 - \tanh\left(-\frac{t}{\tau_{\mathrm{w}}}\right)\right], \quad \alpha \doteq -\frac{\mathrm{i}}{2}\tau_{\mathrm{w}}\omega_{-}, \quad \beta \doteq -\frac{\mathrm{i}}{2}\tau_{\mathrm{w}}\omega_{+}, \\ &a_{\pm} \doteq 1 + \alpha + \beta \mp \mathrm{i}\tau_{\mathrm{w}} m_{2\mathrm{R}}, \quad b_{\pm} \doteq \alpha + \beta \pm \mathrm{i}\tau_{\mathrm{w}} m_{2\mathrm{R}}, \quad c \doteq 1 + 2\alpha. \end{aligned} \tag{5.7}$$

The solutions for $\bar{\phi}^{\pm}_{h\boldsymbol{k}}$ are obtained by simply switching $h \to -h$ in equations (5.6). In the derivation of these solutions the imaginary part of m_2 has been removed by a global rotation of the fermion fields [97], and the remaining imaginary part of the mass will be denoted by m_{I}. For a general t the functions (5.6) are mixtures of positive and negative frequency solutions, but asymptotically they reduce to one or the other: $\phi^{\pm(1)}_{h\boldsymbol{k}} \xrightarrow{t\to-\infty} C^{\pm(1)}_{h\boldsymbol{k}}\, \mathrm{e}^{-\mathrm{i}t\omega_{-}}$ and $\phi^{\pm(2)}_{h\boldsymbol{k}} \xrightarrow{t\to-\infty} C^{\pm(2)}_{h\boldsymbol{k}}\, \mathrm{e}^{\mathrm{i}t\omega_{-}}$. This makes it simple to construct different initial states, representing particles or antiparticles in the asymptotic limit, for later analysis.

5.1.2 Phase space structure and quantum coherence

Now that we have the exact mode functions at hand, we turn back to the phase space structure of the two-point function predicted by the cQPA-formalism. As implied in section 4.2, we expect that due to the particle-antiparticle correlations generated by the changing mass there exists a shell-like structure located at $k_0 = 0$. Using the exact solutions we can now verify this with no approximations included. Since both of the Wightman functions $S^{<}$ and $S^{>}$ contain qualitatively the same features, it suffices to concentrate on either one of them. We choose to work with $S^{>}$.

Using the expansion of the spinor field (5.3), the (anti)commutation properties of the creation and annihilation operators, the decompositions of the mode functions (5.4) and the definition of the larger Wightman function $\mathrm{i}S^{>}(u,v) = \langle\psi(u)\bar{\psi}(v)\rangle$, we can write

$$\bar{S}^{>}(u,v) = \sum_{h}\int \frac{\mathrm{d}^3\boldsymbol{k}}{(2\pi)^3}\, \mathrm{e}^{-\mathrm{i}\boldsymbol{k}\cdot(\boldsymbol{u}-\boldsymbol{v})} M_{h\boldsymbol{k}}(u_0, v_0) \otimes \xi_{h\boldsymbol{k}}\xi^{\dagger}_{h\boldsymbol{k}}, \tag{5.8}$$

where we defined

$$M_{h\boldsymbol{k}}(u_0, v_0) \doteq \frac{1}{2\omega_-} \begin{bmatrix} \eta_{h\boldsymbol{k}}(u_0)\eta^*_{h\boldsymbol{k}}(v_0) & \eta_{h\boldsymbol{k}}(u_0)\zeta^*_{h\boldsymbol{k}}(v_0) \\ \zeta_{h\boldsymbol{k}}(u_0)\eta^*_{h\boldsymbol{k}}(v_0) & \zeta_{h\boldsymbol{k}}(u_0)\zeta^*_{h\boldsymbol{k}}(v_0) \end{bmatrix}. \tag{5.9}$$

The next step would be to Wigner-transform this Wightman function to get to the phase space picture. There is however one delicate point which we wish to discuss first. The exact mode functions found above are solutions to the *free* Dirac equation (5.2), i.e., there are no decohering interactions. As the integration in the Wigner transformation (in our spatially homogeneous and isotropic case) correlates for each t structures at $\pm\frac{r_0}{2}$ with $r_0 \in [-\infty, \infty]$, there are non-zero correlations coming from arbitrarily large time differences in the free case. Although this is a perfectly consistent result, in any realistic scenario there are interactions suppressing such broad correlations. In a complete treatment these interactions would have to be taken into account by solving the full Kadanoff–Baym equations, which is an important research topic but not relevant for our current purposes – we are merely interested in the qualitative phase space structures around the transition region. We will instead take the effect of decohering interactions into account by adding a temporal damping factor Γ in the Wigner transformation:

$$\bar{S}^{>}_{\Gamma}(k, x) \doteq \int \mathrm{d}^4 r\, \mathrm{e}^{\mathrm{i}k\cdot r - \Gamma|r_0|}\, \bar{S}^{>}\left(x + \frac{r}{2}, x - \frac{r}{2}\right) \tag{5.10}$$

(see article [PI] for reasoning on how this kind of a damping structure arises naturally in the interacting case). Transforming the constructed Wightman function of equation (5.8) accordingly results in

$$\begin{aligned} \bar{S}^{>}_{\Gamma}(k, t) &= \sum_h \int \mathrm{d}r_0\, \mathrm{e}^{\mathrm{i}k_0 r_0 - \Gamma|r_0|}\, M_{h\boldsymbol{k}}\left(t + \frac{r_0}{2}, t - \frac{r_0}{2}\right) \otimes \xi_{h\boldsymbol{k}}\xi^{\dagger}_{h\boldsymbol{k}} \\ &\doteq \sum_h W_{h\boldsymbol{k}}(k_0, t) \otimes \xi_{h\boldsymbol{k}}\xi^{\dagger}_{h\boldsymbol{k}}, \end{aligned} \tag{5.11}$$

where in the second equality we defined $W_{h\boldsymbol{k}}(k_0, t)$ to separate the relevant time-dependent part of the Wigner transformation.

Figure 6 shows the absolute value of the $(1,1)$-component of $W_{h\boldsymbol{k}}(k_0, t)$, constructed using the exact solutions (5.6) and performing the Wigner transformation numerically, for sets of parameters specified in the caption. The other components exhibit the same qualitative behaviour. The initial state has been chosen to represent a positive frequency solution. In all three cases the shell structure predicted by the cQPA is evident: after the initial positive frequency solution has gone through the mass change (centered around $t = 0$), it splits into a mixture of positive and negative frequency solutions *and their mutual coherence at $k_0 = 0$*. In the uppermost case the damping factor Γ is the largest, resulting in a relatively strong smearing of the shells. In the midmost case we chose a smaller Γ, and the shell structure is accordingly sharper. We also used a larger magnitude of the three-momentum $|\boldsymbol{k}|$, which causes the antiparticle shell emerging

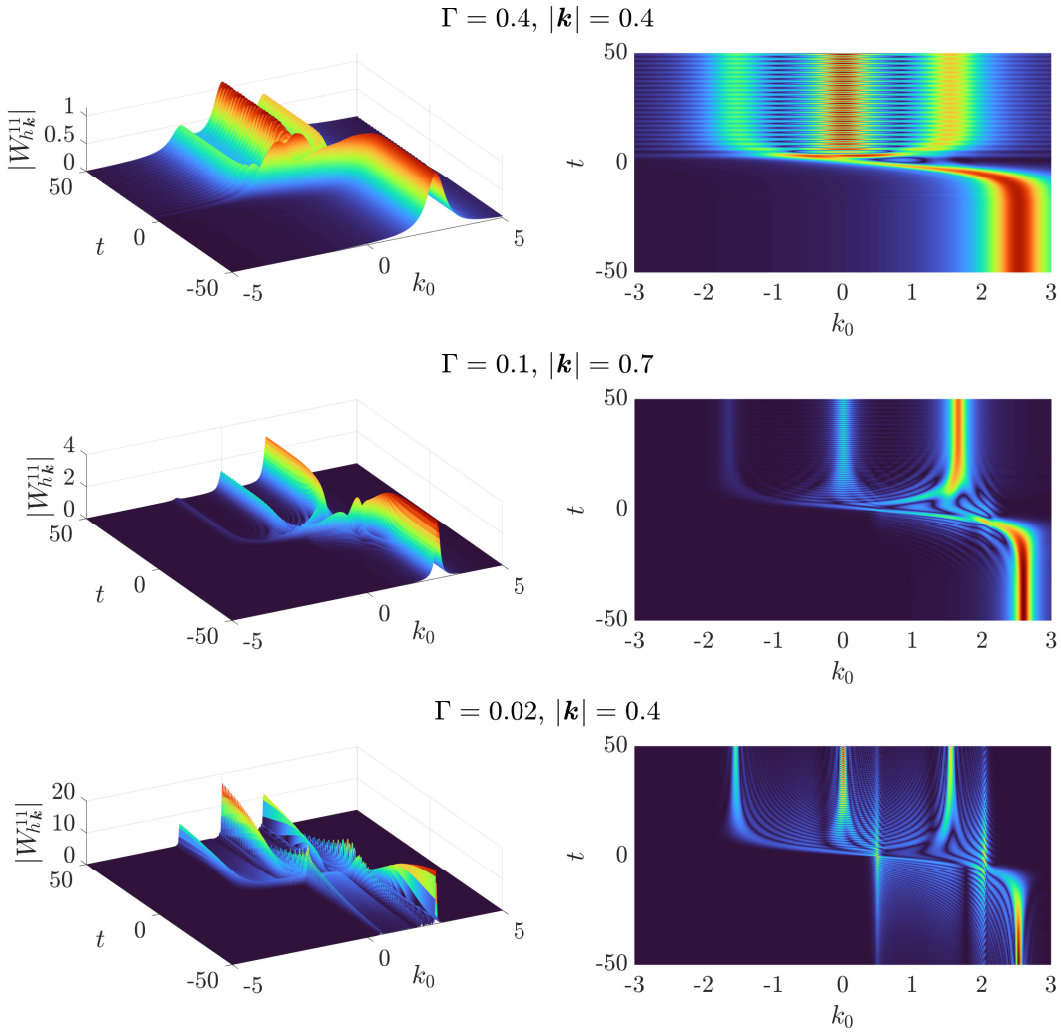

FIGURE 6 Absolute value of the $(1,1)$-component of the Wightman function $W_{hk}(k_0, t)$ defined in equation (5.11). All cases have $m_{1R} = 0.5$, $m_{2R} = 2$, $m_I = 0.5$ and $\tau_w = 5$ and the values for Γ and $|\boldsymbol{k}|$ are indicated above the plots. Adapted from article [PI] under the license CC BY 4.0.

after the mass change to be less pronounced, as the initial energy is in this case relatively larger compared to the mass change.

In the bottom case of figure 6 the value of Γ is the smallest. The particle, antiparticle and coherence shells are again correspondingly sharper, but on top of this there are structures not seen in the two other cases. Peaking at the mass change around $t = 0$ are two shell-like structures, located at roughly $k_0 \simeq 0.5$ and $k_0 \simeq 2.1$. These novel structures originate from *non-local correlations across the wall*: the early time positive frequency solution is correlated with the late time positive and negative frequency solutions. The location of the structures in frequency space is indeed at $k_0 = \frac{1}{2}(\omega_- \pm \omega_+)$, corresponding to the possible mixtures of the early and late time solutions. The emergence of these new shell structures for sharp wall profiles can also be verified analytically by examining a step function mass profile [100], and in the limit $\Gamma \to 0$ they actually completely dominate the phase space of the system. The cQPA does not predict

them, since the ansatz (4.18) is entirely spanned by the local correlation function (see equation (5.16) below). The non-local features we are observing are indeed examples of memory effects, relevant in systems with little or no dissipation. It is hard to say how much physical significance these solutions carry, as in a realistic setting interactions are expected to inhibit such long-range correlations, but their existence is nevertheless an interesting and to our knowledge previously unobserved phenomenon in the Wigner space context.

5.1.3 Range of validity of the semiclassical approximation

In the previous section we verified the phase space structure predicted by the cQPA using the exact solutions constructed from the mode functions. Next we will make use of the exact solutions to compute local currents and compare them to those obtained using the *semiclassical approximation*. Similarly to the cQPA, the semiclassical approximation is a method to compute quantities of interest in situations with a varying background, for example in the context of baryogenesis or phase transitions in general. For space-dependent backgrounds the formalism was introduced in references [65–68] and extended to include thermal corrections in reference [70], while the treatment of time-dependent systems can be found in reference [69]. Our focus is naturally on the temporal case, and especially on the expected range of validity of the formalism: the semiclassical method is on general grounds expected to work for $|\boldsymbol{k}|$-values satisfying $\frac{2\pi}{|\boldsymbol{k}|} < \tau_{\mathrm{w}}$ [PI].

A generic fermionic current $j^{\mathcal{O}}(x) \doteq \langle\overline{\psi}(x)\mathcal{O}\psi(x)\rangle$ can be written in terms of the Wigner-transformed Wightman function as

$$j^{\mathcal{O}}(x) = \int \frac{\mathrm{d}^4k}{(2\pi)^4}\,\mathrm{Tr}\big[\mathcal{O}\,\mathrm{i}S^{<}(k,x)\big]. \tag{5.12}$$

We will in particular be interested in the axial charge density $j^{\gamma^0\gamma^5} \doteq j^{05}$ related to particle asymmetries via the axial anomaly [50, 97]. Its Fourier transform in our spatially homogeneous and isotropic case can be written as

$$j^{05}_{\boldsymbol{k}}(t) = \sum_h j^{05}_{h\boldsymbol{k}}(t) \doteq \sum_h \int \frac{\mathrm{d}k_0}{2\pi}\,\mathrm{Tr}\big[\gamma^0\gamma^5\,\mathrm{i}S^{<}_{h\boldsymbol{k}}(k_0,t)\big]. \tag{5.13}$$

With the exact solutions (5.6) at hand it is easy to construct $j^{05}_{\boldsymbol{k}}$ for the kink-profile (5.1).

On the other hand, the semiclassical method predicts that for a general time-dependent mass $m = |m|\mathrm{e}^{\mathrm{i}\theta}$ the current for a given helicity is given by the formula

$$j^{05}_{h\boldsymbol{k}}(t) = \frac{\omega_- j^-_{h\boldsymbol{k}}}{\omega_{\boldsymbol{k}}(t) + h\frac{|m(t)|^2\partial_t\theta(t)}{2|\boldsymbol{k}|\omega_{\boldsymbol{k}}(t)}}, \tag{5.14}$$

where $j^-_{h\boldsymbol{k}} \doteq j^{05}_{h\boldsymbol{k}}(t \to -\infty)$ [PI, 97]. For the kink-profile (5.1) and with the posi-

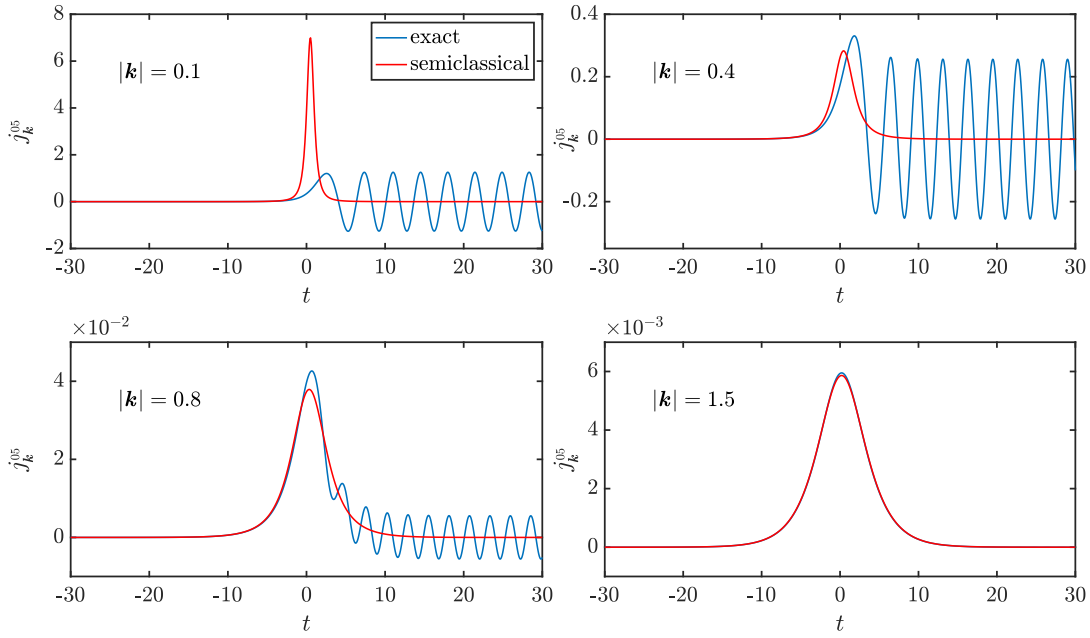

FIGURE 7 The axial charge density $j_{\boldsymbol{k}}^{05}(t)$ from the exact solutions (blue) and from the semiclassical approximation (red) for $|\boldsymbol{k}| \in \{0.1, 0.4, 0.8, 1.5\}$. The other parameters in each panel are $m_{1\mathrm{R}} = 0.1$, $m_{2\mathrm{R}} = 1$, $m_{\mathrm{I}} = 0.1$, $\tau_{\mathrm{w}} = 5$ and $\Gamma = 0.2$.

tive frequency initial solution chosen in the previous section this results in the following helicity-summed expression:

$$j_{\boldsymbol{k}}^{05}(t) = \frac{m_{\mathrm{I}} m_{2\mathrm{R}}}{\tau_{\mathrm{w}}\, \omega_{\boldsymbol{k}}^{3}(t) \cosh^{2}(t/\tau_{\mathrm{w}})}. \tag{5.15}$$

Using this result we can compare the semiclassical method to the exact results for different momentum scales.[10]

Before heading into the comparison we make an important remark on the cQPA: *in the collisionless limit the cQPA is exact for local quantities*, such as the current of equation (5.13). At first sight this might seem surprising, since the cQPA ansatz (4.18) relies on a truncation of gradients in the full equation. At the integrated level however a one-to-one correspondence between the cQPA shell-functions $f_{h\boldsymbol{k}}^{(m,c)\varepsilon}$ and the components of the local Wightman function $S_{h\boldsymbol{k}}^{<}(t,t)$ can be established [PI, 94]. This relation can be seen by integrating both the Wigner-transformed Wightman function and the cQPA-function of equation (4.18):

$$\begin{aligned}\int \frac{\mathrm{d}k_0}{2\pi}\, \bar{S}_{\boldsymbol{k}}^{<}(k_0,t) &= \int \frac{\mathrm{d}k_0}{2\pi} \int \mathrm{d}r_0\, \mathrm{e}^{\mathrm{i}k_0 r_0}\, \bar{S}_{\boldsymbol{k}}^{<}\Big(t + \frac{r_0}{2}, t - \frac{r_0}{2}\Big) = \bar{S}_{\boldsymbol{k}}^{<}(t,t) \\ &= \sum_{h,\varepsilon}\Big[\mathcal{B}_{h\boldsymbol{k}}^{\varepsilon\varepsilon}\frac{\varepsilon\omega_{\boldsymbol{k}}}{m_{\mathrm{R}}} f_{h\boldsymbol{k}}^{m\varepsilon} + \mathcal{B}_{h\boldsymbol{k}}^{\varepsilon(-\varepsilon)} f_{h\boldsymbol{k}}^{c\varepsilon}\Big],\end{aligned} \tag{5.16}$$

[10] Equation (5.15) as well as the currents in the following figure 7 have a different overall sign compared to those in the article [PI], which had an incorrect sign for the initial value $j_{h\boldsymbol{k}}^{-}$. This has no effect on the actual results of the article.

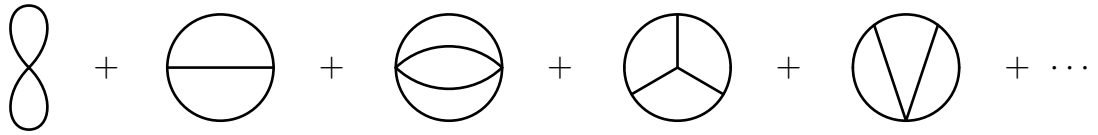

FIGURE 8 The first few terms contributing to Γ_2 in the ϕ^4-theory. Including just the first (local) diagram is called the Hartree approximation.

where the second line followed from equation (4.18). This relation parametrizes the local Wightman function in terms of the cQPA distribution functions $f^{m\varepsilon}_{h\boldsymbol{k}}$ and $f^{c\varepsilon}_{h\boldsymbol{k}}$. Note that adding the damping factor Γ in the Wigner transformation does not affect the above equality in any way. In the article [PI] this feature of the cQPA was confirmed also numerically when studying the local currents. It therefore suffices to compare the exact and semiclassical cases.

Figure 7 displays the axial charge density $j^{05}_{\boldsymbol{k}}(t)$ of equation (5.13), computed using the exact results and the semiclassical approximation (5.15) for $|\boldsymbol{k}| \in \{0.1, 0.4, 0.8, 1.5\}$. The other parameters are given in the caption. Starting from the lower right panel, we see that for $|\boldsymbol{k}| = 1.5$ the semiclassical result matches nearly perfectly the exact solution. This is not that surprising, as the condition $2\pi/|k| < \tau_{\mathrm{w}}$ is manifestly fulfilled. For smaller $|\boldsymbol{k}|$ the agreement is weakened, as the exact result develops oscillations completely absent in the semiclassical current. For $|\boldsymbol{k}| = 0.1$ the approximation predicts a peak reaching well above the actual result, and we are clearly outside the validity range of the method. However, for the intermediate values $|\boldsymbol{k}| \in \{0.4, 0.8\}$ the initial peak and the average value of the consequential oscillation in the exact result are quite well caught by the semiclassical result, even though for the smaller $|\boldsymbol{k}|$-value only a third of a wavelength fits inside the wall width. This suggests that the semiclassical approximation might be applicable even for relatively abrupt transitions.

5.2 Spinodal quantum dynamics in the ϕ^4-theory

In this and the following section we will employ the general moment equations derived in section 4.3 in two different scenarios. First we shall consider a scalar field in a static Minkowski background with the well known Mexican hat potential, defined by a Lagrangian density with a negative mass term:

$$\mathcal{L} = \frac{1}{2}(\partial_\mu \phi)^2 + \frac{1}{2}\mu^2\phi^2 - \frac{\lambda}{4!}\phi^4. \tag{5.17}$$

Such a potential is typically used as an example of spontaneous symmetry breaking in phase transitions [102–104]. We will be working in the lowest non-trivial loop expansion of the 2PI effective action, the so-called *Hartree approximation*. In this truncation the interaction part Γ_2 consists solely of the figure-eight-diagram

depicted as the first one in the series of figure 8:

$$\Gamma_2 = -\frac{\lambda}{8}\int \mathrm{d}^4x\,\Delta^2(x,x), \tag{5.18}$$

where we have denoted the two-point function by $\Delta(x,y)$ for consistency with the articles [PII, PIII]. We assume that the system is spatially homogeneous and isotropic.

With the above choices for the potential and Γ_2 the system is found [PII] to obey the moment equations (4.28) (or (4.26) in the frictionless case) with the effective mass function

$$M^2_{\mathrm{eff}}(t) = M^2_{\mathrm{eff}}(\varphi,\Delta) = -\mu^2 + \frac{\lambda}{2}\Big[\varphi^2(t) + \Delta(t,t)\Big]. \tag{5.19}$$

Note that this is actually a *gap equation* for the mass function: the local correlation function $\Delta(t,t)$ depends on M^2_{eff}. The equation for the one-point function (3.23) in the Hartree approximation is

$$\Big[\partial_t^2 + M^2_{\mathrm{eff}}(t)\Big]\varphi(t) = \frac{\lambda}{3}\varphi^3(t). \tag{5.20}$$

These equations allow us to study the coupled evolution of the one- and two-point functions numerically, taking properly into account the quantum backreaction from the out-of-equilibrium modes of the two-point function. Especially interesting are the *spinodal instabilities* present in the system: for certain $|\boldsymbol{k}|$-modes the combination $\omega_{\boldsymbol{k}}^2 \doteq |\boldsymbol{k}|^2 + M^2_{\mathrm{eff}}$ will tend negative due to the occasional negativity of the effective mass squared function M^2_{eff}, resulting in instabilities and particle production.[11] This process has been studied widely in reference to early universe phase transitions, as it may play an important role in e.g. inflationary particle production [34, 39, 103–106].

In article [PII] the system was studied extensively with several scenarios. The article also includes a detailed renormalization of the system, which we do not repeat here (the renormalized quantities are denoted with a subscript R).[12] We identified and studied particle production both via parametric resonance and spinodal instabilities and examined the role of different effective potentials that can be defined for the system. We also included the phenomenological friction terms, and finally used the equations to study the self-thermalization of the system. Here we will show some exemplary results to illustrate the qualitative features present in the system and point the reader to the article [PII] for a more

[11] In terms of plane waves: for a set of modes $\omega_{\boldsymbol{k}}$ turns imaginary, and the oscillatory solutions $\sim \mathrm{e}^{\pm\mathrm{i}\omega_k t}$ split into exponentially growing and decaying parts. In the literature the terms *spinodal* and *tachyonic* are used interchangeably when referring to these instabilities.

[12] The article contains an erroneous treatment of the renormalization factor $Z_{(2)}$ which was incorrectly set to unity. A proper calculation [107] yields a marginal correction: in equations (3.24a) and (4.4d) of the article [PII] the derivative terms become multiplied by a factor $\# = \frac{1}{18}\left(\sqrt[3]{1+\frac{27\lambda_{\mathrm{R}}}{32\pi^2}} - 1\right)$. Although this does not affect the main results, the figures in this thesis are produced with the corrected factor.

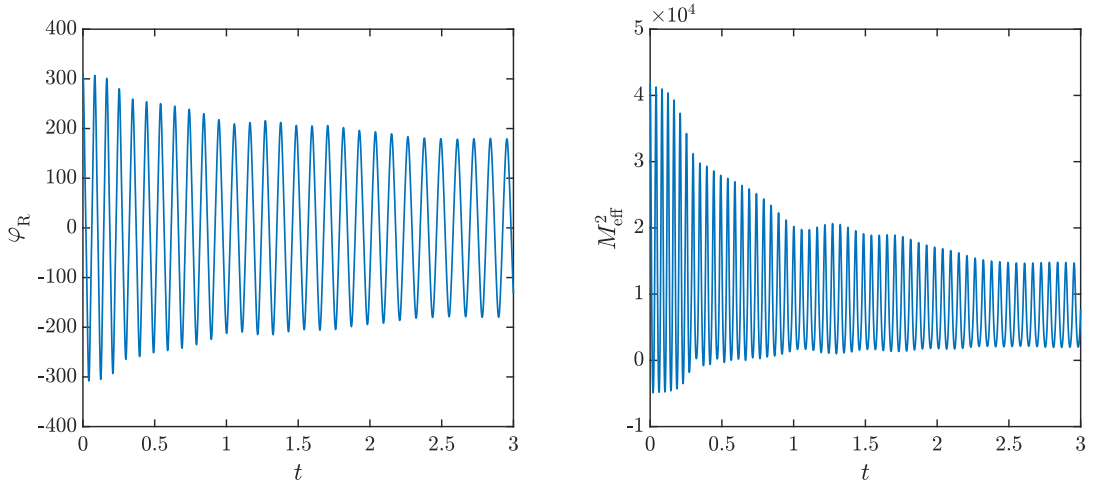

FIGURE 9 The one-point function φ_R (left panel) and the effective mass function $M^2_{\rm eff}$ (right panel). The parameters used were $m_R = 100$ GeV and $\lambda_R = 1$ with the initial values $\varphi_R^{\rm in} = 310$ GeV and $\partial_t \varphi_R^{\rm in} = 0$ GeV^2. The results are for the collisionless case: $\#_i = 0$ GeV.

thorough analysis. The units in all figures of this section are (some powers of) GeV.

In figure 9 we show the one-point function φ_R and the effective mass function $M^2_{\rm eff}$ as functions of time. The mass parameter was given the value $m_R = 100$ GeV, characteristic for an electroweak phase transition, while the coupling was chosen to be $\lambda_R = 1$. The one-point function was initialized as $\varphi_R^{\rm in} = 310$ GeV and $\partial_t \varphi_R^{\rm in} = 0$ GeV^2, while the moment functions ρ_{ik} were initialized to their vacuum values:

$$\rho_{0k}^{\rm vac} \doteq \frac{\Theta_k}{2\omega_k}, \qquad \partial_t \rho_{0k}^{\rm vac} \doteq 0, \qquad \rho_{1k}^{\rm vac} \doteq -\frac{1}{2} \quad \text{and} \quad \rho_{2k}^{\rm vac} \doteq \frac{\omega_k}{2}\Theta_k, \tag{5.21}$$

where the Heaviside theta function $\Theta_k \doteq \theta\big(\omega_k^2(t)\big)$ excludes spinodal modes from the vacuum. These forms for the moment functions follow straightforwardly by inserting in the definition (4.24) the thermal propagator $iG^<_{\rm eq}(k) = 2\pi\,\mathrm{sgn}(k_0) n_{\rm BE}(k_0)\delta\big(k^2 - m^2\big)$, where $n_{\rm BE}(k_0) \doteq \big(e^{k_0/T} - 1\big)^{-1}$ is the Bose–Einstein distribution function [69,72]. Finally, in this case we assumed no friction, setting $\#_i = 0$ in equations (4.28). In the figure we see that the one-point function oscillates at a decaying amplitude, as does also the effective mass function. While the average value of the effective mass squared stays positive during the evolution, at early times the function obtains negative values during the oscillations. This causes spinodal instabilities, whose role can be seen in the behaviour of the two-point function described next.

Figure 10 shows the fluctuation contribution of the finite (renormalized) local two-point function $\delta\Delta_F(t,t)$ and the momentum structure of the corresponding zeroth fluctuation moment $\delta\rho_{0k}(t)$ as a function of time. The fluctuation is

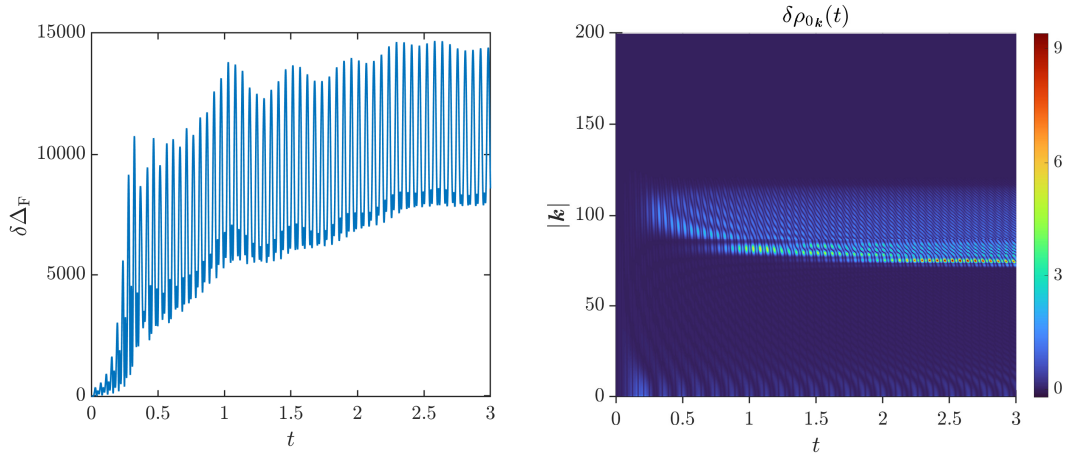

FIGURE 10 The fluctuation part of the two-point function $\delta\Delta_F$ (left panel) and the momentum structure of the zeroth fluctuation moment $\delta\rho_{0k}$ (right panel) for the same values of parameters as in figure 9.

defined by subtracting the vacuum contribution of equation (5.21):

$$\delta\Delta_F(t,t) = \int \frac{d^3\boldsymbol{k}}{(2\pi)^3}\,\delta\rho_{0k} \doteq \int \frac{d^3\boldsymbol{k}}{(2\pi)^3}\,(\rho_{0k} - \rho_{0k}^{\mathrm{vac}}). \tag{5.22}$$

We can see that at initial times, for roughly $t \in [0, 0.3]$, the (average value of the) two-point function grows strongly. This is due to the spinodal instability, as can be seen by comparing with the effective mass function of figure 9: this is the stage during which M_{eff}^2 gets periodically negative. For later times the mass function remains positive, oscillating with a decaying amplitude. The two-point function in figure 10 is seen to continue growing during this period, while the momentum space structure of $\delta\rho_{0k}$ exhibits clear band-like "Moby-Dick" structures. These bands and the corresponding growth in the two-point function are due to parametric resonance caused by the oscillating mass – a phenomenon familiar from reheating scenarios [29, 102, 108] and systems with external oscillation frequencies in general [109, 110].

In the above case most of the time evolution was dominated by the parametric resonance. To see the spinodal instabilities better in effect, we show in figure 11 again the evolution of the one-point function and the effective mass function, but this time with a smaller initial value for the field: $\varphi_R^{\mathrm{in}} = 246$ GeV. We also included non-zero friction terms, $\#_i = 0.4$ GeV, and assumed that the corresponding interactions drive the system to a vacuum state by choosing $\rho_{ik}^{\mathrm{eq}} = \rho_{ik}^{\mathrm{vac}}$. The other parameters are the same as in the earlier example. The evolution of the one-point function, shown in solid blue in the left panel, is drastically different to the previous case. Due to the smaller initial value, the field does not cross to the other side of the potential on the first oscillation, but does spend a longer time at the spinodal region. On the second oscillation cycle it however penetrates slowly to the other side of the potential, with the effective mass function staying close to zero, and then spends the rest of the time evolution oscillating around the other minimum. This is an example of a spinodal

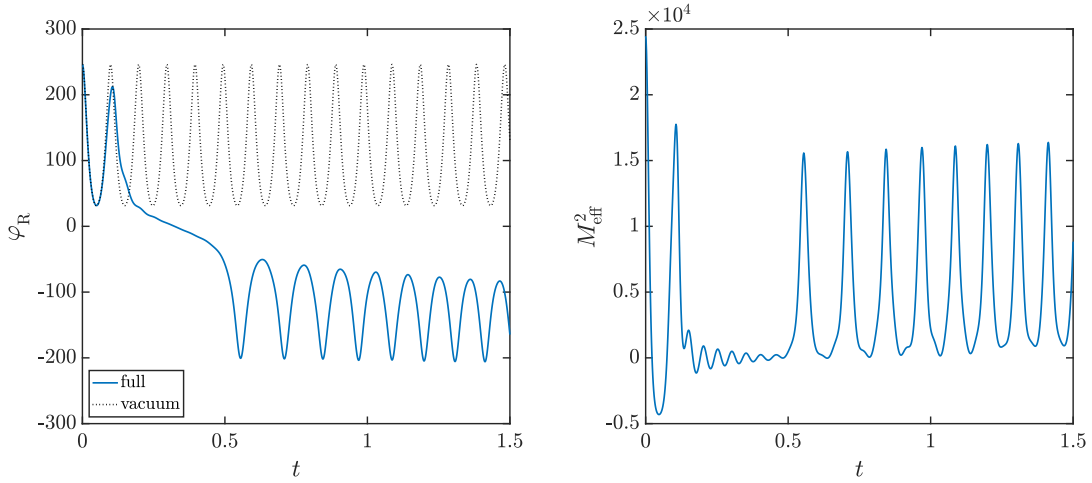

FIGURE 11 The full evolution of the one-point function φ_R (left panel, solid blue) and the vacuum evolution (left panel, dotted black) along with the effective mass function M^2_{eff} (right panel). The parameters used were $m_R = 100$ GeV, $\lambda_R = 1$ and $\#_i = 0.4$ GeV with the initial values $\varphi^{\text{in}}_R = 246$ GeV and $\partial_t \varphi^{\text{in}}_R = 0$ GeV^2.

tunneling, where the unstable modes excited during the first oscillation allow the field to cross the classically forbidden potential barrier. To better illustrate this, we have also plotted the evolution of the one-point function with just the vacuum contributions taken into account, meaning that we set by hand $\delta\Delta_F = 0$ in the mass function in equation (5.20). This evolution is shown as the black dotted line in the left panel of figure 11 and, as expected, the field simply oscillates around the positive minimum in a fixed potential.

In figure 12 we show, similarly to figure 10, the fluctuation contributions to the local two-point function and the zeroth moment for the parameters used in figure 11. The strong spinodal instability can be seen in the left panel in the evolution of the two-point function as a rapid growth at initial times. The spinodal nature of the growth is more transparent in the heat plot in the right panel, where we can see that all the generated structure in the momentum space of $\delta\rho_{0k}$ is concentrated at small $|\boldsymbol{k}|$-values. These are the modes that spend the longest time in the spinodal region where M^2_{eff} tends negative, or for which ω^2_k is negative the longest.

The main objective in this section has been to underline the existence, importance and complicated dynamics of backreaction effects on the coupled evolution of the one- and two-point functions. It is clear that methods with a fixed background, like using the standard effective potential, are not adequate to capture these effects [20]. There are ways to treat these non-equilibrium systems to some degree without resorting to the 2PI methods, like the mode function approaches of references [103, 104], but the non-linearity of the equations makes the situation complicated. In the next section we employ our moment equation methods within inflationary reheating.

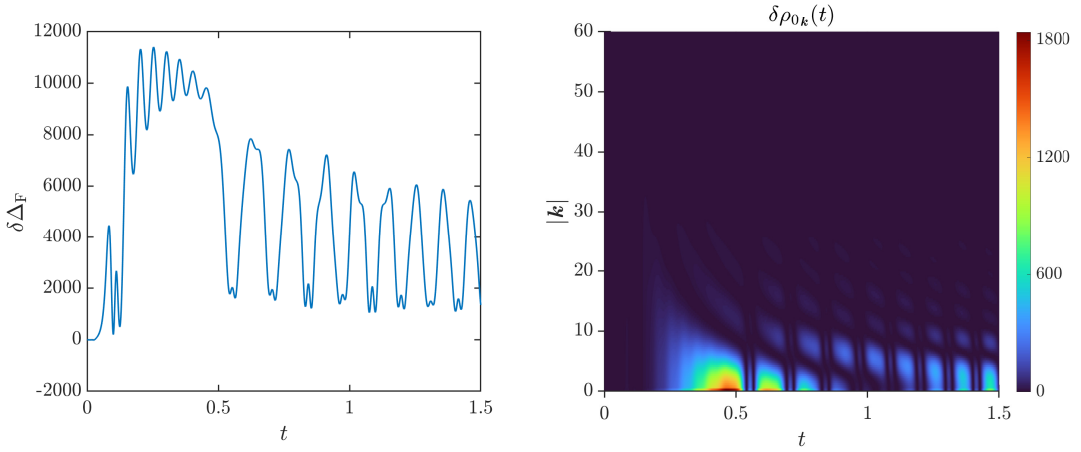

FIGURE 12 The fluctuation part of the two-point function $\delta\Delta_F$ (left panel) and the momentum structure of the zeroth fluctuation moment $\delta\rho_{0k}$ (right panel) for the same values of parameters as in figure 11.

5.3 Particle production during reheating with quantum backreaction

In the previous section we discussed the complicated dynamics of the coupled one- and two-point functions in a toy model exhibiting spinodal instabilities, using the methods introduced in section 4.3. Now we will study similar dynamics in a more specific setting, as explored in article [PIII].

The model studied in the article consists of a scalar spectator field χ which is indirectly coupled to an inflaton field ϕ via the curvature scalar R:

$$\mathcal{S}_\chi \doteq \int \mathrm{d}^4x\,\sqrt{-g}\left[\frac{1}{2}g^{\mu\nu}(\nabla_\mu\chi)(\nabla_\nu\chi) - \frac{1}{2}m^2\chi^2 + \frac{1}{2}\xi R\chi^2 - \frac{\lambda}{4}\chi^4\right]. \tag{5.23}$$

Originally this setup was introduced in references [35,36] as a mechanism to produce dark matter during reheating, with the following principal idea. The scalar χ is assumed to stay energetically subdominant to the inflaton ϕ, whose evolution (with the quadratic form $V(\phi) = \frac{1}{2}m_\phi^2\phi^2$ for the potential) is then dictated classically by its equation of motion [6] coupled to the Friedmann equation (2.4) as

$$\partial_t^2\phi = -3H\,\partial_t\phi - m_\phi^2\phi, \tag{5.24a}$$

$$H^2 = \frac{8\pi}{6M_{\mathrm{Pl}}^2}\left[(\partial_t\phi)^2 + m_\phi^2\phi^2\right], \tag{5.24b}$$

with $H = \frac{\partial_t a}{a}$. Furthermore, the curvature scalar R, obtained as a trace of the Einstein tensor, reads in terms of ϕ as

$$R = \frac{8\pi}{M_{\mathrm{Pl}}^2}\left[(\partial_t\phi)^2 - 2m_\phi^2\phi^2\right]. \tag{5.25}$$

During reheating the inflaton ϕ will oscillate around the minimum of its potential. This will in turn cause the curvature R to oscillate between positive and negative values according to the above equation, and through the $\xi R\chi^2$-term in the scalar action (5.23) the χ-field will periodically have a negative effective mass squared. These spinodal instabilities ($M^2_{\text{eff}} < 0$) can lead to efficient production of χ-particles, which could then constitute the observed dark matter abundance [35,36].

In reference [36] the model was studied using adiabatic methods to treat the spinodal effects. Our formalism introduced in section 4.3 can be straightforwardly applied to the setup with quantum backreaction effects properly included, and this was done in article [PIII]. We will now summarize the analysis and its main outcomes. First of all, defining the scaled field $\sigma \doteq a\chi$ the scalar action $\mathcal{S}_\chi$ can in conformal time η be written in an effectively Minkowski-spacetime form

$$\mathcal{S}_\sigma = \int \mathrm{d}\eta\, \mathrm{d}^3\boldsymbol{x} \left\{ \frac{1}{2}(\partial_\eta \sigma)^2 - \frac{1}{2}(\nabla\sigma)^2 - \frac{1}{2}a^2 \left[m^2 - \left(\xi - \frac{1}{6} \right) R \right] \sigma^2 - \frac{\lambda}{4}\sigma^4 \right\}, \quad (5.26)$$

where the scale factor a and the curvature scalar R give the σ-field an effective time-dependent mass. Working again in the Hartree approximation (see figure 8) we have $\Gamma_2 = -\frac{3\lambda}{4}\int \mathrm{d}\eta\, \mathrm{d}^3\boldsymbol{x}\, \Delta^2$, where Δ is the local two-point function of the σ-field. The system then obeys in the spatially homogeneous and isotropic case the moment equations (4.26) with the effective mass function given by [PIII]

$$M^2_{\text{eff}}(\eta) \doteq a^2(\eta) \left[m^2 - \left(\xi - \tfrac{1}{6} \right) R(\eta) \right] + 3\lambda \left[\sigma^2(\eta) + \Delta(\eta,\eta) \right], \quad (5.27)$$

and the equation of motion of the one-point function (3.23) is

$$\left[\partial_\eta^2 + M^2_{\text{eff}}(\eta) \right] \sigma(\eta) = 2\lambda\sigma^3(\eta). \quad (5.28)$$

We again refer the reader to the article [PIII] for the details on the renormalization of the equations – and again we will use a subscript R to denote a renormalized parameter.

Solving the moment equations together with the one-point function numerically is in principal straightforward, albeit they are again strongly coupled through the effective mass function. They are solved simultaneously with the equations for the inflaton (5.24a) and the scale factor (5.24b), although since the scalar χ is energetically subdominant at all times, the inflaton sector merely acts as a varying background via the curvature term. We will now show solutions from the equations for an exemplary set of parameters. To be specific, we initialize the inflaton field at $\phi_{\text{in}} = 15 M_{\text{Pl}}$ with a mass of $m_\phi = 1.5 \cdot 10^{13}$ GeV, while for the spectator field χ we set $m_{\text{R}} = 150$ GeV and use Minkowski vacuum initial values (5.21) for the two-point sector. We also give a small non-zero initial value for the one-point function σ_{R} to allow for its evolution, and choose $\bar{\xi}_{\text{R}} = 50$ for the non-minimal coupling, so that we can compare with the results

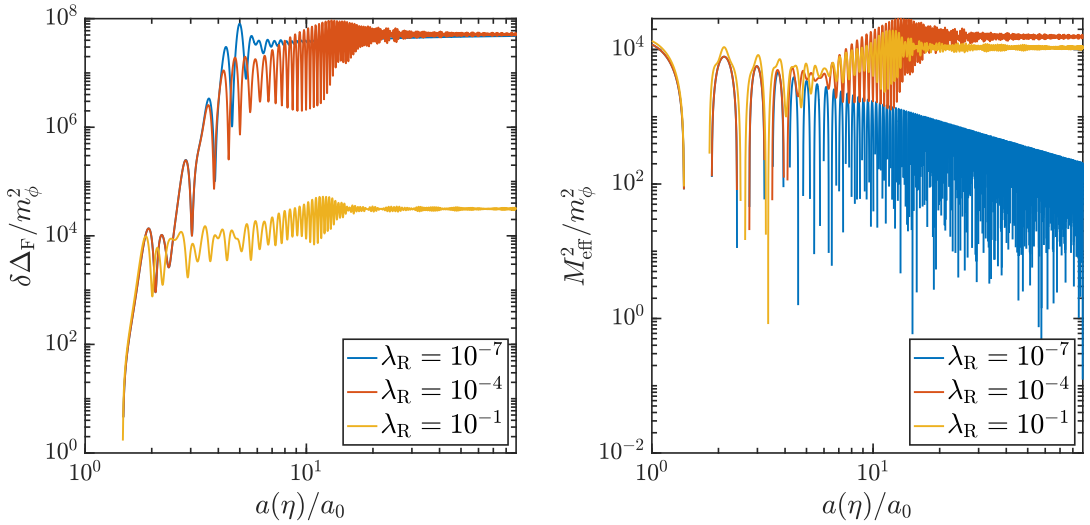

FIGURE 13 The fluctuation contribution $\delta\Delta_F$ to the two-point function (left panel) and the effective mass function M^2_{eff} (right panel) for the self-coupling values $\lambda_R = 10^{-7}$ (blue), $\lambda_R = 10^{-4}$ (red) and $\lambda_R = 10^{-1}$ (yellow). From article [PIII], reproduced under the license CC BY 4.0.

of reference [36].

Figure 13 shows the time evolution of the fluctuation part of the two point function $\delta\Delta_F$ defined in equation (5.22) for the values of the coupling $\lambda_R \in \{10^{-7}, 10^{-4}, 10^{-1}\}$, along with the corresponding effective mass functions M^2_{eff}. The negativity of the effective mass function at initial times is evident (note that the scale is logarithmic) – this is the spinodal stage caused by the oscillating curvature contribution at the onset of reheating. In the fluctuation of the local two-point function $\delta\Delta_F$ this is reflected as successive periods of growth at the spinodal stages. After this the two-point function exhibits more non-trivial behaviour, especially for $\lambda_R \in \{10^{-4}, 10^{-1}\}$. This, together with the difference in the behaviour for different values of the coupling, can be elucidated by scrutinizing the mass functions more thoroughly.

We can split the effective mass function M^2_{eff} into three pieces, depending on the contributing sector:

$$M_R^2 \doteq -a^2\left(\bar{\xi}_R - \tfrac{1}{6}\right)R \qquad \text{(curvature)}, \tag{5.29a}$$

$$M_\Delta^2 \doteq 3\lambda_R \delta\Delta_F \qquad \text{(fluctuations)}, \tag{5.29b}$$

$$M_\sigma^2 \doteq M^2_{\text{eff}} - M_R^2 - M_\Delta^2 \qquad \text{(field and background)}. \tag{5.29c}$$

Figure 14 shows the time evolution of these three components along with the full effective mass function for the three couplings considered earlier. There are essentially two competing elements: the curvature contribution $\langle M_R^2\rangle_{\text{osc}}$ and the fluctuation contribution $\langle M_\Delta^2\rangle_{\text{osc}}$, where the angle brackets $\langle\rangle_{\text{osc}}$ stand for averaging over oscillation. In all cases the background contribution M_σ^2 stays subdominant during the evolution. Looking first at the case with $\lambda_R = 10^{-7}$, we can see that the contribution from the two-point function $\langle M_\Delta^2\rangle_{\text{osc}}$ actually

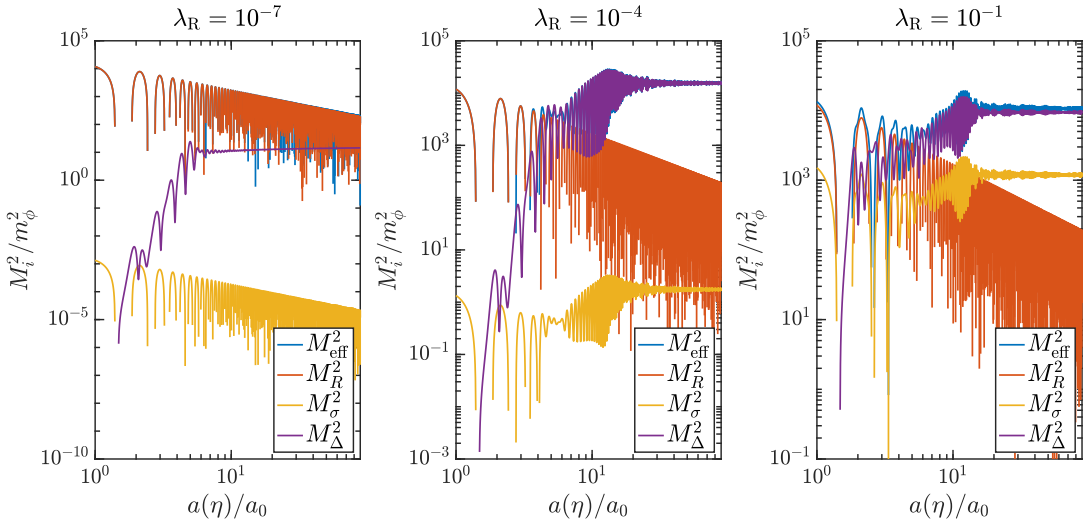

FIGURE 14 The effective mass function $M^2_{\rm eff}$ (blue) and its components M^2_R (red), M^2_σ (yellow) and M^2_Δ (violet) defined in equations (5.29) for the self-coupling values $\lambda_{\rm R} \in \{10^{-7}, 10^{-4}, 10^{-1}\}$. From article [PIII], reproduced under the license CC BY 4.0.

does not reach that coming from the curvature. Typically one would assume the spinodal growth to terminate once the positive definite contribution from the two-point function overrides the curvature part: $\langle M^2_\Delta \rangle_{\rm osc} \simeq \langle M^2_R \rangle_{\rm osc}$ [34, 36]. Here we can see that the situation is a bit more delicate: the growing two-point function is still the reason behind the termination of the spinodal stage, but instead of making the effective mass function entirely positive, its contribution renders the spinodal windows $M^2_{\rm eff} < 0$ so narrow that there is simply no time for coherent growth. Comparing with reference [36] we find that this leads to an order of magnitude smaller final value for the two-point function.

For $\lambda_{\rm R} \in \{10^{-4}, 10^{-1}\}$ the situation is different, as the larger couplings allow $\langle M^2_\Delta \rangle_{\rm osc}$ to reach $\langle M^2_R \rangle_{\rm osc}$, closing the spinodal windows entirely. This is however not the end of the dynamics, as the backreacting two-point function leads to a subsequent period of parametric resonance. This can be seen as lumps in the two-point function $\delta\Delta_{\rm F}$ and the effective mass function $M^2_{\rm eff}$ before and around $a/a_0 \simeq 10$, and more illuminatingly in figure 15 where we show the full momentum structure of the zeroth fluctuation moment $\delta\rho_{0k}$ (the two-point function $\delta\Delta_{\rm F}$ is the k-integral of $\delta\rho_{0k}$). The horizontal $|\boldsymbol{k}|$-bands result from the parametric resonance caused by the backreacting fluctuation, and looking back at figure 13 we see that this actually gives the dominant contribution to the final value of the two-point function for $\lambda_{\rm R} \in \{10^{-4}, 10^{-1}\}$. This effect is not captured at all in the adiabatic treatment of reference [36], which results in an order of magnitude larger final values in our case. Interestingly, figure 15 shows resonance-like bands also for $\lambda_{\rm R} = 10^{-7}$, which are inevitably due to the curvature contribution as it dominates the mass function in that case. Even in that case particle production is hence a combination of spinodal and resonant effects. Finally, we note that the initial vertical stripes present in figure 15 near $a/a_0 \simeq 2$, corresponding to the first spinodal instabilities, are essentially the

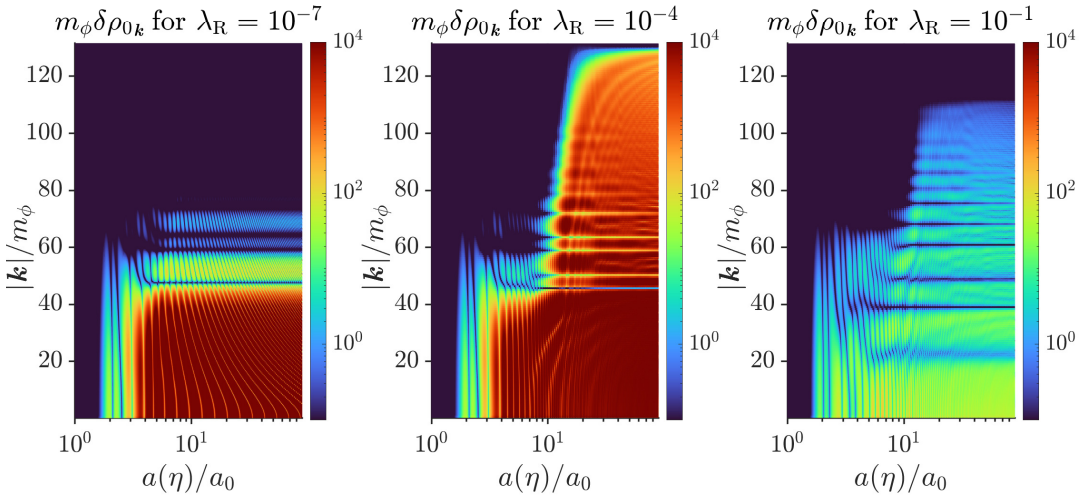

FIGURE 15 The momentum structure of the zeroth fluctuation moment $\delta\rho_{0\boldsymbol{k}}$ for the self-coupling values $\lambda_\mathrm{R} \in \{10^{-7}, 10^{-4}, 10^{-1}\}$. From article [PIII], reproduced under the license CC BY 4.0.

same for all values of the coupling. This is as expected, since the evolution is then completely dominated by the curvature term $\langle M_R^2 \rangle_\mathrm{osc}$ which is independent of the coupling.

Overall, the system exhibits strongly non-linear behaviour. Describing the spinodal instabilities and parametric resonances, which are seen to partly coexist and whose driving forces can couple in intricate ways, is a complicated task. A full description of the picture with a proper inclusion of backreaction effects is however necessary if one wishes to make reliable calculations within such systems. Indeed, we saw that in the example studied above a transient resonant phase following the initial spinodal stages can completely dominate the generated final values – an effect that was entirely missed in the earlier simpler analysis [36]. Our 2PI approach offers a straightforward yet comprehensive way of dealing with these phenomena. The natural next step would be to couple the spectator χ to other matter fields which could be described with the cQPA-equations of section 4.2. It would be also interesting to include a full quantum treatment of the inflaton field ϕ.

6 CONCLUSIONS AND OUTLOOK

We have developed non-equilibrium quantum field theory techniques for dynamical systems in which quantum effects play an important role. There are various examples of such systems in nature, emerging in the early universe as well as in condensed matter physics. We have applied our methods to the study of (early universe) phase transitions and reheating after inflation.

The coherent quasiparticle approximation (cQPA) [88–94] is a comprehensive approximation scheme for quantum transport equations derived from the 2PI effective action. For certain space-time symmetries the cQPA predicts for the two-point function a novel singular phase space structure encompassing quantum coherence effects. We have shown the emergence of this structure in an analytically solvable spatially homogeneous and isotropic fermionic system with a time-dependent mass term by constructing the two-point function exactly from analytical solutions for the mode functions. We also studied the effects of damping on the phase space structures, demonstrating how in systems with very weak interactions additional non-local shell structures emerge around the transition region.

With the exact solutions at hand we also studied the range of validity of the semiclassical approximation [65–70], which is an approximation scheme expected to hold for smooth mass profiles. By computing local currents for different momenta we found out that the semiclassical method can be surprisingly accurate: the agreement with the exact result was rather good even when only one third of a wavelength fit inside the transition region. We also pointed out that for non-interacting systems the cQPA is formally exact for local quantities.

The cQPA is an approximative formalism, whose true strength lies in its capability to treat interacting systems without losing information on quantum coherence effects. Another very closely related approach suitable for studying similar quantum transport problems is using moment functions. For scalars we have shown that for spatially homogeneous and isotropic systems with the 2PI loop expansion consisting of local diagrams the coupled evolution of the one- and two-point functions can be described by a closed set of simple moment equations. We then used these equations to study two different setups, using

the Hartree approximation for the loop hierarchy.

First, we considered the Mexican hat -potential as a simple phase transition model. Solving the coupled system and studying the phase space structure of the moment functions we identified the processes of spinodal decomposition and parametric resonance taking place. The spinodal effects, emerging due to the effective mass squared taking negative values, were seen to strongly influence the behaviour of the system. We also studied the effect of adding phenomenological friction terms to the moment equations.

In the second setup we analyzed a spectator field coupled non-minimally to gravity during the reheating stage after inflation. The oscillations of the inflaton field translate into an oscillating Ricci scalar, which causes the effective mass squared of the spectator field to attain negative values. This results again in spinodal instabilities, which are further accompanied and followed by a stage of parametric resonance. The interplay of these effects can cause the final value of the two-point function to differ easily by an order of magnitude compared to the results obtained earlier in the literature using adiabatic methods [36]. Altogether we saw that the non-linear backreaction of the two-point function leads to highly complicated and delicate dynamics that could not be captured with the usual simpler approximations.

There are several ways to further refine and apply the methods presented in this thesis. In regards to the cQPA, it is a long-term objective within our research group to generalize the current formalism to planar symmetric systems with one non-trivial spatial coordinate z. It is known, that in that case the coherence information condenses onto a zero-momentum shell $k_z = 0$ [88,90], and this could be verified using exact solutions similarly to the time-dependent case of section 5.1. The z-dependent cQPA formalism could be directly applied to compute reflection problems within the baryogenesis scenario. Another future application of the cQPA would be to study neutrino oscillations in an inhomogeneous background.

An obvious generalization of the moment equation methods would be to go beyond local diagrams. An interesting example on this would be to couple the scalar to one or more fermions via Yukawa-type interactions, which would then allow one to calculate the friction terms in equations (4.28) from first principles. The tools for doing this already exist within the cQPA formalism [PI,88,93]. Furthermore, combining the cQPA for fermions with the moment equations would for example allow one to study the spectator setup of section 5.3 with decays into fermionic degrees of freedom included.

REFERENCES

[1] G. Aad, T. Abajyan, B. Abbott, J. Abdallah, S. A. Khalek, A. Abdelalim et al., *Observation of a new particle in the search for the standard model higgs boson with the ATLAS detector at the LHC*, *Physics Letters B* **716** (2012) 1.

[2] S. Chatrchyan, V. Khachatryan, A. Sirunyan, A. Tumasyan, W. Adam, E. Aguilo et al., *Observation of a new boson at a mass of 125 GeV with the CMS experiment at the LHC*, *Physics Letters B* **716** (2012) 30.

[3] D. W. Hogg, D. J. Eisenstein, M. R. Blanton, N. A. Bahcall, J. Brinkmann, J. E. Gunn et al., *Cosmic homogeneity demonstrated with luminous red galaxies*, *Astrophys. J.* **624** (2005) 54 [astro-ph/0411197].

[4] M. I. Scrimgeour, T. Davis, C. Blake, J. B. James, G. B. Poole, L. Staveley-Smith et al., *The WiggleZ dark energy survey: the transition to large-scale cosmic homogeneity*, *Monthly Notices of the Royal Astronomical Society* **425** (2012) 116.

[5] M. Davis, *Is the universe homogeneous on large scales?*, in *Conference on Critical Dialogs in Cosmology*, pp. 13–23, 10, 1996 [astro-ph/9610149].

[6] S. M. Carroll, *Spacetime and Geometry*, Cambridge University Press (7, 2019).

[7] Planck collaboration, *Planck 2018 results. VI. Cosmological parameters*, *Astron. Astrophys.* **641** (2020) A6 [1807.06209].

[8] J. A. Wheeler and K. Ford, *Geons, black holes, and quantum foam: A life in physics*, W. W. Norton & Company (1998).

[9] R. Penrose, *Difficulties with inflationary cosmology*, *Annals N. Y. Acad. Sci.* **571** (1989) 249.

[10] J. Earman and J. Mosterin, *A critical look at inflationary cosmology*, *Phil. Sci.* **66** (1999) 1.

[11] A. Ijjas, P. J. Steinhardt and A. Loeb, *Inflationary paradigm in trouble after Planck2013*, *Phys. Lett. B* **723** (2013) 261 [1304.2785].

[12] A. Ijjas, P. J. Steinhardt and A. Loeb, *Inflationary schism*, *Phys. Lett. B* **736** (2014) 142 [1402.6980].

[13] A. H. Guth, *The Inflationary Universe: A Possible Solution to the Horizon and Flatness Problems*, *Phys. Rev. D* **23** (1981) 347.

[14] A. D. Linde, *A New Inflationary Universe Scenario: A Possible Solution of the Horizon, Flatness, Homogeneity, Isotropy and Primordial Monopole Problems*, *Phys. Lett. B* **108** (1982) 389.

[15] A. Linde, *Scalar field fluctuations in the expanding universe and the new inflationary universe scenario*, *Physics Letters B* **116** (1982) 335.

[16] K. Sato, *Cosmological Baryon Number Domain Structure and the First Order Phase Transition of a Vacuum*, *Phys. Lett. B* **99** (1981) 66.

[17] D. Kazanas, *Dynamics of the Universe and Spontaneous Symmetry Breaking*, *Astrophys. J. Lett.* **241** (1980) L59.

[18] A. A. Starobinsky, *A New Type of Isotropic Cosmological Models Without Singularity*, *Phys. Lett. B* **91** (1980) 99.

[19] V. F. Mukhanov and G. V. Chibisov, *The Vacuum energy and large scale structure of the universe*, *Sov. Phys. JETP* **56** (1982) 258.

[20] A. H. Guth and S. Y. Pi, *Fluctuations in the New Inflationary Universe*, *Phys. Rev. Lett.* **49** (1982) 1110.

[21] D. H. Lyth and A. Riotto, *Particle physics models of inflation and the cosmological density perturbation*, *Phys. Rept.* **314** (1999) 1 [hep-ph/9807278].

[22] D. Baumann, *Inflation*, in *Theoretical Advanced Study Institute in Elementary Particle Physics: Physics of the Large and the Small*, pp. 523–686, 2011, DOI [0907.5424].

[23] A. Albrecht and P. J. Steinhardt, *Cosmology for Grand Unified Theories with Radiatively Induced Symmetry Breaking*, *Phys. Rev. Lett.* **48** (1982) 1220.

[24] A. Berera, *Interpolating the stage of exponential expansion in the early universe: A Possible alternative with no reheating*, *Phys. Rev. D* **55** (1997) 3346 [hep-ph/9612239].

[25] A. Berera and T. W. Kephart, *The Ubiquitous Inflaton in String-Inspired Models*, *Phys. Rev. Lett.* **83** (1999) 1084 [hep-ph/9904410].

[26] R. Rangarajan, *Current Status of Warm Inflation*, in *18th Lomonosov Conference on Elementary Particle Physics*, pp. 339–345, 2019, DOI [1801.02648].

[27] B. A. Bassett, S. Tsujikawa and D. Wands, *Inflation dynamics and reheating*, *Rev. Mod. Phys.* **78** (2006) 537 [astro-ph/0507632].

[28] L. Kofman, A. D. Linde and A. A. Starobinsky, *Reheating after inflation*, *Phys. Rev. Lett.* **73** (1994) 3195 [hep-th/9405187].

[29] L. Kofman, A. D. Linde and A. A. Starobinsky, *Towards the theory of reheating after inflation*, *Phys. Rev. D* **56** (1997) 3258 [hep-ph/9704452].

[30] P. B. Greene, L. Kofman, A. D. Linde and A. A. Starobinsky, *Structure of resonance in preheating after inflation*, *Phys. Rev. D* **56** (1997) 6175 [hep-ph/9705347].

[31] J. Braden, L. Kofman and N. Barnaby, *Reheating the Universe After Multi-Field Inflation*, *JCAP* **07** (2010) 016 [1005.2196].

[32] G. N. Felder, J. Garcia-Bellido, P. B. Greene, L. Kofman, A. D. Linde and I. Tkachev, *Dynamics of symmetry breaking and tachyonic preheating*, *Phys. Rev. Lett.* **87** (2001) 011601 [hep-ph/0012142].

[33] G. N. Felder, L. Kofman and A. D. Linde, *Tachyonic instability and dynamics of spontaneous symmetry breaking*, *Phys. Rev. D* **64** (2001) 123517 [hep-th/0106179].

[34] J. F. Dufaux, G. N. Felder, L. Kofman, M. Peloso and D. Podolsky, *Preheating with trilinear interactions: Tachyonic resonance*, *JCAP* **07** (2006) 006 [hep-ph/0602144].

[35] T. Markkanen and S. Nurmi, *Dark matter from gravitational particle production at reheating*, *JCAP* **02** (2017) 008 [1512.07288].

[36] M. Fairbairn, K. Kainulainen, T. Markkanen and S. Nurmi, *Despicable Dark Relics: generated by gravity with unconstrained masses*, *JCAP* **04** (2019) 005 [1808.08236].

[37] A. Tranberg, S. Tähtinen and D. J. Weir, *Gravitational waves from non-Abelian gauge fields at a tachyonic transition*, *JCAP* **04** (2018) 012 [1706.02365].

[38] A. Arrizabalaga, J. Smit and A. Tranberg, *Tachyonic preheating using 2PI-1/N dynamics and the classical approximation*, *JHEP* **10** (2004) 017 [hep-ph/0409177].

[39] D. Boyanovsky, D. Cormier, H. J. de Vega and R. Holman, *Out-of-equilibrium dynamics of an inflationary phase transition*, *Phys. Rev. D* **55** (1997) 3373 [hep-ph/9610396].

[40] T. Markkanen, A. Rajantie and T. Tenkanen, *Spectator Dark Matter*, *Phys. Rev. D* **98** (2018) 123532 [1811.02586].

[41] B. D. Fields, K. A. Olive, T.-H. Yeh and C. Young, *Big-Bang Nucleosynthesis after Planck*, *JCAP* **03** (2020) 010 [1912.01132].

[42] M. Dine and A. Kusenko, *Origin of the matter-antimatter asymmetry*, *Rev. Mod. Phys.* **76** (2003) 1.

[43] A. D. Sakharov, *Violation of CP Invariance, C asymmetry, and baryon asymmetry of the universe*, *Pisma Zh. Eksp. Teor. Fiz.* **5** (1967) 32.

[44] K. Kajantie, M. Laine, K. Rummukainen and M. E. Shaposhnikov, *The Electroweak phase transition: A Nonperturbative analysis*, *Nucl. Phys. B* **466** (1996) 189 [hep-lat/9510020].

[45] K. Kajantie, M. Laine, K. Rummukainen and M. E. Shaposhnikov, *Is there a hot electroweak phase transition at $m_H \gtrsim m_W$?*, *Phys. Rev. Lett.* **77** (1996) 2887 [hep-ph/9605288].

[46] P. Huet, *Electroweak baryogenesis and the standard model*, in *1st International Conference on Phenomenology of Unification: from Present to Future*, pp. 77–91, 6, 1994 [hep-ph/9406301].

[47] M. B. Gavela, P. Hernandez, J. Orloff and O. Pene, *Standard model CP violation and baryon asymmetry*, *Mod. Phys. Lett. A* **9** (1994) 795 [hep-ph/9312215].

[48] M. B. Gavela, P. Hernandez, J. Orloff, O. Pene and C. Quimbay, *Standard model CP violation and baryon asymmetry. Part 2: Finite temperature*, *Nucl. Phys. B* **430** (1994) 382 [hep-ph/9406289].

[49] P. Huet and E. Sather, *Electroweak baryogenesis and standard model CP violation*, *Phys. Rev. D* **51** (1995) 379 [hep-ph/9404302].

[50] M. D. Schwartz, *Quantum Field Theory and the Standard Model*, Cambridge University Press (3, 2014).

[51] G. 't Hooft, *Symmetry breaking through bell-jackiw anomalies*, *Phys. Rev. Lett.* **37** (1976) 8.

[52] C. Balazs, *Baryogenesis: A small review of the big picture*, 1411.3398.

[53] V. A. Kuzmin, V. A. Rubakov and M. E. Shaposhnikov, *On the Anomalous Electroweak Baryon Number Nonconservation in the Early Universe*, *Phys. Lett. B* **155** (1985) 36.

[54] M. Fukugita and T. Yanagida, *Baryogenesis Without Grand Unification*, *Phys. Lett. B* **174** (1986) 45.

[55] I. Affleck and M. Dine, *A New Mechanism for Baryogenesis*, *Nucl. Phys. B* **249** (1985) 361.

[56] S. Weinberg, *Cosmology*, Oxford University Press (2008).

[57] H. Jukkala, K. Kainulainen and P. M. Rahkila, *Flavour mixing transport theory and resonant leptogenesis*, *JHEP* **09** (2021) 119 [2104.03998].

[58] H. Jukkala, *Quantum coherence in relativistic transport theory : applications to baryogenesis*, Ph.D. thesis, University of Jyväskylä, 2022. 2211.11785.

[59] T. Konstandin, *Quantum Transport and Electroweak Baryogenesis*, *Phys. Usp.* **56** (2013) 747 [1302.6713].

[60] A. Tranberg, A. Hernandez, T. Konstandin and M. G. Schmidt, *Cold electroweak baryogenesis with Standard Model CP violation*, *Phys. Lett.* **B690** (2010) 207 [0909.4199].

[61] J. M. Cline, K. Kainulainen and D. Tucker-Smith, *Electroweak baryogenesis from a dark sector*, *Phys. Rev.* **D95** (2017) 115006 [1702.08909].

[62] J. M. Cline, A. Friedlander, D.-M. He, K. Kainulainen, B. Laurent and D. Tucker-Smith, *Baryogenesis and gravity waves from a UV-completed electroweak phase transition*, *Phys. Rev. D* **103** (2021) 123529 [2102.12490].

[63] K. Fujikura, K. Harigaya, Y. Nakai and I. R. Wang, *Electroweak-like baryogenesis with new chiral matter*, *JHEP* **07** (2021) 224 [2103.05005].

[64] S. H. Im, K. S. Jeong and Y. Lee, *Electroweak baryogenesis by axionlike dark matter*, *Phys. Rev. D* **105** (2022) 035028 [2111.01327].

[65] J. M. Cline, M. Joyce and K. Kainulainen, *Supersymmetric electroweak baryogenesis*, *JHEP* **07** (2000) 018 [hep-ph/0006119].

[66] J. M. Cline, M. Joyce and K. Kainulainen, *Erratum for 'Supersymmetric electroweak baryogenesis'*, hep-ph/0110031.

[67] K. Kainulainen, T. Prokopec, M. G. Schmidt and S. Weinstock, *First principle derivation of semiclassical force for electroweak baryogenesis*, *JHEP* **06** (2001) 031 [hep-ph/0105295].

[68] K. Kainulainen, T. Prokopec, M. G. Schmidt and S. Weinstock, *Semiclassical force for electroweak baryogenesis: Three-dimensional derivation*, *Phys. Rev.* **D66** (2002) 043502 [hep-ph/0202177].

[69] T. Prokopec, M. G. Schmidt and S. Weinstock, *Transport equations for chiral fermions to order h bar and electroweak baryogenesis. Part 1*, *Annals Phys.* **314** (2004) 208 [hep-ph/0312110].

[70] K. Kainulainen, *CP-violating transport theory for electroweak baryogenesis with thermal corrections*, *JCAP* **11** (2021) 042 [2108.08336].

[71] J. I. Kapusta and C. Gale, *Finite-temperature field theory: Principles and applications*, Cambridge Monographs on Mathematical Physics, Cambridge University Press (2011), 10.1017/CBO9780511535130.

[72] M. L. Bellac, *Thermal Field Theory*, Cambridge Monographs on Mathematical Physics, Cambridge University Press (3, 2011), 10.1017/CBO9780511721700.

[73] F. C. Khanna, A. P. C. Malbouisson, J. M. C. Malbouisson and A. R. Santana, *Thermal quantum field theory - Algebraic aspects and applications*, World Scientific (2009).

[74] J. S. Schwinger, *Brownian motion of a quantum oscillator*, *J. Math. Phys.* **2** (1961) 407.

[75] K. T. Mahanthappa, *Multiple production of photons in quantum electrodynamics*, *Phys. Rev.* **126** (1962) 329.

[76] P. M. Bakshi and K. T. Mahanthappa, *Expectation value formalism in quantum field theory. 1.*, *J. Math. Phys.* **4** (1963) 1.

[77] P. M. Bakshi and K. T. Mahanthappa, *Expectation value formalism in quantum field theory. 2.*, *J. Math. Phys.* **4** (1963) 12.

[78] L. V. Keldysh, *Diagram technique for nonequilibrium processes*, *Zh. Eksp. Teor. Fiz.* **47** (1964) 1515.

[79] J. Berges, *Nonequilibrium Quantum Fields: From Cold Atoms to Cosmology*, 1503.02907.

[80] M. E. Peskin and D. V. Schroeder, *An Introduction to quantum field theory*, Addison-Wesley, Reading, USA (1995).

[81] J. Berges, *Introduction to nonequilibrium quantum field theory*, *AIP Conf. Proc.* **739** (2004) 3 [hep-ph/0409233].

[82] G. Aarts and J. Berges, *Nonequilibrium time evolution of the spectral function in quantum field theory*, *Phys. Rev. D* **64** (2001) 105010 [hep-ph/0103049].

[83] J. Berges, S. Borsanyi and J. Serreau, *Thermalization of fermionic quantum fields*, *Nucl. Phys. B* **660** (2003) 51 [hep-ph/0212404].

[84] A. X. Arrizabalaga, *Quantum field dynamics and the 2PI effective action*, Ph.D. thesis, Amsterdam U., 2004.

[85] E. A. Calzetta and B.-L. B. Hu, *Nonequilibrium Quantum Field Theory*, Cambridge Monographs on Mathematical Physics, Cambridge University Press (9, 2008), 10.1017/CBO9780511535123.

[86] J. M. Cornwall, R. Jackiw and E. Tomboulis, *Effective action for composite operators*, *Phys. Rev. D* **10** (1974) 2428.

[87] J. Berges, *N-particle irreducible effective action techniques for gauge theories*, *Phys. Rev. D* **70** (2004) 105010 [hep-ph/0401172].

[88] M. Herranen, K. Kainulainen and P. M. Rahkila, *Towards a kinetic theory for fermions with quantum coherence*, *Nucl. Phys.* **B810** (2009) 389 [0807.1415].

[89] M. Herranen, K. Kainulainen and P. M. Rahkila, *Quantum kinetic theory for fermions in temporally varying backgrounds*, *JHEP* **09** (2008) 032 [0807.1435].

[90] M. Herranen, K. Kainulainen and P. M. Rahkila, *Kinetic theory for scalar fields with nonlocal quantum coherence*, *JHEP* **05** (2009) 119 [0812.4029].

[91] M. Herranen, *Quantum kinetic theory with nonlocal coherence*, Ph.D. thesis, University of Jyväskylä, 2009. 0906.3136.

[92] M. Herranen, K. Kainulainen and P. M. Rahkila, *Coherent quasiparticle approximation (cQPA) and nonlocal coherence*, *J. Phys. Conf. Ser.* **220** (2010) 012007 [0912.2490].

[93] M. Herranen, K. Kainulainen and P. M. Rahkila, *Coherent quantum Boltzmann equations from cQPA*, *JHEP* **12** (2010) 072 [1006.1929].

[94] C. Fidler, M. Herranen, K. Kainulainen and P. M. Rahkila, *Flavoured quantum Boltzmann equations from cQPA*, *JHEP* **02** (2012) 065 [1108.2309].

[95] A. Ayala, J. Jalilian-Marian, L. D. McLerran and A. P. Vischer, *Scattering in the presence of electroweak phase transition bubble walls*, *Phys. Rev.* **D49** (1994) 5559 [hep-ph/9311296].

[96] K. Funakubo, A. Kakuto, S. Otsuki, K. Takenaga and F. Toyoda, *Fermion scattering off CP violating electroweak bubble wall*, *Phys. Rev. D* **50** (1994) 1105 [hep-ph/9402204].

[97] T. Prokopec, M. G. Schmidt and J. Weenink, *Exact solution of the Dirac equation with CP violation*, *Phys. Rev.* **D87** (2013) 083508 [1301.4132].

[98] G. D. Moore and T. Prokopec, *Bubble wall velocity in a first order electroweak phase transition*, *Phys. Rev. Lett.* **75** (1995) 777 [hep-ph/9503296].

[99] G. D. Moore and T. Prokopec, *How fast can the wall move? A Study of the electroweak phase transition dynamics*, *Phys. Rev. D* **52** (1995) 7182 [hep-ph/9506475].

[100] O. Koskivaara, *Exact solutions of a Dirac equation with a varying CP-violating mass profile and coherent quasiparticle approximation*, Master's thesis, University of Jyväskylä, 2015.

[101] B. Garbrecht, T. Prokopec and M. G. Schmidt, *Particle number in kinetic theory*, *Eur. Phys. J. C* **38** (2004) 135 [hep-th/0211219].

[102] J. H. Traschen and R. H. Brandenberger, *Particle Production During Out-of-equilibrium Phase Transitions*, *Phys. Rev. D* **42** (1990) 2491.

[103] D. Boyanovsky and H. J. de Vega, *Quantum rolling down out-of-equilibrium*, *Phys. Rev. D* **47** (1993) 2343 [hep-th/9211044].

[104] D. Boyanovsky, D.-s. Lee and A. Singh, *Phase transitions out-of-equilibrium: Domain formation and growth*, *Phys. Rev. D* **48** (1993) 800 [hep-th/9212083].

[105] A. A. Abolhasani, H. Firouzjahi and M. M. Sheikh-Jabbari, *Tachyonic Resonance Preheating in Expanding Universe*, *Phys. Rev. D* **81** (2010) 043524 [0912.1021].

[106] E. J. Copeland, S. Pascoli and A. Rajantie, *Dynamics of tachyonic preheating after hybrid inflation*, *Phys. Rev. D* **65** (2002) 103517 [hep-ph/0202031].

[107] K. Kainulainen, *2PI-approach to particle production and phase transition dynamics*, talk given at the online workshop Physics of the Early Universe, 15.6.2022, https://indi.to/8FnJS.

[108] J. Berges and J. Serreau, *Parametric resonance in quantum field theory*, *Phys. Rev. Lett.* **91** (2003) 111601 [hep-ph/0208070].

[109] L. D. Landau and E. M. Lifshitz, *Mechanics*, Butterworth–Heinemann (1976).

[110] N. W. McLachlan, *Theory and Application of Mathieu Functions*, Oxford University Press (1947).

ORIGINAL PAPERS

PI

QUANTUM TRANSPORT AND THE PHASE SPACE STRUCTURE OF THE WIGHTMAN FUNCTIONS

by

Henri Jukkala, Kimmo Kainulainen and Olli Koskivaara (2020)

Journal of High Energy Physics, **01** 012

Published for SISSA by Springer

Received: October 30, 2019
Accepted: December 16, 2019
Published: January 3, 2020

Quantum transport and the phase space structure of the Wightman functions

Henri Jukkala,[a,b] **Kimmo Kainulainen**[a,b,c] **and Olli Koskivaara**[a,b]

[a] *Department of Physics, University of Jyväskylä, P.O. Box 35 (YFL), FI-40014 Jyväskylä, Finland*
[b] *Helsinki Institute of Physics, University of Helsinki, P.O. Box 64, FI-00014 Helsinki, Finland*
[c] *Theoretical Physics Department, CERN, 1211 Geneva 23, Switzerland*

E-mail: henri.a.jukkala@student.jyu.fi, kimmo.kainulainen@jyu.fi, olli.a.koskivaara@student.jyu.fi

Abstract: We study the phase space structure of exact quantum Wightman functions in spatially homogeneous, temporally varying systems. In addition to the usual mass shells, the Wightman functions display additional coherence shells around zero frequency $k_0 = 0$, which carry the information of the local quantum coherence of particle-antiparticle pairs. We find also other structures, which encode non-local correlations in time, and discuss their role and decoherence. We give a simple derivation of the cQPA formalism, a set of quantum transport equations, that can be used to study interacting systems including the local quantum coherence. We compute quantum currents created by a temporal change in a particle's mass, comparing the exact Wightman function approach, the cQPA and the semiclassical methods. We find that the semiclassical approximation, which is fully encompassed by the cQPA, works surprisingly well even for very sharp temporal features. This is encouraging for the application of semiclassical methods in electroweak baryogenesis with strong phase transitions.

Keywords: Thermal Field Theory, CP violation, Quantum Dissipative Systems

ArXiv ePrint: 1910.10979

https://doi.org/10.1007/JHEP01(2020)012

JHEP01(2020)012

Contents

JHEP01(2020)012

1 Introduction

Quantum coherence plays an important role in many physical problems in cosmology. Examples include CP-violating particle-wall interactions during the electroweak phase transition, out-of-equilibrium decay of nearly degenerate heavy neutrinos during leptogenesis, particle production during phase transitions and reheating at the end of inflation. The key quantity in the analysis of such intrinsically quantum systems is the two-point correlation function, whose evolution is described by the Schwinger-Dyson equations [1, 2], or in the phase space picture by the Kadanoff-Baym equations [3–5]. The phase space picture in particular has provided a useful basis for deriving approximate transport formalisms, the prime example being the standard Boltzmann theory.

In this paper we study an exact, damped, spatially homogeneous and isotropic two-point correlation function of a fermion with a possibly complex, time-varying mass term. We show that the mixed representation correlation function contains novel shell structures which carry information about different types of quantum coherences. For example we find

a shell at $k_0 = 0$, which encodes the information of a coherently mixing particle-antiparticle system. This shell was previously seen in the context of the coherent quasiparticle approximation (cQPA) [6–12] in the spectral limit, but our derivation is more general, being exact in the non-interacting case. In addition we find also other shell-structures, corresponding to non-local (in the relative time coordinate), long range correlations.

All phase space structures depend sensitively on the existence and the magnitude of damping. In the non-interacting case non-local coherences dominate the system, preventing a free particle interpretation of the phase space structure in non-trivial backgrounds. Damping suppresses the non-local coherences and leads to the emergence of a local limit for time intervals $\Delta t > 1/\Gamma$, where Γ is the damping width. For small enough Γ the local correlation function can be well approximated by a spectral ansatz, leading to the cQPA-picture mentioned above.

We will introduce a new, elegant way to reorganise the gradient expansion in the mixed representation Kadanoff-Baym equations. We then use it to give a simple derivation of the cQPA equations complete with explicit collision integrals for arbitrary types of interactions. These equations are one of the main results of this paper: they generalise the usual Boltzmann transport theory to systems including coherent particle-antiparticle states. In particular we argue that the cQPA completely encompasses the well known semiclassical effects. Possible applications of these equations include baryogenesis during phase transitions and particle production during and after inflation.

We compute the axial current densities using the exact mixed representation correlation functions as well as their cQPA counterparts and compare these to the ones obtained in the semiclassical approximation. We find that the semiclassical methods work reasonably well even in systems where the relevant modes have a wavelength as small as half of the wall width.[1] This is encouraging for the application of semiclassical methods in the related problem of electroweak phase baryogenesis with very strong electroweak phase transitions. These typically create sharp transition walls and are often encountered in the context of models producing large, observable gravitational wave signals [13–18].

This paper is organised as follows: in section 2 we first review the derivation of the cQPA formalism including the spectral Wightman functions. In section 3 we construct the exact free Wightman function from mode functions, generalised to account for the damping. Some numerical examples for the phase space solutions are shown in section 4. In section 5, we compute and compare currents in different approximations in the non-interacting case. In section 6 we present cQPA transport equations in the interacting case with explicit expressions for collision terms and compute cQPA currents with interactions. Finally, in section 7, we give our conclusions.

[1] Throughout this paper we use the word 'wall' to refer to the temporal transition in the mass, see e.g. figure 2a.

JHEP01(2020)012

2 Wightman functions and cQPA

We are using the Schwinger-Keldysh formalism [1, 2] of finite temperature field theory. The key quantities are the two-point Wightman functions

$$\begin{aligned} \mathrm{i}S^{<}(u,v) &= \big\langle \overline{\psi}(v)\psi(u)\big\rangle, \\ \mathrm{i}S^{>}(u,v) &= \big\langle \psi(u)\overline{\psi}(v)\big\rangle, \end{aligned} \tag{2.1}$$

which describe the quantum statistical properties of the non-equilibrium system.[2] We also need the retarded and advanced correlation functions $\mathrm{i}S^{\mathrm{r}}(u,v) = 2\theta(u_0-v_0)\mathcal{A}(u,v)$ and $\mathrm{i}S^{\mathrm{a}}(u,v) = -2\theta(v_0-u_0)\mathcal{A}(u,v)$, where the *spectral function* is $\mathcal{A} \equiv \frac{1}{2}\langle\{\psi(u),\overline{\psi}(v)\}\rangle = \frac{\mathrm{i}}{2}(S^{>}+S^{<}) = \frac{\mathrm{i}}{2}(S^{\mathrm{r}}-S^{\mathrm{a}})$.

To get a phase space description of the system we perform the Wigner transformation

$$S(k,x) \equiv \int \mathrm{d}^4 r\, \mathrm{e}^{\mathrm{i}k\cdot r} S\left(x+\frac{r}{2}, x-\frac{r}{2}\right), \tag{2.2}$$

where $r \equiv u-v$ and $x \equiv \frac{1}{2}(u+v)$ are the relative and average coordinates, corresponding to microscopic and macroscopic scales, respectively. In this mixed Wigner representation correlation functions obey the Kadanoff-Baym equations [3]

$$\left(\not{k} + \frac{\mathrm{i}}{2}\not{\partial}\right) S^{p} - \mathrm{e}^{-\mathrm{i}\diamondsuit}\{\Sigma^{p}\}\{S^{p}\} = 1, \tag{2.3}$$

$$\left(\not{k} + \frac{\mathrm{i}}{2}\not{\partial}\right) S^{s} - \mathrm{e}^{-\mathrm{i}\diamondsuit}\{\Sigma^{\mathrm{r}}\}\{S^{s}\} = \mathrm{e}^{-\mathrm{i}\diamondsuit}\{\Sigma^{s}\}\{S^{\mathrm{a}}\}, \tag{2.4}$$

where $s = <, >$ and $p = \mathrm{r}, \mathrm{a}$ refer to the retarded and advanced functions, respectively, Σ is the fermion self-energy and $\diamondsuit\{f\}\{g\} \equiv \frac{1}{2}[\partial_x f\cdot\partial_k g - \partial_k f\cdot\partial_x g]$ is the Moyal product. Note that we absorb the mass terms into the singular parts of $\Sigma^{\mathrm{r,a}}$, unless explicitly stated otherwise.

Moyal products are not the optimal way for organising the gradient expansions, and we find it useful to introduce another self-energy function:

$$\Sigma_{\mathrm{out}}(k,x) \equiv \int \mathrm{d}^4 z\, \mathrm{e}^{\mathrm{i}k\cdot(x-z)}\Sigma(x,z) = \mathrm{e}^{\frac{\mathrm{i}}{2}\partial_x^{\Sigma}\cdot\partial_k^{\Sigma}}\Sigma(k,x). \tag{2.5}$$

Using equation (2.5) we can rewrite Moyal products in a form that reorganises the gradients into total k-derivatives controlled by the scale of variation of Σ, while all dependence on (dynamical) gradients acting on S is fully accounted for by iterative resummation:

$$\not{\hat{K}} S^{p} - \mathrm{e}^{-\frac{\mathrm{i}}{2}\partial_x^{\Sigma}\cdot\partial_k}[\Sigma^{p}_{\mathrm{out}}(\hat{K},x)S^{p}] = 1, \tag{2.6}$$

$$\not{\hat{K}} S^{s} - \mathrm{e}^{-\frac{\mathrm{i}}{2}\partial_x^{\Sigma}\cdot\partial_k}[\Sigma^{\mathrm{r}}_{\mathrm{out}}(\hat{K},x)S^{s}] = \mathrm{e}^{-\frac{\mathrm{i}}{2}\partial_x^{\Sigma}\cdot\partial_k}[\Sigma^{s}_{\mathrm{out}}(\hat{K},x)S^{\mathrm{a}}], \tag{2.7}$$

where $\hat{K} \equiv k + \frac{\mathrm{i}}{2}\partial_x$. This form of the Kadanoff-Baym equations is particularly well suited for obtaining finite order expansions and iterative solutions. The mass operator is included in the singular part Σ_{sg} of the retarded/advanced self-energy functions:

$$\Sigma^{\mathrm{r,a}}(k,x) = \Sigma_{\mathrm{sg}}(x) + \Sigma^{\mathrm{H}}_{\mathrm{nsg}}(k,x) \mp \mathrm{i}\Sigma^{\mathcal{A}}(k,x), \tag{2.8}$$

[2] Note that we define the Wightman function $S^{<}$ with a positive sign. We also suppress Dirac indices when there is no danger of confusion.

JHEP01(2020)012

where $\Sigma^{\rm H}_{\rm nsg}$ is the non-singular Hermitian part and $\Sigma^{\mathcal{A}}$ is the anti-Hermitian part of the self-energy. To be specific, we consider a fermion field with a complex, spacetime-dependent mass $m(x)$:

$$\mathcal{L} = \mathrm{i}\overline{\psi}\partial\!\!\!/\psi - m^*(x)\overline{\psi}_{\rm R}\psi_{\rm L} - m(x)\overline{\psi}_{\rm L}\psi_{\rm R}, \tag{2.9}$$

where $\psi_{\rm L,R} \equiv \frac{1}{2}(1 \mp \gamma^5)\psi$. In the Wigner representation the spacetime-dependent mass gives rise to an operator:

$$(\hat{m}_{\rm R} + \mathrm{i}\gamma^5\hat{m}_{\rm I})S(k,x) \equiv \mathrm{e}^{-\frac{\mathrm{i}}{2}\partial_x^m\cdot\partial_k}\left\{[m_{\rm R}(x) + \mathrm{i}\gamma^5 m_{\rm I}(x)]S(k,x)\right\}, \tag{2.10}$$

where $m_{\rm R}(x)$ and $m_{\rm I}(x)$ are the real and imaginary parts of $m(x)$, respectively.

Equations (2.6) and (2.7) are practically impossible to solve exactly and one needs to find approximation schemes that maintain the essential physics at hand. The cQPA developed in refs. [6–12] is one such scheme, which allows to study particular non-equilibrium systems with quantum coherence. The crux of the cQPA is to solve equations (2.6) and (2.7) in two steps. First one solves for the phase space structure of the system at the lowest order in gradients and ignoring collision terms. This leads to spectral solutions for both pole and Wightman functions, where the latter contain new coherence shells in addition to the usual mass shell solutions. In the second step, one inserts these solutions back to the full equations, which are then reduced to a set of Boltzmann-like equations for generalised particle distribution functions [10, 11].

2.1 cQPA-solution in a spatially homogeneous system

Let us consider a spatially homogeneous and isotropic system, where $m(x) \to m(t)$ in equations (2.9) and (2.10). The Wigner transform (2.2) with respect to spatial coordinates then reduces to a Fourier transform, and we will denote the Wigner transform $S(k,x)$ as $S_{\boldsymbol{k}}(k_0,t)$. We also consider explicitly only the equation for $S^<$, as the derivation for $S^>$ is completely analogous. At first we will ignore interactions and work to the lowest order in gradients. The Hermitian part of equation (2.7) for $\overline{S}^< \equiv \mathrm{i}S^<\gamma^0$ then reduces to

$$2k_0\overline{S}^<_{\boldsymbol{k}}(k_0,t) = \{H_{\boldsymbol{k}}(t), \overline{S}^<_{\boldsymbol{k}}(k_0,t)\}, \tag{2.11}$$

where $H_{\boldsymbol{k}}(t) \equiv \boldsymbol{\alpha}\cdot\boldsymbol{k} + \gamma^0[m_{\rm R}(t) + \mathrm{i}\gamma^5 m_{\rm I}(t)]$ is the free Dirac Hamiltonian.

In spatially homogeneous and isotropic systems the Wightman functions have 8 independent components and can be parametrised without any loss of generality as follows:

$$\overline{S}^<_{\boldsymbol{k}}(k_0,t) \equiv \sum_{h,\pm,\pm'} P^{(4)}_{h\boldsymbol{k}} P^{\pm}_{\boldsymbol{k}}\gamma^0 P^{\pm'}_{\boldsymbol{k}}\, D^{\pm\pm'}_{h\boldsymbol{k}}(k_0,t), \tag{2.12}$$

where the helicity and energy projection operators are defined, respectively, as

$$P^{(4)}_{h\boldsymbol{k}} \equiv \frac{1}{2}\big(\mathbb{1} + h\boldsymbol{\alpha}\cdot\hat{\boldsymbol{k}}\gamma^5\big), \qquad P^{\pm}_{\boldsymbol{k}} \equiv \frac{1}{2}\left(\mathbb{1} \pm \frac{H_{\boldsymbol{k}}}{\omega_{\boldsymbol{k}}}\right), \tag{2.13}$$

with $\hat{\boldsymbol{k}} \equiv \boldsymbol{k}/|\boldsymbol{k}|$ and $\omega_{\boldsymbol{k}} \equiv \sqrt{\boldsymbol{k}^2 + |m(t)|^2}$. Inserting the parametrisation (2.12) to equation (2.11) gives algebraic constraints to the time- and energy-dependent coefficient functions $D^{\pm\pm'}_{h\boldsymbol{k}}(k_0,t)$:

$$\begin{aligned}(k_0 \mp \omega_{\boldsymbol{k}})D^{\pm\pm}_{h\boldsymbol{k}}(k_0,t) &= 0,\\ k_0 D^{\pm\mp}_{h\boldsymbol{k}}(k_0,t) &= 0.\end{aligned} \tag{2.14}$$

JHEP01(2020)012

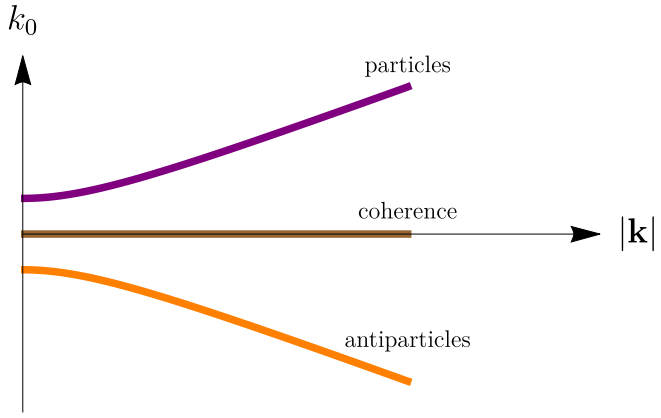

Figure 1. The shell structure of the cQPA Wightman function $S^<_{\boldsymbol{k}}(k_0, t)$, showing the particle shell where $k_0 = \omega_{\boldsymbol{k}}$ (purple), the antiparticle shell where $k_0 = -\omega_{\boldsymbol{k}}$ (orange) and the particle-antiparticle coherence shell where $k_0 = 0$ (brown).

Functions $D^{\pm\pm}_{h\boldsymbol{k}}(k_0, t) \propto \delta(k_0 \mp \omega_{\boldsymbol{k}})$ correspond to the usual mass shell excitations, while $D^{\pm\mp}_{h\boldsymbol{k}}(k_0, t) \propto \delta(k_0)$ are the new coherence functions found in refs. [7–11]. The spectral cQPA-solution can then be written as:

$$\overline{S}^<_{\boldsymbol{k}}(k_0, t) = 2\pi \sum_{h,\pm} \left[P^{m\pm}_{h\boldsymbol{k}} f^{m\pm}_{h\boldsymbol{k}} \delta(k_0 \mp \omega_{\boldsymbol{k}}) + P^{c\pm}_{h\boldsymbol{k}} f^{c\pm}_{h\boldsymbol{k}} \delta(k_0) \right]. \tag{2.15}$$

where we defined the projection operators

$$\begin{aligned} P^{m\pm}_{h\boldsymbol{k}} &\equiv \pm \frac{\omega_{\boldsymbol{k}}}{m_{\mathrm{R}}} P^{(4)}_{h\boldsymbol{k}} P^{\pm}_{\boldsymbol{k}} \gamma^0 P^{\pm}_{\boldsymbol{k}} = P^{(4)}_{h\boldsymbol{k}} P^{\pm}_{\boldsymbol{k}}, \\ P^{c\pm}_{h\boldsymbol{k}} &\equiv P^{(4)}_{h\boldsymbol{k}} P^{\pm}_{\boldsymbol{k}} \gamma^0 P^{\mp}_{\boldsymbol{k}} = P^{(4)}_{h\boldsymbol{k}} \left(\gamma^0 \pm \frac{m_{\mathrm{R}}}{\omega_{\boldsymbol{k}}} \right) P^{\mp}_{\boldsymbol{k}}. \end{aligned} \tag{2.16}$$

With this normalisation the mass shell functions $f^{m\pm}_{h\boldsymbol{k}}(t)$ coincide with the usual Fermi-Dirac distributions in the thermal limit: $f^{m\pm}_{h\boldsymbol{k}} \to f_{\mathrm{eq}}(\pm\omega_{\boldsymbol{k}})$, where $f_{\mathrm{eq}}(k_0) \equiv (\mathrm{e}^{k_0/T} + 1)^{-1}$. Note that due to the Hermiticity of $\overline{S}^<_{h\boldsymbol{k}}(k_0, t)$ the shell functions obey $(f^{m\pm}_{h\boldsymbol{k}})^* = f^{m\pm}_{h\boldsymbol{k}}$ and $(f^{c\pm}_{h\boldsymbol{k}})^* = f^{c\mp}_{h\boldsymbol{k}}$. The phase space structure of the cQPA Wightman functions is shown in figure 1.

The cQPA evolution equations are then obtained by inserting the spectral ansatz (2.15) to the anti-Hermitian part of equation (2.7), now including all gradients and interaction terms, and integrating over the energy. However, let us again first consider this equation in the non-interacting limit and to lowest order in gradients:

$$\mathrm{i}\partial_t \overline{S}^<_{\boldsymbol{k}}(k_0, t) = \left[H_{\boldsymbol{k}}, \overline{S}^<_{\boldsymbol{k}}(k_0, t) \right]. \tag{2.17}$$

Substituting the spectral solution (2.15) for $\overline{S}^<_{\boldsymbol{k}}(k_0, t)$ to equation (2.17) and integrating over k_0 it is easy to derive the leading behaviour of the shell-functions:

$$\begin{aligned} \partial_t f^{m\pm}_{h\boldsymbol{k}} &= \ldots, \\ \partial_t f^{c\pm}_{h\boldsymbol{k}} &= \mp 2\mathrm{i}\omega_{\boldsymbol{k}} f^{c\pm}_{h\boldsymbol{k}} + \ldots, \end{aligned} \tag{2.18}$$

JHEP01(2020)012

where the ellipses denote terms proportional to gradient terms (and eventually self-energy terms when interactions are included).

The point we wish to make here is that the coherence shell solutions $f^{c\pm}_{h\boldsymbol{k}}$ are oscillating rapidly with frequencies that are not suppressed by gradients. Anticipating this oscillation was the reason for our careful organisation of gradient terms in equations (2.6) and (2.7): whenever the operator $\hat{K}_0 = k_0 + \frac{\mathrm{i}}{2}\partial_t$ is acting on a coherence shell function $f^{c\pm}_{h\boldsymbol{k}}$, one must replace $\hat{K}_0 \to k_0 \pm \omega_{\boldsymbol{k}}$ as the effective momentum argument of the operator, at the *lowest* order in gradients. Indeed, in cQPA:

$$
\begin{aligned}
&\int \frac{\mathrm{d}k_0}{2\pi}\, \mathrm{e}^{-\frac{\mathrm{i}}{2}\partial^{\Sigma}_x\cdot\partial_k}\left[\Sigma_{\mathrm{out},\boldsymbol{k}}\left(k_0+\frac{\mathrm{i}}{2}\partial_t\right)\overline{S}^{<}_{h\boldsymbol{k}}(k_0,t)\right]\\
&=\sum_{\pm}\int \mathrm{d}k_0\,\Sigma_{\mathrm{out},\boldsymbol{k}}\left(k_0+\frac{\mathrm{i}}{2}\partial_t\right)\left[P^{m\pm}_{h\boldsymbol{k}}(t)f^{m\pm}_{h\boldsymbol{k}}(t)\delta(k_0\mp\omega_{\boldsymbol{k}})+P^{c\pm}_{h\boldsymbol{k}}(t)f^{c\pm}_{h\boldsymbol{k}}(t)\delta(k_0)\right]\\
&\simeq\sum_{\pm}\int \mathrm{d}k_0\left[\Sigma_{\mathrm{out},\boldsymbol{k}}(k_0)P^{m\pm}_{h\boldsymbol{k}}(t)f^{m\pm}_{h\boldsymbol{k}}(t)\delta(k_0\mp\omega_{\boldsymbol{k}})+\Sigma_{\mathrm{out},\boldsymbol{k}}(k_0\pm\omega_{\boldsymbol{k}})P^{c\pm}_{h\boldsymbol{k}}(t)f^{c\pm}_{h\boldsymbol{k}}(t)\delta(k_0)\right]\\
&=\sum_{\pm}\Sigma_{\mathrm{out},\boldsymbol{k}}(\pm\omega_{\boldsymbol{k}})\left[P^{m\pm}_{h\boldsymbol{k}}(t)f^{m\pm}_{h\boldsymbol{k}}(t)+P^{c\pm}_{h\boldsymbol{k}}(t)f^{c\pm}_{h\boldsymbol{k}}(t)\right]
\end{aligned}
\tag{2.19}
$$

for a generic self-energy function Σ. That is, coherence shell projections are not evaluated at the shell $k_0 = 0$, but on the mass shells instead. It would be straightforward to include higher order gradient corrections to shell positions generated by the $\hat{K}_0$-operator, but doing so consistently, we should also solve the cQPA-ansatz to higher order in gradients. The gradient corrections to collision terms arising from such an expansion (collisional source terms) were studied in ref. [19] for the electroweak baryogenesis problem using semiclassical methods. They were in general found to be very small and we shall not pursue them here further. For the same reason we shall, in what follows, set $\Sigma_{\mathrm{out},\boldsymbol{k}} \to \Sigma_{\boldsymbol{k}}$, dropping the corrections coming from the expansion of the Σ_{out}-function in equation (2.5).[3]

We will also work with the vacuum dispersion relations, setting $\Sigma^{\mathrm{H}}_{\mathrm{nsg}} \to 0$ and $\Sigma_{\mathrm{sg}} \to m_{\mathrm{R}} + \mathrm{i}\gamma^5 m_{\mathrm{I}}$. Furthermore, we shall drop the term $\propto S_{\mathrm{H}}\Sigma^{<}$, as this is required by the consistency of the spectral limit with respect to the pole equations [7]. With these simplifications it is now straightforward to show that the full cQPA equations can be written as

$$
\partial_t f^{m\pm}_{h\boldsymbol{k}} = \pm\frac{1}{2}\sum_s \dot{\Phi}^s_{h\boldsymbol{k}} f^{cs}_{h\boldsymbol{k}} + \mathrm{Tr}\big[\mathcal{C}_{\mathrm{coll}}P^{m\pm}_{h\boldsymbol{k}}\big], \tag{2.20a}
$$

$$
\partial_t f^{c\pm}_{h\boldsymbol{k}} = \mp 2\mathrm{i}\omega_{\boldsymbol{k}} f^{c\pm}_{h\boldsymbol{k}} + \xi_{\boldsymbol{k}}\dot{\Phi}^{\mp}_{h\boldsymbol{k}}\left[\frac{m_{\mathrm{R}}}{\omega_{\boldsymbol{k}}}f^{c\pm}_{h\boldsymbol{k}} - \frac{1}{2}\left(f^{m+}_{h\boldsymbol{k}} - f^{m-}_{h\boldsymbol{k}}\right)\right] + \xi_{\boldsymbol{k}}\,\mathrm{Tr}\big[\mathcal{C}_{\mathrm{coll}}P^{c\mp}_{h\boldsymbol{k}}\big], \tag{2.20b}
$$

where

$$
\mathcal{C}_{\mathrm{coll}} = \sum_{h,s}\left[\left(\frac{1}{2}\overline{\Sigma}^{<}_{\boldsymbol{k}}(s\omega_{\boldsymbol{k}}) - f^{ms}_{h\boldsymbol{k}}\,\overline{\Sigma}^{\mathcal{A}}_{\boldsymbol{k}}(s\omega_{\boldsymbol{k}})\right)P^{ms}_{h\boldsymbol{k}} - f^{cs}_{h\boldsymbol{k}}\,\overline{\Sigma}^{\mathcal{A}}_{\boldsymbol{k}}(s\omega_{\boldsymbol{k}})P^{cs}_{h\boldsymbol{k}}\right] + \mathrm{h.c.} \tag{2.21}
$$

[3] Note however that the expansion of $\Sigma_{\mathrm{out},\boldsymbol{k}}$ may contain lowest order gradients that need to be resummed in the same way as we did above in equation (2.19). This is the case whenever the self-energy function contains an internal propagator containing the coherence function connected to the external leg in the diagram. For more details see refs. [11, 12].

JHEP01(2020)012

and we defined

$$\dot{\Phi}^{\pm}_{h\boldsymbol{k}} \equiv \partial_t\left(\frac{m_{\mathrm{R}}}{\omega_{\boldsymbol{k}}}\right) \pm \mathrm{i}\frac{h|\boldsymbol{k}|}{\omega^2_{\boldsymbol{k}}}\,\partial_t m_{\mathrm{I}}, \qquad \xi_{\boldsymbol{k}} \equiv \frac{\omega^2_{\boldsymbol{k}}}{\omega^2_{\boldsymbol{k}} - m^2_{\mathrm{R}}}. \tag{2.22}$$

We shall return to study interacting theories in section 6. For now, we shall take a closer look into the phase space structure of the exact non-interacting Wightman functions.

3 Constructing the exact Wightman function

In the previous section we showed that Wightman functions may acquire novel phase space structures in the spectral limit. The new coherence functions $f^{c\pm}_{h\boldsymbol{k}}$ on the $k_0 = 0$ shell describe quantum coherence in correlated particle-antiparticle states. These correlations can be interpreted in terms of squeezed states and the functions $f^{c\pm}_{h\boldsymbol{k}}$ can be related to Bogolyubov coefficients [12]. Condensation of the coherence information onto a sharp phase space shell is still surprising. It is therefore of interest to see how such structures arise in an exactly solvable system.

3.1 Non-interacting Wightman function

The Lagrangian density (2.9) provides a suitable system for our study. In the spatially homogeneous case it implies the equation of motion

$$\mathrm{i}\partial\!\!\!/\psi - m^*(t)\psi_{\mathrm{L}} - m(t)\psi_{\mathrm{R}} = 0. \tag{3.1}$$

We quantise this model with the usual canonical procedure. Because three-momentum $\boldsymbol{k}$ and helicity h are conserved, the field operator $\hat{\psi}(x)$ may be expanded in terms of mode functions as

$$\hat{\psi}_{\mathrm{free}}(t,\boldsymbol{x}) = \sum_h \int \frac{\mathrm{d}^3\boldsymbol{k}}{(2\pi)^3 2\omega_-}\left[\hat{a}_{h\boldsymbol{k}} U_{h\boldsymbol{k}}(t)\mathrm{e}^{\mathrm{i}\boldsymbol{k}\cdot\boldsymbol{x}} + \hat{b}^\dagger_{h\boldsymbol{k}} V_{h\boldsymbol{k}}(t)\mathrm{e}^{-\mathrm{i}\boldsymbol{k}\cdot\boldsymbol{x}}\right], \tag{3.2}$$

where $\omega_- = \sqrt{\boldsymbol{k}^2 + |m(-\infty)|^2}$. The vacuum state is annihilated as $\hat{a}_{h\boldsymbol{k}}|\Omega\rangle = \hat{b}_{h\boldsymbol{k}}|\Omega\rangle = 0$ and our normalisation is such that

$$\begin{aligned}\{\hat{a}_{h\boldsymbol{k}}, \hat{a}^\dagger_{h'\boldsymbol{k}'}\} &= (2\pi)^3 2\omega_- \delta^{(3)}(\boldsymbol{k}-\boldsymbol{k}')\delta_{hh'},\\ \{\hat{b}_{h\boldsymbol{k}}, \hat{b}^\dagger_{h'\boldsymbol{k}'}\} &= (2\pi)^3 2\omega_- \delta^{(3)}(\boldsymbol{k}-\boldsymbol{k}')\delta_{hh'},\end{aligned} \tag{3.3}$$

while all other anticommutators vanish. The normalisation of the spinor $\hat{\psi}_{\mathrm{free}}$ is chosen to be such that

$$\{\hat{\psi}_{\mathrm{free},\alpha}(t,\boldsymbol{x}), \hat{\psi}^\dagger_{\mathrm{free},\beta}(t,\boldsymbol{y})\} = \delta_{\alpha\beta}\delta^{(3)}(\boldsymbol{x}-\boldsymbol{y}), \tag{3.4}$$

with the mode functions $U_{h\boldsymbol{k}}$ and $V_{h\boldsymbol{k}}$ normalised accordingly. The particle and antiparticle spinors can be decomposed in terms of helicity as follows:

$$U_{h\boldsymbol{k}}(t) = \begin{bmatrix}\eta_{h\boldsymbol{k}}(t)\\ \zeta_{h\boldsymbol{k}}(t)\end{bmatrix} \otimes \xi_{h\boldsymbol{k}}, \qquad V_{h\boldsymbol{k}}(t) = \begin{bmatrix}\bar{\eta}_{h\boldsymbol{k}}(t)\\ \bar{\zeta}_{h\boldsymbol{k}}(t)\end{bmatrix} \otimes \xi_{h\boldsymbol{k}}, \tag{3.5}$$

JHEP01(2020)012

where $\xi_{h\boldsymbol{k}}$ are the eigenfunctions of helicity satisfying

$$(\boldsymbol{\sigma}\cdot\hat{\boldsymbol{k}})\xi_{h\boldsymbol{k}} = h\,\xi_{h\boldsymbol{k}}, \qquad h=\pm 1, \tag{3.6}$$

and $\eta_{h\boldsymbol{k}}$, $\zeta_{h\boldsymbol{k}}$, $\bar{\eta}_{h\boldsymbol{k}}$ and $\bar{\zeta}_{h\boldsymbol{k}}$ are yet unknown mode functions that depend on $m(t)$.[4] The particle mode functions $\eta_{h\boldsymbol{k}}$ and $\zeta_{h\boldsymbol{k}}$ satisfy the equations

$$\mathrm{i}\partial_t\eta_{h\boldsymbol{k}} + h|\boldsymbol{k}|\eta_{h\boldsymbol{k}} = m(t)\zeta_{h\boldsymbol{k}}, \tag{3.7a}$$

$$\mathrm{i}\partial_t\zeta_{h\boldsymbol{k}} - h|\boldsymbol{k}|\zeta_{h\boldsymbol{k}} = m^*(t)\eta_{h\boldsymbol{k}}, \tag{3.7b}$$

while the equations for the antiparticle mode functions $\bar{\eta}_{h\boldsymbol{k}}$ and $\bar{\zeta}_{h\boldsymbol{k}}$ contained in $V_{h\boldsymbol{k}}(t)$ can be obtained from equations (3.7) by the replacements $h\to -h$ and $m\to -m^*$.

The exact Wightman functions for the non-interacting system can now be constructed as expectation values of field operators in the vacuum defined by our annihilation operators. While both Wightman functions $S^>$ and $S^<$ contain the same degrees of freedom, the positive energy solutions, which we shall be using as an example below, are most straightforward to identify from $S^>$. Continuing to work in the helicity basis we find

$$\mathrm{i}S^>_{hh'\boldsymbol{k}}(k_0,t) = \int \mathrm{d}^4 r\, \mathrm{e}^{\mathrm{i}k_0 r_0 - \mathrm{i}\boldsymbol{k}\cdot\boldsymbol{r}} \big\langle\Omega\big|\hat{\psi}_{h,\mathrm{free}}\Big(x+\frac{r}{2}\Big)\hat{\bar{\psi}}_{h',\mathrm{free}}\Big(x-\frac{r}{2}\Big)\big|\Omega\big\rangle. \tag{3.8}$$

Using the definition (3.2) (with $\hat{\psi}_{\mathrm{free}}\equiv\sum_h\hat{\psi}_{h,\mathrm{free}}$), decompositions (3.5) and spatial translation invariance, this can be written as

$$\bar{S}^>_{hh'\boldsymbol{k}}(k_0,t) = \delta_{hh'}\int_{-\infty}^{\infty}\mathrm{d}r_0\,\mathrm{e}^{\mathrm{i}k_0 r_0} M^>_{h\boldsymbol{k}}\Big(t+\frac{r_0}{2}, t-\frac{r_0}{2}\Big)\otimes P^{(2)}_{h\boldsymbol{k}}, \tag{3.9}$$

where $P^{(2)}_{h\boldsymbol{k}} = \xi_{h\boldsymbol{k}}\xi^\dagger_{h\boldsymbol{k}} = \frac{1}{2}(\mathbb{1}+h\boldsymbol{\sigma}\cdot\hat{\boldsymbol{k}})$ and only the chiral component matrix $M^>_{h\boldsymbol{k}}$ depends on the mode functions:

$$M^>_{h\boldsymbol{k}}\Big(t+\frac{r_0}{2}, t-\frac{r_0}{2}\Big) \equiv \frac{1}{2\omega_-}\begin{bmatrix} \eta_{h\boldsymbol{k}}\big(t+\frac{r_0}{2}\big)\eta^*_{h\boldsymbol{k}}\big(t-\frac{r_0}{2}\big) & \eta_{h\boldsymbol{k}}\big(t+\frac{r_0}{2}\big)\zeta^*_{h\boldsymbol{k}}\big(t-\frac{r_0}{2}\big) \\ \zeta_{h\boldsymbol{k}}\big(t+\frac{r_0}{2}\big)\eta^*_{h\boldsymbol{k}}\big(t-\frac{r_0}{2}\big) & \zeta_{h\boldsymbol{k}}\big(t+\frac{r_0}{2}\big)\zeta^*_{h\boldsymbol{k}}\big(t-\frac{r_0}{2}\big)\end{bmatrix}. \tag{3.10}$$

When the component mode functions are solved, it is straightforward to construct the Wightman function using fast Fourier transform methods.

3.2 Including damping

In the absence of dissipative processes, the free particle solutions (3.9) are correlated over arbitrarily large time intervals, because the Wigner transform correlates mode functions over all relative times $\pm\frac{r_0}{2}$ at each value of t. This is of course a physical result. However, our typical applications concern interacting systems, where such correlations are naturally suppressed by decohering interactions.

Taking interactions completely into account would require solving the full Kadanoff-Baym equations, which is beyond the scope of this paper. However, one can account for

[4] We are using the chiral basis, where the Dirac matrices are given by $\gamma^0 = \rho^1\otimes\mathbb{1}$, $\gamma^i = \mathrm{i}\rho^2\otimes\sigma^i$ and $\gamma^5 = -\rho^3\otimes\mathbb{1}$. Here both ρ^i and σ^i are just the usual 2×2 Pauli matrices. The former encode the chiral and the latter the helicity degrees of freedom of a given spinor.

JHEP01(2020)012

their most important effect for the phase space structure in a rather simple manner. We observe that the information encoded in the relative coordinate must be damped by the rate of interactions that measure the state of the system (in this case whether the system is a particle or an antiparticle). If we denote this rate by $\Gamma_{h\boldsymbol{k}}$ for each mode with momentum $\boldsymbol{k}$ and helicity h, then the appropriately damped correlation function should be

$$\begin{aligned}\overline{S}^{>}_{h\boldsymbol{k},\Gamma}(k_0,t) &\equiv \int \mathrm{d}^4 r\, \mathrm{e}^{\mathrm{i}k_0 r_0 - \mathrm{i}\boldsymbol{k}\cdot\boldsymbol{r} - \Gamma_{h\boldsymbol{k}}|r_0|} \langle\Omega|\hat{\psi}_{h,\mathrm{free}}\left(x+\frac{r}{2}\right)\hat{\bar{\psi}}_{h,\mathrm{free}}\left(x-\frac{r}{2}\right)|\Omega\rangle\gamma^0 \\ &= \int_{-\infty}^{\infty} \mathrm{d}r_0\, \mathrm{e}^{\mathrm{i}k_0 r_0 - \Gamma_{h\boldsymbol{k}}|r_0|} M^{>}_{h\boldsymbol{k}}\left(t+\frac{r_0}{2}, t-\frac{r_0}{2}\right) \otimes P^{(2)}_{h\boldsymbol{k}} \\ &\equiv W^{>}_{h\boldsymbol{k},\Gamma}(k_0,t) \otimes P^{(2)}_{h\boldsymbol{k}}. \end{aligned} \tag{3.11}$$

The only difference to the exact free case (3.9) is the introduction of the exponential damping factor $\mathrm{e}^{-\Gamma_{h\boldsymbol{k}}|r_0|}$, where the damping rate $\Gamma_{h\boldsymbol{k}}$ is the imaginary part of the pole of the full propagator. The exponential accounts for the most relevant effect of interactions here. Taking the self-energy fully into account would also modify the matrix $M^{>}_{h\boldsymbol{k}}$, which we here approximate with the free result. Equation (3.11) is thus reasonable in the usual weak coupling limit, where particles are assumed to propagate freely between relatively infrequent collisions.[5] When collisions occur they affect "measurements" of the quantum state, which over time leads to a loss of coherence.

The appearance of the exponential damping factor in equation (3.11) can also be motivated by studying the case of thermal equilibrium, where the full correlation function in Wigner representation is given by $\overline{S}^{>}_{h\boldsymbol{k}}(k_0,t) = 2\overline{\mathcal{A}}_{h\boldsymbol{k}}(k_0,t)(1-f_{\mathrm{eq}}(k_0))$. (Remember that $\overline{S}^{>}_{h\boldsymbol{k}} + \overline{S}^{<}_{h\boldsymbol{k}} = 2\overline{\mathcal{A}}_{h\boldsymbol{k}}$). The damping factor in this case arises from the absorptive self-energy corrections to the single particle poles of the pole propagators $S^{\mathrm{r,a}}_{h\boldsymbol{k}}$. When neglecting gradient corrections one can show that in the small coupling limit

$$\overline{S}^{>}_{h\boldsymbol{k}}(k_0,t) \simeq \int \mathrm{d}r_0\, \mathrm{e}^{\mathrm{i}k_0 r_0 - \Gamma_{h\boldsymbol{k}}(t)|r_0|} \overline{S}^{>}_{0,h\boldsymbol{k}}\left(t+\frac{r_0}{2}, t-\frac{r_0}{2}\right), \tag{3.12}$$

where

$$\overline{S}^{>}_{0,h\boldsymbol{k}}\left(t+\frac{r_0}{2}, t-\frac{r_0}{2}\right) = \sum_{\pm} \mathrm{e}^{\mp\mathrm{i}\omega_{\boldsymbol{k}}(t) r_0}\left[1 - f_{\mathrm{eq}}\big(\pm\omega_{\boldsymbol{k}}(t)\big)\right] P^{(4)}_{h\boldsymbol{k}} P^{\pm}_{\boldsymbol{k}}(t) \tag{3.13}$$

is the two-time representation of the free thermal correlation function (derived using the usual plane wave mode functions). We have only kept the absorptive corrections to the single particle poles of $S^{\mathrm{r,a}}_{h\boldsymbol{k}}(k_0,t)$, which are then located at $k_0 = \omega_{\boldsymbol{k}}(t) \mp \mathrm{i}\Gamma_{h\boldsymbol{k}}(t)$. The damping factor in equation (3.11) relates the free correlation function to the full one in exactly the same way as in equation (3.12), generalising the latter into the case of a non-thermal system with coherence structures.

3.3 Explicit solutions for mode functions

We shall now study the correlation function (3.11) explicitly in a simple toy model. For quantitative results we must define the mass function $m(t)$. We assume that it approaches

[5] In fact we are accounting also for the soft interactions with the background fields that lead to the time-varying mass term. It would be straightforward to extend this to other dispersive processes by the use of quasiparticle eigenstates.

JHEP01(2020)012

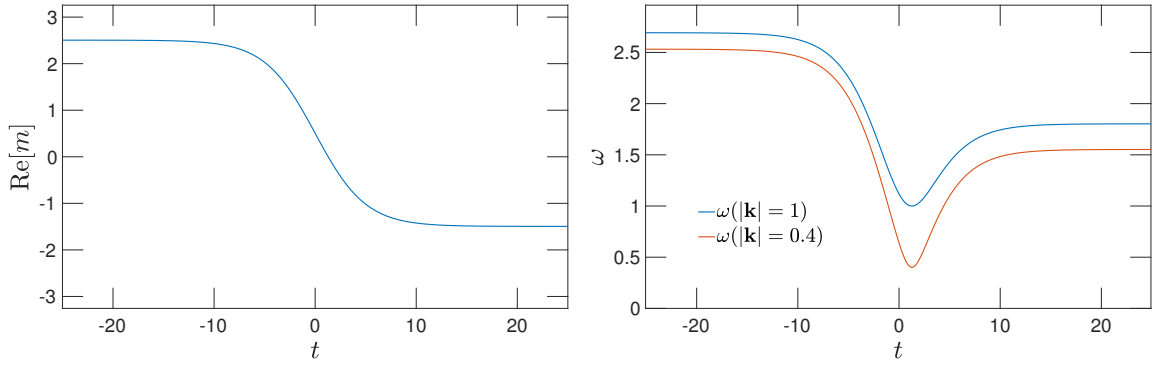

(a) (b)

Figure 2. Left panel (a): the real part of the mass profile $m(t)$ of equation (3.15), with parameters $m_1 = 0.5 + 0.005\mathrm{i}$, $m_2 = 2$ and $\tau_\mathrm{w} = 5$, in arbitrary units. Right panel (b): the positive energy eigenvalue $\omega_{\boldsymbol{k}}(t) = \sqrt{\boldsymbol{k}^2 + |m(t)|^2}$ with the same mass function as in the left panel and with both $|\boldsymbol{k}| = 1$ and 0.4.

asymptotically constant values $m_\mp$ at early and late times, respectively, and that it changes between the asymptotic values over a characteristic time interval τ_w around time $t = 0$. This is the situation e.g. in a phase transition interpolating between the broken and unbroken phases. At early and late times such solutions approach asymptotically plane waves (with spinor normalisation $U^\dagger_{h\boldsymbol{k}} U_{h\boldsymbol{k}} = V^\dagger_{h\boldsymbol{k}} V_{h\boldsymbol{k}} = 2\omega_-$):

$$U^\infty_{h\boldsymbol{k}} = \begin{bmatrix} \sqrt{\omega_- - h|\boldsymbol{k}|} \\ \sqrt{\omega_- + h|\boldsymbol{k}|}\mathrm{e}^{-\mathrm{i}\theta} \end{bmatrix} \otimes \xi_{h\boldsymbol{k}} \mathrm{e}^{-\mathrm{i}\omega_- t}, \tag{3.14a}$$

$$V^\infty_{h\boldsymbol{k}} = \begin{bmatrix} \sqrt{\omega_- + h|\boldsymbol{k}|} \\ -\sqrt{\omega_- - h|\boldsymbol{k}|}\mathrm{e}^{\mathrm{i}\theta} \end{bmatrix} \otimes \xi_{h\boldsymbol{k}} \mathrm{e}^{\mathrm{i}\omega_- t}, \tag{3.14b}$$

where θ is the phase of the constant mass in the asymptotic limit: $m \to |m_\pm|\mathrm{e}^{\mathrm{i}\theta_\pm}$. To be specific, we use the following mass profile for which the mode functions can be solved analytically [20]:

$$m(t) = m_1 + m_2 \tanh\left(-\frac{t}{\tau_\mathrm{w}}\right), \tag{3.15}$$

where $m_1 = m_{1\mathrm{R}} + \mathrm{i}m_{1\mathrm{I}}$ and $m_2 = m_{2\mathrm{R}} + \mathrm{i}m_{2\mathrm{I}}$ are constant complex coefficients and τ_w is a parameter describing the width of the transition in time. At early times ($t \to -\infty$) we then have $m \to m_- = m_1 + m_2$ and at late times ($t \to \infty$) $m \to m_+ = m_1 - m_2$. For solving the mode functions, the imaginary part of m_2 is removed by a global rotation of the spinors (see ref. [20] for details), which of course does not change the dynamics of the system. The remaining imaginary part is simply denoted by m_I. Figure 2 illustrates the shape of the mass function and the corresponding energy for representative parameters.

JHEP01(2020)012

Equations (3.7) with the mass profile (3.15) were solved in ref. [20] and here we just quote the results relevant for our purposes. Defining a new basis for the mode functions,

$$\phi^{\pm}_{h\boldsymbol{k}}(t) \equiv \frac{1}{\sqrt{2}}\big[\eta_{h\boldsymbol{k}}(t) \pm \zeta_{h\boldsymbol{k}}(t)\big], \tag{3.16a}$$

$$\bar{\phi}^{\pm}_{h\boldsymbol{k}}(t) \equiv \frac{1}{\sqrt{2}}\big[\bar{\eta}_{h\boldsymbol{k}}(t) \pm \bar{\zeta}_{h\boldsymbol{k}}(t)\big], \tag{3.16b}$$

one can show that the solutions can be written in terms of Gauss' hypergeometric functions:

$$\phi^{\pm(1)}_{h\boldsymbol{k}} = C^{\pm(1)}_{h\boldsymbol{k}}\, z^{\alpha}(1-z)^{\beta}\ {}_2F_1(a_\pm, b_\pm, c; z), \tag{3.17a}$$

$$\phi^{\pm(2)}_{h\boldsymbol{k}} = C^{\pm(2)}_{h\boldsymbol{k}}\, z^{-\alpha}(1-z)^{\beta}\ {}_2F_1(1+a_\pm-c, 1+b_\pm-c, 2-c; z), \tag{3.17b}$$

where $C^{\pm(1,2)}_{h\boldsymbol{k}}$ are constants and

$$\begin{aligned} z &= \frac{1}{2}\left[1-\tanh\left(-\frac{t}{\tau_{\rm w}}\right)\right], \qquad \alpha = -\frac{\mathrm{i}}{2}\tau_{\rm w}\omega_-, \qquad \beta = -\frac{\mathrm{i}}{2}\tau_{\rm w}\omega_+, \\ \omega_\mp &= \sqrt{\boldsymbol{k}^2 + m_{\rm I}^2 + (m_{1\rm R} \pm m_{2\rm R})^2}, \\ a_\pm &\equiv 1+\alpha+\beta \mp \mathrm{i}\tau_{\rm w} m_{2\rm R}, \qquad b_\pm \equiv \alpha+\beta \pm \mathrm{i}\tau_{\rm w} m_{2\rm R}, \quad c \equiv 1+2\alpha. \end{aligned} \tag{3.18}$$

Superscripts (1) and (2) label the two linearly independent solutions. The solutions for $\bar{\phi}^{\pm}_{h\boldsymbol{k}}$ can be obtained by changing the sign of helicity in equations (3.17), $h \to -h$. (Helicity enters the solution through the boundary conditions as will be seen below.)

Using the properties of the hypergeometric functions it is easy to check that at early times

$$\phi^{\pm(1)}_{h\boldsymbol{k}} \xrightarrow{t\to-\infty} C^{\pm(1)}_{h\boldsymbol{k}} \mathrm{e}^{-\mathrm{i}t\omega_-}, \qquad \phi^{\pm(2)}_{h\boldsymbol{k}} \xrightarrow{t\to-\infty} C^{\pm(2)}_{h\boldsymbol{k}} \mathrm{e}^{\mathrm{i}t\omega_-}. \tag{3.19}$$

At late times these solutions split into mixtures of positive and negative frequency states:

$$\phi^{\pm(1)}_{h\boldsymbol{k}} \xrightarrow{t\to\infty} C^{\pm(1)}_{h\boldsymbol{k}} \frac{\Gamma(c)\Gamma(c-a_\pm-b_\pm)}{\Gamma(c-a_\pm)\Gamma(c-b_\pm)} \mathrm{e}^{\mathrm{i}t\omega_+} + C^{\pm(1)}_{h\boldsymbol{k}} \frac{\Gamma(c)\Gamma(a_\pm+b_\pm-c)}{\Gamma(a_\pm)\Gamma(b_\pm)} \mathrm{e}^{-\mathrm{i}t\omega_+}, \tag{3.20}$$

which manifests the fact that a varying mass mixes particle and antiparticle states. Indeed, in systems without time-translation invariance the division to particles and antiparticles is not unique. Locally a clear identification can be made however, and with the asymptotic limits given above we can construct different initial and final states we wish to study.

Let us now specify our initial state as a positive frequency particle, i.e. the solution (3.17a), corresponding to the constant mass one-particle state (3.14a) at $t \to -\infty$. This determines the constants

$$C^{\pm(1)}_{h\boldsymbol{k}} = \frac{1}{\sqrt{2}}\left(\sqrt{\omega_- - h|\boldsymbol{k}|} \pm \sqrt{\omega_- + h|\boldsymbol{k}|}\mathrm{e}^{-\mathrm{i}\theta_-}\right), \tag{3.21}$$

where $\theta_- = \mathrm{Arg}(m_{1\rm R} + m_{2\rm R} + \mathrm{i}m_{\rm I})$. Figure 3 shows these solutions for a representative set of parameters. It is evident that the solutions asymptote to plane waves very quickly on each side of the transition region.

JHEP01(2020)012

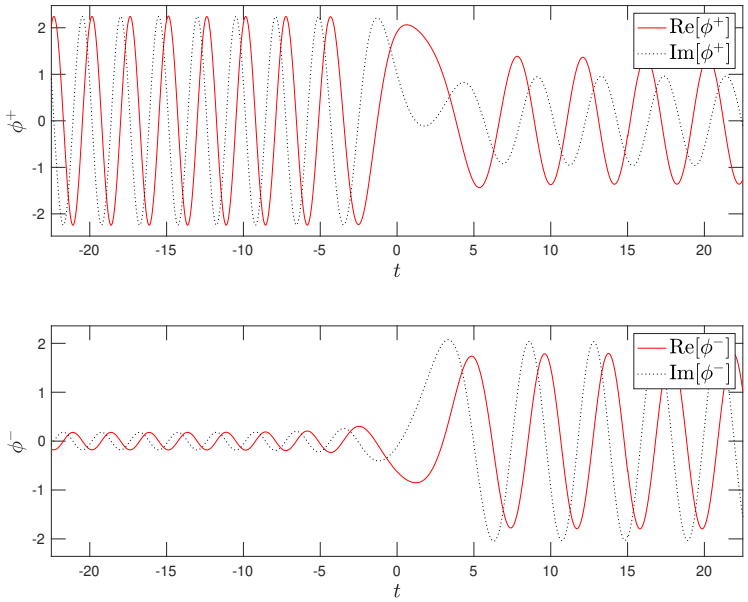

Figure 3. Shown are the real and imaginary parts of the exact free mode functions $\phi^{\pm(1)}_{h\boldsymbol{k}}$, defined in equation (3.17a), across the transition defined by the mass profile (3.15). We used the initial conditions (3.21) and the same parameters as in figure 2a with $|\boldsymbol{k}| = 0.4$ and $h = 1$.

4 Phase space of the exact Wightman function

Having solved the mode functions, we can now calculate the Wightman functions $S^s_{h\boldsymbol{k}}$ and $S^s_{h\boldsymbol{k},\Gamma}$. It suffices to concentrate on one type of them, say $S^>$, since both functions exhibit the same phase space structures. We evaluate the Wightman functions by inserting the mode functions solved from equations (3.16) and (3.17) with the boundary conditions (3.21) into the matrix $M^>_{h\boldsymbol{k}}$ (3.10) and performing the integral over the relative coordinate in equation (3.11) numerically for each $\boldsymbol{k}$-mode. Results of these computations for varying parameter sets are shown in figures 4–6.

Figure 4 shows the absolute value of the $(1,1)$-component of the function $W^>_{h\boldsymbol{k},\Gamma}(k_0,t)$, defined in equation (3.11), for a system initially prepared to a pure positive frequency state. (Other three chiral components are qualitatively similar.) The surface plot in the left panel displays a clearly peaked structure, where the initial particle peak branches at the transition region to three separate peaks corresponding to particle and antiparticle solutions at $k_0 = \pm\omega_{\boldsymbol{k}}(t)$ and a coherence peak at $k_0 = 0$. This reproduces the cQPA-shell structure predicted in the previous section. Note that the coherence shell solution is rapidly oscillating in time as predicted by the cQPA equation (2.18). The feature is slightly obscured by the absolute value, but it shows up in the "digitised" structure of the coherence solution in the projected plot on the right panel. Due to a rather large interaction rate Γ the shell structures are wide enough in frequency to overlap a little, which can after the transition be seen as a leakage of the coherence shell oscillations into the mass shells. At early times the sole positive frequency shell contains no oscillations. Physically, what we are seeing, is particle production by a temporally changing mass parameter and the

JHEP01(2020)012

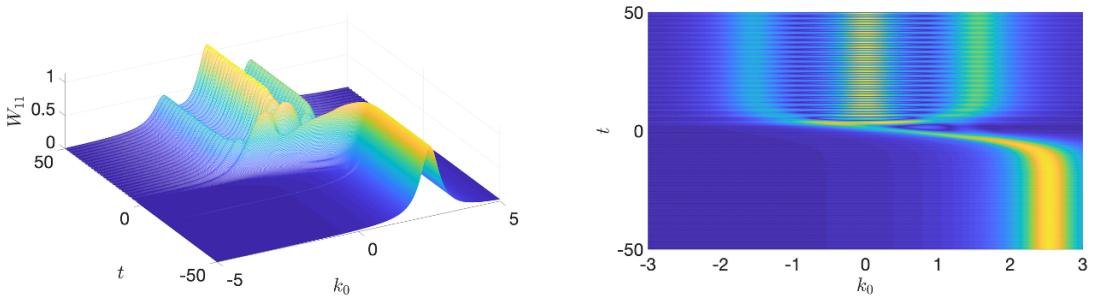

Figure 4. Shown is the absolute value of the $(1,1)$-component of the exact free Wightman function $W^{>}_{h\boldsymbol{k},\Gamma}$ defined in equation (3.11), for parameters $h = 1$, $|\boldsymbol{k}| = 0.4$, $m_{1\mathrm{R}} = 0.5$, $m_{2\mathrm{R}} = 2$, $m_{\mathrm{I}} = -0.005$, $\tau_{\mathrm{w}} = 5$ and $\Gamma = 0.4$. Note that time flows from bottom to top in the right panel.

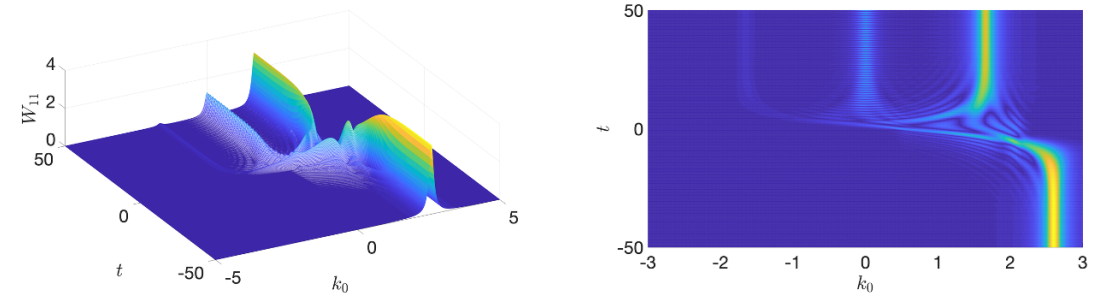

Figure 5. The same as in figure 4, but for parameters $h = 1$, $|\boldsymbol{k}| = 0.7$, $m_{1\mathrm{R}} = 0.5$, $m_{2\mathrm{R}} = 2$, $m_{\mathrm{I}} = -0.005$, $\tau_{\mathrm{w}} = 5$ and $\Gamma = 0.1$.

fundamental relation of the phenomenon to the quantum coherence between positive and negative frequency states.

In figure 4 we assumed a quite large damping factor and correspondingly the shell structures were rather broad in frequency. In figure 5 we show for comparison a solution with a smaller wavelength and a much smaller damping coefficient. As expected, the shell structure gets more sharply peaked because of the smaller width.[6] At the same time the antiparticle shell after the transition becomes much less pronounced, reflecting the fact that a larger initial energy is less affected by the mass change. (The same qualitative behaviour would of course be obtained by increasing the width of the wall, leading to less efficient particle production.) Indeed, for a very large $|\boldsymbol{k}|$ the whole novel shell structure vanishes, making way for a single shell following a classical energy path such as the ones shown in figure 2b.

Right at the transition region one can distinguish additional fine-structures, which are not related to the cQPA solution of equation (2.15). This is partly because our derivation of cQPA assumed lowest order expansion in gradients. It would be interesting (and possible) to generalise cQPA to a singular higher order expansion in gradients and check if the emerging discrete sequence of shells could reproduce the structures seen here. However,

[6] In fact it is easy to show in an even simpler toy model, where the mass-function is replaced by a step-function, that the peaks become Breit-Wigner-functions in frequency [21]. The spectral cQPA-solution can then be seen explicitly as the Breit-Wigner forms approach delta functions in the limit $\Gamma \to 0$.

JHEP01(2020)012

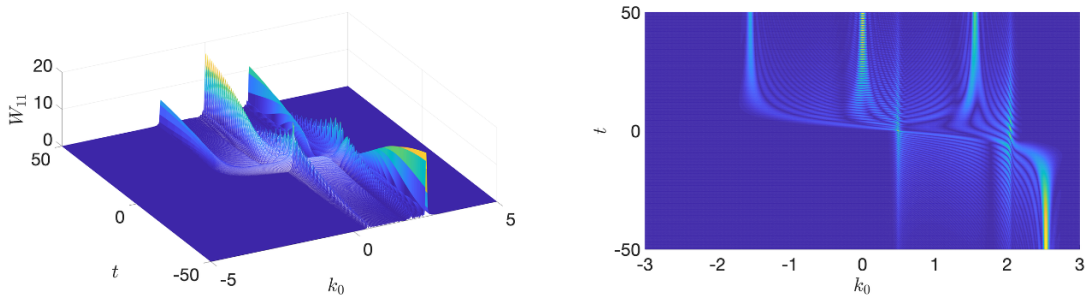

Figure 6. The same as in figure 4, but for parameters $h = 1$, $|\boldsymbol{k}| = 0.4$, $m_{1\mathrm{R}} = 0.5$, $m_{2\mathrm{R}} = 2$, $m_{\mathrm{I}} = -0.005$, $\tau_{\mathrm{w}} = 5$ and $\Gamma = 0.02$.

these structures may also reflect the onset of the new non-local correlations that we shall turn to next.[7]

4.1 Non-local coherence in time

In figure 6 we again plot $|W^{>}_{h\boldsymbol{k},\Gamma,11}|$ with the same parameters as in figure 4, but with a much smaller decay term. The shells become even more peaked as expected, but in addition a much richer phase space structure emerges, extending well outside the transition region. From the projection plot one recognises that two new spectral shells have entered the play, together with a rich network of secondary fine-structures around the transition region. From the surface plot it is evident, compared to the earlier cases, that the cQPA-shells are suppressed near the transition region, while the new shells grow in amplitude there. Far away from the transition region the situation is reversed and the new shells (which are also oscillating) fade away, making room for the usual cQPA-shells that allow for a clear particle and antiparticle identification.

The new shells correspond to non-local correlations between the early- and late-time solutions across the wall; in the particle interpretation the system appears to become aware of the change in its energy levels already before the transition occurs. This is completely expected behaviour for a quantum system and, again, these shells can also be seen analytically in the simple step-function model [21]. One can show, and also observe in the projection plot, that the new shells coincide with the average frequencies

$$k_0 = \frac{1}{2}\left(\sqrt{\boldsymbol{k}^2 + |m_-|^2} \pm \sqrt{\boldsymbol{k}^2 + |m_+|^2}\right), \tag{4.1}$$

which reveals that they correspond to particle-particle and particle-antiparticle correlations across the wall. The reason why these solutions are suppressed at large time differences is the damping; the information about the transition can be propagated only up to a distance

[7] Let us clarify our use of the notion of (non-)locality in this paper: first, by non-local coherence we mean coherence over the relative coordinate in the two-point correlation function. Then, by local limit, we mean the limit where the two time-arguments in the correlation function are the same. The local correlation function still supports the particle-antiparticle coherence, which is non-local in the sense that creating it requires coherent evolution over a finite interval in the average time uninterrupted by collisions, which differentiate particles from antiparticles.

JHEP01(2020)012

$\Delta t \sim 1/\Gamma$ in the relative coordinate. Beyond this time interval only local correlations can survive. Decreasing Γ further makes the non-local coherence structures ever more prominent and if one removes damping entirely, the system becomes completely overwhelmed by them. In this limit the system is intrinsically quantum; local particle-like solutions are irrelevant and the system is globally sensitive to the initial conditions and the size of the time-domain.

4.2 Physical and practical significance of the phase space structures

We have seen that a quantum system with negligible damping is strongly correlated over large time intervals. However, in interacting systems damping suppresses non-local correlations, eventually reducing correlation functions to the local limit. This decoherence enables the quasiparticle picture and eventually the Boltzmann limit in slowly varying backgrounds. In the language of a direct space Kadanoff-Baym approach, damping removes contributions from memory integrals over long relative time differences. Note however, that damping does *not* destroy the coherence shell at $k_0 = 0$; spectral cQPA shells get finite widths, but the coherence between particles and antiparticles survives. Of course, equations (2.6) and (2.7) contain also other (hard) collisions terms, which we have omitted so far. If these collisions depend on the particle-antiparticle nature of the state, they constitute measurements which destroy this coherence. A complete treatment of particle production in phase transitions, for example, should account for this effect as well, as was indeed done for example in refs. [7, 8] in the cQPA context.

From a practical point of view our solutions show that in the weakly interacting limit $\tau_{\rm w}\Gamma \ll 1$, a complete phase space solution of the interacting problem would require very fine resolution in frequency space in order to account for all the fine-structures in the transition region. In this region, because of the large number of transient shell structures, the quasiparticle picture appears impractical.[8] On the other hand, even for a moderately strongly interacting system $\tau_{\rm w}\Gamma \gtrsim 0.5$, the phase space structure is smoothed out and the *coherent* quasiparticle picture of refs. [6–12] should provide a good description of the system.

5 Currents and connection to the semiclassical limit

In the previous sections we showed that the phase space of a system with a varying mass profile has non-trivial phase space structures, whose intricacy depends on the size of the mode momentum $\boldsymbol{k}$ and the damping strength Γ. We also argued that the quasiparticle picture may provide a reasonable description of the system (even for very small $\tau_{\rm w}\Gamma$). We now change slightly our perspective, and ask how our results compare with the semiclassical treatment, which should be applicable when $\tau_{\rm w}|\boldsymbol{k}| \gg 1$. Semiclassical methods have been

[8] The situation is not as bad as one might think even in the limit $\tau_{\rm w}\Gamma \ll 1$. Let us consider the problem from the point of view of the cQPA method, which includes local coherence shells but ignores the non-local structures. Because the quasiparticle picture is appropriate far from the transition region and one expects only few interactions within the transition area, the evolution of the quasiparticle distributions may be only weakly sensitive to the new transient structures (the evolution of the quasiparticle functions is affected by the new shells only through the collision integrals). If the physics one is interested in is sensitive only to the late time correlations, it should be rather well described by the cQPA.

JHEP01(2020)012

widely used to describe CP-violating dynamics in electroweak baryogenesis models [5, 19, 22–30]. While we are dealing with a purely time-dependent system here, the results should be qualitatively representative.

To be specific, we shall compare different methods for computing the expectation values of fermionic currents. A generic current corresponding to a Dirac operator $\mathcal{O}$ can be computed as

$$j^{\mathcal{O}}_{h\boldsymbol{k}}(t) \equiv \int \frac{\mathrm{d}^3\boldsymbol{r}}{(2\pi)^3}\, \mathrm{e}^{\mathrm{i}\boldsymbol{k}\cdot\boldsymbol{r}} \big\langle \hat{\bar{\psi}}_h\big(t, \boldsymbol{x}+\boldsymbol{r}\big)\mathcal{O}\hat{\psi}_h\big(t,\boldsymbol{x}\big)\big\rangle = \int \frac{\mathrm{d}k_0}{2\pi}\, \mathrm{Tr}\big[\mathcal{O}\,\mathrm{i}S^<_{h\boldsymbol{k}}(k_0,t)\big]. \tag{5.1}$$

In particular, we will be interested in the axial charge density

$$j_{5,h\boldsymbol{k}}(t) \equiv \int \frac{\mathrm{d}^3\boldsymbol{r}}{(2\pi)^3}\, \mathrm{e}^{\mathrm{i}\boldsymbol{k}\cdot\boldsymbol{r}} \big\langle \hat{\bar{\psi}}_h\big(t, \boldsymbol{x}+\boldsymbol{r}\big)\gamma^0\gamma^5\hat{\psi}_h\big(t,\boldsymbol{x}\big)\big\rangle, \tag{5.2}$$

which is related to particle asymmetries.

With the exact solutions (3.17) at hand it is a simple numerical task to compute $j_{5,h\boldsymbol{k}}$ for the kink profile using equation (5.1). Furthermore, in cQPA it can be calculated in terms of the shell functions $f^{(m,c)\pm}_{h\boldsymbol{k}}$ as follows:

$$j^{\mathrm{cQPA}}_{5,h\boldsymbol{k}} = \sum_{s=\pm}\left[-\frac{sh|\boldsymbol{k}|}{\omega_{\boldsymbol{k}}}\, f^{ms}_{h\boldsymbol{k}} + \left(\frac{h|\boldsymbol{k}|m_{\mathrm{R}}}{\omega^2_{\boldsymbol{k}}} + \frac{\mathrm{i}sm_{\mathrm{I}}}{\omega_{\boldsymbol{k}}}\right) f^{cs}_{h\boldsymbol{k}}\right]. \tag{5.3}$$

5.1 Collisionless case

We first point out that currents computed with the exact Wightman function fully agree with the cQPA currents in the collisionless limit. This may look surprising, because cQPA relies on a spectral ansatz derived to lowest order in gradients. Yet, at the integrated level the collisionless cQPA is in fact *exact* and cQPA shell functions are in one-to-one correspondence with the *local limit* of the correlation functions [12], and the correspondence is not affected by the introduction of a damping term. This can be illustrated explicitly e.g. with equations (3.12) and (2.15): integrating equation (3.12) over k_0 gives

$$\begin{aligned}\int \frac{\mathrm{d}k_0}{2\pi}\, \overline{S}^<_{h\boldsymbol{k},\Gamma}(k_0,t) &= \int \frac{\mathrm{d}k_0}{2\pi} \int \mathrm{d}r_0\, \mathrm{e}^{\mathrm{i}k_0 r_0 - \Gamma_{h\boldsymbol{k}}|r_0|}\overline{S}^<_{h\boldsymbol{k}}\left(t+\frac{r_0}{2}, t-\frac{r_0}{2}\right)\\ &= \overline{S}^<_{h\boldsymbol{k}}(t,t) \overset{\mathrm{cQPA}}{\longrightarrow} \sum_{\pm}\left[P^{m\pm}_{h\boldsymbol{k}} f^{m\pm}_{h\boldsymbol{k}} + P^{c\pm}_{h\boldsymbol{k}} f^{c\pm}_{h\boldsymbol{k}}\right],\end{aligned} \tag{5.4}$$

where in the last line we used the cQPA-ansatz (2.15). Thus, *the essential feature of the cQPA is* not the expansion in gradients or the ensuing spectral approximation, but *the assumption that non-local degrees of freedom are not dynamical.* In particular this result shows that cQPA retains the full quantum information relative to the average time coordinate t.

Finally, let us stress the delicate role the decay width Γ plays in the emergence of the cQPA-scheme. On one hand, we have seen that if Γ was vanishing, non-local temporal correlations would dominate the correlation function; the quality of the local approximation then crucially depends on a non-zero damping. Yet, the spectral limit formally corresponds

JHEP01(2020)012

to taking $\Gamma \to 0$. That is, Γ must be large enough to ensure that non-local correlations can be neglected, and yet small enough so that a spectral quasiparticle picture is valid. Fortunately this is typically the case. We shall elaborate more on these issues in a forthcoming publication [31].

5.2 Semiclassical approximation

While the cQPA is designed to capture the local quantum effects in a generic evolving background, a different method exists for systems in slowly varying backgrounds. The *semiclassical approximation* was introduced in refs. [22–25] for systems with spatial inhomogeneities, and the details for temporally varying systems can be found in ref. [5]. The semiclassical approximation is also local, but in contrast to cQPA, one applies the gradient expansion directly to the *unintegrated* equations of motion, eliminating off-diagonal chiral degrees of freedom. This leads to a loss of information in comparison to cQPA.

We do not get into the details of the derivation, but merely quote the results relevant for our purposes. The Wightman function is decomposed into a helicity block-diagonal form

$$2\mathrm{i}\gamma^0 S^<_{h\boldsymbol{k}}(k_0,t) = \sigma^a g_{ah\boldsymbol{k}}(k_0,t) \otimes P^{(2)}_{h\boldsymbol{k}}, \tag{5.5}$$

where $a \in \{0,1,2,3\}$, $\sigma^0 \equiv \mathbb{1}$, σ^i are the Pauli matrices, and g_{ah} are the unknown coefficient functions to be solved. The main outcome of the semiclassical formalism is that, when considered to the first order in the gradients of a time-dependent mass $m = |m|\mathrm{e}^{\mathrm{i}\theta}$, the axial part of the helicity correlation function $g_{3h\boldsymbol{k}}$ is found to be living on a shifted energy shell: $g_{3h\boldsymbol{k}} \sim \delta\left(k_0^2 - \omega^2_{3h\boldsymbol{k}}\right)$, with

$$\omega_{3h\boldsymbol{k}} \equiv \omega_{\boldsymbol{k}}(t) + h\frac{|m|^2\partial_t\theta(t)}{2|\boldsymbol{k}|\omega_{\boldsymbol{k}}(t)}. \tag{5.6}$$

The shift has an opposite sign for particles with opposite helicities, and it obviously vanishes for translationally invariant systems.[9]

Defining the integrated phase space densities

$$f_{ah\boldsymbol{k}}(t) \equiv \int \frac{\mathrm{d}k_0}{2\pi}\, g_{ah\boldsymbol{k}}(k_0,t) \tag{5.7}$$

one finds the following collisionless equation of motion for the axial density $f_{3h\boldsymbol{k}}$ [5]:

$$\left[\omega_{3h\boldsymbol{k}}\partial_t + F_{h\boldsymbol{k}}\partial_{k_0}\right] f_{3h\boldsymbol{k}} = 0, \tag{5.8}$$

where $F_{h\boldsymbol{k}}$ is the *semiclassical force*

$$F_{h\boldsymbol{k}} = \frac{\partial_t|m|^2}{2\omega_{3h\boldsymbol{k}}} + h\frac{\partial_t(|m|^2\partial_t\theta)}{2|\boldsymbol{k}|\omega_{\boldsymbol{k}}}. \tag{5.9}$$

This process of going from quantum equations (cQPA) to the semiclassical force is analogous to going from the Schrödinger equation to a spin-dependent force when calculating

[9] For problems with a spatially varying mass a similar shift occurs for the zeroth component g_0, and is proportional to the spin of the particle [24, 25].

JHEP01(2020)012

an electron's movement in a magnetic field (the Stern-Gerlach experiment). Noticing that $F_{h\boldsymbol{k}} = \partial_t \omega_{3h\boldsymbol{k}}$, one can see that the collisionless equation (5.8) is solved by

$$f^{\rm sc}_{3h\boldsymbol{k}}(t) = \frac{\omega_- f^-_{3h\boldsymbol{k}}}{\omega_{3h\boldsymbol{k}}(t)}, \tag{5.10}$$

where $f^-_{3h\boldsymbol{k}} \equiv f_{3h\boldsymbol{k}}(t \to -\infty)$ is determined by the desired initial conditions. These formulae are valid for an arbitrary form of the mass function. Note that the definition of the phase space function $f_{3h\boldsymbol{k}}$ exactly coincides with our definition of the current $j_{5,h\boldsymbol{k}}$ in equations (5.1) and (5.2).

5.3 Range of validity of the different formalism

Let us now compare the axial quantum currents to their semiclassical approximation in different kinematical regions. We use the initial conditions described in section 3.3, which correspond to choosing $f^-_{3h\boldsymbol{k}} = h|\boldsymbol{k}|/\omega_-$ in equation (5.10). In cQPA the equivalent initial configuration for $S^<$ is $f^{m-}_{h\boldsymbol{k}}(-\infty) = 1$ with other shell functions vanishing. In this case the semiclassical approximation gives the following form for the helicity-summed axial density of our kink-mass system:

$$j^{\rm sc}_{5,\boldsymbol{k}}(t) = \sum_h f^{\rm sc}_{3h\boldsymbol{k}}(t) = -\frac{m_{\rm I} m_{\rm 2R}}{\tau_{\rm w}\, \omega^3_{\boldsymbol{k}}(t) \cosh^2(t/\tau_{\rm w})}. \tag{5.11}$$

In figure 7 we show the helicity summed axial density $j_{5,\boldsymbol{k}} \equiv \sum_h j_{5,h\boldsymbol{k}}$ as a function of time for a few representative values for $|\boldsymbol{k}|$, computed from the semiclassical equation (5.11), using our exact solutions with equation (5.1) and using the cQPA methods via equation (5.3). As explained above, the full cQPA-currents coincide with the exact currents in the collisionless limit. In this case the cQPA-current is *pure coherence*, since the cQPA-solution restricted to mass shells (green dashed lines) gives a vanishing axial current.

The general comparison to the semiclassical approximation is as expected: prominent oscillations appearing in the exact solutions for small $|\boldsymbol{k}|$ are absent in the semiclassical solution. This is as it should be, since quantum coherence effects are included in the semiclassical formalism only in an average sense. However, the oscillations turn off quickly for large $|\boldsymbol{k}|$, such that already for $|\boldsymbol{k}| = 1.5$ the semiclassical and quantum currents are practically identical. Moreover, the semiclassical current captures the *average* of the exact solution very well for $|\boldsymbol{k}| = 0.8$ and reasonably well even for $|\boldsymbol{k}| = 0.4$. The broad range of validity of the semiclassical approximation is slightly surprising. On general grounds one would assume it to work when at least one wavelength fits to the wall width, corresponding to $\frac{2\pi}{|\boldsymbol{k}|} < \tau_{\rm w}$. However, our results suggest that it works quite well even when the wall width is but a fraction of the wave length of the mode.

The validity of the semiclassical approximation is even more pronounced when one considers the integrated current

$$j_5(t) \equiv \frac{1}{2\pi^2} \int {\rm d}|\boldsymbol{k}|\, \boldsymbol{k}^2 \sum_h j_{5,h\boldsymbol{k}}(t). \tag{5.12}$$

JHEP01(2020)012

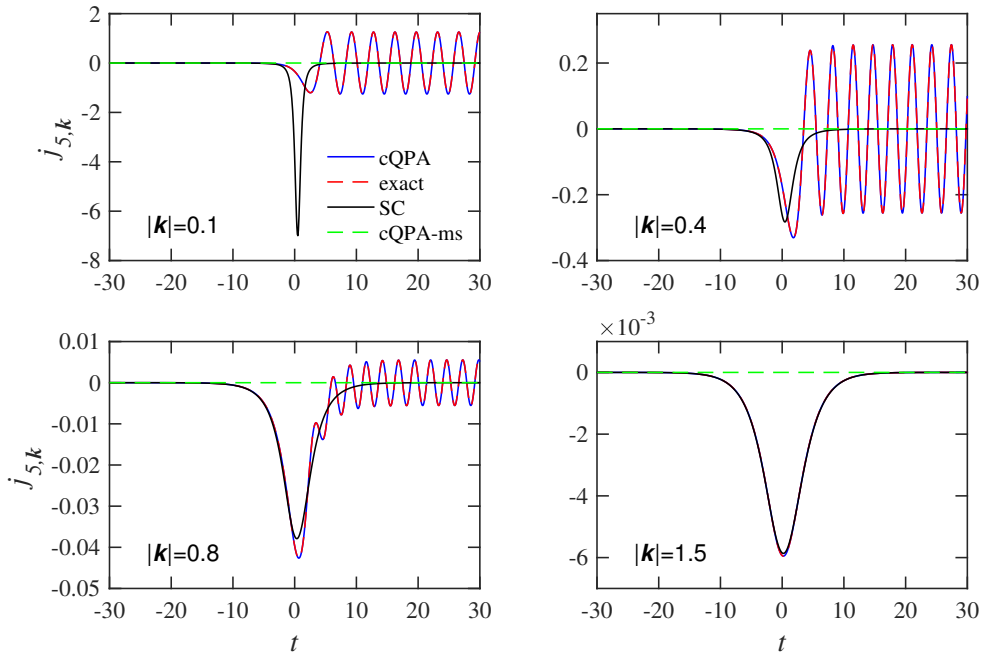

Figure 7. The helicity summed axial charge density $j_{5,\boldsymbol{k}}$ from the exact solutions (red dashed line), and from the semiclassical approximation (black line). Blue solid line (exactly matching the red dashed line) is the full cQPA solution and the green line is cQPA solution restricted to the mass shells. In each figure we have $m_{1\mathrm{R}} = 0.1$, $m_{2\mathrm{R}} = 1$, $m_{\mathrm{I}} = 0.1$, $\tau_{\mathrm{w}} = 5$ and $\Gamma = 0.2$, while $|\boldsymbol{k}| = 0.1$, 0.4, 0.8 and 1.5 in different panels as indicated.

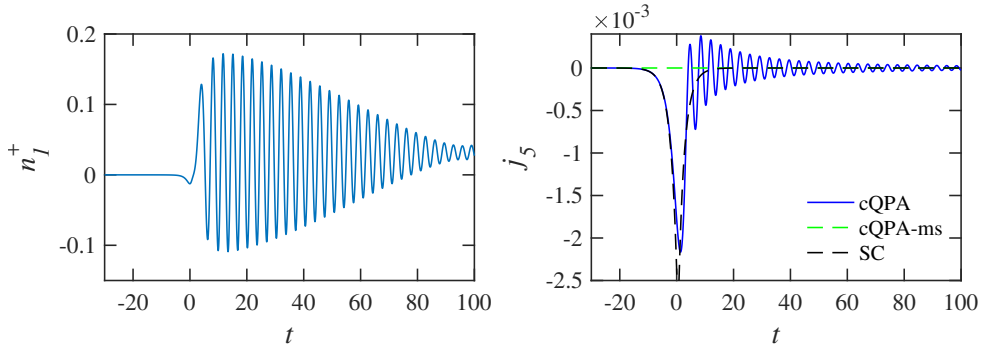

Figure 8. Shown is the integrated number density n_1^+ of positive helicity particles (left graph) and the integrated axial charge density j_5 (right graph) for a vacuum initial condition in the non-interacting case. We used the same set of mass parameters as in figure 7.

In the right panel of figure 8 we show the result of the calculation of $j_5(t)$ for the same set of parameters as considered in figure 7. Apart from the oscillations right after the mass change, the semiclassical solution follows the full solution quite well. In the left panel we show the behaviour of the integrated number density n_1^+ of positive helicity particles. (The individual number densities are defined below in section 6.) Indeed, oscillations tend to be much larger in the individual components, but they mostly cancel out at the level of currents.

JHEP01(2020)012

Our results in the non-interacting case are qualitatively similar to those of ref. [20]; the semiclassical approximation captures the mean trend of the currents quite well. However, while ref. [20] emphasized the fact that the semiclassical approximation misses the late time oscillations, we do not think that this is necessarily a significant problem. First, we see that the oscillations damp quite quickly. Second, a typical application of a calculation presented here would be to compute the particle-antiparticle asymmetry arising from the transition. The axial current would then be closely related to the source of the asymmetry. In such a case the effect of oscillations around the mean would tend to cancel out, leaving a mean effect that could be well captured by the semiclassical result.

Let us emphasize that the cQPA result for the current indeed contains and generalises the semiclassical result. This is so despite the fact that the cQPA-dispersion relation was derived formally to lower order in gradients than the semiclassical one. The reason for this apparently contradicting result was already emphasized in the beginning of this section: at the integrated level the non-interacting cQPA is in fact exact. Similarly then, the interacting cQPA-equations (2.20) constitute a generalisation of the interacting semiclassical Boltzmann theory to the fully quantum case. We now turn to study such interacting systems in the context of cQPA. This requires that we define explicitly the collision terms in equations (2.20).

6 cQPA with collisions

Let us now assume that the self-energy satisfies the KMS-relation $\Sigma^{>} = \mathrm{e}^{\beta k_0}\Sigma^{<}$. This is perhaps the most often recurring application, so we write down the full single flavour interacting cQPA-equations (2.20) explicitly for this case. After some algebra we find:

$$\partial_t n^{\pm}_{h\boldsymbol{k}} = \frac{1}{2}\sum_s \dot{\Phi}^s_{h\boldsymbol{k}}\, f^{cs}_{h\boldsymbol{k}} - \sum_s \Big[\big(n^s_{h\boldsymbol{k}} - n^s_{\mathrm{eq}}\big)T^{hs\pm}_{mm} + f^{cs}_{h\boldsymbol{k}}\, T^{hs\pm}_{cm}\Big], \tag{6.1a}$$

$$\begin{aligned}\partial_t f^{c\pm}_{h\boldsymbol{k}} = {}& \mp 2\mathrm{i}\omega_{\boldsymbol{k}} f^{c\pm}_{h\boldsymbol{k}} + \xi_{\boldsymbol{k}}\dot{\Phi}^{\mp}_{h\boldsymbol{k}}\left[\frac{m_{\mathrm{R}}}{\omega_{\boldsymbol{k}}} f^{c\pm}_{h\boldsymbol{k}} + \frac{1}{2}\big(1 - n^{+}_{h\boldsymbol{k}} - n^{-}_{h\boldsymbol{k}}\big)\right] \\ & - \xi_{\boldsymbol{k}}\sum_s \Big[\big(n^s_{h\boldsymbol{k}} - n^s_{\mathrm{eq}}\big)T^{hs\pm}_{mc} + f^{cs}_{h\boldsymbol{k}}\, T^{hs\pm}_{cc}\Big],\end{aligned} \tag{6.1b}$$

where $\dot{\Phi}^{\pm}_{h\boldsymbol{k}}$ and $\xi_{\boldsymbol{k}}$ were defined in equation (2.22) and we replaced the mass shell functions by the number densities $n^{+}_{h\boldsymbol{k}} \equiv f^{m+}_{h\boldsymbol{k}}$ and $n^{-}_{h\boldsymbol{k}} \equiv 1 - f^{m-}_{h\boldsymbol{k}}$ (these are the usual 1-particle Boltzmann distribution functions) and $n^s_{\mathrm{eq}} \equiv f_{\mathrm{eq}}(+\omega_{\boldsymbol{k}})$. Finally, the $T^{hs\pm}_{ab}$-functions encode the collision terms for generic thermal interactions. In the spatially homogeneous and isotropic system the most general form of the self-energy function can be expanded as

$$\Sigma^{\mathcal{A}}_{\boldsymbol{k}}(k_0, t) \equiv \sum_i c^{\mathcal{A}}_i(k, t)\sigma_i(k). \tag{6.2}$$

Here $\sigma_i(k)$ are the Dirac structures given in the leftmost column of table 1 and $c^{\mathcal{A}}_i(k,t)$ are some four-momentum- and possibly time-dependent functions.[10] Interaction terms

[10] Note that the last four rows in table 1 contain redundant information. For example, using the fact that $\not{k}P_{h\boldsymbol{k}} = (k_0\gamma^0 - h|\boldsymbol{k}|\gamma^0\gamma^5)P_{h\boldsymbol{k}}$, one finds that $(\mathcal{T}_{\not{k}})^{hss'}_{ab} = \omega_{\boldsymbol{k}}(\mathcal{T}_{\mathrm{sgn}(k_0)\gamma^0})^{hss'}_{ab} - h|\boldsymbol{k}|(\mathcal{T}_{\gamma^0\gamma^5})^{hss'}_{ab}$. It is easy to

JHEP01(2020)012

σ_i	$(\mathcal{T}_i)^{hss'}_{mm}$	$(\mathcal{T}_i)^{hss'}_{cm}$	$(\mathcal{T}_i)^{hss'}_{mc}$	$(\mathcal{T}_i)^{hss'}_{cc}$
$\mathbb{1}$	$2s\delta_{ss'}\frac{m_\mathrm{R}}{\omega_{\boldsymbol{k}}}$	$s'/\xi_{\boldsymbol{k}}$	$s/\xi_{\boldsymbol{k}}$	$2s\delta_{ss'}\frac{m_\mathrm{R}}{\omega_{\boldsymbol{k}}}/\xi_{\boldsymbol{k}}$
γ^5	$-2\mathrm{i}s\delta_{ss'}\frac{m_\mathrm{I}}{\omega_{\boldsymbol{k}}}$	$s'B^{s}_{h\boldsymbol{k}}$	$sB^{-s'}_{h\boldsymbol{k}}$	$-2\mathrm{i}s\delta_{ss'}\frac{m_\mathrm{I}}{\omega_{\boldsymbol{k}}}/\xi_{\boldsymbol{k}}$
$\mathrm{sgn}(k_0)\gamma^0$	$2s\delta_{ss'}$	0	0	$2s\delta_{ss'}/\xi_{\boldsymbol{k}}$
$\gamma^0\gamma^5$	$2s\delta_{ss'}h\frac{\lvert\boldsymbol{k}\rvert}{\omega_{\boldsymbol{k}}}$	$-s'A^{s}_{h\boldsymbol{k}}$	$-sA^{-s'}_{h\boldsymbol{k}}$	$2s\delta_{ss'}h\frac{\lvert\boldsymbol{k}\rvert}{\omega_{\boldsymbol{k}}}/\xi_{\boldsymbol{k}}$
$\not{k}$	$2s\delta_{ss'}\frac{\lvert m\rvert^2}{\omega_{\boldsymbol{k}}}$	$s'h\lvert\boldsymbol{k}\rvert A^{s}_{h\boldsymbol{k}}$	$sh\lvert\boldsymbol{k}\rvert A^{-s'}_{h\boldsymbol{k}}$	$2s\delta_{ss'}\frac{\lvert m\rvert^2}{\omega_{\boldsymbol{k}}}/\xi_{\boldsymbol{k}}$
$\not{k}\gamma^5$	0	$\omega_{\boldsymbol{k}}A^{s}_{h\boldsymbol{k}}$	$-\omega_{\boldsymbol{k}}A^{-s'}_{h\boldsymbol{k}}$	0
$\frac{1}{2}[\gamma^0,\not{k}]$	$2\mathrm{i}s\delta_{ss'}h\lvert\boldsymbol{k}\rvert\frac{m_\mathrm{I}}{\omega_{\boldsymbol{k}}}$	$-s'h\lvert\boldsymbol{k}\rvert B^{s}_{h\boldsymbol{k}}$	$-sh\lvert\boldsymbol{k}\rvert B^{-s'}_{h\boldsymbol{k}}$	$2\mathrm{i}s\delta_{ss'}h\lvert\boldsymbol{k}\rvert\frac{m_\mathrm{I}}{\omega_{\boldsymbol{k}}}/\xi_{\boldsymbol{k}}$
$\frac{1}{2}[\gamma^0,\not{k}]\gamma^5$	$-2s\delta_{ss'}h\lvert\boldsymbol{k}\rvert\frac{m_\mathrm{R}}{\omega_{\boldsymbol{k}}}$	$-s'h\lvert\boldsymbol{k}\rvert/\xi_{\boldsymbol{k}}$	$-sh\lvert\boldsymbol{k}\rvert/\xi_{\boldsymbol{k}}$	$-2s\delta_{ss'}h\lvert\boldsymbol{k}\rvert\frac{m_\mathrm{R}}{\omega_{\boldsymbol{k}}}/\xi_{\boldsymbol{k}}$

Table 1. Collision term coefficients for different self-energy components $\sigma_i(k)$ of $\Sigma_{\boldsymbol{k}}$.

corresponding to equation (6.2) are given by

$$\begin{aligned}
T^{hss'}_{mm}(|\boldsymbol{k}|,t) &= \sum_i c_i^{\mathcal{A}}(s)(\mathcal{T}_i)^{hss'}_{mm}(|\boldsymbol{k}|),\\
T^{hss'}_{cm}(|\boldsymbol{k}|,t) &= \sum_i \left[\frac{c_i^{\mathcal{A}}(s)+c_i^{\mathcal{A}}(-s)}{2} - ss'\frac{c_i^{\mathcal{A}}(s)-c_i^{\mathcal{A}}(-s)}{2}\right](\mathcal{T}_i)^{hss'}_{cm}(|\boldsymbol{k}|),\\
T^{hss'}_{mc}(|\boldsymbol{k}|,t) &= \sum_i c_i^{\mathcal{A}}(s)(\mathcal{T}_i)^{hss'}_{mc}(|\boldsymbol{k}|),\\
T^{hss'}_{cc}(|\boldsymbol{k}|,t) &= \sum_i \frac{c_i^{\mathcal{A}}(s)-c_i^{\mathcal{A}}(-s)}{2}(\mathcal{T}_i)^{hss'}_{cc}(|\boldsymbol{k}|),
\end{aligned} \tag{6.3}$$

where $c_i^{\mathcal{A}}(s) \equiv c_i^{\mathcal{A}}(s\omega_{\boldsymbol{k}},|\boldsymbol{k}|,t)$ and the functions $(\mathcal{T}_i)^{hss'}_{ab}$ can be read from table 1, where we further defined

$$A^{s}_{h\boldsymbol{k}} \equiv h\frac{|\boldsymbol{k}|m_\mathrm{R}}{\omega_{\boldsymbol{k}}^2} + \mathrm{i}s\frac{m_\mathrm{I}}{\omega_{\boldsymbol{k}}}, \tag{6.4}$$

$$B^{s}_{h\boldsymbol{k}} \equiv sh\frac{|\boldsymbol{k}|}{\omega_{\boldsymbol{k}}} + \mathrm{i}\frac{m_\mathrm{R}m_\mathrm{I}}{\omega_{\boldsymbol{k}}^2}. \tag{6.5}$$

The collision terms of equations (6.3) together with table 1 allow for completely general coefficient functions $c_i(k,t)$ of the self-energy (6.2). However, in thermal equilibrium the functions $c_i(k,t)$ are typically either even or odd functions of k_0. As an example, we consider a thermal self-energy with a chiral interaction given by

$$\Sigma^{\mathcal{A}}_{\boldsymbol{k}}(k_0) = (a\not{k} + b\not{u})P_\mathrm{L}, \tag{6.6}$$

check that this relation is satisfied by the entries of table 1. Similarly $\frac{1}{2}[\gamma^0,\not{k}]P_{h\boldsymbol{k}} = -h|\boldsymbol{k}|\gamma^5 P_{h\boldsymbol{k}}$, which implies that the last two rows are just $-h|\boldsymbol{k}|$ times the first two lines in reverse order. However, rather than being minimalistic, we give a complete list of the possible structures.

JHEP01(2020)012

where u_μ is the fluid four-velocity. We further assume that, in the rest frame of the thermal plasma where $\not{u} \to \gamma^0$, the coefficient $a = a(k_0, |\boldsymbol{k}|)$ is an odd and $b = b(k_0, |\boldsymbol{k}|)$ an even function of k_0. Using table 1, we then get the following collision terms for equations (6.1):

$$\begin{aligned}
T^{hss'}_{mm}(|\boldsymbol{k}|, t) &= \left[\frac{|m|^2}{\omega_{\boldsymbol{k}}} a_{\boldsymbol{k}} + \left(1 - sh\frac{|\boldsymbol{k}|}{\omega_{\boldsymbol{k}}}\right) b_{\boldsymbol{k}}\right] \delta_{ss'}, \\
T^{hss'}_{cm}(|\boldsymbol{k}|, t) &= \frac{s'}{2}\Big[(\omega_{\boldsymbol{k}} - s'h|\boldsymbol{k}|)a_{\boldsymbol{k}} + b_{\boldsymbol{k}}\Big] A^{s}_{h\boldsymbol{k}}, \\
T^{hss'}_{mc}(|\boldsymbol{k}|, t) &= \frac{s}{2}\Big[(\omega_{\boldsymbol{k}} + sh|\boldsymbol{k}|)a_{\boldsymbol{k}} + b_{\boldsymbol{k}}\Big] A^{-s'}_{h\boldsymbol{k}}, \\
T^{hss'}_{cc}(|\boldsymbol{k}|, t) &= \frac{1}{\xi_{\boldsymbol{k}}}\left[\frac{|m|^2}{\omega_{\boldsymbol{k}}} a_{\boldsymbol{k}} + b_{\boldsymbol{k}}\right] \delta_{ss'}.
\end{aligned} \tag{6.7}$$

Here $a_{\boldsymbol{k}} \equiv a(\omega_{\boldsymbol{k}}, |\boldsymbol{k}|)$, $b_{\boldsymbol{k}} \equiv b(\omega_{\boldsymbol{k}}, |\boldsymbol{k}|)$ and we used the parity properties $a(s\omega_{\boldsymbol{k}}, |\boldsymbol{k}|) = s a_{\boldsymbol{k}}$ and $b(s\omega_{\boldsymbol{k}}, |\boldsymbol{k}|) = b_{\boldsymbol{k}}$. Also, given that $a_{\boldsymbol{k}}, b_{\boldsymbol{k}} > 0$, note how $T^{hss'}_{mm}$ and $T^{hss'}_{cc}$ are always positive.

Let us finally point out that it is easy to generalise equations (6.1) to the case with a non-thermal self-energy that does *not* obey the KMS-relation. One just needs to replace the two terms involving the equilibrium distribution function $n^s_{\rm eq}$ as follows:

$$(n^s_{h\boldsymbol{k}} - n^s_{\rm eq}) T^{hss'}_{ma}(|\boldsymbol{k}|, t) \to \sum_i s\left(f^{ms}_{h\boldsymbol{k}} c^{\mathcal{A}}_i(s) - \frac{1}{2} c^{<}_i(s)\right) (\mathcal{T}_i)^{hss'}_{ma}(|\boldsymbol{k}|, t) \tag{6.8}$$

for $a = m, c$, where we defined $\mathrm{i}\Sigma^{<}_{\boldsymbol{k}}(k_0, t) \equiv \sum_i c^{<}_i(k, t)\sigma_i(k)$. We remind, however, that evaluating the self-energy diagrams involving coherent propagators as internal lines requires special techniques developed in refs. [11, 12].

6.1 A numerical example

In figure 9 we show a result of a model calculation with a non-vanishing interaction rate using a self-energy of the form (6.6) with $a_{\boldsymbol{k}} = 0.03$ and $b_{\boldsymbol{k}} = 0$. The left panels, where we imposed the vacuum initial conditions $n^{\pm}_{h\boldsymbol{k}} = f^{c\pm}_{h\boldsymbol{k}} = 0$, correspond to the interacting version of the case studied in figure 8. Initially, the particle number approaches smoothly the thermal value. At the onset of the transition it again starts oscillating, but the amplitude is strongly damped in comparison to the non-interacting case. In the right panels we show the analogous calculation with equilibrium initial conditions $n^{\pm}_{h\boldsymbol{k}} = n^{\pm}_{\rm eq}$ with $T = 1$ in the units we are working with and $f^{c\pm}_{h\boldsymbol{k}} = 0$. Now the particle number stays unchanged until the onset of the transition, after which it oscillates approaching asymptotically the same post-transition equilibrium value as in the case with vacuum initial conditions. Pushing the starting point further away from the transition region would make the later evolution indistinguishable in the two cases.

The main difference to the non-interacting case is that the left-chiral interaction, in connection with the coherent CP-violating oscillations, creates a temporary non-zero average chiral current after transition. This is due to the fact that the chiral interaction term (6.6) breaks the helicity symmetry. The average current is well captured at late times by the pure mass shell contribution, shown in green dashed line in figure 9. However at

JHEP01(2020)012

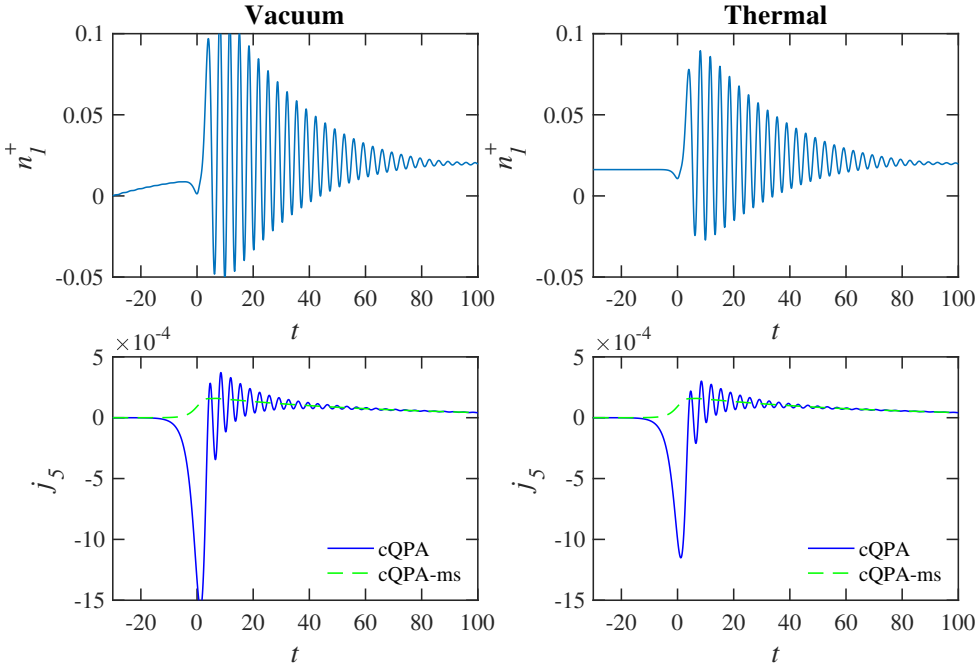

Figure 9. Shown is the integrated number density n_1^+ of positive helicity particles (the upper panels) and the integrated axial charge density j_5 (the lower panels) in interacting cQPA. The left panels correspond to the vacuum initial condition and the right panels to the thermal initial condition with $T = 1$. We used the same set of mass parameters as in figure 7.

the transition point the main peak is still pure coherence. While the current eventually equilibrates to zero, the region where it is non-vanishing could act as a seed for example for a particle-antiparticle asymmetry creation in such a transition.

The calculation we presented here was just a toy model whose sole purpose was to show how to implement the method and display some of the effects of interactions. There are several interesting applications for the formalism that we shall pursue in the future. One avenue is the study of baryogenesis in abrupt spatially homogeneous phase transitions in the early universe, such as the models considered in the context of the cold baryogenesis [32–34]. Another application is to study the reheating phase after inflation. It is straightforward to couple equations (6.1) with an equation of motion for the inflaton and model the reheating phase including all quantum effects and interactions. Our formalism, extended to the flavour mixing case [12], can also be applied to the study of leptogenesis. It is of particular interest to compare our approach with several other transport theory formulations that also employ the closed time path (CTP) methods, such as those presented in refs. [35–42].

7 Conclusions and outlook

We have studied the phase space structure of a fermionic two-point function with a varying complex mass. We computed the Wightman function of a non-interacting system for a specific mass profile, and demonstrated that its phase space contains, in addition to the usual mass shell solutions, a shell-like structure located at $k_0 = 0$. This zero-momentum

JHEP01(2020)012

shell describes local-in-time quantum coherence between particles and antiparticles and it was discovered earlier in the context of the cQPA-formalism [6–12]. However, our present derivation did not rely on any approximations, but derived the free Wightman function from the exact mode functions of the system.

In addition to the cQPA-solutions we found other, non-local coherence structures in the exact Wightman function. These structures look peculiar, appearing to let the system become aware of the transition before it actually takes place in the local time coordinate, but of course they are just a reflection of the usual quantum non-locality in the phase space picture. We argued that the non-local correlations would dominate the phase space structure in large non-dissipative systems. However, when dissipation is included (modelled here by a damping term coupled to the relative time coordinate), the non-locality gets confined to the neighbourhood of the transition region. These results underline the delicate role of dissipation in the emergence of the local (cQPA) limit, and eventually (in the nearly translationally invariant systems) of the familiar Boltzmann transport theory.

In section 2 we introduced a new and particularly useful way to reorganise the gradient expansion in the mixed representation Kadanoff-Baym equations. Then, based on this form, we gave a simple and transparent derivation of the cQPA equations. In section 6 we completed the analysis by providing explicit collision integrals for generic interaction self-energies. The resulting equations (6.1) are one of the main results of this paper: they generalise the Boltzmann transport theory to systems with local coherence between particles and antiparticles. In particular they fully encompass the well known semiclassical effects. Such coherences may be relevant for example for baryogenesis during phase transitions and for particle production at the end of inflation.

We further computed axial phase space densities out of the Wightman functions and compared these to the same quantities obtained from the semiclassical approximation. We found out that the semiclassical methods work reasonably well even in systems where the relevant modes have wavelengths down to a half of the wall width. This is encouraging for baryogenesis studies in very strong electroweak phase transitions, often encountered in the context of models producing large, observable gravitational wave signals [17, 18].

In this work we only considered a time-dependent mass. A natural follow-up, relevant for the baryogenesis problem, would be to generalise the analysis to a mass depending on one spatial coordinate. Part of this program is straightforward, but some new features emerge as well, such as the tunneling solutions, whose proper description at the phase space level is non-trivial. But there are practical applications of the time-dependent formalism as well, which we shall be pursuing. One is the baryogenesis at a phase transition as discussed in section 6 and already studied in the context of a simple toy model in ref. [11]. Another immediate goal is to use equations (6.1), coupled to the one-point function of the inflaton, to model accurately the reheating phase at the end of the inflation. Also, we are pursuing a generalisation of the present formalism to the case with mixing fermion fields, in the context of resonant leptogenesis [43].

JHEP01(2020)012

Acknowledgments

This work was supported by the Academy of Finland grant 318319. HJ was in addition supported by grants from the Väisälä Fund of the Finnish Academy of Science and Letters and OK by a grant from the Magnus Ehrnrooth Foundation. We wish to thank Pyry Rahkila and Werner Porod for many enlightening discussions.

JHEP01(2020)012

References

[1] J.S. Schwinger, *Brownian motion of a quantum oscillator*, *J. Math. Phys.* **2** (1961) 407 [INSPIRE].

[2] L.V. Keldysh, *Diagram technique for nonequilibrium processes*, *Zh. Eksp. Teor. Fiz.* **47** (1964) 1515 [*Sov. Phys. JETP* **20** (1965) 1018] [INSPIRE].

[3] G. Baym and L.P. Kadanoff, *Conservation laws and correlation functions*, *Phys. Rev.* **124** (1961) 287 [INSPIRE].

[4] G. Mahan, *Quantum transport equation for electric and magnetic fields*, *Phys. Rept.* **145** (1987) 251.

[5] T. Prokopec, M.G. Schmidt and S. Weinstock, *Transport equations for chiral fermions to order ħ and electroweak baryogenesis. Part* 1, *Annals Phys.* **314** (2004) 208 [hep-ph/0312110] [INSPIRE].

[6] M. Herranen, K. Kainulainen and P.M. Rahkila, *Towards a kinetic theory for fermions with quantum coherence*, *Nucl. Phys.* **B 810** (2009) 389 [arXiv:0807.1415] [INSPIRE].

[7] M. Herranen, K. Kainulainen and P.M. Rahkila, *Quantum kinetic theory for fermions in temporally varying backgrounds*, *JHEP* **09** (2008) 032 [arXiv:0807.1435] [INSPIRE].

[8] M. Herranen, K. Kainulainen and P.M. Rahkila, *Kinetic theory for scalar fields with nonlocal quantum coherence*, *JHEP* **05** (2009) 119 [arXiv:0812.4029] [INSPIRE].

[9] M. Herranen, *Quantum kinetic theory with nonlocal coherence*, Ph.D. thesis, Jyväskylä U., Jyväskylä, Finland (2009) [arXiv:0906.3136] [INSPIRE].

[10] M. Herranen, K. Kainulainen and P.M. Rahkila, *Coherent quasiparticle approximation (cQPA) and nonlocal coherence*, *J. Phys. Conf. Ser.* **220** (2010) 012007 [arXiv:0912.2490] [INSPIRE].

[11] M. Herranen, K. Kainulainen and P.M. Rahkila, *Coherent quantum Boltzmann equations from cQPA*, *JHEP* **12** (2010) 072 [arXiv:1006.1929] [INSPIRE].

[12] C. Fidler, M. Herranen, K. Kainulainen and P.M. Rahkila, *Flavoured quantum Boltzmann equations from cQPA*, *JHEP* **02** (2012) 065 [arXiv:1108.2309] [INSPIRE].

[13] M. Hindmarsh, S.J. Huber, K. Rummukainen and D.J. Weir, *Gravitational waves from the sound of a first order phase transition*, *Phys. Rev. Lett.* **112** (2014) 041301 [arXiv:1304.2433] [INSPIRE].

[14] M. Hindmarsh, S.J. Huber, K. Rummukainen and D.J. Weir, *Numerical simulations of acoustically generated gravitational waves at a first order phase transition*, *Phys. Rev.* **D 92** (2015) 123009 [arXiv:1504.03291] [INSPIRE].

[15] M. Hindmarsh, S.J. Huber, K. Rummukainen and D.J. Weir, *Shape of the acoustic gravitational wave power spectrum from a first order phase transition*, *Phys. Rev.* **D 96** (2017) 103520 [arXiv:1704.05871] [INSPIRE].

[16] D. Cutting, M. Hindmarsh and D.J. Weir, *Gravitational waves from vacuum first-order phase transitions: from the envelope to the lattice*, *Phys. Rev.* **D 97** (2018) 123513 [arXiv:1802.05712] [INSPIRE].

[17] G.C. Dorsch, S.J. Huber, T. Konstandin and J.M. No, *A second Higgs doublet in the early universe: baryogenesis and gravitational waves*, *JCAP* **05** (2017) 052 [arXiv:1611.05874] [INSPIRE].

[18] V. Vaskonen, *Electroweak baryogenesis and gravitational waves from a real scalar singlet*, *Phys. Rev.* **D 95** (2017) 123515 [arXiv:1611.02073] [INSPIRE].

[19] T. Prokopec, M.G. Schmidt and S. Weinstock, *Transport equations for chiral fermions to order ħ and electroweak baryogenesis. Part* 2, *Annals Phys.* **314** (2004) 267 [hep-ph/0406140] [INSPIRE].

[20] T. Prokopec, M.G. Schmidt and J. Weenink, *Exact solution of the Dirac equation with CP-violation*, *Phys. Rev.* **D 87** (2013) 083508 [arXiv:1301.4132] [INSPIRE].

[21] O. Koskivaara, *Exact solutions of a Dirac equation with a varying CP-violating mass profile and coherent quasiparticle approximation*, Master's thesis, Jyväskylä U., Jyväskylä, Finland (2015).

[22] J.M. Cline, M. Joyce and K. Kainulainen, *Supersymmetric electroweak baryogenesis*, *JHEP* **07** (2000) 018 [hep-ph/0006119] [INSPIRE].

[23] J.M. Cline, M. Joyce and K. Kainulainen, *Erratum for 'Supersymmetric electroweak baryogenesis'*, hep-ph/0110031 [INSPIRE].

[24] K. Kainulainen, T. Prokopec, M.G. Schmidt and S. Weinstock, *First principle derivation of semiclassical force for electroweak baryogenesis*, *JHEP* **06** (2001) 031 [hep-ph/0105295] [INSPIRE].

[25] K. Kainulainen, T. Prokopec, M.G. Schmidt and S. Weinstock, *Semiclassical force for electroweak baryogenesis: three-dimensional derivation*, *Phys. Rev.* **D 66** (2002) 043502 [hep-ph/0202177] [INSPIRE].

[26] L. Fromme, S.J. Huber and M. Seniuch, *Baryogenesis in the two-Higgs doublet model*, *JHEP* **11** (2006) 038 [hep-ph/0605242] [INSPIRE].

[27] L. Fromme and S.J. Huber, *Top transport in electroweak baryogenesis*, *JHEP* **03** (2007) 049 [hep-ph/0604159] [INSPIRE].

[28] J.M. Cline and K. Kainulainen, *Electroweak baryogenesis and dark matter from a singlet Higgs*, *JCAP* **01** (2013) 012 [arXiv:1210.4196] [INSPIRE].

[29] J.M. Cline, K. Kainulainen, P. Scott and C. Weniger, *Update on scalar singlet dark matter*, *Phys. Rev.* **D 88** (2013) 055025 [*Erratum ibid.* **D 92** (2015) 039906] [arXiv:1306.4710] [INSPIRE].

JHEP01(2020)012

[30] J.M. Cline, K. Kainulainen and D. Tucker-Smith, *Electroweak baryogenesis from a dark sector*, *Phys. Rev.* **D 95** (2017) 115006 [arXiv:1702.08909] [INSPIRE].

[31] H. Jukkala, K. Kainulainen and O. Koskivaara, in preparation.

[32] A. Tranberg, A. Hernandez, T. Konstandin and M.G. Schmidt, *Cold electroweak baryogenesis with Standard Model CP-violation*, *Phys. Lett.* **B 690** (2010) 207 [arXiv:0909.4199] [INSPIRE].

[33] A. Tranberg and B. Wu, *On using cold baryogenesis to constrain the two-Higgs doublet model*, *JHEP* **01** (2013) 046 [arXiv:1210.1779] [INSPIRE].

[34] A. Tranberg and B. Wu, *Cold electroweak baryogenesis in the two Higgs-doublet model*, *JHEP* **07** (2012) 087 [arXiv:1203.5012] [INSPIRE].

[35] M. Beneke, B. Garbrecht, M. Herranen and P. Schwaller, *Finite number density corrections to leptogenesis*, *Nucl. Phys.* **B 838** (2010) 1 [arXiv:1002.1326] [INSPIRE].

[36] M. Beneke, B. Garbrecht, C. Fidler, M. Herranen and P. Schwaller, *Flavoured leptogenesis in the CTP formalism*, *Nucl. Phys.* **B 843** (2011) 177 [arXiv:1007.4783] [INSPIRE].

[37] B. Garbrecht and M. Herranen, *Effective theory of resonant leptogenesis in the closed-time-path approach*, *Nucl. Phys.* **B 861** (2012) 17 [arXiv:1112.5954] [INSPIRE].

[38] B. Garbrecht, *Why is there more matter than antimatter? Calculational methods for leptogenesis and electroweak baryogenesis*, arXiv:1812.02651 [INSPIRE].

[39] B. Dev, M. Garny, J. Klaric, P. Millington and D. Teresi, *Resonant enhancement in leptogenesis*, *Int. J. Mod. Phys.* **A 33** (2018) 1842003 [arXiv:1711.02863] [INSPIRE].

[40] M. Garny, A. Kartavtsev and A. Hohenegger, *Leptogenesis from first principles in the resonant regime*, *Annals Phys.* **328** (2013) 26 [arXiv:1112.6428] [INSPIRE].

[41] A. Kartavtsev, P. Millington and H. Vogel, *Lepton asymmetry from mixing and oscillations*, *JHEP* **06** (2016) 066 [arXiv:1601.03086] [INSPIRE].

[42] P.S. Bhupal Dev, P. Millington, A. Pilaftsis and D. Teresi, *Kadanoff-Baym approach to flavour mixing and oscillations in resonant leptogenesis*, *Nucl. Phys.* **B 891** (2015) 128 [arXiv:1410.6434] [INSPIRE].

[43] H. Jukkala, K. Kainulainen and P. Rahkila, in preparation.

JHEP01(2020)012

PII

NON-EQUILIBRIUM DYNAMICS OF A SCALAR FIELD WITH QUANTUM BACKREACTION

by

Kimmo Kainulainen and Olli Koskivaara (2021)

Journal of High Energy Physics, **12** 190

Published for SISSA by Springer

Received: May 25, 2021
Revised: December 13, 2021
Accepted: December 20, 2021
Published: December 27, 2021

Non-equilibrium dynamics of a scalar field with quantum backreaction

Kimmo Kainulainen and Olli Koskivaara

Department of Physics, University of Jyväskylä,
P.O. Box 35 (YFL), FI-40014 Jyväskylä, Finland
Helsinki Institute of Physics, University of Helsinki,
P.O. Box 64, FI-00014 Helsinki, Finland

E-mail: kimmo.kainulainen@jyu.fi, olli.a.koskivaara@student.jyu.fi

Abstract: We study the dynamical evolution of coupled one- and two-point functions of a scalar field in the 2PI framework at the Hartree approximation, including backreaction from out-of-equilibrium modes. We renormalize the 2PI equations of motion in an on-shell scheme in terms of physical parameters. We present the Hartree-resummed renormalized effective potential at finite temperature and critically discuss the role of the effective potential in a non-equilibrium system. We follow the decay and thermalization of a scalar field from an initial cold state with all energy stored in the potential, into a fully thermalized system with a finite temperature. We identify the non-perturbative processes of parametric resonance and spinodal instability taking place during the reheating stage. In particular we study the unstable modes in the region where the vacuum 1PI effective action becomes complex and show that such spinodal modes can have a dramatic effect on the evolution of the one-point function. Our methods can be easily adapted to simulate reheating at the end of inflation.

Keywords: Nonperturbative Effects, Thermal Field Theory, Quantum Dissipative Systems

ArXiv ePrint: 2105.09598

https://doi.org/10.1007/JHEP12(2021)190

JHEP12(2021)190

Contents

JHEP12(2021)190

1 Introduction

Classical scalar fields coupled to quantum matter play an important role in various settings in cosmology. They are used to study the creation of seed perturbations for structure formation, reheating processes, particle production and the creation of baryon asymmetry. Almost exclusively in these treatments it is assumed that the scalar field evolves in some classical, possibly quantum corrected but fixed effective potential. One rarely accounts for the backreaction of the non-equilibrium quanta that may be created during the dynamical process. However, such quanta may be produced copiously during out-of-equilibrium phase transitions [1, 2] by parametric resonance [3–7] or by spinodal instability [6, 8–13], and they could significantly affect the evolution of the system [14–18]. In this paper we study the effects of quantum backreaction on the scalar field evolution using two-particle irreducible (2PI) effective action methods.

A crucial step in the rigorous analysis of the problem is performing a consistent renormalization of the equations of motion derived from the 2PI effective action. This is a highly non-trivial task, because in any finite truncation of the 2PI expansion, a number of auxiliary vertex and self-energy functions appear that require setting up consistent renormalization conditions [19]. Other works on the renormalization of 2PI-truncated theories

include for example references [20–22]. In this paper we carefully go through the renormalization of our model using the method of cancellation of the sub-divergences [23–26]. We emphasize that while the renormalization counterterms are constants, the divergences that get subtracted, and hence also the vacuum state of the system, depend on the infrared physics, such as temperature, or even the shape of the non-equilibrium particle spectrum.

To be specific, we study a simple $\lambda\phi^4$-model with a spontaneous symmetry breaking tree-level potential. We work in the Hartree approximation and perform the auxiliary renormalizations using the $\overline{\text{MS}}$ subtraction scheme. The renormalized equations of motion and the 2PI effective action are however scale independent and completely specified in terms of physical parameters. We present explicit results for the vacuum and finite temperature effective potentials as well as for the vacuum potential in the presence of non-equilibrium fluctuations. We stress that in the non-equilibrium case the effective potential can only be constructed *a posteriori* and it is not in general a useful quantity for solving the equations of motion.

With our renormalized equations we can follow in real time how the potential energy of the classical field is transferred into quantum fluctuations by the non-perturbative processes. We identify a strong parametric resonance, even though our self-coupled system is too complicated to admit a comprehensive analytical stability analysis. We also show that due to backreaction from spinodal instability the field can pass through a potential barrier even when starting with less energy than the initial barrier height. We also follow the full thermal history of a system that starts with pure potential energy, until it is fully thermalized with nearly all of its energy stored in thermal plasma. We also show that at the initial stages of reheating the quantum system is highly coherent, but the coherence is gradually erased by interactions as the system thermalizes.

This paper is organized as follows. In section 2 we review the 2PI effective action techniques and introduce our truncation scheme, the Hartree approximation. In section 3 we show how to self-consistently renormalize the 2PI equations of motion and express them in terms of physical quantities. We also study both resummed vacuum and thermal effective potentials in the Hartree case and compare them with other approximations. In section 4 we write our equations of motion in the Wigner space in terms of moment functions following references [27, 28], and also complement the equations with phenomenological friction terms. Section 5 is dedicated to numerical results. We compute the evolution of various quantities, such as the classical field, particle number and coherence functions using the fully coupled 2PI equations. Finally, section 6 contains our conclusions.

2 2PI effective action and equations of motion

We will study the non-equilibrium dynamics of a scalar field theory with the potential $V(\phi) = -\frac{1}{2}\mu^2\phi^2 + \frac{1}{4!}\lambda\phi^4$ using the two-particle irreducible (2PI) effective action technique of non-equilibrium quantum field theory [29, 30]. The 2PI effective action for this theory is

$$\Gamma_{2\text{PI}}[\varphi, \Delta] = \mathcal{S}[\varphi] - \frac{\mathrm{i}}{2}\text{Tr}_{\mathcal{C}}\left[\ln(\Delta)\right] + \frac{\mathrm{i}}{2}\text{Tr}_{\mathcal{C}}\left[\Delta_0^{-1}\Delta\right] + \Gamma_2[\varphi, \Delta], \tag{2.1}$$

JHEP12(2021)190

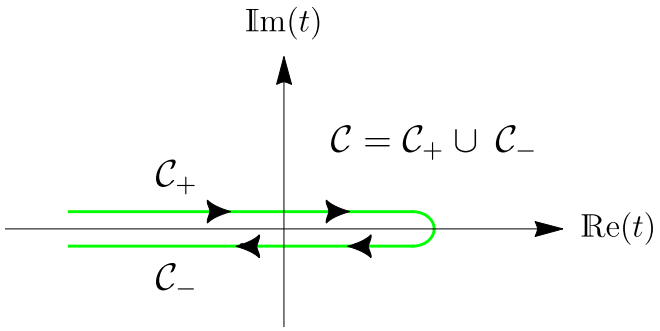

Figure 1. The Keldysh contour in the complex time plane, running from some initial time to an arbitrary future time and back again.

where $\varphi(x)$ is the classical field and $\Delta(x, y)$ is the classical connected two-point function and the trace contains integration over the Keldysh contour [31] $\mathcal{C}$ of figure 1. Moving to a real-time representation the classical action can be written as $\mathcal{S}[\varphi] = \sum_{a=\pm} a\delta^{ab}\mathcal{S}[\varphi_b]$, where a and b indicate the branch on the complex time-contour, and

$$\mathcal{S}[\varphi_b] = \int \mathrm{d}^4x \left[\frac{1}{2}(\partial_\mu\varphi_b)^2 + \frac{1}{2}\mu^2\varphi_b^2 - \frac{1}{4!}\lambda\varphi_b^4\right]. \tag{2.2}$$

Similarly, the inverse classical propagator is given by

$$\mathrm{i}\Delta^{-1}_{0,ab}(x, y; \varphi) = -\left(\Box_x - \mu^2 + \frac{1}{2}\lambda\varphi_a^2\right)\delta^{(4)}(x - y)\delta_{ab}. \tag{2.3}$$

Finally, Γ_2 consists of all 2PI vacuum graphs with lines corresponding to the full propagator Δ and interactions inferred from the shifted action

$$S_{\mathrm{int}}[\varphi, \phi_q] = -\sum_{a=\pm} a\delta^{ab}\int \mathrm{d}^4x \left(\frac{1}{3!}\lambda\varphi_b\phi_{qb}^3 + \frac{1}{4!}\lambda\phi_{qb}^4\right), \tag{2.4}$$

where $\phi = \varphi + \phi_q$ and ϕ_q is the quantum field.

The stationarity conditions of $\Gamma_{2\mathrm{PI}}$ will give the equations of motion for the one- and two-point functions:

$$\frac{\delta\Gamma_{2\mathrm{PI}}}{\delta\varphi_a} = 0 \qquad \text{and} \qquad \frac{\delta\Gamma_{2\mathrm{PI}}}{\delta\Delta_{ab}} = 0. \tag{2.5}$$

When the classical solution to the latter equation, parametrized in terms of φ, is reinserted back into the effective action, we *formally* recover the 1PI action $\hat{\Gamma}_{1\mathrm{PI}}[\varphi] = \Gamma_{2\mathrm{PI}}[\varphi, \Delta[\varphi]]$. In the full dynamical case the two equations are however strongly coupled and should be solved simultaneously, as we will do in our study. For the classical field $\varphi_+(x) = \varphi_-(x)$ and we may drop the branch index and find:

$$\left[\Box_x - \mu^2 + \frac{1}{6}\lambda\varphi^2(x) + \frac{1}{2}\lambda\Delta(x, x)\right]\varphi(x) = \frac{\delta\Gamma_2}{\delta\varphi(x)}. \tag{2.6}$$

We also left the branch indices out from the local correlation function $\Delta(x, x)$, which is the same for all components of the two-point function $\Delta^{ab}(x, y)$. The stationarity condition

JHEP12(2021)190

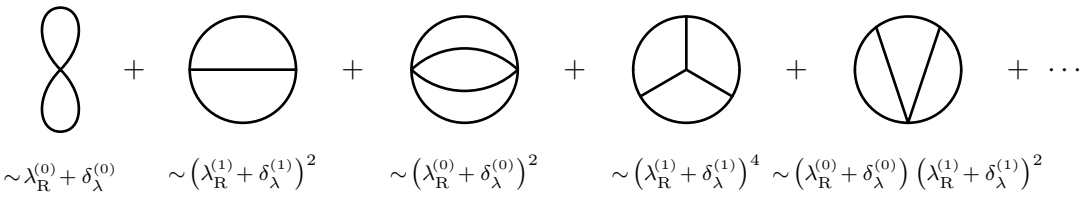

Figure 2. The first few terms contributing to Γ_2, including their precise coupling constant dependences.

for $\Delta^{ab}(x,y)$ leads to the Schwinger-Dyson equation

$$\left[\Box_x-\mu^2+\frac{1}{2}\lambda\varphi^2(x)\right]\mathrm{i}\Delta^{ac}(x,y)=a\delta^{ac}\delta^{(4)}(x-y)+b\int\mathrm{d}^4z\,\Pi^{ab}(x,z)\Delta^{bc}(z,y), \tag{2.7}$$

where summation over b is implied and the self-energy function is given by

$$\Pi^{ab}(x,y)=2\mathrm{i}ab\,\frac{\delta\Gamma_2[\varphi,\Delta]}{\delta\Delta^{ba}(y,x)}=a\delta^{ab}\delta^{(4)}(x-y)\Pi_{\mathrm{sg}}(x)+\Pi^{ab}_{\mathrm{nsg}}(x,y). \tag{2.8}$$

To proceed we also have to specify an approximation for the interaction term Γ_2.

2.1 Hartree approximation

The first few terms contributing to Γ_2, arising from the action (2.4), are shown in figure 2 (the role of the indices in the couplings is related to renormalization and will be explained in the next section). In this work we shall work in the Hartree approximation, which includes only the first term in the series, given by

$$\Gamma_2^{\mathrm{H}}=-\frac{\lambda}{8}\int\mathrm{d}^4x\,\Delta^2(x,x). \tag{2.9}$$

In this case the self-energy has only a singular or local part:

$$\Pi_{\mathrm{sg}}(x)=-\frac{\mathrm{i}\lambda}{2}\Delta(x,x), \tag{2.10}$$

while $\Pi^{ab}_{\mathrm{nsg}}(x,y)=0$. Obviously $\partial\Gamma_2^{\mathrm{H}}/\partial\varphi=0$ as well, so there is no contribution to equation (2.6) in the Hartree approximation. We can now write the non-renormalized equations of motion compactly as

$$\left[\Box_x-\mu^2+\frac{1}{6}\lambda\varphi^2(x)+\frac{1}{2}\lambda\Delta(x,x)\right]\varphi(x)=0, \tag{2.11a}$$

$$\left[\Box_x-\mu^2+\frac{1}{2}\lambda\varphi^2(x)+\frac{1}{2}\lambda\Delta(x,x)\right]\mathrm{i}\Delta^{ab}(x,y)=a\delta^{ab}\delta^{(4)}(x-y), \tag{2.11b}$$

Eventually we will move to the Wigner space defined in section 4 and solve these equations numerically in some example cases for homogeneous systems, but before we can do that, we have to address the divergences in Δ^{ab} and in particular in the local correlation function $\Delta(x,x)$.

JHEP12(2021)190

3 Renormalization

Systematic renormalization in the context of the 2PI expansion was thoroughly discussed in reference [19]. Here we use the method introduced in reference [23], and later used in references [24, 26], and we include also a connection to physical parameters. The key issue is that any finite order truncation of $\Gamma_2[\varphi, \Delta]$ leads to an approximation for $\hat{\Gamma}_{1\mathrm{PI}}[\varphi]$ that contains infinite resummations of 1PI diagrams and the associated counterterms. This gives rise to a number of *auxiliary* n-point functions which need independent renormalization conditions. These conditions can be defined by requiring that all sub-divergences cancel [23], but one needs to introduce a different renormalized parameter for each different operator. To be precise, all n-point functions can be classified in terms of the number of classical fields that connect to them, and all functions that are connected also to propagator lines are auxiliary.

Below we shall first renormalize the auxiliary n-point functions in the $\overline{\mathrm{MS}}$-scheme and show that the resulting 1PI action is independent of the renormalization scale. We start by defining the renormalized fields, propagators, couplings and masses:

$$\begin{aligned} \phi &\equiv Z_{(2)}^{1/2}\phi_{\mathrm{R}}, & \lambda &\equiv \lambda_{\mathrm{R}}^{(\mathrm{I})} + \delta\lambda^{(\mathrm{I})}, \\ \Delta &\equiv Z_{(0)}\Delta_{\mathrm{R}}, & \mu^2 &\equiv \mu_{\mathrm{R}(\mathrm{I})}^2 - \delta\mu_{(\mathrm{I})}^2, \end{aligned} \tag{3.1}$$

where the index, $\mathrm{I} = 0, 1, 2, 4$, follows the power of the classical field associated with the n-point function. Written in terms of the renormalized quantities, the 2PI effective action becomes:

$$\begin{aligned} \Gamma_{2\mathrm{PI}}[\varphi_{\mathrm{R}}, \Delta_{\mathrm{R}}] = \mathcal{S}[\varphi_{\mathrm{R}}] - \frac{\mathrm{i}}{2}\mathrm{Tr}_{\mathcal{C}}\big[\ln(Z_{(0)}\Delta_{\mathrm{R}})\big] + \frac{\mathrm{i}}{2}\mathrm{Tr}_{\mathcal{C}}\left[\Delta_{0\mathrm{R}}^{-1}\Delta_{\mathrm{R}}\right] \\ + \delta\mathcal{S}[\varphi_{\mathrm{R}}] + \frac{\mathrm{i}}{2}\mathrm{Tr}_{\mathcal{C}}\big[\delta\Delta_0^{-1}\Delta_{\mathrm{R}}\big] + \Gamma_2\Big[\varphi_{\mathrm{R}}, \Delta_{\mathrm{R}}; \lambda_{\mathrm{R}}^{(\mathrm{I})} + \delta_{\lambda}^{(\mathrm{I})}\Big], \end{aligned} \tag{3.2}$$

where $S[\varphi_{\mathrm{R}}]$ is the same as in equation (2.2) with $\varphi \to \varphi_{\mathrm{R}}$, $\mu^2 \to \mu_{\mathrm{R}(2)}^2$ and $\lambda \to \lambda_{\mathrm{R}}^{(4)}$, and $\Delta_{0\mathrm{R}}^{-1}$ is the same as (2.3) with $\varphi \to \varphi_{\mathrm{R}}$, $\mu^2 \to \mu_{\mathrm{R}(0)}^2$ and $\lambda \to \lambda_{\mathrm{R}}^{(2)}$. Moreover we defined the classical counterterm action

$$\delta\mathcal{S}[\varphi_{\mathrm{R}b}] \equiv \int \mathrm{d}^4x \left[\frac{\delta_{\varphi}^{(2)}}{2}(\partial_\mu\varphi_{\mathrm{R}b})^2 - \frac{1}{2}\delta_{\mu}^{(2)}\varphi_{\mathrm{R}b}^2 - \frac{1}{4!}\delta_{\lambda}^{(4)}\varphi_{\mathrm{R}b}^4\right] \tag{3.3}$$

and the inverse classical counterterm propagator

$$\mathrm{i}\delta\Delta_{0,ab}^{-1}(x, y; \varphi_{\mathrm{R}}) \equiv -\left(\delta_{\varphi}^{(0)}\Box_x + \delta_{\mu}^{(0)} + \frac{1}{2}\delta_{\lambda}^{(2)}\varphi_{\mathrm{R}a}^2\right)\delta^{(4)}(x - y)\delta_{ab}, \tag{3.4}$$

where $\delta_{\varphi}^{(\mathrm{I})} \equiv Z_{(\mathrm{I})} - 1$ and the other effective counterterms are defined as:

$$\delta_{\lambda}^{(0)} \equiv Z_{(0)}^2\big(\lambda_{\mathrm{R}}^{(0)} + \delta\lambda^{(0)}\big) - \lambda_{\mathrm{R}}^{(0)}, \tag{3.5a}$$

$$\delta_{\lambda}^{(2)} \equiv Z_{(0)}Z_{(2)}\big(\lambda_{\mathrm{R}}^{(2)} + \delta\lambda^{(2)}\big) - \lambda_{\mathrm{R}}^{(2)}, \tag{3.5b}$$

$$\delta_{\lambda}^{(4)} \equiv Z_{(2)}^2\big(\lambda_{\mathrm{R}}^{(4)} + \delta\lambda^{(4)}\big) - \lambda_{\mathrm{R}}^{(4)}, \tag{3.5c}$$

$$\delta_{\mu}^{(\mathrm{I})} \equiv Z_{(\mathrm{I})}\big(-\mu_{\mathrm{R}(\mathrm{I})}^2 + \delta\mu_{(\mathrm{I})}^2\big) + \mu_{\mathrm{R}(\mathrm{I})}^2. \tag{3.5d}$$

JHEP12(2021)190

Also in the interaction term in (3.2) the renormalized couplings in the combination $\lambda_{\mathrm{R}}^{(\mathrm{I})}+\delta_{\lambda}^{(\mathrm{I})}$ follow the power of the classical field in the interaction term (2.4), rewritten in terms of the renormalized quantities.

The renormalized equations of motion can now be derived from the renormalized effective action, or more directly from (2.11a) and (2.11b), by writing the non-renormalized quantities in terms of the renormalized ones:

$$\Big[Z_{(2)}\Box_x - \mu^2_{\mathrm{R}(2)} + \delta^{(2)}_{\mu} + \frac{1}{6}\Big(\lambda^{(4)}_{\mathrm{R}} + \delta^{(4)}_{\lambda}\Big)\varphi^2_{\mathrm{R}} + \frac{1}{2}\Big(\lambda^{(2)}_{\mathrm{R}} + \delta^{(2)}_{\lambda}\Big)\Delta_{\mathrm{R}}\Big]\varphi_{\mathrm{R}} = 0, \tag{3.6a}$$

$$\Big[Z_{(0)}\Box_x - \mu^2_{\mathrm{R}(0)} + \delta^{(0)}_{\mu} + \frac{1}{2}\Big(\lambda^{(2)}_{\mathrm{R}} + \delta^{(2)}_{\lambda}\Big)\varphi^2_{\mathrm{R}} + \frac{1}{2}\Big(\lambda^{(0)}_{\mathrm{R}} + \delta^{(0)}_{\lambda}\Big)\Delta_{\mathrm{R}}\Big]\mathrm{i}\Delta^{ab}_{\mathrm{R}}(x,y) = a\delta^{ab}\delta^{(4)}. \tag{3.6b}$$

Here we suppressed the arguments in the local functions $\varphi_{\mathrm{R}}(x)$ and $\Delta_{\mathrm{R}}(x,x)$, as well as in $\delta^{(4)}(x-y)$, for brevity. We now proceed to determine the various counterterms appearing in these equations and in the end find the renormalized equations of motion that include the effects of quantum corrections.

Auxiliary renormalization conditions. Because the operator acting on Δ^{ab}_{R} in (3.6b) is independent of branch indices, we can concentrate on the time ordered component Δ^{11}_{R} of the two-point function. We choose the mass-shell renormalization condition in the vacuum configuration $\varphi_{\mathrm{R}} = v_{\mathrm{R}}$, which simultaneously minimizes the effective action. That is, we set

$$\mathrm{i}(\Delta^{11}_{\mathrm{R}})^{-1} = p^2 - m^2_{\mathrm{R}}, \quad \frac{\mathrm{d}}{\mathrm{d}p^2}\mathrm{i}(\Delta^{11}_{\mathrm{R}})^{-1} = 1, \quad \text{and} \quad \frac{\delta\Gamma_{2\mathrm{PI}}}{\delta\varphi_{\mathrm{R}}}\Big|_{\varphi_{\mathrm{R}}=v_{\mathrm{R}}} = 0. \tag{3.7}$$

These conditions imply that $Z_{(0)} = 1$ in the Hartree approximation, and in our current scheme we can also set $Z_{(2)} = 1$ (see footnote 2 below). The renormalization conditions (3.7) then become:

$$-\mu^2_{\mathrm{R}(2)} + \delta^{(2)}_{\mu} + \frac{1}{6}\Big(\lambda^{(4)}_{\mathrm{R}} + \delta^{(4)}_{\lambda}\Big)v^2_{\mathrm{R}} + \frac{1}{2}\Big(\lambda^{(2)}_{\mathrm{R}} + \delta^{(2)}_{\lambda}\Big)\Delta_{\mathrm{R}}(v_{\mathrm{R}}) = 0, \tag{3.8a}$$

$$-\mu^2_{\mathrm{R}(0)} + \delta^{(0)}_{\mu} + \frac{1}{2}\Big(\lambda^{(2)}_{\mathrm{R}} + \delta^{(2)}_{\lambda}\Big)v^2_{\mathrm{R}} + \frac{1}{2}\Big(\lambda^{(0)}_{\mathrm{R}} + \delta^{(0)}_{\lambda}\Big)\Delta_{\mathrm{R}}(v_{\mathrm{R}}) = m^2_{\mathrm{R}}, \tag{3.8b}$$

where $\Delta_{\mathrm{R}}(v_{\mathrm{R}})$ refers to the still divergent local correlator computed at the renormalization point. It should be noted that Δ^{ab}_{R} is an auxiliary function and the parameter m^2_{R} is not yet related to any physical mass. Similarly, none of the couplings are yet related to observables, and there is considerable amount of choice related to their definition. We will choose the following conditions:[1]

$$\delta^{(0)}_{\lambda} = \delta^{(2)}_{\lambda}, \tag{3.9a}$$

$$-\mu^2_{\mathrm{R}(0)} + \delta^{(0)}_{\mu} = -\mu^2_{\mathrm{R}(2)} + \delta^{(2)}_{\mu}, \tag{3.9b}$$

$$\lambda^{(4)}_{\mathrm{R}} = \lambda^{(2)}_{\mathrm{R}} - \frac{1}{3}\delta^{(4)}_{\lambda} + \delta^{(2)}_{\lambda}. \tag{3.9c}$$

[1]These choices are partly specific for the Hartree approximation, where the self-energy Π^{ab} is proportional to the local correlation function. In any higher order 2PI truncation $\lambda^{(0)}_{\mathrm{R}}$ and $\lambda^{(2)}_{\mathrm{R}}$ would need to be renormalized separately.

JHEP12(2021)190

Because $Z_{(0,2)} = 1$ here, equation (3.9), together with eqs. (3.1) and (3.5) implies that $\lambda_{\mathrm{R}}^{(0)} = \lambda_{\mathrm{R}}^{(2)}$. Equation (3.9b) is less restrictive: it merely states that both renormalized mass terms are related to the same bare mass term. Conditions (3.9b) and (3.9c) still allow us to choose $\delta_\mu^{(2)}$ and $\delta_\lambda^{(4)}$ such that m_{R}^2 and $\lambda_{\mathrm{R}}^{(4)}$ can be matched to a physical mass parameter and a physical coupling. Using the conditions (3.9) and equation (3.8b) we can write equation (3.8a) simply as

$$m_{\mathrm{R}}^2 - \frac{1}{3}\lambda_{\mathrm{R}}^{(4)} v_{\mathrm{R}}^2 = 0. \tag{3.10}$$

That is, we are able to keep the tree-level relation between the coupling $\lambda_{\mathrm{R}}^{(4)}$, the background field v_{R} and the mass parameter m_{R}^2.

Cancelling the sub-divergences. In order to proceed, we need to find out the divergence structure of the local correlation function. Using dimensional regularization we can write

$$\Delta_{\mathrm{R}}(v_{\mathrm{R}}) = Q^\epsilon \int \frac{\mathrm{d}^d p}{(2\pi)^d}\, \Delta_{\mathrm{R}}^{11}(p) = -\frac{m_{\mathrm{R}}^2}{16\pi^2}\left[\frac{2}{\bar{\epsilon}} + 1 - \ln\left(\frac{m_{\mathrm{R}}^2}{Q^2}\right)\right], \tag{3.11}$$

where $\epsilon \equiv 4 - d$ and $2/\bar{\epsilon} \equiv 2/\epsilon - \gamma_{\mathrm{E}} + \ln(4\pi)$ and Q is an arbitrary renormalization scale. We now separate Δ_{R} into divergent and finite parts as follows:

$$\Delta_{\mathrm{R}}(v_{\mathrm{R}}) \equiv m_{\mathrm{R}}^2 \Delta_{\bar{\epsilon}} + \Delta_{\mathrm{F}0}(m_{\mathrm{R}}^2, Q), \tag{3.12}$$

where $\Delta_{\bar{\epsilon}} \equiv -1/(8\pi^2\bar{\epsilon})$. In what follows we will suppress the Q-dependence of the function $\Delta_{\mathrm{F}0}$ for brevity. Next we insert the decomposition (3.12) back into equation (3.8b), use relations (3.9) and let the leading order terms define the renormalized mass independently from the terms containing divergences or counterterms. In this way we get two equations out of the equation (3.8b):

$$m_{\mathrm{R}}^2 \equiv -\mu_{\mathrm{R}(2)}^2 + \frac{1}{2}\lambda_{\mathrm{R}}^{(2)}\left[v_{\mathrm{R}}^2 + \Delta_{\mathrm{F}0}(m_{\mathrm{R}}^2)\right], \tag{3.13}$$

$$0 = \delta_\mu^{(2)} + \frac{1}{2}\delta_\lambda^{(2)}\left[v_{\mathrm{R}}^2 + \Delta_{\mathrm{F}0}(m_{\mathrm{R}}^2)\right] + \frac{1}{2}\left(\lambda_{\mathrm{R}}^{(2)} + \delta_\lambda^{(2)}\right) m_{\mathrm{R}}^2 \Delta_{\bar{\epsilon}}. \tag{3.14}$$

Using definition (3.13) again in equation (3.14) and rearranging we get

$$\delta_\mu^{(2)} - \frac{1}{2}\left(\lambda_{\mathrm{R}}^{(2)} + \delta_\lambda^{(2)}\right)\mu_{\mathrm{R}(2)}^2 \Delta_{\bar{\epsilon}} + \frac{1}{2}\left[v_{\mathrm{R}}^2 + \Delta_{\mathrm{F}0}(m_{\mathrm{R}}^2)\right]\left[\delta_\lambda^{(2)} + \frac{1}{2}\left(\lambda_{\mathrm{R}}^{(2)} + \delta_\lambda^{(2)}\right)\lambda_{\mathrm{R}}^{(2)}\Delta_{\bar{\epsilon}}\right] = 0. \tag{3.15}$$

This equation has a consistent solution where the leading constant terms and the terms multiplying the combination (the sub-divergence part) $v_{\mathrm{R}}^2 + \Delta_{\mathrm{F}0}$ cancel independently. This gives two constraint equations,

$$\delta_\lambda^{(2)} + \frac{1}{2}\left(\lambda_{\mathrm{R}}^{(2)} + \delta_\lambda^{(2)}\right)\lambda_{\mathrm{R}}^{(2)}\Delta_{\bar{\epsilon}} = 0, \tag{3.16a}$$

$$\delta_\mu^{(2)} - \frac{1}{2}\left(\lambda_{\mathrm{R}}^{(2)} + \delta_\lambda^{(2)}\right)\mu_{\mathrm{R}(2)}^2 \Delta_{\bar{\epsilon}} = 0, \tag{3.16b}$$

from which we can finally solve the counterterms $\delta_\lambda^{(2)}$ and $\delta_\mu^{(2)}$:

$$\delta_\lambda^{(2)} = -\frac{\frac{1}{2}\left(\lambda_{\mathrm{R}}^{(2)}\right)^2 \Delta_{\bar{\epsilon}}}{1 + \frac{1}{2}\lambda_{\mathrm{R}}^{(2)}\Delta_{\bar{\epsilon}}} \qquad \text{and} \qquad \delta_\mu^{(2)} = \mu_{\mathrm{R}(2)}^2 \frac{\frac{1}{2}\lambda_{\mathrm{R}}^{(2)}\Delta_{\bar{\epsilon}}}{1 + \frac{1}{2}\lambda_{\mathrm{R}}^{(2)}\Delta_{\bar{\epsilon}}}. \tag{3.17}$$

JHEP12(2021)190

Scale dependence. The scale dependence of the auxiliary couplings and the mass parameters can now be worked out as usual by requiring that the bare parameters do not run: $\partial_Q[Q^\epsilon(\lambda_{\rm R}^{(2)}+\delta_\lambda^{(2)})]=0$ and $\partial_Q[Q^\epsilon(\mu^2_{{\rm R}(\rm I)}-\delta_\mu^{(\rm I)})]=0$. Using equations (3.17) one then immediately finds:

$$Q\frac{\partial\lambda_{\rm R}^{(2)}}{\partial Q}=\frac{(\lambda_{\rm R}^{(2)})^2}{16\pi^2}\qquad\text{and}\qquad Q\frac{\partial\mu^2_{{\rm R}(2)}}{\partial Q}=\frac{\lambda_{\rm R}^{(2)}\mu^2_{{\rm R}(2)}}{16\pi^2}. \tag{3.18}$$

The latter equation applies for both mass parameters, assuming that $\delta_\mu^{(0)}$ and $\delta_\mu^{(2)}$ differ by at most a finite and Q-independent term, which is the case in the Hartree approximation. Equations (3.18) can be easily integrated:

$$\lambda_{\rm R}^{(2)}(Q)=\frac{\lambda_{\rm R}^{(2)}(Q_0)}{1+\frac{\lambda_{\rm R}^{(2)}(Q_0)}{32\pi^2}\ln\!\left(\frac{Q_0^2}{Q^2}\right)}\qquad\text{and}\qquad \mu^2_{{\rm R}(\rm I)}(Q)=\frac{\mu^2_{{\rm R}(\rm I)}(Q_0)}{1+\frac{\lambda_{\rm R}^{(2)}(Q_0)}{32\pi^2}\ln\!\left(\frac{Q_0^2}{Q^2}\right)}. \tag{3.19}$$

Remember that as a result of equation (3.9a) $\lambda_{\rm R}^{(0)}=\lambda_{\rm R}^{(2)}$. On the other hand, the coupling $\lambda_{\rm R}^{(4)}$ does not run at all; indeed, to keep $\lambda_{\rm R}^{(4)}$ finite, we must have $\delta_\lambda^{(4)}=3\delta_\lambda^{(2)}$ up to finite terms according to equation (3.9c), which implies

$$Q\frac{\partial\lambda_{\rm R}^{(4)}}{\partial Q}=0\qquad\Rightarrow\qquad\lambda_{\rm R}^{(4)}=\text{constant}. \tag{3.20}$$

We shall see below that $\lambda_{\rm R}^{(4)}$ can be further fixed by some physical condition.

3.1 Renormalized equations of motion

It is essential to impose a correct treatment of the local correlation function away from the renormalization point in the equations of motion (3.6a) and (3.6b). Analogously to (3.13), we first define a leading order mass function that contains all finite terms in equation (3.6b):

$$m^2(\varphi_{\rm R},\Delta_{\rm F})\equiv-\mu^2_{{\rm R}(2)}+\frac{1}{2}\lambda_{\rm R}^{(2)}\Big(\varphi_{\rm R}^2+\Delta_{\rm F}\Big). \tag{3.21}$$

Here $\Delta_{\rm F}$ is the finite part of the local correlation function, which must be defined analogously to equation (3.12):

$$\Delta_{\rm R}\equiv m^2(\varphi_{\rm R},\Delta_{\rm F})\Delta_{\bar\epsilon}+\Delta_{\rm F}. \tag{3.22}$$

Note that both the finite part and the divergence contain non-trivial contributions from both the vacuum and the non-equilibrium fluctuations. Using definitions (3.21) and (3.22) we can write equation (3.6b) as follows:

$$\begin{aligned}\Big[\Box_x+m^2(\varphi_{\rm R},\Delta_{\rm F})+\delta_\mu^{(2)}+\frac{1}{2}\delta_\lambda^{(2)}\Big(\varphi_{\rm R}^2+\Delta_{\rm F}\Big)\\ +\frac{1}{2}\Big(\lambda_{\rm R}^{(2)}+\delta_\lambda^{(2)}\Big)m^2(\varphi_{\rm R},\Delta_{\rm F})\Delta_{\bar\epsilon}\Big]\mathrm{i}\Delta_{\rm R}^{ab}(x,y)=a\delta^{ab}\delta^{(4)}(x-y).\end{aligned} \tag{3.23}$$

Using definition (3.21) again one can show that all divergent terms in equation (3.23) arrange as in equation (3.15) and cancel as a result of the renormalization conditions (3.16).

JHEP12(2021)190

Then, noting that $\lambda_{\mathrm{R}}^{(4)} + \delta_\lambda^{(4)} = -2\lambda_{\mathrm{R}}^{(4)} + \mathcal{O}(\epsilon)$, the same manipulations can be done also in equation (3.6a). This results in the final renormalized equations of motion:

$$\Big[\Box_x + m^2(\varphi_{\mathrm{R}}, \Delta_{\mathrm{F}})\Big]\varphi_{\mathrm{R}} = \frac{1}{3}\lambda_{\mathrm{R}}^{(4)}\varphi_{\mathrm{R}}^3, \tag{3.24a}$$

$$\Big[\Box_x + m^2(\varphi_{\mathrm{R}}, \Delta_{\mathrm{F}})\Big]\mathrm{i}\Delta_{\mathrm{R}}^{ab}(x,y) = a\delta^{ab}\delta^{(4)}(x-y). \tag{3.24b}$$

These equations appear deceivingly simple: when written for the Wightman function $\Delta_{\mathrm{R}}^{<} = \Delta_{\mathrm{R}}^{+-}$, equation (3.24b) takes the form of a wave equation with a time-dependent mass and, as we shall see in the next section, equation (3.24a) describes the motion of the one-point function in a quantum corrected effective potential including backreaction from non-equilibrium modes. However, despite their apparent simplicity, the equations are strongly coupled through the local correlator in the gap equation (3.21) for the mass term.

3.2 Effective potential and physical parameters

Let us now consider the *adiabatic limit* of the evolution equations, where Δ_{F} is given purely by vacuum fluctuations with no physical excitations. In this case definition (3.21) reduces to

$$\overline{m}^2(\varphi_{\mathrm{R}}) \equiv -\mu_{\mathrm{R}(2)}^2 + \frac{1}{2}\lambda_{\mathrm{R}}^{(2)}\Big[\varphi_{\mathrm{R}}^2 + \Delta_{\mathrm{F}0}\big(\overline{m}^2(\varphi_{\mathrm{R}})\big)\Big], \tag{3.25}$$

and correspondingly

$$\overline{\Delta}_{\mathrm{R}}(\varphi_{\mathrm{R}}) \equiv \overline{m}^2(\varphi_{\mathrm{R}})\Delta_{\bar{\epsilon}} + \Delta_{\mathrm{F}0}\big(\overline{m}^2(\varphi_{\mathrm{R}})\big). \tag{3.26}$$

Note that $\overline{m}^2(\varphi_{\mathrm{R}})$ and $\overline{\Delta}_{\mathrm{R}}$ differ from definitions (3.21) and (3.22) only through a different value of the background field φ_{R}. Using the equation of motion (3.6b) in the renormalized 2PI action (3.2) we can write down the 1PI effective potential in the Hartree approximation as follows:

$$V_{\mathrm{H}}(\varphi_{\mathrm{R}}) = -\frac{1}{V}\,\Gamma_{\mathrm{2PI}}^{\mathrm{H}}(\varphi_{\mathrm{R}}, \overline{\Delta}) = V_0(\varphi_{\mathrm{R}}) + \frac{\mathrm{i}}{2V}\,\mathrm{Tr}\Big[\ln(\overline{\Delta}_{\mathrm{R}})\Big] - \frac{1}{8}\Big(\lambda_{\mathrm{R}}^{(2)} + \delta_\lambda^{(2)}\Big)\overline{\Delta}_{\mathrm{R}}^2(\varphi_{\mathrm{R}}), \tag{3.27}$$

where V is the space-time volume and the tree-level effective potential is

$$V_0(\varphi_{\mathrm{R}}) = \frac{1}{2}\Big(-\mu_{\mathrm{R}(2)}^2 + \delta_\mu^{(2)}\Big)\varphi_{\mathrm{R}}^2 + \frac{1}{4!}\Big(\lambda_{\mathrm{R}}^{(4)} + \delta_\lambda^{(4)}\Big)\varphi_{\mathrm{R}}^4 = -\frac{\lambda_{\mathrm{R}}^{(4)}}{12}\varphi_{\mathrm{R}}^4, \tag{3.28}$$

where in the last step we dropped all terms of order ϵ. Writing $\mathrm{i}\mathrm{Tr}\Big[\ln(\overline{\Delta}_{\mathrm{R}})\Big] = V\int \mathrm{d}\overline{m}^2\,\overline{\Delta}_{\mathrm{R}}$ and using equation (3.26) one finds that the divergences cancel between the two last terms in equation (3.27) and the finite part of $\mathrm{Tr}\Big[\ln(\overline{\Delta}_{\mathrm{R}})\Big]$ creates the one-loop correction to the effective potential. After a little algebra one finds the result:

$$V_{\mathrm{H}}(\varphi_{\mathrm{R}}) = -\frac{\lambda_{\mathrm{R}}^{(4)}}{12}\varphi_{\mathrm{R}}^4 + \frac{\overline{m}^4(\varphi_{\mathrm{R}})}{2\lambda_{\mathrm{R}}^{(2)}} - \frac{\overline{m}^4(\varphi_{\mathrm{R}})}{64\pi^2}\left[\ln\left(\frac{\overline{m}^2(\varphi_{\mathrm{R}})}{Q^2}\right) - \frac{1}{2}\right]. \tag{3.29}$$

This is the vacuum effective potential in the Hartree approximation, found for example in reference [32]. Despite the apparent Q-dependence, $V_{\mathrm{H}}(\varphi_{\mathrm{R}})$ is in fact scale-independent. Indeed, one can first show from definition (3.25), using (3.18), that $\partial_Q\overline{m}^2(\varphi_{\mathrm{R}}) = 0$. Then by a direct differentiation and using equations (3.18) and (3.20) one finds that $\partial_Q V_{\mathrm{H}}(\varphi_{\mathrm{R}}) = 0$.

JHEP12(2021)190

Physical parameters. Differentiating (3.25) with respect to φ_{R} one can first derive the identity

$$\frac{\partial \overline{m}^2}{\partial \varphi_{\mathrm{R}}}\left[1-\frac{\lambda_{\mathrm{R}}^{(2)}}{32\pi^2}\ln\left(\frac{\overline{m}^2}{Q^2}\right)\right]=\lambda_{\mathrm{R}}^{(2)}\varphi_{\mathrm{R}}. \tag{3.30}$$

Using (3.30) it is simple to show that the first derivative of the potential can be written as

$$\frac{\partial V_{\mathrm{H}}}{\partial \varphi_{\mathrm{R}}}=-\frac{1}{3}\lambda_{\mathrm{R}}^{(4)}\varphi_{\mathrm{R}}^3+\overline{m}^2(\varphi_{\mathrm{R}})\varphi_{\mathrm{R}}. \tag{3.31}$$

Comparing equation (3.31) with equation (3.24a) we can see that in the case of pure vacuum fluctuations the equation of motion can be written as $\partial_t^2\varphi_{\mathrm{R}}+\partial V_{\mathrm{H}}/\partial\varphi_{\mathrm{R}}=0$. Differentiating equation (3.31) once more with respect to φ_{R} one finds

$$\frac{\partial^2 V_{\mathrm{H}}}{\partial \varphi_{\mathrm{R}}^2}=\overline{m}^2(\varphi_{\mathrm{R}})+\left[\lambda_{\mathrm{R}}^{(2)}(\overline{m}^2(\varphi_{\mathrm{R}}))-\lambda_{\mathrm{R}}^{(4)}\right]\varphi_{\mathrm{R}}^2. \tag{3.32}$$

Because $\overline{m}^2(v_{\mathrm{R}})=m_{\mathrm{R}}^2$, we now see that the on-shell mass parameter m_{R} of the auxiliary propagator can be identified with a physical mass,[2] if we at the same time define

$$\lambda_{\mathrm{R}}^{(2)}(m_{\mathrm{R}}^2)\equiv\lambda_{\mathrm{R}}^{(4)}. \tag{3.33}$$

This is the choice of parameters we shall use in the rest of this paper.

So far we have defined the counterterm $\delta_\lambda^{(4)}$ only up to a finite constant. This, and other remaining freedom in choosing the counterterms (see footnote 2) would allow us to further match $\lambda_{\mathrm{R}}^{(4)}$ to some observable. Given that $\lambda_{\mathrm{R}}^{(4)}$ does not run, equations (3.33) and (3.32) are enough to fix the parameters of the theory. Going beyond the Hartree approximation would lead to more complicated calculations and relations between the auxiliary parameters, but would not change the derivation conceptually.

3.3 Finite temperature effective potential

In our derivation in section 3.1 we did not specify the finite part of the local correlation function Δ_{F}, and in what follows we will compute it numerically from the equations of motion. Before that it is useful to make one more observation concerning thermal corrections. Indeed, we can include thermal corrections by a simple generalization of equations (3.25) and (3.26):

$$\overline{m}^2(\varphi_{\mathrm{R}},T)\equiv-\mu_{\mathrm{R}(2)}^2+\frac{1}{2}\lambda_{\mathrm{R}}^{(2)}\left[\varphi_{\mathrm{R}}^2+\overline{\Delta}_{\mathrm{F}}(\varphi_{\mathrm{R}},T)\right], \tag{3.34}$$

with $\overline{\Delta}_{\mathrm{R}}(\varphi_{\mathrm{R}},T)\equiv\overline{m}^2(\varphi_{\mathrm{R}},T)\Delta_{\bar{\epsilon}}+\overline{\Delta}_{\mathrm{F}}(\varphi_{\mathrm{R}},T)$ and

$$\overline{\Delta}_{\mathrm{F}}(\varphi_{\mathrm{R}},T)\equiv\Delta_{\mathrm{F}0}(\overline{m}^2(\varphi_{\mathrm{R}},T))+T^2\mathcal{I}(\overline{m}^2(\varphi_{\mathrm{R}},T)/T^2), \tag{3.35}$$

[2] In fact these relations imply that m_{R} corresponds to a mass defined at $p^2=0$, but in the Hartree case this is the same as the physical pole mass. Going beyond Hartree approximation, one can still make m_{R} agree with the physical on-shell mass using the remaining freedom in definitions (3.9) and in the definition of the wave-function counterterm $Z_{(2)}$, which allow adding finite parts to $\delta_\varphi^{(2)}$, $\delta_\mu^{(2)}$ and $\delta_\lambda^{(4)}$.

JHEP12(2021)190

where $\mathcal{I}(x) = 2\partial_x \mathcal{J}(x)$ and $\mathcal{J}(x)$ is the dimensionless bosonic one-loop thermal integral

$$\mathcal{J}(x) \equiv \frac{1}{2\pi^2}\,\mathrm{Re}\int_0^\infty \mathrm{d}y\, y^2 \ln\Big(1 - \mathrm{e}^{-\sqrt{y^2+x-\mathrm{i}\varepsilon}}\Big). \tag{3.36}$$

Here the infinitesimal imaginary part $\mathrm{i}\varepsilon$ defines the correct branch of the logarithm for a negative $\overline{m}^2$. With these definitions one can go through the analysis of the previous paragraph and show that the equation of motion of the homogeneous field is now $\partial_t^2\varphi_\mathrm{R} + \partial V_\mathrm{H}(\varphi_\mathrm{R},T)/\partial\varphi_\mathrm{R} = 0$, where $V_\mathrm{H}(\varphi_\mathrm{R},T)$ is the thermally corrected, scale independent effective potential in the Hartree approximation:

$$V_\mathrm{H}(\varphi_\mathrm{R},T) = V_\mathrm{H}(\varphi_\mathrm{R})\Big|_{m\to\overline{m}_T} - \frac{1}{2}\overline{m}_T^2 T^2 \mathcal{I}(\overline{m}_T^2/T^2) + T^4\mathcal{J}(\overline{m}_T^2/T^2), \tag{3.37}$$

where $\overline{m}_T^2 \equiv \overline{m}^2(\varphi_\mathrm{R},T)$. Note that in the 2PI approach also the vacuum part $V_\mathrm{H}(\varphi_\mathrm{R})$ of the potential is computed with the thermally corrected mass, which is the solution to equations (3.34) and (3.35). It is worth mentioning that in each special case considered above, from the vacuum renormalization (3.12) to the quantum corrected effective action with (3.35) and without (3.26) thermal corrections, and finally to the general case (3.22), the divergence that gets removed by counterterms is different and depends on the value of the background field, the temperature and the particle distribution. This is an unavoidable feature of the 2PI equations with a finite order truncation. However, in all cases the counterterms themselves remain the same, uniquely defined constants.

Comparison to ring-resummed potentials. Equations (3.34), (3.35) and (3.37) provide a consistent resummation of the thermal potential to super-daisy level. They can be seen as a consistent generalization of the Parwani resummation method [33]. In these approaches the thermal corrections affect all modes on equal footing, while in the usual ring resummation method [34, 35] only the long wavelength modes are screened by the short wavelength modes in a thermal plasma. The advantage of the potential (3.37) is that it provides a consistently renormalized, smooth continuation between the non-relativistic and relativistic regimes. In all other ring-resummed potentials this behaviour has to be put in by hand.

To effect a fair comparison of different approximations, we write all potentials using the same renormalization conditions. To be concrete, we use the conditions $\partial_\varphi^2 V(v_\mathrm{R}) = m_\mathrm{R}^2$ and $\partial_\varphi^4 V(v_\mathrm{R}) = \lambda_\mathrm{R}$. With these conditions the standard one-loop corrected potential without the ring-corrections becomes

$$V_\mathrm{1L}(\varphi_\mathrm{R},T) \equiv -\frac{1}{2}\mu_\mathrm{R}^2\varphi_\mathrm{R}^2 + \frac{1}{4!}\lambda_\mathrm{R}\varphi_\mathrm{R}^4 + V_{1-\mathrm{loop}}(\varphi_\mathrm{R}) + T^4\mathcal{J}\bigg(\frac{m_0^2(\varphi_\mathrm{R})}{T^2}\bigg), \tag{3.38}$$

where $m_0^2(\varphi_\mathrm{R}) = -\mu_\mathrm{R}^2 + \frac{1}{2}\lambda_\mathrm{R}\varphi_\mathrm{R}^2$ and the standard one-loop vacuum potential is (this potential also satisfies the condition $\partial_\varphi V_{1-\mathrm{loop}}(v_\mathrm{R}) = 0$)

$$V_{1-\mathrm{loop}}(\varphi_\mathrm{R}) = \frac{1}{64\pi^2}\bigg\{m_0^4(\varphi_\mathrm{R})\bigg[\ln\bigg(\frac{m_0^2(\varphi_\mathrm{R})}{m_\mathrm{R}^2}\bigg) - \frac{3}{2}\bigg] + 2m_\mathrm{R}^2 m_0^2(\varphi_\mathrm{R})\bigg\}. \tag{3.39}$$

In the Parwani approximation [33] one replaces $m_0^2(\varphi_\mathrm{R})$ with the lowest order thermal mass $m_0^2(\varphi_\mathrm{R},T) = m_0^2(\varphi_\mathrm{R}) + \frac{1}{24}\lambda_\mathrm{R}T^2$ in equation (3.38) and in the ring approximation [34, 35],

JHEP12(2021)190

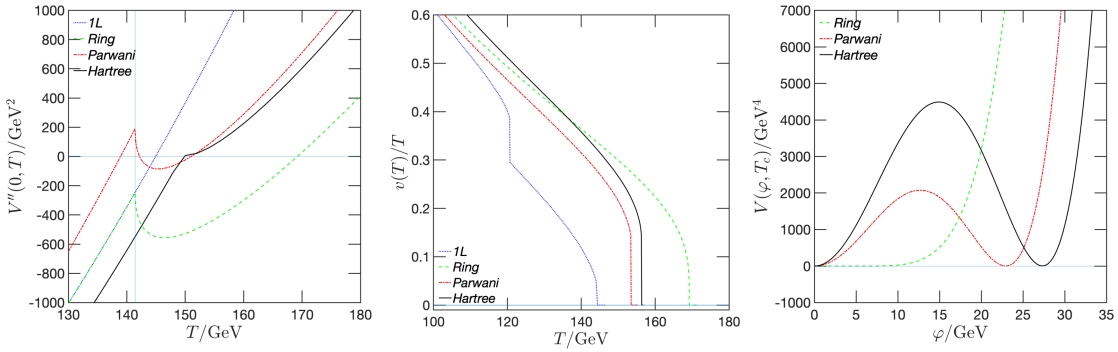

Figure 3. Left: the evolution of the second φ-derivatives of the different potentials at $\varphi_{\mathrm{R}} = 0$. Middle: the evolution of the ratio $v(T)/T$, where $v(T)$ is the position of the second minimum. Right: the potential at critical temperature in each approximation. The critical temperatures are $T_{\mathrm{c}} \approx 169.20\,\mathrm{GeV}$ in the ring, $T_{\mathrm{c}} \approx 153.29\,\mathrm{GeV}$ in the Parwani and $T_{\mathrm{c}} \approx 155.67\,\mathrm{GeV}$ in the Hartree approximation. We used $m_{\mathrm{R}} = 100\,\mathrm{GeV}$ and $\lambda_{\mathrm{R}} = 6$ (which implies $\lambda_{\mathrm{R}}^{(4)} \simeq 5.2$). The vertical line in the left panel shows $T_0 = \sqrt{12/\lambda_{\mathrm{R}}}m_{\mathrm{R}}$, where the high-temperature limit approximated thermal mass vanishes at $\varphi_{\mathrm{R}} = 0$.

where only the zero-mode is dressed by thermal corrections, one finds:

$$V_{\mathrm{Ring}}(\varphi_{\mathrm{R}},T) \equiv V_{1\mathrm{L}}(\varphi_{\mathrm{R}},T) + \frac{T}{12\pi}\mathrm{Re}\Big(m_0^3(\varphi_{\mathrm{R}}) - m_0^3(\varphi_{\mathrm{R}},T)\Big). \tag{3.40}$$

Above we wrote the Hartree potential in terms of the scale dependent variables. However, since the potential is actually scale independent, we can rewrite it at the scale $Q = m_{\mathrm{R}}$, explicitly in terms of the physical parameters:

$$V_{\mathrm{H}}(\varphi_{\mathrm{R}},T) = -\frac{\lambda_{\mathrm{R}}^{(4)}}{12}\varphi_{\mathrm{R}}^4 + \frac{\overline{m}_T^4}{2\lambda_{\mathrm{R}}^{(4)}} - \frac{\overline{m}_T^4}{64\pi^2}\left[\ln\left(\frac{\overline{m}_T^2}{m_{\mathrm{R}}^2}\right) - \frac{1}{2}\right] - \frac{\overline{m}_T^2 T^2}{2}\mathcal{I}\left(\frac{\overline{m}_T^2}{T^2}\right) + T^4\mathcal{J}\left(\frac{\overline{m}_T^2}{T^2}\right), \tag{3.41}$$

where $\overline{m}_T^2$ is the solution to the gap equation, which now becomes

$$\overline{m}_T^2 \equiv m_{\mathrm{R}}^2 + \frac{1}{2}\lambda_{\mathrm{R}}^{(4)}(\varphi_{\mathrm{R}}^2 - v_{\mathrm{R}}^2) + \frac{\lambda_{\mathrm{R}}^{(4)}}{32\pi^2}\left[\overline{m}_T^2\ln\left(\frac{\overline{m}_T^2}{m_{\mathrm{R}}^2}\right) + \overline{m}_T^2 - m_{\mathrm{R}}^2\right] + T^2\mathcal{I}\left(\frac{\overline{m}_T^2}{T^2}\right), \tag{3.42}$$

with $m_{\mathrm{R}}^2 = \frac{1}{3}\lambda_{\mathrm{R}}^{(4)}v_{\mathrm{R}}^2$ and where finally $\lambda_{\mathrm{R}}^{(4)}$ is related to the renormalized coupling $\lambda_{\mathrm{R}} \equiv \partial_\varphi^4 V_{\mathrm{H}}(v_{\mathrm{R}},0)$ by

$$\lambda_{\mathrm{R}} = \lambda_{\mathrm{R}}^{(4)}\left[1 + 3\left(\frac{3\lambda_{\mathrm{R}}^{(4)}}{32\pi^2}\right) + 3\left(\frac{3\lambda_{\mathrm{R}}^{(4)}}{32\pi^2}\right)^2\right], \tag{3.43}$$

as can be shown by direct differentiation of equation (3.41).

In the left panel of figure 3 we show the evolution of the second φ-derivatives of the potentials near the critical temperature at $\varphi_{\mathrm{R}} = 0$. The sharp kinks seen in the ring (green dashed line) and Parwani (red dash-dotted line) cases at $T = T_0$ result from the non-analytic dependence of the resummed potentials on the thermally corrected mass term (we are using the high-temperature expansion for $m^2(\varphi,T)$ in these schemes). The one-loop result (blue dotted line) does not share this feature, because there we are using the

JHEP12(2021)190

non-resummed mass term. Interestingly, the Hartree result (black line) does not show signs of similar non-analyticity. In the middle panel we show the evolution of the ratio $v(T)/T$, where $v(T)$ is the position of the asymmetric minimum as a function of T. There are significant differences between the approximations: in all resummed potentials a metastable minimum emerges, and it has the largest jump in the Hartree case. In the one-loop case the metastability does not develop, but there is a jump in $v(T)/T$ at $T \approx 120\,\mathrm{GeV}$ due to the non-analytic behaviour, now of the vacuum mass term as a function of φ. In the right panel we show the potentials at the critical temperature (whose value for each model is given in the figure caption). The transition strength is dramatically different in the different approximations and it is by far the strongest in the Hartree case. Of course one should keep in mind that this is a very simple model, with only a single scalar field. However, when one compares the one-loop results with lattice calculations, one typically finds that both ring and Parwani approximations give weaker transitions than the lattice or 3d-perturbation theory calculations [36]. It would be interesting to see if the Hartree approximation was in better agreement with these schemes when applied in more complex models.

4 Wigner space equations

We now proceed to solving the general equations (3.24b) and (3.24a) for homogeneous non-equilibrium systems. Of these, equation (3.24a) is already in the desired form, when we assume that field φ_{R} is homogeneous, but equation (3.24b) for the correlation function will be easier to handle in the mixed representation. Because of the homogeneity an ordinary Fourier transformation is sufficient for the spatial coordinates, but for the time variable we need the Wigner transformation:

$$\Delta^{ab}_{\mathrm{R}\boldsymbol{k}}(k_0, t) = \int \mathrm{d}r_0\, \Delta^{ab}_{\mathrm{R}\boldsymbol{k}}\Big(t + \frac{r_0}{2}, t - \frac{r_0}{2}\Big) \mathrm{e}^{\mathrm{i}k_0 r_0}, \tag{4.1}$$

where $t \equiv \frac{1}{2}(x_0 + y_0)$ and $r_0 \equiv x_0 - y_0$. Because all correlation functions $\Delta^{ab}(x, y)$ have the same local limit, it suffices to consider the equation for the lesser Wightman function $\Delta^{+-} \equiv \Delta^{<}$. Starting from equation (3.24b), we find that in the Wigner representation it satisfies the equation,

$$\Big[\frac{1}{4}\partial_t^2 - k^2 - \mathrm{i}k_0\partial_t + \mathrm{e}^{-\frac{\mathrm{i}}{2}\partial_t^m \partial_{k_0}} m^2(\varphi_{\mathrm{R}}, \Delta_{\mathrm{R}})\Big]\, \Delta^{<}_{\mathrm{R}\boldsymbol{k}}(k_0, t) = 0. \tag{4.2}$$

Here the index m in the derivative ∂_t^m signals that the time-derivative acts only on the mass function and not on the propagator. Equation (4.2) is still equivalent to (3.24b) and highly complicated because of the infinite tower of t- and k_0-derivatives involved. It can be recast into a simpler form by introducing a moment expansion. Following reference [27] we first introduce the moment functions:

$$\rho_{\boldsymbol{k}n}(t) = \int \frac{\mathrm{d}k_0}{2\pi}\, k_0^n\, \Delta^{<}_{\mathrm{R}\boldsymbol{k}}(k_0, t). \tag{4.3}$$

Then taking the real and imaginary parts of equation (4.2) integrated over k_0 and the imaginary part of the same equation integrated over k_0 and weighted by k_0, we get three

JHEP12(2021)190

equations coupling the moments $\rho_{n\boldsymbol{k}}$ with $n = 0, 1, 2$ to the field equation for a homogeneous field $\varphi_{\mathrm{R}}(t)$:

$$\frac{1}{4}\partial_t^2 \rho_{0\boldsymbol{k}} - \rho_{2\boldsymbol{k}} + \omega_{\boldsymbol{k}}^2(t)\, \rho_{0\boldsymbol{k}} = 0, \tag{4.4a}$$

$$\partial_t \rho_{1\boldsymbol{k}} = 0, \tag{4.4b}$$

$$\partial_t \rho_{2\boldsymbol{k}} - \frac{1}{2}\Big[\partial_t\big(m_{\mathrm{eff}}^2(t)\big)\Big]\rho_{0\boldsymbol{k}} = 0, \tag{4.4c}$$

$$\Big[\partial_t^2 + m_{\mathrm{eff}}^2(t)\Big]\varphi_{\mathrm{R}} = \frac{1}{3}\lambda_{\mathrm{R}}^{(2)}\varphi_{\mathrm{R}}^3. \tag{4.4d}$$

We used the shorthand $m_{\mathrm{eff}}^2(t) \equiv m^2(\varphi_{\mathrm{R}}, \Delta_{\mathrm{R}})$ for the mass defined in (3.22) and (3.21) and defined $\omega_{\boldsymbol{k}}^2(t) \equiv \boldsymbol{k}^2 + m_{\mathrm{eff}}^2(t)$. The gap equation (3.21), including the out-of-equilibrium (or thermal) modes, can be written explicitly as

$$m_{\mathrm{eff}}^2(t) = -\mu_{\mathrm{R}(2)}^2 + \frac{1}{2}\lambda_{\mathrm{R}}^{(2)}\left\{\varphi_{\mathrm{R}}^2 + \Delta_{\mathrm{F}0}\big(m_{\mathrm{eff}}^2(t)\big) + \int_{\boldsymbol{k}}\left[\rho_{0\boldsymbol{k}}(t) - \frac{\theta\big(\omega_{\boldsymbol{k}}^2(t)\big)}{2\omega_{\boldsymbol{k}}(t)}\right]\right\}, \tag{4.5}$$

where we defined $\int_{\boldsymbol{k}} \equiv \frac{1}{2\pi^2}\int_0^\infty \mathrm{d}|\boldsymbol{k}||\boldsymbol{k}|^2$, and the Heaviside theta-function $\theta\big(\omega_{\boldsymbol{k}}^2(t)\big)$ ensures that the vacuum does not contain the unstable spinodal modes.[3]

If $\rho_{0\boldsymbol{k}}(t)$ is identified with a thermal distribution (including the vacuum part), equation (4.5) clearly reduces to (3.34). After discretizing the momentum variable, equations (4.4c), (4.4a), (4.4d) and (4.5) can be written as a closed set of coupled first order differential equations, which include backreaction from the non-equilibrium modes into the evolution of the homogeneous field φ_{R}. The gap equation (4.5) must be solved first at the entry to the routine, after which the solution is advanced using (4.4c), (4.4a) and (4.4d). In practice one must introduce a UV-cutoff for the magnitude of the momentum $|\boldsymbol{k}|$, but results should not depend on its precise value, because all non-trivial physics results from gradient terms acting in the infrared region. We have indeed shown that this is the case in our numerical examples.

Friction. Our main goal is to study the dynamical evolution of φ_{R} including the backreaction from the modes excited during the zero-crossings (parametric resonance) and from the unstable modes (spinodal, or tachyonic, instability). We would also like to study dissipative interactions in our system. To do this correctly, we should go beyond the Hartree approximation. This would be in principle a straightforward but very laborious task. Some formal results can be found for example in [37]. Here we will instead add phenomenological friction terms to our equations. Following references [27] and [28] we

[3] Spinodal modes are the unstable modes that appear when the effective mass function is negative. We define them explicitly in equation (5.1) below. Note that the vacuum energy integral in the spinodal region, computed with the Heaviside function, is identical with the integral computed taking the absolute value of the mass squared function and integrating over all momenta.

JHEP12(2021)190

generalize equations (4.4a), (4.4b) and (4.4c) as follows:

$$\frac{1}{4}\partial_t^2\rho_{0\boldsymbol{k}} - \rho_{2\boldsymbol{k}} + \omega_{\boldsymbol{k}}^2(t)\rho_{0\boldsymbol{k}} = -c_1\partial_t\rho_{0\boldsymbol{k}}, \tag{4.6a}$$

$$\partial_t\rho_1 = -c_2(\delta\rho_{1\boldsymbol{k}} - \delta\rho_{1\boldsymbol{k}}^{\mathrm{eq}}), \tag{4.6b}$$

$$\partial_t\rho_{2\boldsymbol{k}} - \frac{1}{2}\Big[\partial_t(m_{\mathrm{eff}}^2(t))\Big]\rho_{0\boldsymbol{k}} = -c_2(\delta\rho_{2\boldsymbol{k}} - \delta\rho_{2\boldsymbol{k}}^{\mathrm{eq}}), \tag{4.6c}$$

where $\delta\rho_{n\boldsymbol{k}} \equiv \rho_{n\boldsymbol{k}} - \rho_{n\boldsymbol{k}}^{\mathrm{vac}}$ with $\rho_{n\boldsymbol{k}}^{\mathrm{vac}}$ being the vacuum moments defined in equations (4.8) below, and the explicit forms for the equilibrium distributions $\rho_{n\boldsymbol{k}}^{\mathrm{eq}}$ have to be provided externally depending on the problem. Collision integrals could be computed accurately in the context of the cQPA formalism following reference [28] (see also [38]), but here we are only interested in qualitative effects, for which the above phenomenological approach is sufficient. Even then the coefficients c_i could be some momentum dependent functions, but for simplicity we will assume that they are constants. Note that $\rho_{n\boldsymbol{k}}$ and $\rho_{n\boldsymbol{k}}^{\mathrm{eq}}$ in general have different vacuum distributions due to different respective solutions to mass gap equations.

Number densities and coherence function. We can get a better understanding of the physical meaning of the moments by comparing them with the spectral cQPA solutions found in reference [27]. As explained in section 4.2 of reference [27], the moments are in a one-to-one correspondence with the cQPA mass-shell functions $f_{\boldsymbol{k}\pm}^m$ and the coherence function $f_{\boldsymbol{k}}^c$. The former can be further related to the particle and antiparticle number densities $n_{\boldsymbol{k}}$ and $\bar{n}_{\boldsymbol{k}}$, so that one eventually finds [27, 28]:

$$n_{\boldsymbol{k}} = \frac{1}{\omega_{\boldsymbol{k}}}\rho_{2\boldsymbol{k}} + \rho_{1\boldsymbol{k}}, \tag{4.7a}$$

$$\bar{n}_{\boldsymbol{k}} = \frac{1}{\omega_{\boldsymbol{k}}}\rho_{2\boldsymbol{k}} - \rho_{1\boldsymbol{k}} - 1, \tag{4.7b}$$

$$f_{\boldsymbol{k}}^{c\pm} = \omega_{\boldsymbol{k}}\rho_{0\boldsymbol{k}} - \frac{1}{\omega_{\boldsymbol{k}}}\rho_{2\boldsymbol{k}} \pm \frac{\mathrm{i}}{2}\partial_t\rho_{0\boldsymbol{k}}. \tag{4.7c}$$

The coherence functions $f_{\boldsymbol{k}}^{c\pm}$ measure the degree of quantum coherence, or squeezing, between particle-antiparticle pairs with opposite 3-momenta [39]. A *non-coherent* vacuum state must then be defined as a state with no squeezing in addition to having no particles. This corresponds to setting $n_{\boldsymbol{k}} = \bar{n}_{\boldsymbol{k}} = f_{\boldsymbol{k}}^{c\pm} \equiv 0$, which is equivalent to:

$$\rho_{0\boldsymbol{k}}^{\mathrm{vac}} = \frac{\Theta_{\boldsymbol{k}}}{2\omega_{\boldsymbol{k}}}, \qquad \partial_t\rho_{0\boldsymbol{k}}^{\mathrm{vac}} = 0, \qquad \rho_{1\boldsymbol{k}}^{\mathrm{vac}} = -\frac{1}{2} \quad \text{and} \quad \rho_{2\boldsymbol{k}}^{\mathrm{vac}} = \frac{\omega_{\boldsymbol{k}}}{2}\Theta_{\boldsymbol{k}}, \tag{4.8}$$

where $\Theta_{\boldsymbol{k}} \equiv \theta(\omega_{\boldsymbol{k}}^2(t))$. Because we are assuming that φ_{R} is a real scalar field we also have $\bar{n}_{\boldsymbol{k}} = n_{\boldsymbol{k}}$, which implies that $\rho_{1\boldsymbol{k}} = -1/2$ at all times, so that the equation for $\rho_{1\boldsymbol{k}}$ is actually redundant. This is indeed a consistent solution even with the friction terms included.

5 Numerical results

We shall now solve the coupled dynamical equations (4.6a), (4.6b), (4.6c), (4.5) and (4.4d) in a few examples chosen to illustrate the rich physics of the strongly coupled system

JHEP12(2021)190

including the quantum backreaction. We will uncover some known results and find new phenomena associated with spinodal and resonant particle production at phase transitions.[4] We will show that a strong spinodal instability can cause a quantum assisted barrier penetration without tunneling, and we emphasize the difficulty of giving any sensible definition for the effective potential in a non-equilibrium system. Eventually, we will follow the full thermalization process of a scalar field starting at rest in the vacuum potential until the end, when the energy in the field is almost completely transformed into thermal fluctuations.[5]

5.1 Particle production and reheating via parametric resonance

We first consider a case where the field starts from a relatively large value and oscillates several times between positive and negative field values. Because we are also interested in the spinodal instability, we consider a tree-level potential with a negative mass term. As physical parameters we use $m_{\rm R} = 100\,\text{GeV}$ and $\lambda_{\rm R}^{(4)} = 1$, given which, $\mu^2_{{\rm R}(2)}(Q_0)$ can be solved from (3.13), while the running couplings and masses are defined in (3.19). We compute the initial value for the effective mass function $m^2(\varphi_{\rm R}, \Delta_{\rm R})$ using the vacuum Hartree approximation (3.25). We used running parameters everywhere in our calculations. This served as a useful consistency check, since all final results must be (and indeed were) scale independent. In this example we also set the friction terms to zero, $c_i = 0$.

The essential results for this run are shown in figures 4 and 5. In the left panel of figure 4 we show the evolution of the classical field $\varphi_{\rm R}$, which here displays an orderly oscillation pattern with a slowly decaying amplitude. The middle panel of figure 4 shows the evolution of the fluctuations in the zeroth moment integrated over the 3-momentum, which is the non-equilibrium contribution to the local correlation function: $\int_{\boldsymbol{k}} \delta\rho_{0\boldsymbol{k}} = \int_{\boldsymbol{k}} (\rho_{0\boldsymbol{k}} - \rho^{\rm vac}_{0\boldsymbol{k}}) \equiv \delta\Delta_{\rm F}(t,t)$. These results are in good agreement with reference [16], where this problem was studied earlier using the mode equation approach. The rapid increase of $\delta\Delta_{\rm F}(t,t)$ at early times is caused by two non-perturbative processes, the spinodal instability and the parametric resonance.

Spinodal instability. The presence of a spinodal instability is manifest in the right panel of figure 4, where the effective mass term $m^2(\varphi_{\rm R}, \Delta_{\rm R})$ is seen to become periodically negative in the region $t \lesssim 0.25$. Indeed, whenever the mass-function is negative, all $\boldsymbol{k}$-modes satisfying

$$\boldsymbol{k}^2 + m^2(\varphi_{\rm R}, \Delta_{\rm R}) < 0 \tag{5.1}$$

[4] The use of the term phase transition is not very accurate here, as we do not have a phase transition in the same sense as for example in the electroweak transition. Rather, we have a situation where the universe evolves from a cold initial state to a hot final state. It is a common practice however to refer to this phenomenon as a phase transition as well, and we will also do so in what follows.

[5] Let us make a note on units: in section 3.3, when discussing the thermal effective potentials, we gave the mass parameter a value characteristic for the electroweak phase transition, $m_{\rm R} = 100\,\text{GeV}$. Below we continue to use the same value as a benchmark, and we shall be measuring all dimensionful quantities in the GeV-units. In particular, we will be measuring time in units GeV^{-1}, while we will be suppressing time-units in all plots. However, in all examples that we will consider below, the physical mass $m_{\rm R}$ is the only mass scale in the problem. Thus, all results are in fact valid as such for an arbitrary mass value, if only one rescales all dimensionful parameters by a suitable power of $m_{\rm R}/\text{GeV}$.

JHEP12(2021)190

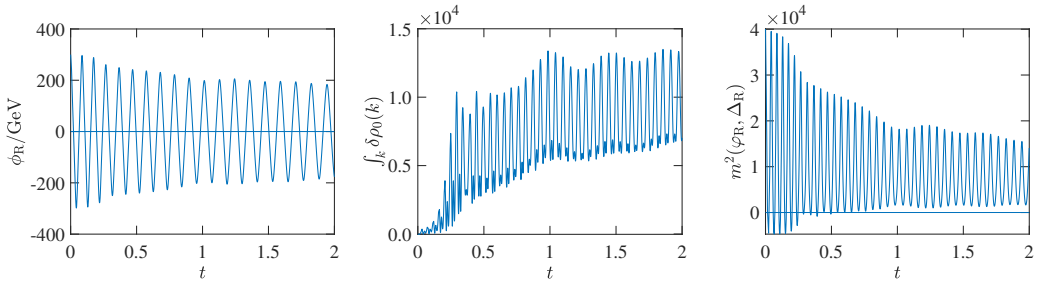

Figure 4. Shown is the evolution of the classical field as a function of time (left), evolution of the integrated non-equilibrium part of the local correlation function (middle), and the effective mass function $m^2(\varphi_{\rm R}, \Delta_{\rm R})$ (right). We used $\lambda_{\rm R}^{(4)} = 1$, $m_{\rm R} = 100\,\text{GeV}$, $\varphi_{\rm R,in} = 300\,\text{GeV}$ and $\partial_t \varphi_{\rm R,in} = 0$. The moment functions were initialized to the non-coherent vacuum values (4.8). We also assumed no friction, setting c_i to zero.

are unstable and can grow exponentially. This is the *spinodal* or *tachyonic* instability. One might then be tempted to associate the growth in fluctuations in the period $t \lesssim 0.25$ fully to the spinodal instability. If this was true, the excited modes should satisfy the condition (5.1), which here translates to $|\boldsymbol{k}| \lesssim 60\,\text{GeV}$. However, from figure 5 we see that this is not the case. The fast production of modes is clearly visible in the upper panels which show the integrated particle number (left) and the integrated modulus of the coherence functions (right). But from the lower panels, showing time-momentum heat plots of the same quantities, we see that the excited modes are concentrated on a frequency band which lies entirely above the spinodal region (5.1).

Parametric resonance. While our equations are highly non-linear and strongly self-coupled, it is apparent that the structures seen in the heat plots in figure 5 correspond to Mathieu instabilities associated with parametric resonance, familiar from the studies of inflationary reheating [4]. This problem was also studied using 2PI methods in reference [7], albeit with a different set of approximations and a different potential. If we identify the mass squared of the mode function in the Mathieu equation with our mass function $m^2(\varphi_{\rm R}, \Delta_{\rm R})$, and follow the analysis of section V in reference [4], we can (very roughly) estimate the Mathieu equation q-parameter in our case to be

$$q \sim 2\frac{\Delta m_{\rm eff}^2}{(2\pi\nu)^2} \approx 2, \tag{5.2}$$

where $\Delta m_{\rm eff}^2 \approx 2 \times 10^4\,\text{GeV}^2$ is the instantaneous amplitude and $\nu \approx 21\,\text{GeV}$ is the local frequency of oscillations of the effective mass term $m^2(\varphi_{\rm R}, \Delta_{\rm R})$, shown in figure 4. The value of the q-parameter, which remains roughly the same throughout the calculation, suggests an intermediate resonance between the narrow and broad regimes. Similarly, the expected position of the first resonance band is by and large estimated to be

$$|\boldsymbol{k}|_{\rm rb} \sim \frac{\pi\nu}{\sqrt[4]{2}} \approx 60\,\text{GeV}. \tag{5.3}$$

This result, and the expected width of the resonance [4] $\Delta|\boldsymbol{k}| \sim |\boldsymbol{k}|_{\rm rb} \approx 60\,\text{GeV}$ are in qualitative agreement with our results. In figure 5 we can even observe a second, much narrower

JHEP12(2021)190

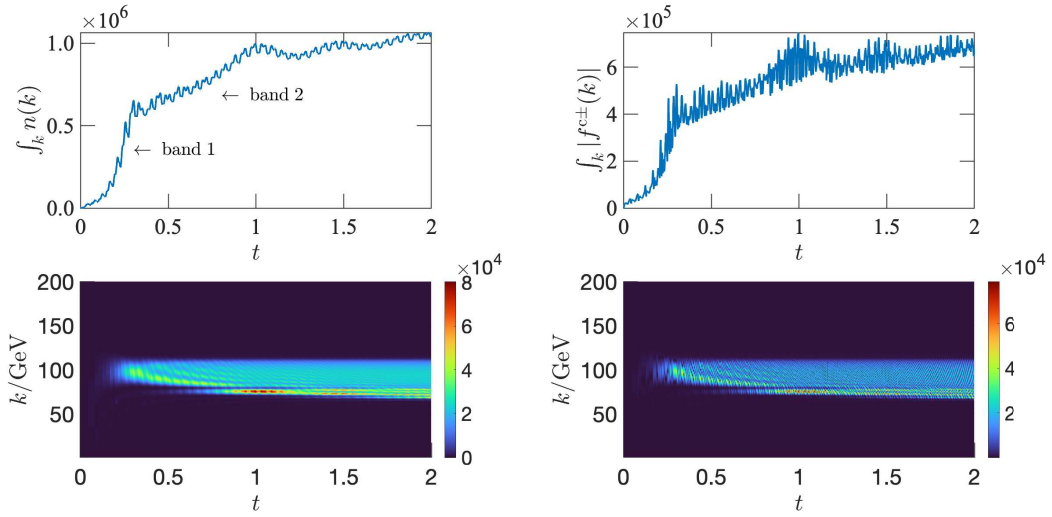

Figure 5. Shown is the evolution of the integrated number density (top left) and the absolute value of the integrated coherence function $\left|f_{\boldsymbol{k}}^{c\pm}\right|$ (top right), defined in equations (4.7), for the same parameters as in figure 4. The bottom row shows the heat plots in the momentum and time variables for the unintegrated distributions multiplied by the phase space factors: $\frac{\boldsymbol{k}^2}{2\pi^2} n_{\boldsymbol{k}}$ (lower left) and $\frac{\boldsymbol{k}^2}{2\pi^2}\left|f_{\boldsymbol{k}}^{c\pm}\right|$ (lower right).

band below the first one, which dominates the particle production at $t \approx 1$. While this is again in agreement with the qualitative expectations, its interpretation via Mathieu equation methods becomes even more tenuous. At late times $t \gtrsim 0.3$ the shape of the growth pattern fits well in the standard picture [4], but in the spinodal region the resonant production appears to be more efficient than usual: upon spinodal zero-crossings the resonant production that normally shows (as it indeed does at later times also in our example) a period of anti-correlation, is here always positively correlated. While individual growth bursts are not enhanced, this positive correlation leads to particularly strong particle production.

Because we did not include interactions in this run, the fluctuation band structure remains stable at all times. The system also remains highly coherent, as is evident both from the increase of the integrated coherence function and the stability of the heat plot of the coherence function shown in the right panels of figure 5.

5.2 Strong spinodal instability

In the above analysis we made little reference to the effective potential. Indeed, the one-particle irreducible effective action is not a very useful quantity in an out-of-equilibrium setting and it can even be defined only *after* the equations of motion have been solved. Even then one cannot define it universally, but only as a quantity evaluated locally in time. We will now study this question in the case of a very strong spinodal instability. To be specific, we still use the values $m_{\mathrm{R}} = 100\,\mathrm{GeV}$, $\lambda_{\mathrm{R}}^{(4)} = 1$ and $\partial_t \varphi_{\mathrm{R,in}} = 0$, but we take $\varphi_{\mathrm{R,in}} = 243.5\,\mathrm{GeV}$ and include also friction. We assume that collisions drive the system to the vacuum state, i.e. we take $\delta\rho_{n\boldsymbol{k}}^{\mathrm{eq}} \equiv 0$, and we specify the coefficients to be

JHEP12(2021)190

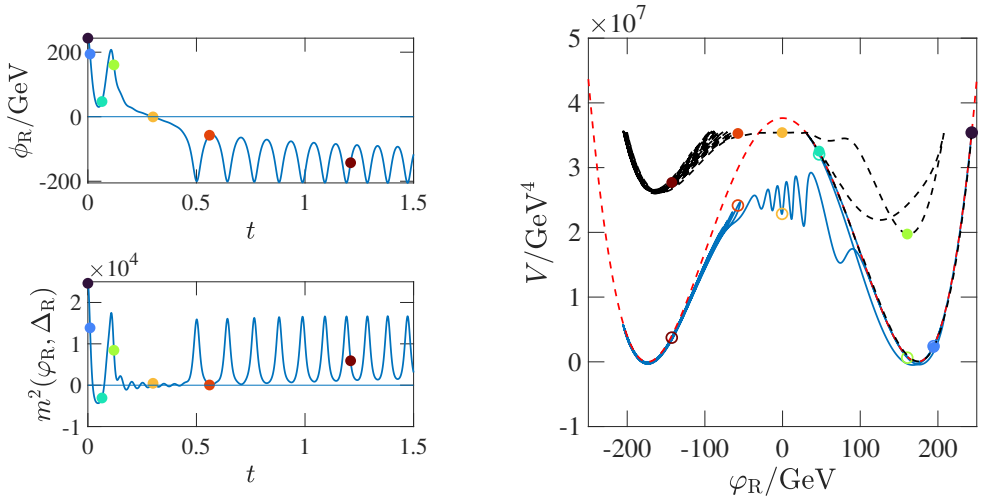

Figure 6. The upper left panel shows the time evolution of φ_R (in units GeV) and the lower left panel that of the effective mass function $m^2(\varphi_R, \Delta_R)$ (in units GeV^2) in the case of a strong spinodal instability. In the right panel we show the time-evolution of the instantaneous effective potential (5.4) (dashed black line), embedded in a plot of the vacuum Hartree potential (dashed red line). The colored dots indicate select times at which the instantaneous potential was evaluated as indicated in the left panels. The solid blue line shows the instantaneous value of the non-equilibrium vacuum potential (5.5).

$c_{1,2} = 0.6\,\text{GeV}$.[6] In this case the initial potential energy of the field is lower than the peak of the vacuum potential at $\varphi_R = 0$. This can be seen in the right panel of figure 6, where we plot the Hartree-resummed vacuum potential (red dashed line) and indicate the initial field value by the black dot.

Obviously, if the potential was held fixed, the field would simply oscillate around the positive minimum with a decaying amplitude. However, when backreaction is included, the picture changes dramatically. The actual field evolution is shown in the upper left panel of figure 6. Curiously, the field stays around the positive minimum during only one oscillation cycle, after which it apparently passes through the potential barrier, spending a rather long time near the middle of the potential with the effective mass function close to zero. Of course what happens is that in the first passage of the field into the spinodal region, an explosive creation of fluctuations takes place. This is clearly demonstrated in figure 7, which shows the integrated fluctuations in the moment functions (upper panels) and the associated heat plots in the time-momentum plane (lower panels). These fluctuations absorb a large amount of entropy, which decreases the *free energy* in the system and lowers the barrier between the minima allowing the field to pass to the negative side. The key issue is to not confuse the total internal energy of the system and the free energy, which may vary strongly depending on the entropy production.

[6] Although we gave the friction terms only in a qualitative form, we can provide an estimate for the magnitude of the c_i-coefficients. From equations (4.6) it is clear that c_i have the dimensions of mass. The lowest order contribution to the collision integrals arises at the second order in coupling in the 2PI expansion. Hence the naïve scale of the coefficients c_i is given by $\left(\frac{\lambda}{4\pi}\right)^2 m$, which for $\lambda_R^{(4)} = 1$ and $m_R = 100\,\text{GeV}$ gives $c_i \simeq 0.6\,\text{GeV}$.

JHEP12(2021)190

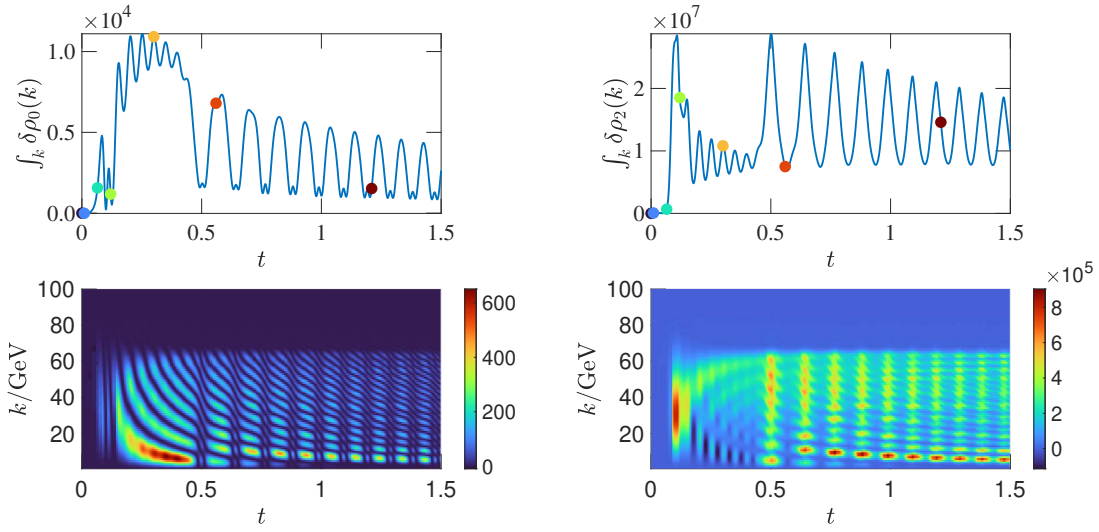

Figure 7. The upper panels: shown are the integrated non-equilibrium fluctuations of the moment functions, $\int_{\boldsymbol{k}} \delta\rho_{0,2\boldsymbol{k}}$. The colored dots have the same interpretation as in figure 6. The lower panels: heat plots showing the momentum distributions $\frac{1}{2\pi^2}\boldsymbol{k}^2\delta\rho_{n\boldsymbol{k}}$ corresponding to the upper panels. The left panels show the zeroth moment $n = 0$ and the right panels the second moment $n = 2$.

Non-equilibrium effective potentials. While the effective potential cannot be defined *a priori*, it is illustrative to construct it *a posteriori* as a time dependent potential that reproduces the equation of motion (4.4d) at all times. This potential can be constructed as the definite integral

$$V_{1\mathrm{PI}}(t;\varphi_{\mathrm{R}}) \equiv \int_{t_{\mathrm{in}}}^{t} \Big[-\frac{1}{3}\lambda_{\mathrm{R}}^{(2)}\varphi_{\mathrm{R}}^3 + m^2(\varphi_{\mathrm{R}},\Delta_{\mathrm{R}})\varphi_{\mathrm{R}}\Big](\partial_{\tilde{t}}\varphi_{\mathrm{R}})\mathrm{d}\tilde{t}, \tag{5.4}$$

where φ_{R} and Δ_{R} are the solutions of the equations of motion. We show this potential as the dashed black line in figure 6. After the crossing to the negative side, the shape of the potential function settles and the field oscillates around the negative minimum with a decaying amplitude. We stress that $V_{1\mathrm{PI}}$ is only useful for the visualization and interpretation of results and there is no unique definition of the effective potential in the non-equilibrium case.

As was already mentioned in section 3.3, in any finite truncation the renormalized 2PI vacuum becomes dependent on the IR-physics. Another interesting potential[7] function then is the equivalent of the vacuum Hartree potential in the presence of fluctuations. This potential is defined as

$$V_{\mathrm{H}\Delta}(\varphi_{\mathrm{R}},\Delta_{\mathrm{R}}) \equiv V_{\mathrm{H}}(\varphi_{\mathrm{R}},\Delta_{\mathrm{R}}) - \frac{1}{2}m^2(\varphi_{\mathrm{R}},\Delta_{\mathrm{R}})\int_{\boldsymbol{k}}\delta\rho_{0\boldsymbol{k}}, \tag{5.5}$$

where $V_{\mathrm{H}}(\varphi_{\mathrm{R}},\Delta_{\mathrm{R}})$ is the 2PI vacuum potential (3.29) evaluated replacing the vacuum mass function $\overline{m}^2(\varphi_{\mathrm{R}})$ with the general mass function $m^2(\varphi_{\mathrm{R}},\Delta_{\mathrm{R}})$. Note that the integral term

[7] In reference [16] yet another dynamical potential was defined as the difference between the total energy of the system and the kinetic energy of the classical field.

JHEP12(2021)190

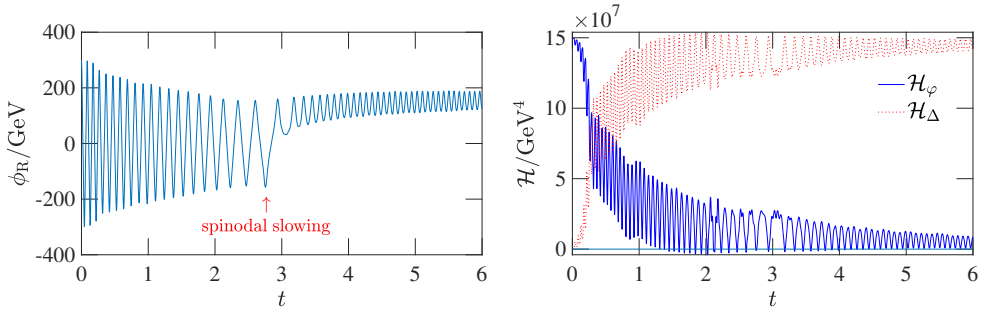

Figure 8. Shown is the time-evolution of the classical field (left panel) and that of the total energy in the fluctuations and the classical field (right panel). $\mathcal{H}_\varphi(t)$ is the energy in the classical field and $\mathcal{H}_\Delta(t)$ is the energy in the fluctuations. The physical parameters and the specific form of the collision integrals used in this run are described in the text.

over the fluctuations of the zeroth moment is a part of the vacuum Hartree potential, similarly to the case with the thermal potential (3.37). The potential (5.5) is shown with the blue solid line in the right panel of figure 6. It represents changes in the 2PI Hartree vacuum energy including the backreaction effects, and like the instantaneous $V_{1\mathrm{PI}}$-potential, its barrier around $\varphi_\mathrm{R} = 0$ is temporarily lowered by the backreaction. This example demonstrates that the final stages of a phase transition may involve very complicated quantum dynamics, where classical expectations and constraints do not hold.

We conclude this subsection by stressing on the difference of the fluctuation spectra in the present case, shown in the lower panels of figure 7, and in the parametric resonance case shown in figure 5. Even though we used the same mass and coupling parameters, essentially all fluctuations are here created by the spinodal instability. Indeed, they occupy a region in the phase space which is consistent with the instability constraint (5.1), continues all the way to zero momentum and lies entirely below the parametric resonance band.

5.3 Self-thermalization

As our final example we study thermalization of the scalar field energy in a self-interacting system. We use the same physical parameters and initial conditions as in section 5.1 but include collision terms with the friction coefficients $c_{0,1} = 0.6\,\mathrm{GeV}$, and assume that the collisions drive the system to thermal equilibrium, i.e. we take $\delta\rho^{\mathrm{eq}}_{n\boldsymbol{k}} \equiv \delta\rho^{\mathrm{th}}_{n\boldsymbol{k}}$. With rigorously computed collision terms the thermal state would emerge automatically as an attractor solution, but in our phenomenological approach we need to give a definition for the instantaneous temperature. In thermal equilibrium a general moment can be written as

$$\rho^{\mathrm{th}}_{n\boldsymbol{k}} = \frac{1}{2}\,\omega_{\boldsymbol{k}}^{n-1}\Big[n_{\mathrm{BE}}(\omega_{\boldsymbol{k}}) + (-1)^n\big(1 + n_{\mathrm{BE}}(\omega_{\boldsymbol{k}})\big)\Big], \tag{5.6}$$

where $n_{\mathrm{BE}}(k_0) = (\mathrm{e}^{k_0/T} - 1)^{-1}$ is the Bose-Einstein distribution function. In particular

$$\delta\rho^{\mathrm{th}}_{0\boldsymbol{k}} = \frac{1}{\omega_{\boldsymbol{k}}} n_{\mathrm{BE}}(\omega_{\boldsymbol{k}}) \quad \text{and} \quad \delta\rho^{\mathrm{th}}_{2\boldsymbol{k}} = \omega_{\boldsymbol{k}} n_{\mathrm{BE}}(\omega_{\boldsymbol{k}}). \tag{5.7}$$

JHEP12(2021)190

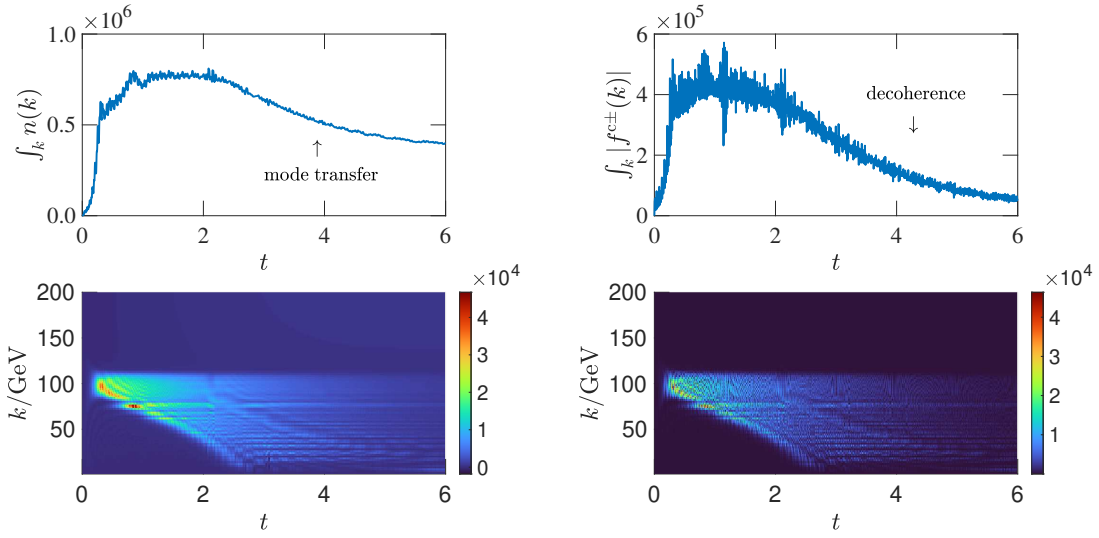

Figure 9. Shown are the evolution of the number density (left) and the modulus of the coherence functions (right). In the upper panels the quantities are integrated over momentum. We used the same parameters as in figure 5, except for non-zero friction coefficients $c_i = 0.6\,\mathrm{GeV}$ in the collision integrals with thermal equilibrium solutions.

while $\delta\rho^{\mathrm{th}}_{1\boldsymbol{k}} = 0$. We define the equivalent temperature $T = T(t)$ by requiring that the thermal state has the same energy as what is stored in the fluctuations:

$$\mathcal{H}_\Delta(t) \equiv \int_{\boldsymbol{k}} \delta\rho_{2\boldsymbol{k}}(t) \equiv \int_{\boldsymbol{k}} \omega_{\boldsymbol{k}} n_{\mathrm{BE}}(\omega_{\boldsymbol{k}}). \tag{5.8}$$

In all these equations $\omega^2_{\boldsymbol{k}} = \boldsymbol{k}^2 + m^2(\varphi_{\mathrm{R}}, \Delta_{\mathrm{R}})$ is a function of time. The energy stored in the classical field is

$$\mathcal{H}_\varphi(t) \equiv \frac{1}{2}\big(\partial_t\varphi_{\mathrm{R}}(t)\big)^2 + V_{\mathrm{H}\Delta}(\varphi_{\mathrm{R}}(t), \Delta_{\mathrm{R}}(t)). \tag{5.9}$$

With our definitions of the temperature and the collision integrals the total energy $\mathcal{H} = \mathcal{H}_\varphi + \mathcal{H}_\Delta$ should be conserved, and we checked that this is indeed the case to a high accuracy in our calculations. For more details on this, and on the numerical setup in general, see appendix A.

Spinodal slowing. In the left panel of figure 8 we show the evolution of the classical field φ_{R}. Initially φ_{R} evolves as in the collisionless case, oscillating with a nearly constant frequency and a large amplitude, but around $t \sim 2$ the frequency starts to decrease until it reaches a minimum around $t \sim 3$. After this the field gets trapped around the positive minimum while the oscillation frequency increases again. This *spinodal slowing* effect was already seen in connection with the barrier crossing in section 5.2. The bearing of the spinodal modes is revealed in the inset in the left panel of figure 11, which shows that the effective mass term $m^2(\varphi_{\mathrm{R}}, \Delta_{\mathrm{R}})$ repeatedly becomes negative in this region. In the right panel of figure 8 we show the energy components $\mathcal{H}_\varphi$ and $\mathcal{H}_\Delta$. Initially all energy is stored in the classical field, but the fraction of energy in the fluctuations increases until the system is *reheated*, with almost all of the energy contained in the fluctuations.

JHEP12(2021)190

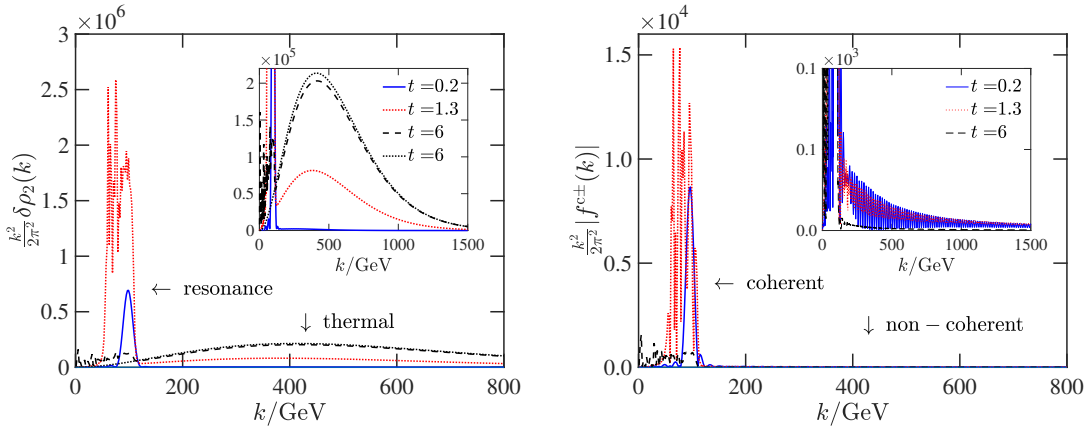

Figure 10. Shown are the momentum distributions $\frac{\boldsymbol{k}^2}{2\pi^2}\delta\rho_{2\boldsymbol{k}}$ (left) and $\frac{\boldsymbol{k}^2}{2\pi^2}\left|f^{c\pm}_{\boldsymbol{k}}\right|$ (right) for three different times: $t = 0.2$ (solid blue lines) $t = 1.3$ (red dotted lines) and $t = 6$ (black dashed lines). Also shown in the left plot is the weighted thermal distribution $\frac{\boldsymbol{k}^2}{2\pi^2}\omega_{\boldsymbol{k}} n_{\rm BE}(\omega_{\boldsymbol{k}})$ for the equivalent temperature $T(t = 6) = 144.9\,\text{GeV}$ (black dotted line).

Mode transfer and decoherence. In figure 9 we again show the evolution of the number density and coherence functions, including both the integrated quantities and the time-momentum heat plots. There are striking, but expected differences between these plots and the corresponding non-interacting results shown in figure 5. First, the number density stops growing already at $t \sim 1$ and eventually starts to decrease for $t \gtrsim 2$. As is seen from figure 8, fluctuations dominate the total energy already for $t \gtrsim 1$, and the subsequent decrease of particle number results from a transfer of modes to higher energies. Thermalization process should also lead to decoherence, and this is indeed clearly visible in the upper right panel of figure 9, which shows the integrated function $\left|f^{c\pm}_{\boldsymbol{k}}\right|$. From the heat plots we see that particle production gets progressively less efficient and moves to smaller frequencies, as less and less energy is left in the classical field. From the heat plot in the lower right panel we see that coherence is erased throughout the phase space at late times.

Thermalization. In figure 10 we show the $|\boldsymbol{k}|$-distributions of $\delta\rho_{2\boldsymbol{k}}$ (left panel) and the coherence function $\left|f^{c\pm}_{\boldsymbol{k}}\right|$ (right panel) weighted by the phase space factor, for selected times during the evolution. At a relatively early time $t = 0.2$ the distributions shown in solid blue still display a clear parametric resonance band structure. At a later time $t = 1.3$ (red dotted lines) the resonant spectrum is already much more complex, apparently with contributions from many narrow bands. Also a significant mode-transfer to the thermal region has already taken place. Indeed, from the main plot in the left panel of figure 11 we see that the equivalent temperature at $t = 1.3$ is roughly 140 GeV, and as the field is relatively light, $\langle m^2_{\rm eff}\rangle^{1/2}/T \lesssim 1$ with $\langle m^2_{\rm eff}\rangle$ being the local average of the oscillating effective mass function, the expected maximum of the thermal spectrum is located at $\langle|\boldsymbol{k}|\rangle \approx 3T \approx 400\,\text{GeV}$. At the end of the simulation, $t = 6$ (black dashed curve), the system has essentially thermalized. Almost all energy is in the fluctuations and very little particle production activity remains. The particle number in the resonance bands is small and the coherence is almost vanishing everywhere and in particular in the thermal region.

JHEP12(2021)190

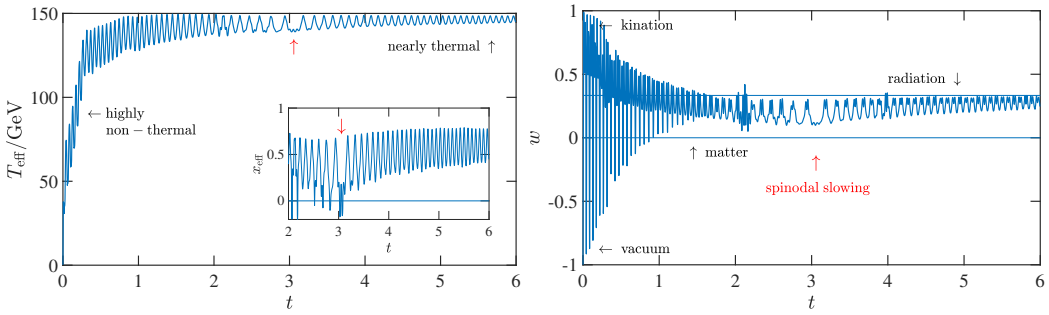

Figure 11. In the left panel we show the equivalent temperature defined through equation (5.8) as a function of time. The inset shows the parameter $x_{\rm eff} \equiv \mathrm{sgn}\big(m^2_{\rm eff}\big)\big|m^2_{\rm eff}\big|^{1/2}/T$. In the right panel we show the EOS-parameter of the system defined in equation (5.10). The black arrows indicate the limiting cases of vacuum ($w = -1$) and kinetic ($w = 1$) energy dominance as well as matter ($w = 0$) and radiation ($w = 1/3$) EOS's, shown by horizontal lines. In all graphs shown the red arrow points the region of maximal spinodal slowing.

Also the fluctuations in the equivalent temperature have but a small residual amplitude left. For the final time we also plotted (black dotted line in the left panel of figure 10) the equivalent thermal spectrum $\frac{\boldsymbol{k}^2}{2\pi^2}\omega_{\boldsymbol{k}} n_{\rm BE}(\omega_{\boldsymbol{k}})$ with $T = 144.9\,\mathrm{GeV}$, corresponding to the equivalent temperature at $t = 6$. The close agreement between the actual and thermal distributions shows that the system has indeed thermalized to a very high accuracy.

Equation of state. Let us finally study the evolution of the equation of state (EOS) in the system. The EOS-parameter is defined as

$$w \equiv \frac{\mathcal{P}}{\mathcal{H}}, \tag{5.10}$$

where $\mathcal{H} = \mathcal{H}_\varphi + \mathcal{H}_\Delta$ is the total energy and the total pressure $\mathcal{P} = \mathcal{P}_\varphi + \mathcal{P}_\Delta$ is similarly the sum of the pressures in the classical field and in the fluctuations. The former is given by

$$\mathcal{P}_\varphi = \frac{1}{2}(\partial_t \varphi_{\rm R})^2 - V_{\rm H\Delta}(\varphi_{\rm R}, \Delta_{\rm R}), \tag{5.11}$$

where $V_{\rm H\Delta}$ was defined in (5.5). The pressure contained in the fluctuations can be computed as the spatial component of the energy-momentum tensor [27], and it can be written in terms of the moment functions as follows:

$$\mathcal{P}_\Delta(\varphi_{\rm R}, \Delta_{\rm R}) = \int_{\boldsymbol{k}} \left[\delta\rho_{2\boldsymbol{k}}(t) + \left(\frac{1}{3}\boldsymbol{k}^2 - \omega^2_{\boldsymbol{k}} \right) \delta\rho_{0\boldsymbol{k}}(t) \right]. \tag{5.12}$$

It is easy to see that in the thermal limit (5.12) reduces to the negative of the thermal part of the effective potential in the Hartree approximation: $\mathcal{P}_\Delta = -T^4 \mathcal{J}(\overline{m}^2_T/T^2)$.

We plot the EOS-parameter w in the right panel of figure 11. The EOS-parameter starts from $w = -1$ and initially oscillates between $w = -1$, corresponding to total vacuum energy dominance, and $w = 1$, corresponding to kinetic energy dominance (kination) in the classical field sector. However, as the energy is moved out from the field and the system thermalizes, the EOS-parameter moves to the band $0 < w < 1/3$ corresponding to normal matter. From the inset of the left panel we see that the average value

JHEP12(2021)190

$\langle |x_{\rm eff}| \rangle = \langle |m^2_{\rm eff}|^{1/2}/T \rangle \approx 0.6$ at late times. This indicates that the reheated thermal plasma is almost relativistic and indeed, the EOS-parameter is asymptoting close to $w = 1/3$ at late times. (In a purely thermal plasma with $x_{\rm eff} = 0.6$ one would get $w \approx 0.315$.) The periodic deviation below this value seen in figure 11 is due to the field contributions to energy and pressure.

6 Conclusions

We have studied the non-equilibrium evolution of a system consisting of a classical scalar field coupled to the two-point function describing quantum fluctuations. We derived renormalized evolution equations for the system using 2PI methods in the Hartree approximation. We derived the effective potential for this system in vacuum and in thermal equilibrium and compared the latter with the known one-loop-resummed effective potentials. We showed that the Parwani-resummed thermal potential [33] is closest in spirit to the Hartree-resummed effective potential. We showed that in a non-equilibrium situation the 2PI method, in any finite truncation, leads to an effective vacuum potential (the vacuum state) that depends on the infrared physics. Indeed, even though the renormalization procedure provides unique and constant counterterms, the split of the system into divergent and non-divergent parts depends on the IR-physics.

We wrote our renormalized evolution equations as a set of coupled moment-equations for the correlation function and a field equation for the one-point function in the mixed representation and included phenomenological collision integrals describing friction. We used this system to study the non-perturbative particle production and spinodal instability at the end of phase transitions. We found out that quantum backreaction can have significant effects on the evolution of the system and addressed the problems in trying to define any practical effective potential for such dynamical systems. In particular we were able to follow the full thermal history of a self-interacting system starting from a cold initial state where all energy in the system was stored in the classical potential, until the end when the system was reheated and thermalized and the field stayed at the minimum of the thermal (Hartree) effective potential.

In this work we assumed that the quantum system lived in the Minkowski space-time. Generalization to an expanding FRLW space-time is straightforward by a simple transform to conformal coordinates [40]. Moreover, in many realistic systems the time scales involved in the phase transition are much faster than the Hubble expansion. In those cases our results are representative of the physics as such. Also, we used only a phenomenological form for the collision integrals. It would be interesting to derive more realistic collision terms using the methods developed in [28, 39]. Also it would be interesting to couple the scalar field also to other quantum fields. This should be straightforward by combining the current results with the quantum transport equations for fermions developed in [41]. In this way one should be able to study reheating at the end of inflation in a realistic setup.

JHEP12(2021)190

Acknowledgments

This work was supported by the Academy of Finland grant 318319. OK was in addition supported by a grant from the Magnus Ehrnrooth Foundation. We wish to thank Alexandre Alvarez, Amitayus Banik, Haye Hinrichsen, Sami Nurmi, Werner Porod and Anna Tokareva for discussions and comments on the manuscript.

A Numerical implementation

In this appendix we discuss some technical points that are relevant for an accurate and efficient solution of the evolution equations. The first one concerns identifying a conserved quantity in the non-interacting limit. The equations rewritten using this variable are much more stable than the original equations. The second point concerns discretization. In a naïve binning of the momentum variable, the discrete integral of the vacuum term in equation (4.5) is badly behaved numerically near the edges of the spinodal regions. This problem can be avoided by a more careful definition of the binned variables. Finally, we show how our numerical setup conserves the total energy of the solved system to a high accuracy with the self-thermalizing system as a case study.

Stabilized equations. It was noted already in reference [27] that the moment equations (4.4a), (4.4b) and (4.4c) can be written in a form that is more resistant to numerical instabilities, using the variable

$$X_{\boldsymbol{k}} \equiv 2\rho_{0\boldsymbol{k}}\rho_{2\boldsymbol{k}} - \omega_{\boldsymbol{k}}^2(t)\rho_{0\boldsymbol{k}}^2 - \frac{1}{4}(\partial_t\rho_{0\boldsymbol{k}})^2. \tag{A.1}$$

Indeed, if we multiply (4.4a) by $2\partial_t\rho_{0\boldsymbol{k}}$ and (4.4c) by $2\rho_{0\boldsymbol{k}}$ and subtract the resulting equations, we can show that $X_{\boldsymbol{k}}$ is conserved in the collisionless limit: $\partial_t X_{\boldsymbol{k}} = 0$. With non-vanishing friction terms $X_{\boldsymbol{k}}$ is no longer conserved, but the derivation with equations (4.6) including friction proceeds analogously, and one finds:

$$\frac{1}{4}\partial_t^2\rho_{0\boldsymbol{k}} - \rho_{2\boldsymbol{k}} + \omega_{\boldsymbol{k}}^2(t)\rho_{0\boldsymbol{k}} = -c_1\partial_t\rho_{0\boldsymbol{k}}, \tag{A.2a}$$

$$\partial_t\rho_{1\boldsymbol{k}} = -c_2(\delta\rho_{1\boldsymbol{k}} - \delta\rho_{1\boldsymbol{k}}^{\mathrm{eq}}), \tag{A.2b}$$

$$\partial_t X_{\boldsymbol{k}} = 2c_1(\partial_t\rho_{0\boldsymbol{k}})^2 - 2c_2\rho_{0\boldsymbol{k}}(\delta\rho_{2\boldsymbol{k}} - \delta\rho_{2\boldsymbol{k}}^{\mathrm{eq}}). \tag{A.2c}$$

We have thus replaced $\rho_{2\boldsymbol{k}}$ by $X_{\boldsymbol{k}}$ as a dynamical variable. We will use (A.1) to set the initial condition for $X_{\boldsymbol{k}}$ in terms of the initial values for $\rho_{0\boldsymbol{k}}$, $\partial_t\rho_{0\boldsymbol{k}}$ and $\rho_{2\boldsymbol{k}}$, and at any point during and at the end of the calculation we can compute $\rho_{2\boldsymbol{k}}$ from $X_{\boldsymbol{k}}$ using the inverse relation

$$\rho_{2\boldsymbol{k}} = \frac{1}{2\rho_{0\boldsymbol{k}}}\left[X_{\boldsymbol{k}} + \frac{1}{4}(\partial_t\rho_{0\boldsymbol{k}})^2 + \omega_{\boldsymbol{k}}^2(t)\rho_{0\boldsymbol{k}}^2\right]. \tag{A.3}$$

Coarse-grained binning. Whenever the effective mass term is negative there is a momentum for which $m^2(\varphi_{\mathrm{R}}, \Delta_{\mathrm{R}}) = -\boldsymbol{k}^2$ and at this point the zeroth momentum vacuum function $\rho_{0\boldsymbol{k}}^{\mathrm{vac}} = \Theta_{\boldsymbol{k}}/(2\omega_{\boldsymbol{k}})$ diverges. This is a mild, integrable singularity that does not

JHEP12(2021)190

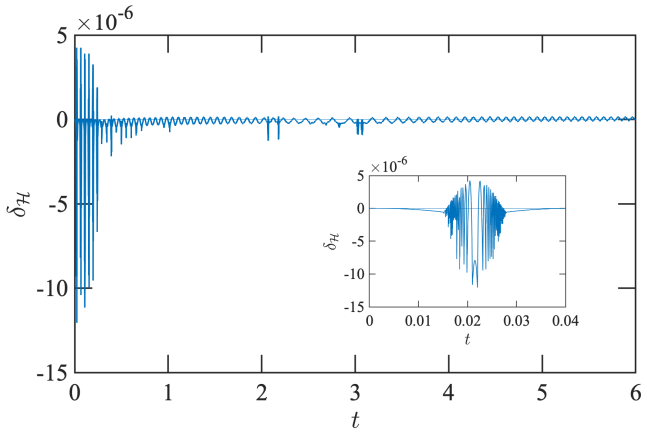

Figure 12. Shown is the relative change in energy $\delta_{\mathcal{H}} = \mathcal{H}/\mathcal{H}_0 - 1$ during calculation in the self-thermalization case studied in section 5.3. Inset shows a close-up on the first spinodal instability region.

affect the continuum limit, but it can cause overflows and numerical inaccuracy in a system with a finite discretization. This problem can be avoided by a careful choice of binned variables for the vacuum distribution. That is, we replace the vacuum distribution by a coarse-grained distribution defined by an integration over each momentum bin $q \in [q_i, q_{i+1}]$:

$$\frac{1}{2\omega_{q_{ci}}} \to \frac{1}{2q_{ci}^2 \Delta q_i}\big[i_0(q_{i+1}) - i_0(q_i)\big], \tag{A.4}$$

where $q_{ci} \equiv \frac{1}{2}(q_i + q_{i+1})$, $\Delta q_i \equiv q_{i+1} - q_i$ and

$$i_0(q) \equiv \frac{1}{2}\left[q\omega_q - m^2 \mathrm{artanh}\left(\frac{q}{\omega_q}\right)\right]. \tag{A.5}$$

When the bin width goes to zero, the replacement (A.4) does not make any difference. However, for a finite discretization it avoids the singularity that would occur in the spinodal region when the effective mass function coincides with one of the bin-momenta squared, $m^2(\varphi_{\mathrm{R}}, \Delta_{\mathrm{R}}) = -q_{ci}^2$.

Energy conservation. In figure 12 we show the relative change in the total energy $\delta_{\mathcal{H}} \equiv \mathcal{H}/\mathcal{H}_0 - 1$ in the example we studied in section 5.3. The total energy is $\mathcal{H} = \mathcal{H}_\varphi + \mathcal{H}_\Delta$, where partial energies in the fluctuations $\mathcal{H}_\Delta$ and in the classical field $\mathcal{H}_\varphi$ were defined in equations (5.8) and (5.9). In this example the total energy should be conserved, and this is indeed true to a very high accuracy. In this run we used a discretized momentum $|\boldsymbol{k}| \in [0, 2000]$ GeV with 1000 grid points. As can be seen in the figure, the error is essentially negligible between the spinodal regions. Within the spinodal regions there is some residual noise at early times. This arises from the integrable singularity near $m^2(\varphi_{\mathrm{R}}, \Delta_{\mathrm{R}}) = 0$, even with the coarse grained binning, but even this error is small and can be further reduced by reducing the bin width. We conclude that numerical errors are well under control in our calculations.

JHEP12(2021)190

References

[1] J.H. Traschen and R.H. Brandenberger, *Particle production during out-of-equilibrium phase transitions*, *Phys. Rev. D* **42** (1990) 2491 [INSPIRE].

[2] M.A. Amin, M.P. Hertzberg, D.I. Kaiser and J. Karouby, *Nonperturbative dynamics of reheating after inflation: a review*, *Int. J. Mod. Phys. D* **24** (2014) 1530003 [arXiv:1410.3808] [INSPIRE].

[3] L. Kofman, A.D. Linde and A.A. Starobinsky, *Reheating after inflation*, *Phys. Rev. Lett.* **73** (1994) 3195 [hep-th/9405187] [INSPIRE].

[4] L. Kofman, A.D. Linde and A.A. Starobinsky, *Towards the theory of reheating after inflation*, *Phys. Rev. D* **56** (1997) 3258 [hep-ph/9704452] [INSPIRE].

[5] P.B. Greene, L. Kofman, A.D. Linde and A.A. Starobinsky, *Structure of resonance in preheating after inflation*, *Phys. Rev. D* **56** (1997) 6175 [hep-ph/9705347] [INSPIRE].

[6] J. Braden, L. Kofman and N. Barnaby, *Reheating the universe after multi-field inflation*, *JCAP* **07** (2010) 016 [arXiv:1005.2196] [INSPIRE].

[7] J. Berges and J. Serreau, *Parametric resonance in quantum field theory*, *Phys. Rev. Lett.* **91** (2003) 111601 [hep-ph/0208070] [INSPIRE].

[8] E. Calzetta, *Spinodal decomposition in quantum field theory*, *Annals Phys.* **190** (1989) 32 [INSPIRE].

[9] A.H. Guth and S.-Y. Pi, *The quantum mechanics of the scalar field in the new inflationary universe*, *Phys. Rev. D* **32** (1985) 1899 [INSPIRE].

[10] E.J. Weinberg and A.-Q. Wu, *Understanding complex perturbative effective potentials*, *Phys. Rev. D* **36** (1987) 2474 [INSPIRE].

[11] J.F. Dufaux, G.N. Felder, L. Kofman, M. Peloso and D. Podolsky, *Preheating with trilinear interactions: tachyonic resonance*, *JCAP* **07** (2006) 006 [hep-ph/0602144] [INSPIRE].

[12] M. Fairbairn, K. Kainulainen, T. Markkanen and S. Nurmi, *Despicable dark relics: generated by gravity with unconstrained masses*, *JCAP* **04** (2019) 005 [arXiv:1808.08236] [INSPIRE].

[13] T. Markkanen and S. Nurmi, *Dark matter from gravitational particle production at reheating*, *JCAP* **02** (2017) 008 [arXiv:1512.07288] [INSPIRE].

[14] D. Boyanovsky and H.J. de Vega, *Quantum rolling down out-of-equilibrium*, *Phys. Rev. D* **47** (1993) 2343 [hep-th/9211044] [INSPIRE].

[15] D. Boyanovsky, D.-S. Lee and A. Singh, *Phase transitions out-of-equilibrium: domain formation and growth*, *Phys. Rev. D* **48** (1993) 800 [hep-th/9212083] [INSPIRE].

[16] J. Baacke and S. Michalski, *Nonequilibrium evolution in scalar $O(n)$ models with spontaneous symmetry breaking*, *Phys. Rev. D* **65** (2002) 065019 [hep-ph/0109137] [INSPIRE].

[17] A. Arrizabalaga, J. Smit and A. Tranberg, *Tachyonic preheating using $2PI - 1/N$ dynamics and the classical approximation*, *JHEP* **10** (2004) 017 [hep-ph/0409177] [INSPIRE].

JHEP12(2021)190

[18] A. Arrizabalaga, J. Smit and A. Tranberg, *Equilibration in ϕ^4 theory in $3+1$ dimensions*, *Phys. Rev. D* **72** (2005) 025014 [hep-ph/0503287] [INSPIRE].

[19] J. Berges, S. Borsányi, U. Reinosa and J. Serreau, *Nonperturbative renormalization for 2PI effective action techniques*, *Annals Phys.* **320** (2005) 344 [hep-ph/0503240] [INSPIRE].

[20] H. van Hees and J. Knoll, *Renormalization in selfconsistent approximations schemes at finite temperature. 1. Theory*, *Phys. Rev. D* **65** (2002) 025010 [hep-ph/0107200] [INSPIRE].

[21] H. Van Hees and J. Knoll, *Renormalization of selfconsistent approximation schemes. 2. Applications to the sunset diagram*, *Phys. Rev. D* **65** (2002) 105005 [hep-ph/0111193] [INSPIRE].

[22] U. Reinosa and Z. Szép, *Broken phase scalar effective potential and Φ-derivable approximations*, *Phys. Rev. D* **83** (2011) 125026 [arXiv:1103.2689] [INSPIRE].

[23] G. Fejos, A. Patkos and Z. Szep, *Renormalisability of the 2PI-Hartree approximation of multicomponent scalar models in the broken symmetry phase*, *Nucl. Phys. A* **803** (2008) 115 [arXiv:0711.2933] [INSPIRE].

[24] T. Arai, *Renormalization of the 2PI Hartree-Fock approximation on de Sitter background in the broken phase*, *Phys. Rev. D* **86** (2012) 104064 [arXiv:1204.0476] [INSPIRE].

[25] A. Pilaftsis and D. Teresi, *Symmetry improved CJT effective action*, *Nucl. Phys. B* **874** (2013) 594 [arXiv:1305.3221] [INSPIRE].

[26] A. Pilaftsis and D. Teresi, *Exact RG invariance and symmetry improved 2PI effective potential*, *Nucl. Phys. B* **920** (2017) 298 [arXiv:1703.02079] [INSPIRE].

[27] M. Herranen, K. Kainulainen and P.M. Rahkila, *Kinetic theory for scalar fields with nonlocal quantum coherence*, *JHEP* **05** (2009) 119 [arXiv:0812.4029] [INSPIRE].

[28] M. Herranen, K. Kainulainen and P.M. Rahkila, *Coherent quantum Boltzmann equations from cQPA*, *JHEP* **12** (2010) 072 [arXiv:1006.1929] [INSPIRE].

[29] J.M. Cornwall, R. Jackiw and E. Tomboulis, *Effective action for composite operators*, *Phys. Rev. D* **10** (1974) 2428 [INSPIRE].

[30] J. Berges, *Introduction to nonequilibrium quantum field theory*, *AIP Conf. Proc.* **739** (2004) 3 [hep-ph/0409233] [INSPIRE].

[31] L.V. Keldysh, *Diagram technique for nonequilibrium processes*, *Zh. Eksp. Teor. Fiz.* **47** (1964) 1515 [*Sov. Phys. JETP* **20** (1965) 1018] [INSPIRE].

[32] G. Amelino-Camelia and S.-Y. Pi, *Selfconsistent improvement of the finite temperature effective potential*, *Phys. Rev. D* **47** (1993) 2356 [hep-ph/9211211] [INSPIRE].

[33] R.R. Parwani, *Resummation in a hot scalar field theory*, *Phys. Rev. D* **45** (1992) 4695 [*Erratum ibid.* **48** (1993) 5965] [hep-ph/9204216] [INSPIRE].

[34] M.E. Carrington, *The effective potential at finite temperature in the Standard Model*, *Phys. Rev. D* **45** (1992) 2933 [INSPIRE].

[35] P.B. Arnold and O. Espinosa, *The effective potential and first order phase transitions: beyond leading-order*, *Phys. Rev. D* **47** (1993) 3546 [*Erratum ibid.* **50** (1994) 6662] [hep-ph/9212235] [INSPIRE].

[36] K. Kainulainen, V. Keus, L. Niemi, K. Rummukainen, T.V.I. Tenkanen and V. Vaskonen, *On the validity of perturbative studies of the electroweak phase transition in the two Higgs doublet model*, *JHEP* **06** (2019) 075 [arXiv:1904.01329] [INSPIRE].

JHEP12(2021)190

[37] G. Aarts, D. Ahrensmeier, R. Baier, J. Berges and J. Serreau, *Far from equilibrium dynamics with broken symmetries from the $2PI - 1/N$ expansion*, *Phys. Rev. D* **66** (2002) 045008 [hep-ph/0201308] [INSPIRE].

[38] P. Millington and A. Pilaftsis, *Perturbative nonequilibrium thermal field theory*, *Phys. Rev. D* **88** (2013) 085009 [arXiv:1211.3152] [INSPIRE].

[39] C. Fidler, M. Herranen, K. Kainulainen and P.M. Rahkila, *Flavoured quantum Boltzmann equations from cQPA*, *JHEP* **02** (2012) 065 [arXiv:1108.2309] [INSPIRE].

[40] H. Jukkala, K. Kainulainen and P.M. Rahkila, *Flavour mixing transport theory and resonant leptogenesis*, *JHEP* **09** (2021) 119 [arXiv:2104.03998] [INSPIRE].

[41] H. Jukkala, K. Kainulainen and O. Koskivaara, *Quantum transport and the phase space structure of the Wightman functions*, *JHEP* **01** (2020) 012 [arXiv:1910.10979] [INSPIRE].

JHEP12(2021)190

PIII

TACHYONIC PRODUCTION OF DARK RELICS: A NON-PERTURBATIVE QUANTUM STUDY

by

Kimmo Kainulainen, Olli Koskivaara and Sami Nurmi (2023)

Journal of High Energy Physics, **04** 043

Published for SISSA by Springer

Received: October 13, 2022
Revised: February 20, 2023
Accepted: March 22, 2023
Published: April 11, 2023

Tachyonic production of dark relics: a non-perturbative quantum study

Kimmo Kainulainen, Olli Koskivaara and Sami Nurmi

Department of Physics, PL 35 (YFL), 40014 University of Jyväskylä, Jyväskylä, Finland
Helsinki Institute of Physics, PL 64, 00014 University of Helsinki, Helsinki, Finland

E-mail: kimmo.kainulainen@jyu.fi, olli.a.koskivaara@student.jyu.fi, sami.t.nurmi@jyu.fi

Abstract: We study production of dark relics during reheating after the end of inflation in a system consisting of a non-minimally coupled spectator scalar field and the inflaton. We derive a set of renormalized quantum transport equations for the one-point function and the two-point function of the spectator field and solve them numerically. We find that our system can embody both tachyonic and parametric instabilities. The former is an expected result due to the non-minimal coupling, but the latter displays new features driven by a novel interplay of the two-point function with the Ricci scalar. We find that when the parametric instability driven by the two-point function takes place, it dominates the total particle production. The quantitative results are also found to be highly sensitive to the model parameters.

Keywords: Early Universe Particle Physics, Non-Equilibrium Field Theory, Models for Dark Matter, Nonperturbative Effects

ArXiv ePrint: 2209.10945

https://doi.org/10.1007/JHEP04(2023)043

JHEP04(2023)043

Contents

JHEP04(2023)043

1 Introduction

Classical scalar fields coupled to out-of-equilibrium quantum matter play an important role in various settings in cosmology. Some key examples include non-perturbative particle production processes during the reheating after inflation, via a parametric resonance [1–5] or via spinodal instability [6–14], as well as the processes leading to the electroweak baryogenesis [15–22] and the leptogenesis mechanism [23–32]. Finding a complete solution of such problems often requires non-perturbative methods and non-equilibrium quantum field theory. In particular in the case of resonant particle production the backreaction of the newly created quanta may have significant effects on the evolution of the coupled system [33–38].

In this work we study tachyonic dark matter production during the reheating epoch in a setup proposed in [13, 14]. Non-minimally coupled scalar fields may undergo a tachyonic instability, or spinodal decomposition, when an effective mass term $\xi R\chi^2$ periodically takes negative values, driven by the oscillating Ricci scalar R during reheating. In [13] it was shown that for stable scalar fields with sufficiently weak couplings to visible matter the tachyonic particle production induced by the curvature coupling produces adiabatic dark matter, whose abundance can be made to agree with the observed value over a wide range of coupling values. The results of [13] and later in [14] are based on perturbative studies of the particle production similar to those applied to the so called tachyonic reheating in [9–11]. In [39], the dynamics of non-minimally coupled scalars were studied using classical lattice simulations. Here we revisit the tachyonic dark matter production of [14] applying a fully non-perturbative 2PI-approach using methods introduced in [38] (for earlier work see [40–44]).

The 2PI-framework is a powerful tool for studying dynamical non-equilibrium problems. It results in evolution equations which naturally include the backreaction from out-of-equilibrium modes on the evolution of the one-point function. We derive the renormalized

2PI equations of motion in an on-shell scheme in terms of physical parameters in the lowest non-trivial loop approximation. We then solve for the coupled dynamics of the one- and two-point functions of the scalar field and investigate the momentum structure of the two-point function. We identify the non-perturbative processes of parametric resonance and spinodal instability taking place during the reheating stage. The efficiency of these processes is found to sensitively depend on the parameters of the theory, such as the spectator self-interaction strength and the inflaton decay rate. Also, the tachyonic and subsequent parametric processes may be coupled in a very intricate way. We note that the methods and their numerical implementation discussed here are not limited to the particular example at hand, but similar techniques can be carried also to more general setups.

This paper is organized as follows. In section 2 we introduce the model and in section 3 we derive the renormalized 2PI equations of motion in the comoving frame in the Hartree approximation. In section 4 we recast the equation for the two-point function into a form of moment equations in the mixed representation. In section 5 we apply the numerical approach introduced in [38] to the physical setup of [14], which included backreaction but assumed adiabatic expansion for the mode functions and some further technical approximations. Finally, section 6 contains our conclusions and outlook.

2 The model

Following [13, 14], we study a $\mathbb{Z}_2$-symmetric scalar singlet model where the singlet χ has no couplings to other matter fields. The singlet action is given by

$$\mathcal{S}_\chi = \int \mathrm{d}^4x\,\sqrt{-g}\Big[\frac{1}{2}(\nabla^\mu\chi)(\nabla_\mu\chi) - \frac{1}{2}m^2\chi^2 + \frac{\xi}{2}R\chi^2 - \frac{\lambda}{4}\chi^4\Big]. \tag{2.1}$$

We use the particle physics convention for the metric signature: $\mathrm{d}s^2 = \mathrm{d}t^2 - a^2\mathrm{d}\boldsymbol{x}^2$. We will assume that the singlet is energetically subdominant during inflation and reheating, $\rho_\chi \ll 3H^2M_\mathrm{P}^2$, and treat it as a test field in a classical background space-time, whose evolution is determined by the inflaton field ϕ. It should be noted that the non-minimal coupling $\xi R\chi^2$ of the field χ quantized in a classical curved space-time acquires radiative corrections already at the one loop level in the presence of the self-interaction [45]. Therefore, although ξ can be renormalized to zero at any given scale, it cannot be made to vanish on all scales.

Rescaling the field χ by the scale factor,

$$\sigma \equiv a(t)\chi, \tag{2.2}$$

and switching to the conformal time η defined through $a\mathrm{d}\eta \equiv \mathrm{d}t$, we can recast the action (2.1) for the χ-field into an effectively flat space form:

$$\mathcal{S}_\sigma = \int \mathrm{d}\eta\,\mathrm{d}^3\boldsymbol{x}\left[\frac{1}{2}(\partial_\eta\sigma)^2 - \frac{1}{2}(\nabla\sigma)^2 - \frac{1}{2}m_\mathrm{eff}^2(\eta)\sigma^2 - \frac{\lambda}{4}\sigma^4\right], \tag{2.3}$$

where the time-dependent effective mass term is defined as

$$m_\mathrm{eff}^2(\eta) \equiv a^2(\eta)\Big[m^2 - \Big(\xi - \frac{1}{6}\Big)R(\eta)\Big]. \tag{2.4}$$

JHEP04(2023)043

This action is the starting point for our derivation of the coupled evolution equations for the one- and two-point functions of the χ-field.

Equation of motion for the inflaton and the scale factor. We will treat the inflaton at the classical level and assume a quadratic inflaton potential. Because we wish to study the χ-evolution beyond the decay of the inflaton, we also add a coupling between the inflaton and a radiation component. The radiation energy density is set to zero before the end of inflation. Moreover, we will treat χ as a test field, so that the Hubble rate and the evolution of the Ricci scalar are determined solely by the inflaton and the radiation component. We then have

$$\begin{aligned} \ddot{\phi} + 3H\dot{\phi} + \Gamma\dot{\phi} + m_\phi^2\phi = 0, \\ \dot{\rho}_{\rm rad} + 4H\rho_{\rm rad} = \Gamma\dot{\phi}^2, \end{aligned} \tag{2.5}$$

where the dots denote differentiation with respect to the cosmic time t.

The above equations are solved together with the Friedmann equation $\dot{a}/a = H$, where the Hubble rate is given by

$$H = \frac{1}{\sqrt{6}M_{\rm P}}\left(\dot{\phi}^2 + m_\phi^2\phi^2 + 2\rho_{\rm rad}\right)^{1/2}, \tag{2.6}$$

with $M_{\rm P}$ being the reduced Planck mass. The time-dependent Ricci scalar in this setup is given by

$$R = \frac{1}{M_{\rm P}^2}\left(\dot{\phi}^2 - 2m_\phi^2\phi^2\right), \tag{2.7}$$

as the conformally invariant radiation component gives no contribution at the classical level. These equations can be solved independently of the equations of motion for the spectator field. In the latter the scale factor a and the Ricci scalar R then appear as external functions that source the non-trivial behaviour of the χ-field.

3 The renormalized 2PI equations of motion

In this section we derive the renormalized equations of motion for the mean σ-field and its two-point function corresponding to the action (2.3), using the 2PI effective action technique of non-equilibrium quantum field theory [46, 47]. The generic form of the 2PI effective action of a scalar field is

$$\Gamma_{\rm 2PI}[\bar{\sigma}, \Delta_\sigma] = \mathcal{S}[\bar{\sigma}] - \frac{\rm i}{2}{\rm Tr}_{\mathcal{C}}\left[\ln(\Delta_\sigma)\right] + \frac{\rm i}{2}{\rm Tr}_{\mathcal{C}}\left[\Delta_{0\sigma}^{-1}\Delta_\sigma\right] + \Gamma_2[\bar{\sigma}, \Delta_\sigma], \tag{3.1}$$

where $\mathcal{S}$ is the classical action, $\bar{\sigma}(x)$ is the classical field and $\Delta_\sigma(x, y)$ is the connected two-point function of the scaled σ-field and the trace contains integration over the Keldysh contour $\mathcal{C}$ [48] and summation over possible field indices. The classical, real-time inverse propagator is

$${\rm i}\Delta_{0\sigma,ab}^{-1}(x, y; \bar{\sigma}) = -\Big[\Box_x + m_{\rm eff}^2(\eta) + 3\lambda\bar{\sigma}_a^2\Big]\delta^{(4)}(x - y)\delta_{ab}, \tag{3.2}$$

JHEP04(2023)043

where $\Box_x = \partial_\eta^2 - \partial_{\boldsymbol{x}}^2$ and $a, b \in \{1, 2\}$ are the time path indices of the Keldysh contour. The interaction term $\Gamma_2[\bar{\sigma}, \Delta_\sigma]$ consists of all two-particle irreducible vacuum graphs with lines corresponding to the full propagator Δ_σ and interactions derived from the shifted Lagrangian density $\mathcal{L}[\sigma \to \bar{\sigma} + \sigma_q]$, where σ_q is the quantum fluctuation around the classical field configuration $\bar{\sigma}$.

The equations of motion of the one- and two-point functions are then obtained as the stationary conditions of the 2PI effective action:

$$\frac{\delta \Gamma_{\text{2PI}}}{\delta \bar{\sigma}_a} = 0 \qquad \text{and} \qquad \frac{\delta \Gamma_{\text{2PI}}}{\delta \Delta_\sigma^{ab}} = 0. \tag{3.3}$$

We will be restricting our attention to the lowest non-trivial order in the 2PI-expansion, called the Hartree approximation. In this case the interaction term is just

$$\Gamma_2[\bar{\sigma}, \Delta_\sigma] \equiv -\frac{3\lambda}{4} \int \mathrm{d}\eta \, \mathrm{d}^3\boldsymbol{x} \, \Delta_\sigma^2(x, x). \tag{3.4}$$

The non-renormalized equations of motion then become

$$\Big[\Box_x + m_{\text{eff}}^2(\eta) + \lambda \bar{\sigma}^2(x) + 3\lambda \Delta_\sigma(x, x)\Big] \bar{\sigma}(x) = 0, \tag{3.5a}$$

$$\Big[\Box_x + m_{\text{eff}}^2(\eta) + 3\lambda \bar{\sigma}^2(x) + 3\lambda \Delta_\sigma(x, x)\Big] \mathrm{i}\Delta_\sigma^{ab}(x, y) = a \delta^{ab} \delta^{(4)}(x - y). \tag{3.5b}$$

In particular the bare local correlation function $\Delta_\sigma(x, x)$ is a divergent quantity and equations (3.5) clearly need to be renormalized. We shall now show how this can be done in the 2PI-context, generalizing the derivation of [38] to a non-static space-time.

3.1 Renormalization

A systematic renormalization in the 2PI-context was developed in [49], but we shall follow an equivalent, more intuitive method introduced in [50] and extended to curved space-time in [51] (see also [52, 53]). A crucial difference between the 1PI- and the 2PI-cases is that in the latter an infinite number of counterterms and loop diagrams get resummed and mix at high orders in the perturbative expansion. This introduces a number of sub-divergences that may depend on finite temperature or even on the out-of-equilibrium quantum corrections and gives rise to auxiliary n-point functions, where some or all of the external field lines are replaced by internal propagators. Each auxiliary function needs a new renormalization condition, but the final equations of motion are independent of the particular choices. We shall closely follow the treatment of [38], extending it to the case of non-zero curvature.

The renormalized quantities are defined from the bare ones through

$$\begin{aligned} \sigma &\equiv Z_{(2)}^{1/2} \sigma_{\text{R}}, & \Delta_\sigma &\equiv Z_{(0)} \Delta_{\text{R}}, & & \\ m_{(i)}^2 &\equiv m_{\text{R}(i)}^2 + \delta m_{(i)}^2, & \lambda_{(i)} &\equiv \lambda_{\text{R}}^{(i)} + \delta \lambda^{(i)}, & \xi_{(i)} &\equiv \xi_{\text{R}}^{(i)} + \delta \xi^{(i)}. \end{aligned} \tag{3.6}$$

The index enclosed in parenthesis tells how many lines in the vertex function corresponding to the coupling or mass parameter in question are associated with external fields, as

JHEP04(2023)043

explained in [38, 50]. Note that both the bare and the renormalized couplings in general are different for different i, as we shall see below. We then define accordingly:

$$\delta_\lambda^{(0)} \equiv Z_{(0)}^2\big(\lambda_{\rm R}^{(0)} + \delta\lambda^{(0)}\big) - \lambda_{\rm R}^{(0)}, \tag{3.7a}$$

$$\delta_\lambda^{(2)} \equiv Z_{(0)}Z_{(2)}\big(\lambda_{\rm R}^{(2)} + \delta\lambda^{(2)}\big) - \lambda_{\rm R}^{(2)}, \tag{3.7b}$$

$$\delta_\lambda^{(4)} \equiv Z_{(2)}^2\big(\lambda_{\rm R}^{(4)} + \delta\lambda^{(4)}\big) - \lambda_{\rm R}^{(4)}, \tag{3.7c}$$

$$\delta_m^{(i)} \equiv Z_{(i)}\big(m_{{\rm R}(i)}^2 + \delta m_{(i)}^2\big) - m_{{\rm R}(i)}^2, \tag{3.7d}$$

$$\delta_\xi^{(i)} \equiv Z_{(i)}\big(\xi_{\rm R}^{(i)} - \tfrac{1}{6} + \delta\xi^{(i)}\big) - \xi_{\rm R}^{(i)} + \tfrac{1}{6}. \tag{3.7e}$$

Given these definitions we can write the unrenormalized equations of motion in terms of the renormalized quantities as follows:

$$\begin{aligned}\Big[&Z_{(2)}\,\Box_x + a^2\Big(m_{{\rm R}(2)}^2 + \delta_m^{(2)}\Big) - a^2\Big(\xi_{\rm R}^{(2)} - \tfrac{1}{6} + \delta_\xi^{(2)}\Big)R \\ &+ 3\Big(\lambda_{\rm R}^{(4)} + \tfrac{1}{3}\delta_\lambda^{(4)}\Big)\sigma_{\rm R}^2 + 3\Big(\lambda_{\rm R}^{(2)} + \delta_\lambda^{(2)}\Big)\Delta_{\rm R}(x,x)\Big]\sigma_{\rm R}(x) = 2\lambda_{\rm R}^{(4)}\sigma_{\rm R}^3\,,\end{aligned} \tag{3.8a}$$

$$\begin{aligned}\Big[&Z_{(0)}\,\Box_x + a^2\Big(m_{{\rm R}(0)}^2 + \delta_m^{(0)}\Big) - a^2\Big(\xi_{\rm R}^{(0)} - \tfrac{1}{6} + \delta_\xi^{(0)}\Big)R \\ &+ 3\Big(\lambda_{\rm R}^{(2)} + \delta_\lambda^{(2)}\Big)\sigma_{\rm R}^2 + 3\Big(\lambda_{\rm R}^{(0)} + \delta_\lambda^{(0)}\Big)\Delta_{\rm R}(x,x)\Big]{\rm i}\Delta_{\rm R}^{bc}(x,y) = b\delta^{bc}\delta^{(4)}(x-y).\end{aligned} \tag{3.8b}$$

Here and in what follows we drop the bar when referring to the classical field $\sigma_{\rm R}$.

Renormalization conditions. To proceed, we must now define the renormalization conditions. We start by setting on-shell conditions for the auxiliary two-point function $\Delta_{\rm R}^{11}$ at a vanishing external vacuum expectation value, $\sigma_{\rm R} = v_{\rm R} = 0$, and some finite $R = R_0$, along with the requirement that the quantum corrections vanish at the minimum of the effective action:

$${\rm i}(\Delta_{\rm R}^{11})^{-1}\Big|_{\substack{\sigma_{\rm R}=0\\R=R_0}} \equiv k^2 - a^2m_\Delta^2, \quad \frac{\rm d}{{\rm d}k^2}\,{\rm i}(\Delta_{\rm R}^{11})^{-1}\Big|_{\substack{\sigma_{\rm R}=0\\R=R_0}} \equiv 1 \quad \text{and} \quad \frac{\delta\Gamma_{\rm 2PI}}{\delta\sigma_{\rm R}}\Big|_{\substack{\sigma_{\rm R}=0\\R=R_0}} \equiv 0. \tag{3.9}$$

Note that we are using the comoving units, so k is also the comoving 4-momentum. These conditions imply that $Z_{(0)} = 1$. Furthermore, one finds $Z_{(2)} = 1$ in the Hartree approximation, when the renormalization is performed at $\sigma_{\rm R} = 0$ [38]. As a result, one can set also $m_\Delta^2 = m_{\rm ph}^2$, where $m_{\rm ph}$ refers to the usual mass parameter defined at the off-shell momentum $p^2 = 0$. The renormalization conditions (3.9), together with the equation of motion (3.8b), then give

$$m_{{\rm R}(0)}^2 + \delta_m^{(0)} - \Big(\xi_{\rm R}^{(0)} - \tfrac{1}{6} + \delta_\xi^{(0)}\Big)R_0 + 3\Big(\lambda_{\rm R}^{(0)} + \delta_\lambda^{(0)}\Big)a^{-2}\Delta_{\rm R} = m_{\rm ph}^2. \tag{3.10}$$

Here $\Delta_{\rm R}$ is computed at the renormalization point. The a^{-2}-factor multiplying $\Delta_{\rm R}$ arises from the scaling of the field σ. In physical units it is absorbed to the correlation function.

In the Hartree approximation we can renormalize $\lambda_{\rm R}^{(0)}$ and $\lambda_{\rm R}^{(2)}$ similarly, by setting

$$\delta_\lambda^{(0)} \equiv \delta_\lambda^{(2)}. \tag{3.11}$$

JHEP04(2023)043

From $Z_{(0,2)} = 1$ it then follows that $\lambda_{\mathrm{R}}^{(0)} = \lambda_{\mathrm{R}}^{(2)}$. So, both bare and renormalized couplings can be chosen equal for these vertex functions. Next we set the bare mass parameters $m_{(i)}^2$ and the $\xi_{(i)}$-parameters equal for $i \in \{0, 2\}$, which gives

$$m_{\mathrm{R}(0)}^2 + \delta_m^{(0)} = m_{\mathrm{R}(2)}^2 + \delta_m^{(2)} \qquad \text{and} \qquad \xi_{\mathrm{R}}^{(0)} + \delta_\xi^{(0)} = \xi_{\mathrm{R}}^{(2)} + \delta_\xi^{(2)}, \tag{3.12}$$

and we finally define

$$\lambda_{\mathrm{R}}^{(4)} + \tfrac{1}{3}\delta_\lambda^{(4)} \equiv \lambda_{\mathrm{R}}^{(0)} + \delta_\lambda^{(0)}. \tag{3.13}$$

This condition ensures that the renormalized effective potential has the same first derivative as the tree level potential for a finite σ_{R} (for more details, see [38]). Note that the bare coupling $\lambda_{(4)}$ is then different from $\lambda_{(0,2)}$, but this has no consequence for the renormalized low-energy theory. Finally, we could relate $\xi_{\mathrm{R}}^{(0)}$ to a physical mass measured in a background with a non-zero R, but we simply define it as an $\overline{\mathrm{MS}}$-parameter instead.

Cancellation of the sub-divergences. Next we impose the conditions on the cancellation of the sub-divergences [50]. To this end we must work out the primitive divergence in the local correlation function, which in the Hartree approximation is given just by the momentum integral over the renormalized correlator $\mathrm{i}\Delta_{\mathrm{R}}^{11}$ defined in the conditions (3.9):

$$\begin{aligned}\Delta_{\mathrm{R}} &= Q^\epsilon \int \frac{\mathrm{d}^d p}{(2\pi)^d}\, \Delta_{\mathrm{R}}^{11}(p) = -\frac{a^2 m_{\mathrm{ph}}^2}{16\pi^2}\left[\frac{2}{\bar\epsilon} + 1 - \ln\left(\frac{a^2 m_{\mathrm{ph}}^2}{Q^2}\right)\right] \\ &\equiv a^2 m_{\mathrm{ph}}^2 \Delta_{\bar\epsilon} + \Delta_{\mathrm{F}0}(a m_{\mathrm{ph}}, Q),\end{aligned} \tag{3.14}$$

where $\Delta_{\bar\epsilon} \equiv -1/(8\pi^2\bar\epsilon)$ and Q is the comoving momentum scale used for the $\overline{\mathrm{MS}}$-renormalization. Substituting this expression back into equation (3.10) and requiring that the finite and divergent parts cancel separately, we find the following two equations:

$$m_{\mathrm{ph}}^2 \equiv m_{\mathrm{R}(0)}^2 - \left(\xi_{\mathrm{R}}^{(0)} - \tfrac{1}{6}\right) R_0 + 3\lambda_{\mathrm{R}}^{(0)} a^{-2} \Delta_{\mathrm{F}0}, \tag{3.15}$$

$$0 = \delta_m^{(0)} - R_0 \delta_\xi^{(0)} + 3\delta_\lambda^{(0)} a^{-2} \Delta_{\mathrm{F}0} + 3\left(\lambda_{\mathrm{R}}^{(0)} + \delta_\lambda^{(0)}\right) m_{\mathrm{ph}}^2 \Delta_{\bar\epsilon}. \tag{3.16}$$

Using equation (3.15) one can rewrite equation (3.16) as

$$\begin{aligned}&\delta_m^{(0)} + 3m_{\mathrm{R}(0)}^2\left(\lambda_{\mathrm{R}}^{(0)} + \delta_\lambda^{(0)}\right)\Delta_{\bar\epsilon} + 3\left[\delta_\lambda^{(0)} + 3\left(\lambda_{\mathrm{R}}^{(0)} + \delta_\lambda^{(0)}\right)\lambda_{\mathrm{R}}^{(0)}\Delta_{\bar\epsilon}\right] a^{-2}\Delta_{\mathrm{F}0} \\ &- \left[\delta_\xi^{(0)} + 3\left(\xi_{\mathrm{R}}^{(0)} - \tfrac{1}{6}\right)\left(\lambda_{\mathrm{R}}^{(0)} + \delta_\lambda^{(0)}\right)\Delta_{\bar\epsilon}\right] R_0 = 0.\end{aligned} \tag{3.17}$$

This equation can hold for arbitrary R_0 and $\Delta_{\mathrm{F}0}$ only if the coefficients multiplying each of these terms vanish separately. This gives us three constraints between the counterterms:

$$\delta_m^{(0)} + 3m_{\mathrm{R}(0)}^2\left(\lambda_{\mathrm{R}}^{(0)} + \delta_\lambda^{(0)}\right)\Delta_{\bar\epsilon} = 0, \tag{3.18a}$$

$$\delta_\lambda^{(0)} + 3\left(\lambda_{\mathrm{R}}^{(0)} + \delta_\lambda^{(0)}\right)\lambda_{\mathrm{R}}^{(0)}\Delta_{\bar\epsilon} = 0, \tag{3.18b}$$

$$\delta_\xi^{(0)} + 3\left(\xi_{\mathrm{R}}^{(0)} - \tfrac{1}{6}\right)\left(\lambda_{\mathrm{R}}^{(0)} + \delta_\lambda^{(0)}\right)\Delta_{\bar\epsilon} = 0. \tag{3.18c}$$

JHEP04(2023)043

From these we find the explicit expressions for the counterterms $\delta_\lambda^{(0)}$, $\delta_m^{(0)}$ and $\delta_\xi^{(0)}$:

$$\delta_\lambda^{(0)} = -\frac{3(\lambda_{\rm R}^{(0)})^2\Delta_{\bar\epsilon}}{1+3\lambda_{\rm R}^{(0)}\Delta_{\bar\epsilon}}, \qquad \delta_m^{(0)} = -\frac{3m_{{\rm R}(0)}^2\lambda_{\rm R}^{(0)}\Delta_{\bar\epsilon}}{1+3\lambda_{\rm R}^{(0)}\Delta_{\bar\epsilon}}, \qquad \delta_\xi^{(0)} = -\frac{3(\xi_{\rm R}^{(0)}-\frac{1}{6})\lambda_{\rm R}^{(0)}\Delta_{\bar\epsilon}}{1+3\lambda_{\rm R}^{(0)}\Delta_{\bar\epsilon}}. \tag{3.19}$$

The running of the renormalized parameters now follows from requiring that the corresponding bare parameters are constants: $\partial_Q[Q^\epsilon(\lambda_{\rm R}^{(0)}+\delta_\lambda^{(0)})]=0$, $\partial_Q[Q^\epsilon(m_{{\rm R}(0)}^2+\delta_m^{(0)})]=0$ and $\partial_Q[Q^\epsilon(\xi_{\rm R}^{(0)}-\frac{1}{6}+\delta_\xi^{(0)})]=0$. For the running of $\lambda_{\rm R}^{(0)}$ and $\xi_{\rm R}^{(0)}$ one then finds

$$\lambda_{\rm R}^{(0)}(Q) = \frac{\lambda_{\rm R0}^{(0)}}{1+\frac{3\lambda_{\rm R0}^{(0)}}{8\pi^2}\ln\left(\frac{Q_0}{Q}\right)} \qquad \text{and} \qquad \xi_{\rm R}^{(0)}(Q)-\tfrac{1}{6} = \frac{\xi_{\rm R0}^{(0)}-\frac{1}{6}}{1+\frac{3\lambda_{\rm R0}^{(0)}}{8\pi^2}\ln\left(\frac{Q_0}{Q}\right)}, \tag{3.20}$$

where $\lambda_{\rm R0}^{(0)} \equiv \lambda_{\rm R}^{(0)}(Q_0)$ and $\xi_{\rm R0}^{(0)} \equiv \xi_{\rm R}^{(0)}(Q_0)$ and our previous choices imply that $\lambda_{\rm R}^{(2)} = \lambda_{\rm R}^{(0)}$. The running of the mass terms is analogous to the running of the couplings [38]. On the other hand, the coupling $\lambda_{\rm R}^{(4)}$ does not run at all. Indeed, $\lambda_{\rm R}^{(4)}$ remains finite because of the condition $\delta_\lambda^{(4)} = 3\delta_\lambda^{(0)}$ up to finite terms, which implies that $\partial_Q\lambda_{\rm R}^{(4)}=0$.

Renormalized equations of motion. Next we show that the full evolution equations (3.8) get renormalized by the counterterms we have defined. We begin by defining a finite effective mass term, which includes general corrections from R, $\sigma_{\rm R}$ and $\Delta_{\rm F}$, as follows:

$$M_{\rm eff}^2(\sigma_{\rm R},\Delta_{\rm F}) \equiv a^2\Big[m_{{\rm R}(0)}^2-\Big(\xi_{\rm R}^{(0)}-\tfrac{1}{6}\Big)R\Big]+3\lambda_{\rm R}^{(0)}\Big(\sigma_{\rm R}^2+\Delta_{\rm F}\Big). \tag{3.21}$$

The finite part $\Delta_{\rm F}$ of the local correlation function $\Delta_{\rm R}$ is defined similarly to equation (3.14):

$$\Delta_{\rm R} \equiv M_{\rm eff}^2(\sigma_{\rm R},\Delta_{\rm F})\Delta_{\bar\epsilon}+\Delta_{\rm F}. \tag{3.22}$$

We furthermore split $\Delta_{\rm F} \equiv \Delta_{\rm F0}(M_{\rm eff},Q)+\delta\Delta_{\rm F}$, where $\Delta_{\rm F0}$ was defined in equation (3.14) and $\delta\Delta_{\rm F}$ represents the remaining non-equilibrium fluctuations. Using this expression, the equation of motion for the two-point function becomes

$$\begin{aligned}\Big[\Box_x+M_{\rm eff}^2+a^2\Big(\delta_m^{(0)}-R\delta_\xi^{(0)}\Big)+3\delta_\lambda^{(0)}\Big(\sigma_{\rm R}^2+\Delta_{\rm F}\Big)\\ +3\Big(\lambda_{\rm R}^{(0)}+\delta_\lambda^{(0)}\Big)M_{\rm eff}^2\Delta_{\bar\epsilon}\Big]{\rm i}\Delta_{\rm R}^{bc}(x,y) = b\delta^{bc}\delta^{(4)}(x-y).\end{aligned} \tag{3.23}$$

Using the definition (3.21) again in the term proportional to $\Delta_{\bar\epsilon}$, we can write equation (3.23) as

$$\begin{aligned}\Big\{\Box_x+M_{\rm eff}^2-a^2\Big[\delta_\xi^{(0)}+3\Big(\xi_{\rm R}^{(0)}-\tfrac{1}{6}\Big)\Big(\lambda_{\rm R}^{(0)}+\delta_\lambda^{(0)}\Big)\Delta_{\bar\epsilon}\Big]R\\ +3\Big[\delta_\lambda^{(0)}+3\Big(\lambda_{\rm R}^{(0)}+\delta_\lambda^{(0)}\Big)\lambda_{\rm R}^{(0)}\Delta_{\bar\epsilon}\Big]\Big(\sigma_{\rm R}^2+\Delta_{\rm F}\Big)\\ +a^2\Big[\delta_m^{(0)}+3m_{{\rm R}(0)}^2\Big(\lambda_{\rm R}^{(0)}+\delta_\lambda^{(0)}\Big)\Delta_{\bar\epsilon}\Big]\Big\}{\rm i}\Delta_{\rm R}^{bc}(x,y) = b\delta^{bc}\delta^{(4)}(x-y).\end{aligned} \tag{3.24}$$

The renormalization conditions (3.18) set all the terms in the square brackets to zero leaving behind only the finite mass term $M_{\rm eff}^2$. It should be appreciated how the *constant* counterterms cancel infinities that depend on the dynamical variables $\sigma_{\rm R}$, R and $\Delta_{\rm F}$.

JHEP04(2023)043

Similar manipulations can be done, crucially dependent on the definition (3.13), in the equation (3.8a) for the one-point function. Our final equations then become

$$\Big[\Box_x + M^2_{\rm eff}(\sigma_{\rm R}, \Delta_{\rm F})\Big]\sigma_{\rm R} = 2\lambda^{(4)}_{\rm R}\sigma^3_{\rm R}, \tag{3.25a}$$

$$\Big[\Box_x + M^2_{\rm eff}(\sigma_{\rm R}, \Delta_{\rm F})\Big]\mathrm{i}\Delta^{ab}_{\rm R}(x,y) = b\delta^{bc}\delta^{(4)}(x-y). \tag{3.25b}$$

Let us finally point out that these equations are independent of the renormalization scale for the auxiliary renormalization conditions: one can show that $\partial_Q(M^2_{\rm eff}) = 0$ using the gap equation (3.21) together with the running equations (3.20).

Physical parameters. We have now renormalized our equations of motion, but we still have not related our parameters to observable quantities. We now address this problem for completeness, even though none of the parameters in the problem are directly observable. We start by specifying the Hartree-corrected effective potential in the limit of constant curvature, consistent with our renormalization conditions. The calculation is identical to the one given in [38] and we only quote the final result, first found in [54]:

$$V_{\rm H}(\sigma_{\rm R}) = -\frac{\lambda^{(4)}_{\rm R}}{2}\sigma^4_{\rm R} + \frac{\overline{m}^4(\sigma_{\rm R})}{12\lambda^{(0)}_{\rm R}} - \frac{\overline{m}^4(\sigma_{\rm R})}{64\pi^2}\left[\ln\left(\frac{\overline{m}^2(\sigma_{\rm R})}{Q^2}\right) - \frac{1}{2}\right], \tag{3.26}$$

where $\overline{m}^2$ is the solution to equation (3.21) for $R = R_0$ and $\Delta_{\rm F} = \Delta_{\rm F0}(\overline{m}^2)$. Now, differentiating the effective potential twice, we find

$$\Gamma^{(2)}_{\rm 1PI}(p^2 = 0, \sigma_{\rm R}) \;=\; \frac{\partial^2 V_{\rm H}(\sigma_{\rm R})}{\partial\sigma^2_{\rm R}} = \overline{m}^2(\sigma_{\rm R}) + 6\Big[\lambda^{(0)}_{\rm R}(\overline{m}(\sigma_{\rm R})) - \lambda^{(4)}_{\rm R}\Big]\sigma^2_{\rm R}. \tag{3.27}$$

Because $\overline{m}^2(0) \equiv a^2 m^2_{\rm ph}$, we see that the mass parameter $m_{\rm ph}$ of the auxiliary propagator equals the value of the full two-point function $\Gamma^{(2)}_{\rm 1PI}(p^2 = 0, \sigma_{\rm R} = 0)$. Equation (3.27) also suggests that it is natural to define $\lambda^{(0)}_{\rm R}(m_{\rm ph}) \equiv \lambda^{(4)}_{\rm R}$.

Finally, one can easily show that $\lambda^{(4)}_{\rm R}$ coincides with the four-point function measured at zero momentum:

$$\lambda_{\rm R} \equiv \Gamma^{(4)}_{\rm 1PI}(p_i = 0, \sigma_{\rm R} = 0) = \frac{1}{6}\frac{\partial^4 V_{\rm H}(\sigma_{\rm R})}{\partial\sigma^4_{\rm R}}\bigg|_{\sigma_{\rm R}=0} = \lambda^{(4)}_{\rm R}. \tag{3.28}$$

The mass $m_{\rm ph}$ and the coupling $\lambda_{\rm R}$ can be related to an on-shell mass and a four-point function in the physical region without further reference to the 2PI-methods. Finally, we define the parameter $\xi^{(0)}_{\rm R}$ as the $\overline{\rm MS}$-parameter at scale $m_{\rm ph}$: $\bar{\xi}_{\rm R} \equiv \xi^{(0)}_{\rm R}(m_{\rm ph})$. These considerations now uniquely define all the parameters in our model.

4 Wigner-space and moment equations

The direct numerical implementation of equations (3.25) would be very difficult and we shall use the phase space picture instead. To this end we define the Wigner transform of a generic function of two variables $\mathcal{O}(u, v)$ as follows:

$$\mathcal{O}(k, X) \equiv \int \mathrm{d}^4 r\, \mathrm{e}^{\mathrm{i}k\cdot r}\, \mathcal{O}\left(X + \frac{r}{2}, X - \frac{r}{2}\right), \tag{4.1}$$

JHEP04(2023)043

where $r = u - v$ and $X = \frac{1}{2}(u + v)$ are the relative and average coordinates, respectively. For a homogeneous and isotropic system relevant here, the transformation with respect to spatial coordinates reduces to the ordinary Fourier transformation. In this case the equation (3.25b) for the two-point function in Wigner-space becomes just

$$\left[\frac{1}{4}\partial_\eta^2 - k^2 - \mathrm{i}k_0\partial_\eta + M_{\mathrm{eff}}^2(\eta - \tfrac{\mathrm{i}}{2}\partial_{k_0})\right]\mathrm{i}\Delta_{\boldsymbol{k}}^{bc}(k_0,\eta) = b\delta^{bc}, \tag{4.2}$$

where we denoted $M_{\mathrm{eff}}^2(\sigma_{\mathrm{R}}, \Delta_{\mathrm{F}}) \equiv M_{\mathrm{eff}}^2(\eta)$.

To study the dynamics of the coupled system of the one- and two-point functions it suffices to concentrate on any of the four components of the propagator Δ^{ab}. We choose to work with $\Delta^{+-} = \Delta^<$ and define its n^{th} moment as

$$\rho_{n\boldsymbol{k}} \equiv \int \frac{\mathrm{d}k_0}{2\pi}\, k_0^n\, \Delta_{\boldsymbol{k}}^<(k_0,\eta). \tag{4.3}$$

Integrating equation (4.2) over k_0, weighted by 1 and by k_0, and taking real and imaginary parts of the resulting equations one finds a closed set of equations for the three lowest moments with $n \in \{0,1,2\}$ [38, 43]. The equation for $\rho_{1\boldsymbol{k}}$ is simple: $\partial_\eta\rho_{1\boldsymbol{k}} = 0$, which implies that $\rho_{1\boldsymbol{k}}$ is a constant. In addition we observe that the quantity

$$X_{\boldsymbol{k}} \equiv 2\rho_{0\boldsymbol{k}}\rho_{2\boldsymbol{k}} - \left(|\boldsymbol{k}|^2 + M_{\mathrm{eff}}^2\right)\rho_{0\boldsymbol{k}}^2 - \tfrac{1}{4}\left(\partial_\eta\rho_{0\boldsymbol{k}}\right)^2 \tag{4.4}$$

is conserved in our setup: $\partial_\eta X_{\boldsymbol{k}} = 0$. This is no longer true in an interacting system [38, 43], but even then using $X_{\boldsymbol{k}}$ as a variable instead of $\rho_{2\boldsymbol{k}}$ leads to numerically more stable equations.

In the end we then have the following equations for the homogeneous field σ_{R} and the moments $\rho_{n\boldsymbol{k}}$:

$$\begin{aligned}\left(\partial_\eta^2 + M_{\mathrm{eff}}^2\right)\sigma_{\mathrm{R}} &= 2\lambda_{\mathrm{R}}\sigma_{\mathrm{R}}^3,\\ \left(\tfrac{1}{4}\partial_\eta^2 + |\boldsymbol{k}|^2 + M_{\mathrm{eff}}^2\right)\rho_{0\boldsymbol{k}} &= \rho_{2\boldsymbol{k}},\end{aligned} \tag{4.5}$$

where $\rho_{2\boldsymbol{k}}$ is evaluated using equation (4.4). The non-trivial nature of the evolution equations is hidden in the gap equation (3.21), which couples all the variables. Using the moments and the fact that M_{eff}^2 is actually Q-independent, we can write the gap equation directly in terms of our chosen physical parameters, choosing $Q = am_{\mathrm{ph}}$:

$$\begin{aligned}M_{\mathrm{eff}}^2 = a^2m_{\mathrm{ph}}^2 - a^2\left(\bar{\xi}_{\mathrm{R}} - \tfrac{1}{6}\right)(R - R_0) + 3\lambda_{\mathrm{R}}\sigma_{\mathrm{R}}^2 + 3\lambda_{\mathrm{R}}\int_{\boldsymbol{k}}\left(\rho_{0\boldsymbol{k}} - \frac{\Theta_{\boldsymbol{k}}}{2\omega_{\boldsymbol{k}}}\right)\\ + \frac{3\lambda_{\mathrm{R}}}{16\pi^2}\left[M_{\mathrm{eff}}^2\ln\left(\frac{M_{\mathrm{eff}}^2}{a^2m_{\mathrm{ph}}^2}\right) - M_{\mathrm{eff}}^2 + a^2m_{\mathrm{ph}}^2\right],\end{aligned} \tag{4.6}$$

where we defined $\int_{\boldsymbol{k}} \equiv \frac{1}{2\pi^2}\int_0^\infty \mathrm{d}|\boldsymbol{k}||\boldsymbol{k}|^2$, $\Theta_{\boldsymbol{k}} \equiv \theta(\omega_{\boldsymbol{k}}^2(t))$, $\omega_{\boldsymbol{k}}^2 \equiv |\boldsymbol{k}|^2 + M_{\mathrm{eff}}^2$, $\bar{\xi}_{\mathrm{R}} \equiv \xi_{\mathrm{R}}^{(0)}(m_{\mathrm{ph}})$ and R_0 is the background Ricci scalar at the renormalization point.[1] We assume that renormalization is performed in a background with no curvature and set $R_0 = 0$ here.

[1] To get to equation (4.6) one uses for example the relation $m_{\mathrm{R}(0)}^2 = m_{\mathrm{ph}}^2\left(1 + \frac{3\lambda_{\mathrm{R}}}{16\pi^2}\right) + \left(\bar{\xi}_{\mathrm{R}} - \frac{1}{6}\right)R_0$, which can be derived from equation (3.15) and the running equations for the mass and the couplings.

JHEP04(2023)043

Finally, we define the particle number density and the quantum coherence functions in terms of the moments as follows [38, 43]:

$$n_{\boldsymbol{k}} \equiv \frac{1}{\omega_{\boldsymbol{k}}}\rho_{2\boldsymbol{k}} + \rho_{1\boldsymbol{k}}, \tag{4.7a}$$

$$\bar{n}_{\boldsymbol{k}} \equiv \frac{1}{\omega_{\boldsymbol{k}}}\rho_{2\boldsymbol{k}} - \rho_{1\boldsymbol{k}} - 1, \tag{4.7b}$$

$$f^{c\pm}_{\boldsymbol{k}} \equiv \omega_{\boldsymbol{k}}\rho_{0\boldsymbol{k}} - \frac{1}{\omega_{\boldsymbol{k}}}\rho_{2\boldsymbol{k}} \pm \frac{\mathrm{i}}{2}\partial_t\rho_{0\boldsymbol{k}}. \tag{4.7c}$$

We will denote the momentum-integrated versions of these functions by $n \equiv \int_{\boldsymbol{k}} n_{\boldsymbol{k}}$ and $f^c \equiv \int_{\boldsymbol{k}} |f^{c\pm}_{\boldsymbol{k}}|$. In our case of a real field with no collisions $\rho_{1\boldsymbol{k}} = -1/2$ throughout, so that $n_{\boldsymbol{k}}$ and $\bar{n}_{\boldsymbol{k}}$ actually coincide. The functions $f^{c\pm}_{\boldsymbol{k}}$ in turn measure the degree of quantum coherence, or squeezing, between particle-antiparticle pairs with opposite 3-momenta [44], and particle production can only take place when $f^{c\pm}_{\boldsymbol{k}} \neq 0$. The unique vacuum which corresponds to a state with no particles nor any coherence can then be defined as

$$\rho^{\mathrm{vac}}_{0\boldsymbol{k}} \equiv \frac{\Theta_{\boldsymbol{k}}}{2\omega_{\boldsymbol{k}}}, \qquad \partial_t\rho^{\mathrm{vac}}_{0\boldsymbol{k}} \equiv 0, \qquad \rho^{\mathrm{vac}}_{1\boldsymbol{k}} \equiv -\frac{1}{2} \quad \text{and} \quad \rho^{\mathrm{vac}}_{2\boldsymbol{k}} \equiv \frac{\omega_{\boldsymbol{k}}}{2}\Theta_{\boldsymbol{k}}. \tag{4.8}$$

The Heaviside theta function $\Theta_{\boldsymbol{k}}$ ensures that no spinodal modes are included in the vacuum. Finally, we define the non-equilibrium fluctuations in the moments as $\delta\rho_{n\boldsymbol{k}} \equiv \rho_{n\boldsymbol{k}} - \rho^{\mathrm{vac}}_{n\boldsymbol{k}}$.

5 Results

We numerically solve the equations (4.5) and (4.6), following the methods of [38]. We focus on a setup where the energy density of σ stays negligible compared to the total energy density, $\rho_\sigma \ll 3H^2M_{\mathrm{P}}^2$, during the entire simulation time. The scale factor a and the Ricci scalar R are therefore entirely set by the inflaton and its decay products via equations (2.5), and they appear as externally given functions in equations (4.5) and (4.6). We choose $m_\phi = 1.5 \times 10^{13}\,\mathrm{GeV}$ and set slow roll initial conditions with $\phi_{\mathrm{in}} = 15M_{\mathrm{P}}$ on the inflaton sector. On the spectator sector we set $m_{\mathrm{ph}} = 150\,\mathrm{GeV}$, initialize the two-point function $\Delta_{\mathrm{R,in}}$ by giving the Minkowski vacuum values (4.8) for the moments, and give a small non-zero initial value for the one-point function $\sigma_{\mathrm{R,in}}$. In the following, we denote by η_0 the moment when $\epsilon_{\mathrm{H}} \equiv -\dot{H}/H^2 = 1$ for the first time. Our main results are summarized in the figures of this section.

Case I: $\bar{\xi}_{\mathrm{R}} = 50, \Gamma = 0$. We will first discuss a case with a non-minimal coupling $\bar{\xi}_{\mathrm{R}} = 50$ and a non-interacting inflaton, $\Gamma = 0$, where the results can be directly compared with those obtained in [14]. The left panel in figure 1 shows the time evolution of the fluctuation in the contact limit for the comoving two-point function $\langle\sigma^2_{\mathrm{R}}\rangle$: $\delta\Delta_{\mathrm{F}} \equiv \Delta_{\mathrm{F}} - \Delta_{\mathrm{F}0}$. The right panel shows the effective mass function M^2_{eff} given by equation (4.6). In both panels the self-coupling is given the values $\lambda_{\mathrm{R}} = 10^{-7}$ (blue lines), 10^{-4} (red lines) and 10^{-1} (orange lines). There are three components of different origin contributing to the effective mass function M^2_{eff}:

$$M^2_R \equiv -a^2(\bar{\xi}_{\mathrm{R}} - \tfrac{1}{6})R \qquad \text{(curvature)}, \tag{5.1a}$$

$$M^2_\Delta \equiv 3\lambda_{\mathrm{R}}\delta\Delta_{\mathrm{F}} = 3\lambda_{\mathrm{R}}\int_{\boldsymbol{k}}\delta\rho_{0\boldsymbol{k}} \qquad \text{(fluctuations)}, \tag{5.1b}$$

JHEP04(2023)043

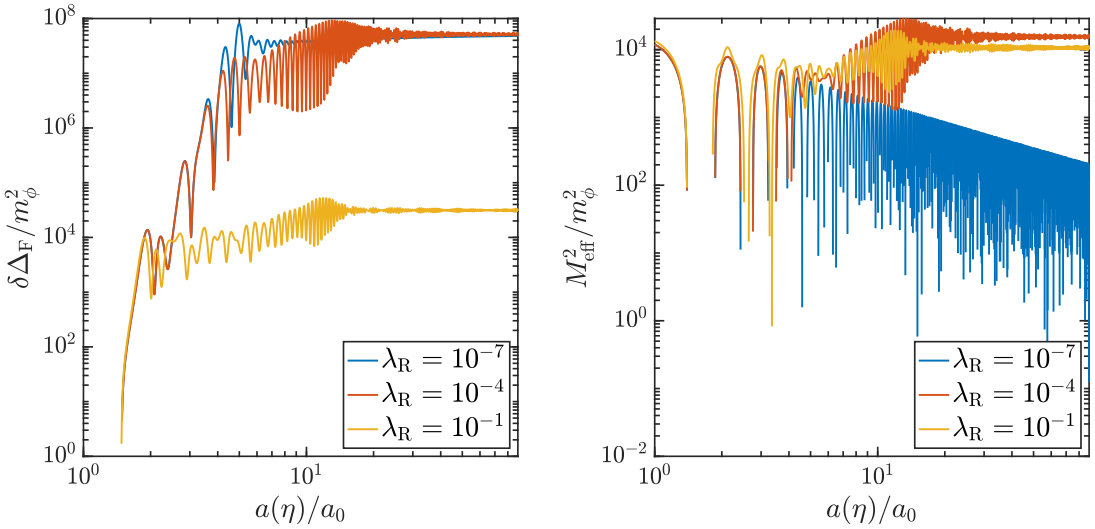

Figure 1. The two-point function $\delta\Delta_{\rm F}$ (left panel) and the effective mass function $M^2_{\rm eff}$ (right panel). The results are shown for $\lambda_{\rm R} \in \{10^{-7}, 10^{-4}, 10^{-1}\}$, $\bar{\xi}_{\rm R} = 50$ and $\Gamma = 0$.

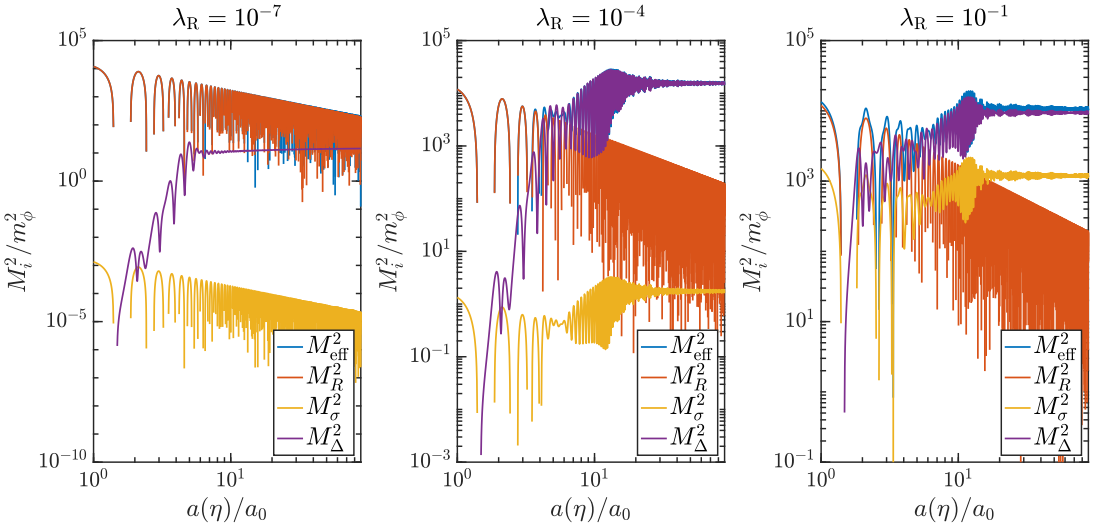

Figure 2. The effective mass function $M^2_{\rm eff}$ (blue) and its component functions M^2_R (red), M^2_Δ (violet) and M^2_σ (yellow), defined in equations (5.1), for $\lambda_{\rm R} \in \{10^{-7}, 10^{-4}, 10^{-1}\}$, $\bar{\xi}_{\rm R} = 50$ and $\Gamma = 0$.

$$M^2_\sigma \equiv M^2_{\rm eff} - M^2_R - M^2_\Delta \qquad \text{(field and background)}. \tag{5.1c}$$

The evolution and magnitudes of these components are displayed in figure 2.

For all three values of $\lambda_{\rm R}$ shown in the figures, the field-dependent mass term M^2_σ is very small compared to the curvature and fluctuation corrections. In all cases the initial evolution is characterized by a rapid growth of the fluctuation contribution to the two-point function $\delta\Delta_{\rm F}$, which is driven by periodic tachyonic instabilities that occur when $M^2_{\rm eff} < 0$. The growing two-point function gives a positive definite contribution to the fluctuation part M^2_Δ in the effective mass function, which is known to eventually terminate the strong tachyonic growth [9].

JHEP04(2023)043

As seen in figure 2, for $\lambda_{\rm R} = 10^{-7}$ the growth of $\delta\Delta_{\rm F}$ stops while the effective mass is still dominated by the curvature term, $\langle M_\Delta^2 + M_\sigma^2\rangle_{\rm osc} \approx \langle M_\Delta^2\rangle_{\rm osc} \ll \langle M_R^2\rangle_{\rm osc}$, where the brackets $\langle\ldots\rangle_{\rm osc}$ denote averaging over an oscillation cycle of the mean field $\sigma_{\rm R}$. The reason for this ending of the tachyonic growth is that the windows with $M_{\rm eff}^2 < 0$ become too narrow to generate a coherent net particle production. This effect is controlled by the evolution of R, whose oscillation period is a constant in physical time, proportional to the inverse inflaton mass m_ϕ^{-1}, but whose magnitude decreases rapidly, $R \propto a^{-3}$. The time available for tachyonic evolution per oscillation period then shrinks, while the oscillatory evolution between pulses grows, mixing growing and decaying modes. Eventually the tachyonic pulses lose all coherence and no net growth is registered. As a result our final value of $\delta\Delta_{\rm F}$ is about an order of magnitude smaller than in [14],[2] where the tachyonic growth was observed to continue up to $\langle M_\Delta^2\rangle_{\rm osc} \sim \langle M_R^2\rangle_{\rm osc}$. This effect is spurious however, following from the use in [14] of the adiabatic expansion in the regions where the adiabaticity condition $|\dot\omega/\omega^2| \ll 1$ for the mode function frequencies no longer holds between the tachyonic windows.

The case with larger couplings $\lambda_{\rm R} = 10^{-4}$ and 10^{-1} is markedly different. Here the (mostly) tachyonic growth *does* continue until $\langle M_\Delta^2\rangle_{\rm osc} \sim \langle M_R^2\rangle_{\rm osc}$, after which $\delta\Delta_{\rm F}$ starts to backreact into the dynamics of the system. The evolution of R is exactly the same as in the previous case but the larger coupling $\lambda_{\rm R}$ makes $\langle M_\Delta^2\rangle_{\rm osc}$ bigger, and the backreaction limit $\langle M_\Delta^2\rangle_{\rm osc} \sim \langle M_R^2\rangle_{\rm osc}$ is reached before the tachyonic windows become too narrow to support coherent particle production. After the tachyonic growth stops, the strongly non-linear system still undergoes a transient period of resonant particle production driven by the two-point function $\delta\Delta_{\rm F}$ itself, during which $M_{\rm eff}^2$ remains positive. The resonant nature of the particle production can be seen in figure 3, which will be discussed further below. At the onset of the resonance, $M_{\rm eff}^2$ receives roughly equal contributions from the fluctuation term $M_\Delta^2 = 3\lambda_{\rm R}\delta\Delta_{\rm F}$ and from the curvature term $M_R^2 = a^2(\bar\xi_{\rm R} - 1/6)R$, but as the latter redshifts as a^{-1}, it eventually becomes smaller than the fluctuation term. The resonance turns off after the effective mass becomes fully dominated by M_Δ^2, and $\delta\Delta_{\rm F}$ on average settles to a constant value. For $\lambda_{\rm R} = 10^{-4}$ and 10^{-1}, we find that $\delta\Delta_{\rm F}$ at the end of the tachyonic stage agrees relatively well with the adiabatic expansion results of [14]. However, the subsequent strongly non-linear resonant stage is not at all captured in the treatment of [14] and, as seen in figures 1 and 2, this stage gives the dominant contribution to $\delta\Delta_{\rm F}$ for $\lambda_{\rm R} = 10^{-4}$ and 10^{-1}.

The momentum space structure of $\delta\rho_{0\boldsymbol{k}}$ is shown in figure 3. For all three coupling values $\lambda_{\rm R} \in \{10^{-7}, 10^{-4}, 10^{-1}\}$, the leftmost continuous vertical structures, extending from $|\boldsymbol{k}| = 0$ to a finite cutoff set by the effective mass (and of the order of the Hubble scale), are states populated by the tachyonic instability.

For $\lambda_{\rm R} = 10^{-7}$ the ultraviolet region develops, around $a/a_0 \simeq 3$, discrete bands which reach to higher $|\boldsymbol{k}|$-modes than the initial structures, while the evolution is still dominated by M_R^2 (see figure 2). These bands appear to signal a resonant particle production sourced by the $\xi R\chi^2$-term, which can coexist with the tachyonic production [9, 12, 55]. We note

[2]Note that our results are expressed in terms of the comoving field $\sigma = a\chi$ while [14] uses the physical field χ. We have normalized the scale factor to $a_0 = 12.6$.

JHEP04(2023)043

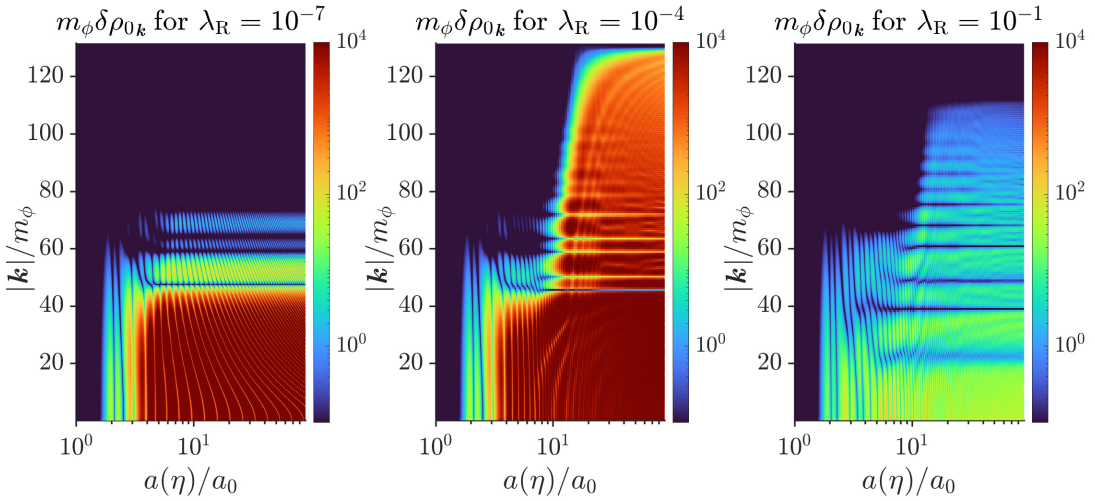

Figure 3. The zeroth moment $\delta\rho_{0\boldsymbol{k}}$ of the two point function for $\lambda_{\rm R} \in \{10^{-7}, 10^{-4}, 10^{-1}\}$ with $\bar{\xi}_{\rm R} = 50$ and $\Gamma = 0$.

that $\delta\rho_{0\boldsymbol{k}}$ continues to be strongly dominated by the lowest band but its peak shifts from $|\boldsymbol{k}| \approx 0$ towards the middle of the band.

For $\lambda_{\rm R} = 10^{-4}$ and 10^{-1} the momentum space evolution looks quantitatively similar as above until the moment when the effective mass gets dominated by the two-point function, $\langle M_\Delta^2 \rangle_{\rm osc} > \langle M_R^2 \rangle_{\rm osc}$, and $\delta\Delta_{\rm F}$ starts to grow rapidly (see figures 2 and 1). At this point, pronounced band structures emerge in figure 3, which we interpret to signal the onset of resonant particle production *driven by the coherent condensate* $\delta\Delta_{\rm F}$ *itself*. These resonance bands carry significant power and extend considerably above the $|\boldsymbol{k}|$-region populated during the M_R^2-dominated stage. Furthermore, it can be seen that the moment at which the resonant growth effectively stops in figure 1 corresponds to a further splitting and narrowing down of the resonance bands in figure 3. After this band splitting the resonant particle production loses efficiency and the average value of $\delta\Delta_{\rm F}$ becomes essentially a constant. While the $\delta\Delta_{\rm F}$-driven resonance is qualitatively similar to resonances driven by coherently oscillating classical fields, its origin from highly non-linear dynamics makes it difficult to develop a parametric understanding of its efficiency or time scale.

The evolution of the comoving particle number density n and the coherence function f^c are shown in figure 4. For $\lambda_{\rm R} = 10^{-7}$ both n and f^c settle to constant values after the end of the tachyonic growth. Comparing with [14], we find an order of magnitude smaller final number density for $\lambda_{\rm R} = 10^{-7}$, the reason being the same as for the difference in $\delta\Delta_{\rm F}$ discussed above. On the other hand, for $\lambda_{\rm R} \in \{10^{-4}, 10^{-1}\}$ the tachyonic stage is followed by a transient resonance, during which n and f^c grow further, and the resonant contribution actually dominates their final values. In these cases our results for the net particle number density exceed the corresponding results of [14] by an order of magnitude. Note that the particle production is necessarily associated with a growing coherence function [44]. The fact that coherence remains constant after particle production ends shows that the final state is highly squeezed. This is a special feature of our non-interacting system. In an

JHEP04(2023)043

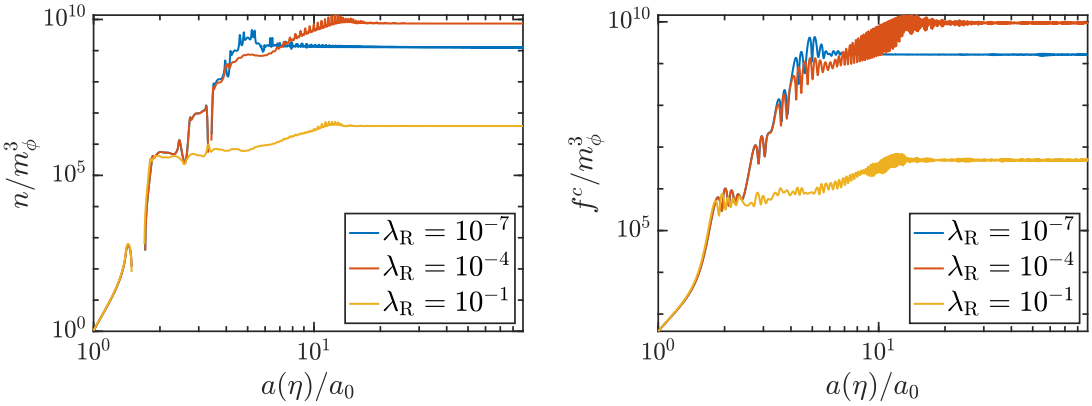

Figure 4. The integrated comoving particle number density n (left panel) and the integrated absolute value of the coherence functions f^c (right panel) for $\lambda_R \in \{10^{-7}, 10^{-4}, 10^{-1}\}$ with $\bar{\xi}_R = 50$ and $\Gamma = 0$.

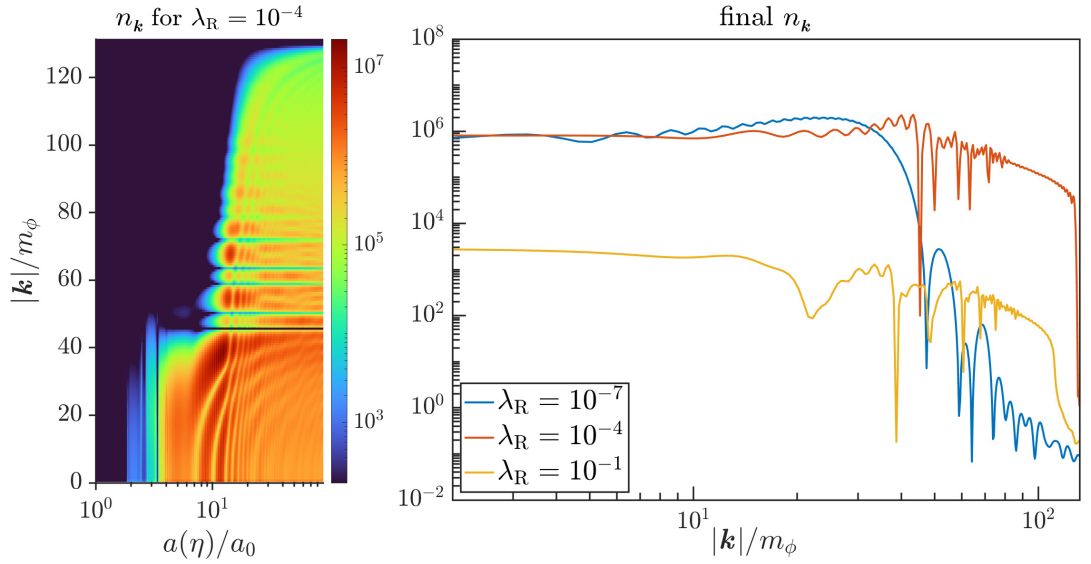

Figure 5. A contour plot of the comoving particle number density $n_{\boldsymbol{k}}$ for $\lambda_R = 10^{-4}$ (left panel), and the final comoving particle number density $n_{\boldsymbol{k}}(\eta_{\rm end})$ as a function of momentum for $\lambda_R \in \{10^{-7}, 10^{-4}, 10^{-1}\}$ (right panel). Both plots have $\bar{\xi}_R = 50$ and $\Gamma = 0$.

interacting system the coherence function would eventually tend to zero, reducing the quantum system to a non-coherent statistical state, even if the interactions were conserving the particle number. Such behaviour was indeed observed and studied in detailed in a toy model in [38].

In figure 5 we show the comoving particle number density per momentum $n_{\boldsymbol{k}}$. The right panel shows the final spectrum $n_{\boldsymbol{k}}$ at the final time of our numerical simulation for all couplings considered: $\lambda_R \in \{10^{-7}, 10^{-4}, 10^{-1}\}$. The left panel shows the full time evolution of $n_{\boldsymbol{k}}$ for the coupling $\lambda_R = 10^{-4}$. Apart from the oscillatory features, the structure of $n_{\boldsymbol{k}}$ is qualitatively in agreement with the results of [14], which, we recall, are obtained using a semianalytical adiabatic expansion approximation for the tachyonic particle production [9]

JHEP04(2023)043

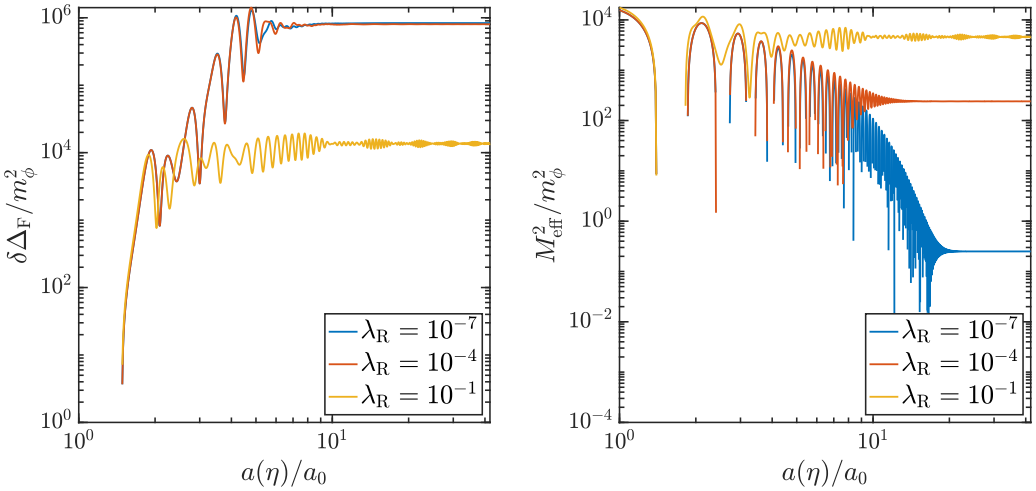

Figure 6. The two-point function $\delta\Delta_{\rm F}$ (left panel) and the effective mass function $M^2_{\rm eff}$ (right panel). The results are shown for $\lambda_{\rm R} \in \{10^{-7}, 10^{-4}, 10^{-1}\}$, $\bar{\xi}_{\rm R} = 50$ and $\Gamma \simeq 0.1H_0$.

and neglecting all resonant particle production (see also [55] for an analysis of resonant production through the $\xi R\chi^2$-term in the absence of self-couplings). The oscillatory features in $n_{\boldsymbol{k}}$ seen in our results arise from the transient resonance after the first tachyonic stage. As seen in the left panel of figure 5, $n_{\boldsymbol{k}}$ displays strong peaks coinciding with the onset of the resonance, located at the resonance bands and with the peak heights varying from band to band. Interestingly, the peaks begin to flatten out while the resonance is still ongoing. This effect is caused by non-linear processes mediated by the self-coupling which, combined with the redshifting, can efficiently redistribute the momenta.

Case II: $\bar{\xi}_{\rm R} = 50, \Gamma \simeq 0.1H_0$. For comparison, we also present results for the case with $\bar{\xi}_{\rm R} = 50$ and a non-zero inflaton decay rate $\Gamma \simeq 0.1H(\eta_0) \equiv 0.1H_0$. As explained in section 2, inflaton decays into radiation, as a result of which the universe evolves from effective matter domination to radiation domination where $R = 0$. The evolution of $\delta\Delta_{\rm F}$ and $M^2_{\rm eff}$, and the components of $M^2_{\rm eff}$ defined in equations (5.1), are shown in figures 6 and 7 for this case. As is seen in figure 7, the initial scaling $\langle R\rangle_{\rm osc} \propto a^{-3}$ is now followed by an exponential decay of $\langle R\rangle_{\rm osc}$ once the inflaton decay becomes efficient. This decreases the efficiency of tachyonic particle production compared to case I.

The evolution of $\delta\Delta_{\rm F}$ seen in figure 6 is now almost identical for the couplings $\lambda_{\rm R} = 10^{-7}$ and 10^{-4}. This is due to the fast decrease of R resulting from the inflaton decay, which ends the tachyonic growth before the two-point function starts to backreact into the dynamics also for $\lambda_{\rm R} = 10^{-4}$. This can also be seen from figure 7, which shows that in both these cases $\delta\Delta_{\rm F}$ stops growing before the two-point function backreacts into the dynamics. The evolution of $\delta\Delta_{\rm F}$ for $\lambda_{\rm R} = 10^{-7}$ is qualitatively similar to case I, but the final value of $\delta\Delta_{\rm F}$ is about two orders of magnitude smaller. For $\lambda_{\rm R} = 10^{-4}$, the evolution of $\delta\Delta_{\rm F}$ substantially differs from case I as the resonant stage that dominated the final value of $\delta\Delta_{\rm F}$ in case I is absent in case II. For the largest coupling $\lambda_{\rm R} = 10^{-1}$ the difference compared to case I is smallest as the tachyonic growth in this case still terminates via the backreaction when

JHEP04(2023)043

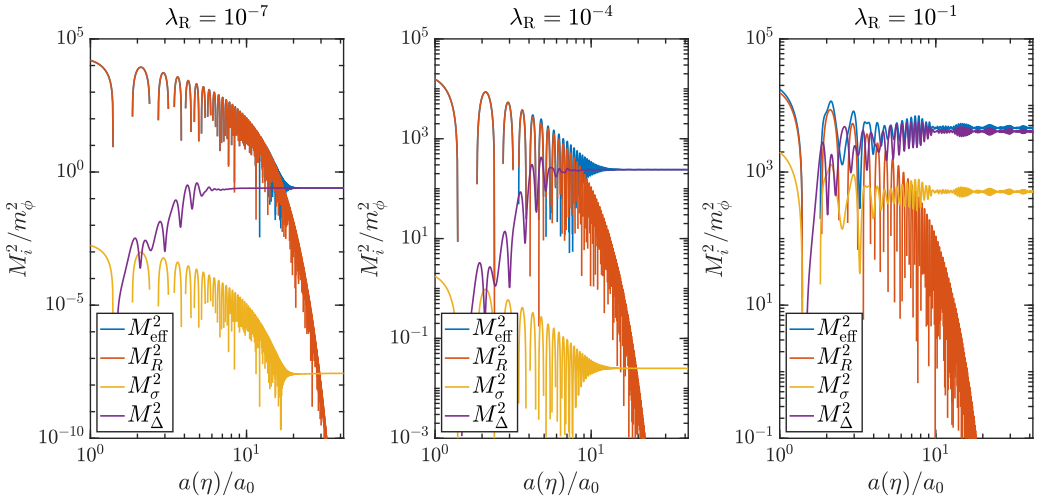

Figure 7. The effective mass function $M^2_{\rm eff}$ (blue) and its component functions M^2_R (red), M^2_Δ (violet) and M^2_σ (yellow), defined in equations (5.1), for $\lambda_{\rm R} \in \{10^{-7}, 10^{-4}, 10^{-1}\}$ in the case $\bar{\xi}_{\rm R} = 50$ and $\Gamma \simeq 0.1 H_0$.

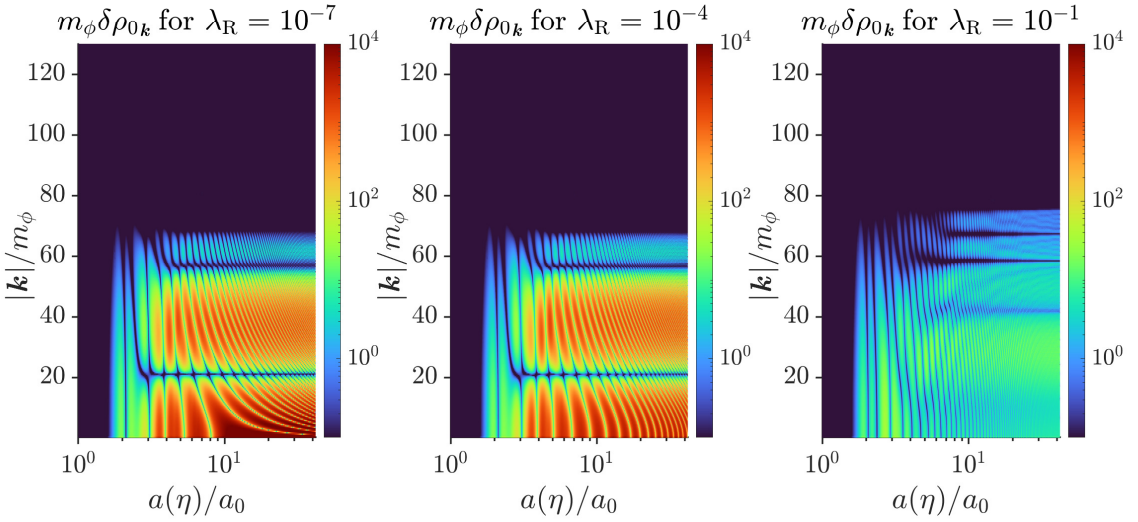

Figure 8. The zeroth moment $\delta\rho_{0\boldsymbol{k}}$ of the two point function for $\lambda_{\rm R} \in \{10^{-7}, 10^{-4}, 10^{-1}\}$ with $\bar{\xi}_{\rm R} = 50$ and $\Gamma \simeq 0.1 H_0$.

$\langle M^2_\Delta \rangle_{\rm osc} \sim \langle M^2_R \rangle$, and this happens before the exponential decrease of R sets in. In this case, the tachyonic stage is followed by resonant amplification of $\delta\Delta_{\rm F}$ driven by $\delta\Delta_{\rm F}$ itself, but the resonance is somewhat less efficient than in case I, leading to a factor of two smaller final value for $\delta\Delta_{\rm F}$.

Finally, the momentum structure of $\delta\rho_{0\boldsymbol{k}}$ is shown in figure 8. For $\lambda_{\rm R} = 10^{-7}$ the result looks qualitatively similar to case I but the band structures generated during the M^2_R-dominated epoch are more pronounced in case II. In particular, in case II the tachyonic region splits into two discrete bands at $a/a_0 \simeq 3$. The results for $\lambda_{\rm R} = 10^{-4}$ look almost identical to those for $\lambda_{\rm R} = 10^{-7}$, and the $\delta\Delta_{\rm F}$-driven resonance that dominated the final

JHEP04(2023)043

$\delta\rho_{0k}$ in case I is now completely absent. For $\lambda_{\rm R} = 10^{-1}$ the structure looks qualitatively similar to case I but it can be seen that the $\delta\Delta_{\rm F}$-driven resonance is less efficient and does not extend to as high momenta as in case II.

All in all, the results of cases I and II manifest the presence of complicated non-linear dynamics after the initial tachyonic particle production which can substantially affect the final value of $\delta\Delta_{\rm F}$. In particular, our results indicate that when the two-point function grows large enough to backreact into the dynamics, the tachyonic instability is followed by resonant particle production driven by the two-point function itself. In all cases studied here, we find that if the resonance takes place it also gives a dominant contribution to the final value of $\delta\Delta_{\rm F}$. However, the amount by which $\delta\Delta_{\rm F}$ grows during the resonance after the tachyonic stage appears to depend quite sensitively on the non-linear evolution of the two-point function coupled to R.

Finally, we note that in [39] classical lattice simulations were used to study a related non-minimally coupled spectator setup. They investigate a self-interacting massless spectator with $\lambda = 10^{-5}$ and $\xi = 100$, which remains energetically subdominant like in our case, but their results do not seem to show the resonant growth phase driven by $\delta\Delta_{\rm F}$. However, the inflaton potential in [39] differs from the quadratic form we use, which leads to different evolution of the curvature scalar R. A direct comparison of our respective results is therefore not possible, because the existence and efficiency of the resonant growth depends sensitively on the detailed interplay between R and the two-point function. It would be very interesting to make a detailed comparison between the 2PI-approach and classical lattice simulations in exactly the same setup, also going beyond the Hartree approximation, as it is not clear to what extent the quantum dynamics can be approximated by a classical system. Investigation of this topic however lies beyond the scope of our current work.

6 Conclusions

We have studied particle production at the end of inflation with a non-minimally coupled spectator scalar field that contributes to dark matter. We first introduced consistently renormalized coupled equations for the one- and two-point functions of the spectator field in the Hartree approximation using 2PI-methods. These equations correctly account for the backreaction of the out-of-equilibrium quantum modes created by the spinodal instability triggered by the oscillating Ricci scalar as well as for the subsequent parametric resonances. This model was studied earlier in [14] with an adiabatic treatment of the spinodal effects. Our results show that the interplay between the backreacting two-point function and the oscillating curvature sector lead to highly non-trivial dynamics which can have a significant effect on the net particle number density.

We solved numerically the coupled equations for the one- and two-point functions of the spectator field (the latter expressed as moment equations in the Wigner representation) together with the dynamical evolution of the inflaton sector for different values of the spectator field self-coupling $\lambda_{\rm R}$ and for the minimal coupling $\bar{\xi}_{\rm R} = 50$. We studied first the case of a non-interacting inflaton field and found that for a small coupling $\lambda_{\rm R} = 10^{-7}$ the generated particle number density is an order of magnitude smaller than that found in [14],

JHEP04(2023)043

whereas for $\lambda_{\rm R} = 10^{-4}$ and 10^{-1} it becomes and order of magnitude larger. For $\lambda_{\rm R} = 10^{-7}$ this is due to the tachyonic particle production shutting off already before the competing mass contributions from the curvature and the two-point function become comparable, while for the larger couplings the difference is due to efficient resonant particle production occurring after the tachyonic stage. In particular the resonant production, which actually dominates the contribution to the particle number density for larger couplings, is completely absent in the adiabatic approach of [14].

We also included a coupling between the inflaton and a radiation component to study the evolution under the transition from effective matter domination to radiation domination with $R = 0$. We found that the exponential decay of R induced by the radiation coupling renders both the spinodal and the resonant particle production processes much less efficient compared to the case with a non-interacting inflaton. For the tachyonic processes this is easy to understand as the oscillating curvature term, which is responsible for the tachyonic bursts in the particle number density, is rapidly driven to zero. Our results suggest the presence of an R-assisted resonance enhancement, where the resonant particle production driven by the two-point function is boosted by the decaying $\xi R\chi^2$-term after the tachyonic stage has come to an end. This is a highly non-linear phenomenon which, when present, appears to dominate the net particle production. It cannot be properly captured without a full treatment of the backreaction effects.

The final momentum distribution of the dark relics generated by the non-perturbative processes is highly non-thermal. This could lead to characteristic and potentially observable imprints in the structure formation, as pointed out in [14]. The evolution of the relic distribution after the epoch of reheating depends on dark sector interactions, possibly including new types not considered here. Although this would be an interesting problem in itself, we do not investigate it further here.

It would obviously be interesting to extend our setup to the case of a spectator field coupled to other matter fields. This could be done rather easily by combining the current results with the quantum transport formalism for interacting fermions introduced in [56]. Also, it would be interesting to extend our classical treatment of the inflaton to quantum level. It would then be particularly interesting to study the gravitational wave production during the reheating stage in the most general computational framework described above.

Acknowledgments

This work was supported by computer capacity from the Finnish Grid and Cloud Infrastructure (persistent identifier urn:nbn:fi:research-infras-2016072533). OK was in addition supported by a grant from the Magnus Ehrnrooth Foundation. We wish to thank Anna Tokareva for many useful discussions and comments on the manuscript.

JHEP04(2023)043

References

[1] L. Kofman, A.D. Linde and A.A. Starobinsky, *Reheating after inflation*, *Phys. Rev. Lett.* **73** (1994) 3195 [hep-th/9405187] [INSPIRE].

[2] L. Kofman, A.D. Linde and A.A. Starobinsky, *Towards the theory of reheating after inflation*, *Phys. Rev. D* **56** (1997) 3258 [hep-ph/9704452] [INSPIRE].

[3] P.B. Greene, L. Kofman, A.D. Linde and A.A. Starobinsky, *Structure of resonance in preheating after inflation*, *Phys. Rev. D* **56** (1997) 6175 [hep-ph/9705347] [INSPIRE].

[4] J. Braden, L. Kofman and N. Barnaby, *Reheating the Universe After Multi-Field Inflation*, *JCAP* **07** (2010) 016 [arXiv:1005.2196] [INSPIRE].

[5] J. Berges and J. Serreau, *Parametric resonance in quantum field theory*, *Phys. Rev. Lett.* **91** (2003) 111601 [hep-ph/0208070] [INSPIRE].

[6] E. Calzetta, *Spinodal Decomposition in Quantum Field Theory*, *Annals Phys.* **190** (1989) 32 [INSPIRE].

[7] A.H. Guth and S.-Y. Pi, *The Quantum Mechanics of the Scalar Field in the New Inflationary Universe*, *Phys. Rev. D* **32** (1985) 1899 [INSPIRE].

[8] E.J. Weinberg and A.-Q. Wu, *Understanding Complex Perturbative Effective Potentials*, *Phys. Rev. D* **36** (1987) 2474 [INSPIRE].

[9] J.F. Dufaux et al., *Preheating with trilinear interactions: Tachyonic resonance*, *JCAP* **07** (2006) 006 [hep-ph/0602144] [INSPIRE].

[10] G.N. Felder et al., *Dynamics of symmetry breaking and tachyonic preheating*, *Phys. Rev. Lett.* **87** (2001) 011601 [hep-ph/0012142] [INSPIRE].

[11] G.N. Felder, L. Kofman and A.D. Linde, *Tachyonic instability and dynamics of spontaneous symmetry breaking*, *Phys. Rev. D* **64** (2001) 123517 [hep-th/0106179] [INSPIRE].

[12] B.A. Bassett and S. Liberati, *Geometric reheating after inflation*, *Phys. Rev. D* **58** (1998) 021302 [*Erratum ibid.* **60** (1999) 049902] [hep-ph/9709417] [INSPIRE].

[13] T. Markkanen and S. Nurmi, *Dark matter from gravitational particle production at reheating*, *JCAP* **02** (2017) 008 [arXiv:1512.07288] [INSPIRE].

[14] M. Fairbairn, K. Kainulainen, T. Markkanen and S. Nurmi, *Despicable Dark Relics: generated by gravity with unconstrained masses*, *JCAP* **04** (2019) 005 [arXiv:1808.08236] [INSPIRE].

[15] J.M. Cline, M. Joyce and K. Kainulainen, *Supersymmetric electroweak baryogenesis*, *JHEP* **07** (2000) 018 [hep-ph/0006119] [INSPIRE].

[16] K. Kainulainen, T. Prokopec, M.G. Schmidt and S. Weinstock, *First principle derivation of semiclassical force for electroweak baryogenesis*, *JHEP* **06** (2001) 031 [hep-ph/0105295] [INSPIRE].

[17] K. Kainulainen, T. Prokopec, M.G. Schmidt and S. Weinstock, *Semiclassical force for electroweak baryogenesis: Three-dimensional derivation*, *Phys. Rev. D* **66** (2002) 043502 [hep-ph/0202177] [INSPIRE].

[18] J.M. Cline, K. Kainulainen, P. Scott and C. Weniger, *Update on scalar singlet dark matter*, *Phys. Rev. D* **88** (2013) 055025 [*Erratum ibid.* **92** (2015) 039906] [arXiv:1306.4710] [INSPIRE].

JHEP04(2023)043

[19] J.M. Cline, K. Kainulainen and D. Tucker-Smith, *Electroweak baryogenesis from a dark sector*, *Phys. Rev. D* **95** (2017) 115006 [arXiv:1702.08909] [INSPIRE].

[20] J.M. Cline and K. Kainulainen, *Electroweak baryogenesis at high bubble wall velocities*, *Phys. Rev. D* **101** (2020) 063525 [arXiv:2001.00568] [INSPIRE].

[21] T. Konstandin, *Quantum Transport and Electroweak Baryogenesis*, *Phys. Usp.* **56** (2013) 747 [arXiv:1302.6713] [INSPIRE].

[22] K. Kainulainen, *CP-violating transport theory for electroweak baryogenesis with thermal corrections*, *JCAP* **11** (2021) 042 [arXiv:2108.08336] [INSPIRE].

[23] W. Buchmüller and S. Fredenhagen, *Quantum mechanics of baryogenesis*, *Phys. Lett. B* **483** (2000) 217 [hep-ph/0004145] [INSPIRE].

[24] M. Beneke et al., *Flavoured Leptogenesis in the CTP Formalism*, *Nucl. Phys. B* **843** (2011) 177 [arXiv:1007.4783] [INSPIRE].

[25] A. Anisimov, W. Buchmüller, M. Drewes and S. Mendizabal, *Quantum Leptogenesis I*, *Annals Phys.* **326** (2011) 1998 [arXiv:1012.5821] [INSPIRE].

[26] P.S.B. Dev et al., *Flavor effects in leptogenesis*, *Int. J. Mod. Phys. A* **33** (2018) 1842001 [arXiv:1711.02861] [INSPIRE].

[27] A. De Simone and A. Riotto, *Quantum Boltzmann Equations and Leptogenesis*, *JCAP* **08** (2007) 002 [hep-ph/0703175] [INSPIRE].

[28] M. Garny, A. Hohenegger, A. Kartavtsev and M. Lindner, *Systematic approach to leptogenesis in nonequilibrium QFT: Self-energy contribution to the CP-violating parameter*, *Phys. Rev. D* **81** (2010) 085027 [arXiv:0911.4122] [INSPIRE].

[29] B. Garbrecht and M. Herranen, *Effective Theory of Resonant Leptogenesis in the Closed-Time-Path Approach*, *Nucl. Phys. B* **861** (2012) 17 [arXiv:1112.5954] [INSPIRE].

[30] M. Garny, A. Kartavtsev and A. Hohenegger, *Leptogenesis from first principles in the resonant regime*, *Annals Phys.* **328** (2013) 26 [arXiv:1112.6428] [INSPIRE].

[31] B. Dev et al., *Resonant enhancement in leptogenesis*, *Int. J. Mod. Phys. A* **33** (2018) 1842003 [arXiv:1711.02863] [INSPIRE].

[32] H. Jukkala, K. Kainulainen and P.M. Rahkila, *Flavour mixing transport theory and resonant leptogenesis*, *JHEP* **09** (2021) 119 [arXiv:2104.03998] [INSPIRE].

[33] D. Boyanovsky and H.J. de Vega, *Quantum rolling down out-of-equilibrium*, *Phys. Rev. D* **47** (1993) 2343 [hep-th/9211044] [INSPIRE].

[34] D. Boyanovsky, D.-S. Lee and A. Singh, *Phase transitions out-of-equilibrium: Domain formation and growth*, *Phys. Rev. D* **48** (1993) 800 [hep-th/9212083] [INSPIRE].

[35] J. Baacke and S. Michalski, *Nonequilibrium evolution in scalar $O(N)$ models with spontaneous symmetry breaking*, *Phys. Rev. D* **65** (2002) 065019 [hep-ph/0109137] [INSPIRE].

[36] A. Arrizabalaga, J. Smit and A. Tranberg, *Tachyonic preheating using $2PI$-$1/N$ dynamics and the classical approximation*, *JHEP* **10** (2004) 017 [hep-ph/0409177] [INSPIRE].

[37] A. Arrizabalaga, J. Smit and A. Tranberg, *Equilibration in ϕ^4 theory in $3+1$ dimensions*, *Phys. Rev. D* **72** (2005) 025014 [hep-ph/0503287] [INSPIRE].

[38] K. Kainulainen and O. Koskivaara, *Non-equilibrium dynamics of a scalar field with quantum backreaction*, *JHEP* **12** (2021) 190 [arXiv:2105.09598] [INSPIRE].

JHEP04(2023)043

[39] D.G. Figueroa, A. Florio, T. Opferkuch and B.A. Stefanek, *Dynamics of Non-minimally Coupled Scalar Fields in the Jordan Frame*, arXiv:2112.08388 [INSPIRE].

[40] M. Herranen, K. Kainulainen and P.M. Rahkila, *Towards a kinetic theory for fermions with quantum coherence*, *Nucl. Phys. B* **810** (2009) 389 [arXiv:0807.1415] [INSPIRE].

[41] M. Herranen, K. Kainulainen and P.M. Rahkila, *Quantum kinetic theory for fermions in temporally varying backgrounds*, *JHEP* **09** (2008) 032 [arXiv:0807.1435] [INSPIRE].

[42] M. Herranen, K. Kainulainen and P.M. Rahkila, *Kinetic theory for scalar fields with nonlocal quantum coherence*, *JHEP* **05** (2009) 119 [arXiv:0812.4029] [INSPIRE].

[43] M. Herranen, K. Kainulainen and P.M. Rahkila, *Coherent quantum Boltzmann equations from cQPA*, *JHEP* **12** (2010) 072 [arXiv:1006.1929] [INSPIRE].

[44] C. Fidler, M. Herranen, K. Kainulainen and P.M. Rahkila, *Flavoured quantum Boltzmann equations from cQPA*, *JHEP* **02** (2012) 065 [arXiv:1108.2309] [INSPIRE].

[45] I.L. Buchbinder, S.D. Odintsov and I.L. Shapiro, *Effective action in quantum gravity*, CRC Press (1992) [ISBN: 9780750301220] [INSPIRE].

[46] J.M. Cornwall, R. Jackiw and E. Tomboulis, *Effective Action for Composite Operators*, *Phys. Rev. D* **10** (1974) 2428 [INSPIRE].

[47] J. Berges, *Introduction to nonequilibrium quantum field theory*, *AIP Conf. Proc.* **739** (2004) 3 [hep-ph/0409233] [INSPIRE].

[48] L.V. Keldysh, *Diagram technique for nonequilibrium processes*, *Zh. Eksp. Teor. Fiz.* **47** (1964) 1515 [INSPIRE].

[49] J. Berges, S. Borsanyi, U. Reinosa and J. Serreau, *Nonperturbative renormalization for 2PI effective action techniques*, *Annals Phys.* **320** (2005) 344 [hep-ph/0503240] [INSPIRE].

[50] G. Fejos, A. Patkos and Z. Szep, *Renormalisability of the 2PI-Hartree approximation of multicomponent scalar models in the broken symmetry phase*, *Nucl. Phys. A* **803** (2008) 115 [arXiv:0711.2933] [INSPIRE].

[51] T. Arai, *Renormalization of the 2PI Hartree-Fock approximation on de Sitter background in the broken phase*, *Phys. Rev. D* **86** (2012) 104064 [arXiv:1204.0476] [INSPIRE].

[52] A. Pilaftsis and D. Teresi, *Exact RG Invariance and Symmetry Improved 2PI Effective Potential*, *Nucl. Phys. B* **920** (2017) 298 [arXiv:1703.02079] [INSPIRE].

[53] A. Pilaftsis and D. Teresi, *Symmetry Improved CJT Effective Action*, *Nucl. Phys. B* **874** (2013) 594 [arXiv:1305.3221] [INSPIRE].

[54] G. Amelino-Camelia and S.-Y. Pi, *Selfconsistent improvement of the finite temperature effective potential*, *Phys. Rev. D* **47** (1993) 2356 [hep-ph/9211211] [INSPIRE].

[55] J.A.R. Cembranos, L.J. Garay and J.M. Sánchez Velázquez, *Gravitational production of scalar dark matter*, *JHEP* **06** (2020) 084 [arXiv:1910.13937] [INSPIRE].

[56] H. Jukkala, K. Kainulainen and O. Koskivaara, *Quantum transport and the phase space structure of the Wightman functions*, *JHEP* **01** (2020) 012 [arXiv:1910.10979] [INSPIRE].

JHEP04(2023)043